



The Journal of Gemmology

Volume 37 / No. 2 / 2020



Characteristics of
Burmese Amber

.....
Cultured Pearls
from Abu Dhabi

.....
Diamonds from
Suriname

.....
Pink Axinite from
Tanzania

SSEF

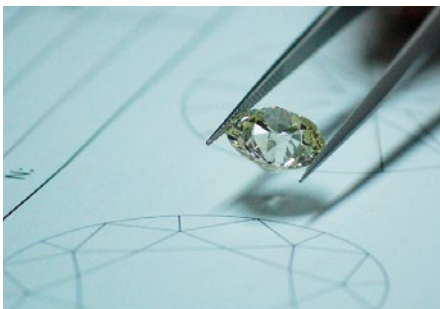
SCHWEIZERISCHES GEMMOLOGISCHES INSTITUT
SWISS GEMMOLOGICAL INSTITUTE
INSTITUT SUISSE DE GEMMOLOGIE



ORIGIN DETERMINATION · TREATMENT DETECTION

DIAMOND GRADING · PEARL TESTING

EDUCATION · RESEARCH



THE SCIENCE OF GEMSTONE TESTING™



Cover photo: An article on pp. 144-162 of this issue describes the characteristics of different varieties of amber from Myanmar. This Burmese amber carving, measuring 99 x 42 x 28 mm and weighing 66.6 g, was inspired by the poem 'A Night Mooring by Maple Bridge' written by Zhang Ji during the Tang Dynasty. The piece incorporates the natural amber textures to show an autumn scene outside Hanshan Temple, where a bridge is surrounded by maple trees. Photo courtesy of Tengchong Huo Ren Carving Studio.

COLUMNS

What's New 115

CIBJO Blue Books | Diamond Terminology Guidelines | GemGuide Articles | GIT Lab Reports on Blue Richterite and a Zultanite Imitation | Jewelry Development Impact Index Reports | Platinum Jewellery Business Review 2020 | SSEF *Facette Magazine* | Centurion Jewelry Show's Lectures in Tucson | Minerals, Materials and Society Programme | Mozambique Ruby Video | Webinars and Other Videos for Online Gemmological Education

Gem Notes 120

Trapiche-like Pattern in Amethyst | Aquamarine with Spodumene Inclusions from the Oceanview Mine, California, USA | Demantoid/Andradite Slices from Iran | Blue Diopside from Russia | Cat's-Eye Emeralds from Colombia | Euchroite from Slovakia | Properties of Green Fluorite from England Showing Daylight Fluorescence | Jewellery Set with Green Fluorite from England | Frankamenite as an Ornamental Gem Material | Colour-Change Garnet from Tanga, Tanzania | Hessonite from Somaliland | Laurentthomasite, a New Gem Mineral | Green Orthoclase with Chatoyancy from Vietnam | Faceted Proustite from Chañarcillo, Chile | Blue Spinel Mining in Vietnam

ARTICLES

Gemmological and Spectroscopic Characteristics of Different Varieties of Amber from the Hukawng Valley, Myanmar **144**

By Xinran Jiang, Zhiqing Zhang, Yamei Wang and Fanli Kong

Saltwater Cultured Pearls from *Pinctada radiata* in Abu Dhabi (United Arab Emirates) **164**

By Abeer Al-Alawi, Zainab Ali, Zainab Rajab, Fatema Albedal and Stefanos Karampelas

Diamonds from the Nassau Mountains, Suriname **180**

By Renoesha Naipal, J. C. (Hanco) Zwaan, Salomon B. Kroonenberg, Leo M. Kriegsman and Paul R. D. Mason

Pink Axinite from Merelani, Tanzania: Origin of Colour and Luminescence **192**

By Maxence Vigier and Emmanuel Fritsch



Photo courtesy of the Abu Dhabi Pearls project



Photo by N. Sardjoe



Photo by Jeff Scovil

Excursions Luc Yen, Vietnam **206**

Gem-A Notices **214** **New Media** **219**

Learning Opportunities **216** **Literature of Interest** **224**

The Journal is published by Gem-A in collaboration with SSEF and with the support of AGL.



The Journal of Gemmology

EDITORIAL STAFF

Editor-in-Chief
Brendan M. Laurs
brendan.laurs@gem-a.com

Executive Editor
Alan D. Hart

Editorial Assistant
Carol M. Stockton

Editor Emeritus
Roger R. Harding

ASSOCIATE EDITORS

Ahmadjan Abduriyim
Tokyo Gem Science LLC,
Tokyo, Japan

Raquel Alonso-Perez
Harvard University,
Cambridge, Massachusetts,
USA

Edward Boehm
RareSource, Chattanooga,
Tennessee, USA

Maggie Campbell Pedersen
Organic Gems, London

Alan T. Collins
King's College London

John L. Emmett
Crystal Chemistry, Brush
Prairie, Washington, USA

Emmanuel Fritsch
University of Nantes,
France

Rui Galopim de Carvalho
PortugalGemas Academy,
Lisbon, Portugal

Al Gilbertson
Gemological Institute
of America, Carlsbad,
California

Lee A. Groat
University of British
Columbia, Vancouver,
Canada

Thomas Hainschwang
GCTL Laboratories,
Balzers, Liechtenstein

Henry A. Hänni
GemExpert, Basel,
Switzerland

Jeff W. Harris
University of Glasgow

Alan D. Hart
Gem-A, London

Ulrich Henn
German Gemmological
Association, Idar-Oberstein

Jaroslav Hyršl
Prague, Czech Republic

Brian Jackson
National Museums
Scotland, Edinburgh

Mary L. Johnson
Mary Johnson Consulting,
San Diego, California, USA

Stefanos Karampelas
Bahrain Institute for Pearls
& Gemstones (DANAT),
Manama

Lore Kiefert
Gübelin Gem Lab Ltd,
Lucerne, Switzerland

Hiroshi Kitawaki
Central Gem Laboratory,
Tokyo, Japan

Michael S. Krzemnicki
Swiss Gemmological
Institute SSEF, Basel

Shane F. McClure
Gemological Institute
of America, Carlsbad,
California

Jack M. Ogden
London

Federico Pezzotta
Natural History Museum
of Milan, Italy

Jeffrey E. Post
Smithsonian Institution,
Washington DC, USA

Andrew H. Rankin
Kingston University, Surrey

Benjamin Rondeau
University of Nantes, France

George R. Rossman
California Institute of
Technology, Pasadena, USA

Karl Schmetzer
Petershausen, Germany

Dietmar Schwarz
Federated International
GemLab, Bangkok, Thailand

Menahem Sevdermish
Gemewizard Ltd, Ramat
Gan, Israel

Andy H. Shen
China University of
Geosciences, Wuhan

Guanghai Shi
China University of
Geosciences, Beijing

James E. Shigley
Gemological Institute
of America, Carlsbad,
California

Christopher P. Smith
American Gemological
Laboratories Inc.,
New York, New York

Evelyne Stern
London

Elisabeth Strack
Gemmologisches Institut
Hamburg, Germany

Tay Thye Sun
Far East Gemological
Laboratory, Singapore

Frederick 'Lin' Sutherland
Port Macquarie, New
South Wales, Australia

Pornsawat Wathanakul
Kasetsart University,
Bangkok

Chris M. Welbourn
Reading, Berkshire

Bert Willems
Leica Microsystems,
Wetzlar, Germany

Bear Williams
Stone Group Laboratories
LLC, Jefferson City,
Missouri, USA

J. C. (Hanco) Zwaan
National Museum of
Natural History 'Naturalis',
Leiden, The Netherlands



Gem-A

THE GEMMOLOGICAL ASSOCIATION
OF GREAT BRITAIN

21 Ely Place
London EC1N 6TD
UK

t: +44 (0)20 7404 3334
f: +44 (0)20 7404 8843
e: information@gem-a.com
w: <https://gem-a.com>

Registered Charity No. 1109555
A company limited by guarantee and
registered in England No. 1945780
Registered office: Palladium House,
1-4 Argyll Street, London W1F 7LD

PRESIDENT

Maggie Campbell Pedersen

VICE PRESIDENTS

David J. Callaghan
Alan T. Collins
Noel W. Deeks
Andrew H. Rankin

HONORARY FELLOWS

Gaetano Cavaliere
Andrew Cody
Terrence S. Coldham
Emmanuel Fritsch

HONORARY DIAMOND MEMBER

Martin Rapaport

CHIEF EXECUTIVE OFFICER

Alan D. Hart

COUNCIL

Justine L. Carmody – Chair
Nevin Bayoumi-Stefanovic
Kathryn L. Bonanno
Louise Goldring
Joanna Hardy
Philip Sadler
Christopher P. Smith

BRANCH CHAIRMEN

Midlands – Louise Ludlam-Snook
North East – Mark W. Houghton

COVERED BY THE FOLLOWING ABSTRACTING AND INDEXING SERVICES:

Clarivate Analytics' (formerly Thomson Reuters/ISI) Science Citation Index Expanded (in the Web of Science), *Journal Citation Reports (Science Edition)* and *Current Contents (Physical, Chemical and Earth Sciences)*; Elsevier's Scopus; Australian Research Council's Excellence in Research for Australia (ERA) Journal List; China National Knowledge Infrastructure (CNKI Scholar); EBSCO's Academic Search Ultimate; ProQuest (Cambridge Scientific Abstracts); GeoRef; CrossRef; Chemical Abstracts (CA Plus); Mineralogical Abstracts; Index Copernicus ICI Journals Master List; Gale Academic OneFile; British Library Document Supply Service; and Copyright Clearance Center's RightFind application.

Science Citation Index
Expanded

Web of Science

CONTENT SUBMISSION

The Editor-in-Chief is glad to consider original articles, news items, conference reports, announcements and calendar entries on subjects of gemmological interest for publication in *The Journal of Gemmology*. A guide to the various sections and the preparation of manuscripts is given at <https://gem-a.com/membership/journal-of-gemmology/submissions>, or contact the Editor-in-Chief.

SUBSCRIPTIONS

Gem-A members receive *The Journal* as part of their membership package, full details of which are given at <https://gem-a.com/membership>. Laboratories, libraries, museums and similar institutions may become direct subscribers to *The Journal*; download the form from *The Journal's* home page.

ADVERTISING

Enquiries about advertising in *The Journal* should be directed to advertising@gem-a.com. For more information, see <https://gem-a.com/membership/media-pack-2020>.

COPYRIGHT AND REPRINT PERMISSION

For full details of copyright and reprint permission contact the Editor-in-Chief. *The Journal of Gemmology* is published quarterly by Gem-A, The Gemmological Association of Great Britain. Any opinions expressed in *The Journal* are understood to be the views of the contributors and not necessarily of the publisher.

DESIGN & PRODUCTION

Zest Design, London. www.zest-uk.com

PRINTER

DG3 Group (Holdings) Ltd, London. www.dg3.com



© 2020 Gem-A (The Gemmological Association of Great Britain)
ISSN 1355-4565 (Print), ISSN 2632-1718 (Online)

What's New

NEWS AND PUBLICATIONS

CIBJO Blue Books Freely Available

The Blue Books from CIBJO, The World Jewellery Confederation, are the most widely accepted set of global standards for the gem and jewellery industry. In response to the economic challenges created by the COVID-19 pandemic, in April 2020 CIBJO made all seven volumes freely available for download, even to non-members. They cover standards for diamonds, coloured stones, gemmological laboratories, pearls, precious metals, coral and responsible sourcing. Download the PDFs at www.cibjo.org/introduction-to-the-blue-books-2.



Diamond Terminology Guidelines



In September 2019, the Diamond Producers Association, in conjunction with seven other leading diamond industry organisations, issued a brief reference guide on standard terminology to use when referring to natural and synthetic diamonds. The document also includes definitions and recommendations based on the internationally accepted standard ISO 18323 ('Jewellery – Consumer Confidence in the Diamond Industry') and CIBJO's Diamond Blue Book. Download the one-page PDF at <https://diamondproducers.com/app/uploads/2019/09/Diamond-Terminology-Guideline-20190925.pdf>.

GemGuide Articles Freely Available

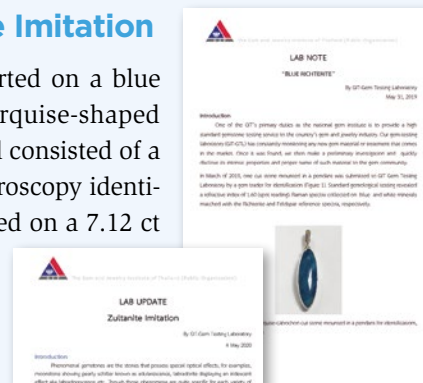
Selected articles from Gemworld International's bimonthly *GemGuide* publication are now freely available at www.gemguide.com/category/web-feature-articles. They cover topics such as Ethiopian emerald, Greenland ruby, Old European-cut diamonds,

and a series on coloured stone value factors, design and cut quality. Also freely available are *GemGuide's* 'Gem Focus & Market Pulse' articles, which focus on specific gem materials, at www.gemguide.com/category/gem-market-pulse.



GIT Lab Reports on Blue Richterite and a Zultanite Imitation

In May 2019, the Gem and Jewelry Institute of Thailand (GIT) reported on a blue richterite submitted to their laboratory for identification. The marquise-shaped cabochon, which was bezel-set in a pendant, had a spot RI of 1.60 and consisted of a granular aggregate of blue and white mineral grains that Raman spectroscopy identified as richterite (blue) and feldspar (white). In May 2020, GIT reported on a 7.12 ct oval modified brilliant showing a colour change that was represented as Zultanite (diaspore). Gemmological, spectral and chemical characteristics clearly identified it as a manufactured glass. Download these and previous GIT lab reports at www.git.or.th/articles_tech_en.html.



Jewelry Development Impact Index Reports

Two more Jewelry Development Impact Index (JDI) studies have been published by researchers from the American University School of International Service, which are titled *A Comparative Case Study of Amethyst Mining in Brazil and Tanzanite Mining in Tanzania* (December 2019) and *A Comparative Case Study of Diamond Mining in Guinea, Sierra Leone, and Zimbabwe* (April 2020). The reports examine the historical and cultural background of mining these deposits, and then provide numerical scores on a variety of areas (governance, economy, environment, health and human rights) for the subject countries. Download these and other JDI publications at www.sustainablegemstones.org/jewelry-development-index-jdi.

Brendan M. Laurs



SSEF Facette Magazine

Issue 26 of the Swiss Gemmological Institute SSEF's annual *Facette Magazine* was released in February 2020. The 76-page issue is packed with short articles that cover boundaries for colour varieties of gems, age dating of coloured stones, SSEF's Gemtrack rough-to-cut documentation service, laser inscription of gems, DNA fingerprinting of pearls and corals, and identification of ivory species, as well as numerous others on topics such as spodumene, emerald, ruby, sapphire, garnet, vesuvianite, diamond, pearls, historical gems and *objets d'art*. The issue ends with news and announcements relating to SSEF, including the discovery of a fraudulent SSEF report. To download this and previous issues of *Facette*, visit www.ssef.ch/ssef-facette.



PLATINUM GUILD
INTERNATIONAL

Tectonic shifts: How the world is moving
and jewellery demand is responding

Platinum Jewellery Business Review, 2020
Web presentation
20th May 2020

Platinum Jewellery Business Review 2020

Platinum Guild International's (PGI) annual *Platinum Jewellery Business Review* was released in May 2020. The report analyses retail sales of platinum jewellery, trade performance and consumer sentiment in order to provide an in-depth analysis of platinum jewellery's performance in 2019, as well as COVID-19's impact in PGI's four key international markets (China, India, Japan and the United States). The report focuses on three trends: digital consolidation, mid-market extinction and branded storytelling. To view a 45-minute video presentation or download the report, visit <https://platinumguild.com/2020-platinum-jewellery-business-review>.

Brendan M. Laurs

OTHER RESOURCES



Centurion Jewelry Show's Lectures in Tucson

The Centurion Jewelry Show in Tucson, Arizona, USA, hosted lectures at its Gem Education Day on 1 February 2020. Videos of six lectures are now available online. These cover markets for Colombian emerald and red beryl; rare and exotic gem materials; millennials and younger demographics; emeralds; ruby and sapphire; and East African gems. Visit www.youtube.com/channel/UC6lT-m_06z_0mObphTTX2uQ.

Minerals, Materials and Society Programme



The Minerals, Materials and Society programme at the University of Delaware (Newark, Delaware, USA) launched in January 2020 and focuses on sustainability and corporate social responsibility in mineral sourcing (<https://sites.udel.edu/ceoe-mms>). Videos on gem and jewellery topics, ranging from understanding coloured gemstones to women's participation in the jewellery supply chain in Madagascar, are hosted on the programme's YouTube channel at www.youtube.com/channel/UCJmN3DG0BVQErNI3HzRGqYA/videos.



Mozambique Ruby Video

In May 2020, GemResearch Swisslab AG (Lucerne, Switzerland) released a documentary video on an exceptional suite of Mozambique rubies initially acquired as rough at a Gemfields ruby auction in Singapore. The video begins with an examination of the rough material by Dr Adolf Peretti, and then follows the rubies through the cutting process in Sri Lanka and Thailand. Each step, from the purchase of rough to the finished gems, is explained in detail. Visit <http://gemresearch.ch/mozambique-ruby-collection>.

Webinars and Other Videos for Online Gemmological Education

A number of educational institutions and gem industry organisations have provided webinars and other archived video content on their websites or YouTube channels, with many added since March 2020 due to the quarantines mandated by the COVID-19 pandemic.

- The **American Gem Trade Association** (Dallas, Texas, USA) has made its AGTA GemFair Tucson Seminar Series freely available for the years 2018, 2019 and 2020. The presentations cover gem identification, appraisals, marketing strategies, industry trends and much more. Visit <https://agta.org/resources>.



- The **Asian Institute of Gemological Sciences** (Bangkok, Thailand) has produced a series of 'AIGS Gem Tips' webinars presented by a diverse group of experts. Topics include the history of emeralds, rubies from Greenland, sapphires from Montana (USA), brown diamonds and gem luminescence. Visit www.aigsthailand.com/AIGS-News/4/master/en.



- The **Bahrain Institute for Pearls and Gemstones** (DANAT; Manama, Bahrain) has webinars on natural pearls of Bahrain, testing for natural vs. cultured pearls, diamonds (natural, synthetic and imitation) and how to buy a gemstone. Visit www.youtube.com/playlist?list=PLa8o6T7AzU1E1oTTBIMzhkpw0jn5Ev5n6.



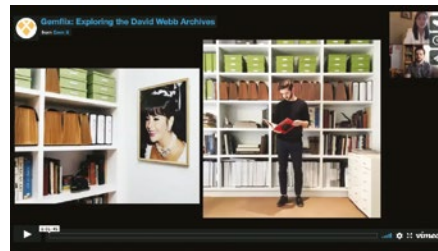
- **Gemewizard** (Ramat Gan, Israel) offers webinars covering coloured stone and coloured diamond grading; colour trends in gemstones during pre- and post-COVID-19 times; and grading, pricing and market trends of yellow diamonds. Visit www.youtube.com/channel/UCQKKaw5_kBupL6BMUsAEO2w.



- **Branko Gems and Gemmological Research Industries Inc.** (Vancouver, British Columbia, Canada) offers webinars by gemmologist Branko Deljanin focusing on gemmological instruments and the screening and identification of coloured stones and diamonds. The videos are available for a fee at www.brankogems.com/shop/product-category/webinars.



- **GemfliX** (New York, New York, USA) has a series of 'online jewelry chats' that feature jewellery design, gem cutting, auctions, history and more at www.gemx.club/gemflix. Chat-series videos are free, but other GemfliX videos require a Gem X membership.



- **CIBJO, The World Jewellery Confederation** (Milan, Italy) hosts gem and jewellery industry webinars at www.cibjo.org/webinars, which are grouped into different series such as 'Home Gemmology', 'Jewellery Industry Voices' and 'Mine to Design'.



- **Gemmology Rocks** (Maidstone, Kent, United Kingdom) offers an extensive series of archived videos and live online seminars by gemmologist Kerry Gregory through its Facebook page at www.facebook.com/pg/gemmologyrocks/videos. The videos cover a wide range of topics such as origin of colour in



gem materials, how to use a polariscope, gemstone inclusions, and gems and minerals of the UK.

- **Gem-A** (London) has produced a series of 'Gem-A Live' webinars on glass-filled rubies and sapphires, flux-healed rubies, composite gemstones, an introduction to diamonds, fluorescence, fracture-filled gemstones, and Be- and Ti-diffused sapphires. Also available are 'How-to Guides' covering how to use a 10x loupe and stone tongs. Visit www.youtube.com/c/GemAOfficialChannel.



- The **Gemological Institute of America** (GIA; Carlsbad, California, USA) has produced a series of webinars for its 'GIA Knowledge Sessions' that cover topics such as diamond formation, synthetic diamonds, jewellery design, origin determination and rubies from Mozambique. Visit www.youtube.com/playlist?list=PLWzLnp9A9J0dF3TjLYqqQ3hAZ0pNC9s.



- The **House of Gübelin** (Lucerne, Switzerland) has posted a variety of educational videos on their YouTube channel at www.youtube.com/channel/UCyeDwZMMnXUNfnP_DWdP7rA, which can be found under the Gemmology and Gübelin Gem Sessions categories.



- **Justin K Prim** (Bangkok, Thailand) explores many facets of the lapidary arts and historical gemmology at www.youtube.com/user/ilostmaterialism.



- **Manufacturing Jewelers & Suppliers of America** (Attleboro, Massachusetts, USA) lists future and past webinars at https://mjsa.org/eventsprograms/mjsa_webinars. These focus on jewellery manufacturing and marketing, particularly in context of the challenges presented by the COVID-19 crisis. MJSA's Article & Video Library is also freely available at https://mjsa.org/publicationsmedia/article_and_video_library.



- The **Responsible Jewellery Council** (RJC, London) offers educational videos from its Code of Practices on topics such as product disclosure, provenance claims and human rights requirements at www.youtube.com/channel/UC6g86jYsgHHhQ1g5rUT8b9Q. As part of a webinar series hosted by the United Nations Global Compact, RJC also participated in a March 2020 event on achieving gender equality in the jewellery industry; the video is posted at www.youtube.com/watch?v=ScGFywXHovo and slides of this webinar are available at https://storage.pardot.com/591891/188386/UNGC_and_RJC_Presentation_Slides.pdf.



Carol M. Stockton and Brendan M. Laurs

What's New provides announcements of new instruments/technology, publications, online resources and more. Inclusion in What's New does not imply recommendation or endorsement by Gem-A. Entries were prepared by Carol M. Stockton unless otherwise noted.

Gem Notes

COLOURED STONES

Trapiche-like Pattern in Amethyst

Among the numerous optical phenomena displayed by quartz are asterism and chatoyancy. However, amethyst is one of the few popular gems that does not show asterism in either reflected light (epiasterim) or transmitted light (diasterism). Amethyst and ametrine displaying trapiche-like patterns were recently documented from Brazil (Lauris 2018; Sun *et al.* 2018), and trapiche-like textures have also been encountered in other quartz varieties (e.g. Krzemnicki & Lauris 2014; Wang & Song 2019). Here, we report on a trapiche-like pattern showing a prominent fixed star in an amethyst sphere that reportedly came from Brazil (Figure 1). The sphere was purchased by author MPS at the Sainte-Marie-aux-Mines Mineral & Gem Show in approximately 2005, and was briefly documented many years later (Steinbach 2016, pp. 815–816).

The amethyst sphere measures 40 mm in diameter and weighs 420.50 ct. It appears translucent due to the presence of fractures and fluid inclusions. The whitish trapiche-like pattern is conspicuous within the purple body colour of the amethyst, and consists of a roughly hexagonal core and six radiating arms. The hexagonal symmetry of the core suggests that the trapiche-like pattern developed along the basal pinacoid of the quartz crystal. Each arm started its growth from one side of the hexagonal core in that basal plane. The six arms are therefore parallel to the growth direction of the first-order hexagonal prism.

The arms consist of mostly fibrous or planar white inclusions aligned parallel to their length, as shown in Figure 2. Raman spectroscopy of the white inclusions in both the arms and the core yielded only spectra consistent with quartz.

The appearance of the trapiche-like pattern in this amethyst is reminiscent of those seen in some trapiche-like sapphires and rubies (see, e.g., Steinbach 2016, pp. 800–803). They both show a hexagonal-shaped core that contains the same fibrous inclusions which form the six arms. In corundum, white and light brown trapiche-like patterns are caused, respectively, by the

presence of rutile and Fe/Ti-rich oxide inclusions (Gübelin & Koivula 2008, pp. 212 and 308). The arms broadened during growth, as typically shown by trapiche-like patterns.

The trapiche-like pattern in the present amethyst is different from typical trapiche texture that is formed by skeletal crystal growth (e.g. in ruby: see Gübelin & Koivula 2008, pp. 88–90). The pattern in this amethyst is also different from that shown by the recently documented trapiche-like ametrine/amethyst from Brazil (Lauris 2018; Sun *et al.* 2018), because in those samples the arms were composed of relatively pure quartz between heavily included areas, whereas the arms in the present amethyst correspond to oriented fibrous inclusions. In addition, the whitish core in the present amethyst is distinctly different from the black hexagonal core that is commonly present in the Brazilian trapiche-like ametrine/amethyst. The relatively large size of the amethyst specimen reported here is not surprising for quartz, but it is exceptional compared to other quartz



Figure 1: The 420.50 ct amethyst sphere described here displays a conspicuous whitish trapiche-like pattern. Photo by J.-P. Gauthier.

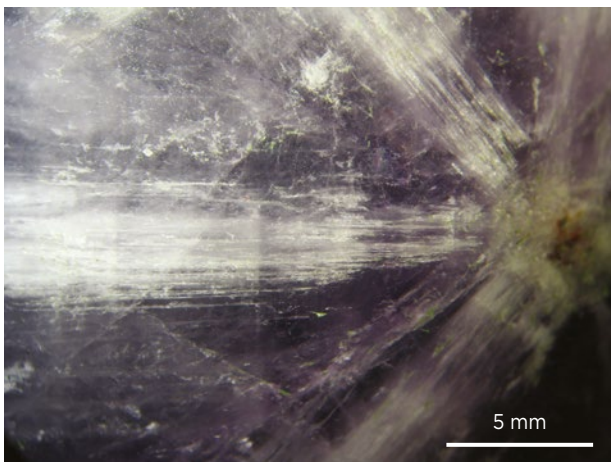


Figure 2: Each of the six arms constituting the trapiche-like pattern consists of fibrous or planar white inclusions aligned along the length of the arms. The colour of the core appears slightly different from the arms due to the presence of green-coloured polishing paste filling surface cavities in that area. Photomicrograph by J.-P. Gauthier, in brightfield illumination.

References

- Gübelin, E.J. & Koivula, J.I. 2008. *Photoatlas of Inclusions in Gemstones*, Vol. 3. Opinio Publishers, Basel, Switzerland, 672 pp.
- Krzemnicki, M.S. & Laurs, B.M. 2014. Gem Notes: Quartz with radiating fibres, sold as ‘trapiche’ quartz. *Journal of Gemmology*, **34**(4), 296–298.
- Laurs, B.M. 2018. Gem Notes: Ametrine with trapiche-like patterns from Brazil. *Journal of Gemmology*, **36**(3), 186–187.
- Steinbach, M.P. 2016. *Asterism – Gems with a Star*. MPS Publishing and Media, Idar-Oberstein, Germany, 896 pp.
- Sun, Z., Muyal, J. & Hand, D. 2018. Gem News International: Trapiche-like amethyst from Brazil. *Gems & Gemology*, **54**(2), 237–238.
- Wang, X. & Song, Y. 2019. Gem News International: A special type of trapiche quartz. *Gems & Gemology*, **55**(2), 285–286.

Aquamarine with Spodumene Inclusions from the Oceanview Mine, California, USA

Since 2000, mining operations at the Oceanview mine in Pala, San Diego County, California, USA, have yielded about 1 t of spodumene, 20 kg of tourmaline and small amounts of beryl (i.e. aquamarine and morganite; Jeff Swanger, pers. comm. 2020). This study documents some unusual inclusions in aquamarine from this granitic pegmatite. We studied a transparent, pale blue sample that was attached to some albite matrix (Figure 3). One side of the sample was cut and polished, while the other side was kept in its natural state.

Refractive indices of this aquamarine were in the range of iron-bearing beryls: $n_o = 1.588$ and $n_e = 1.579$, yielding a birefringence of 0.009. The hydrostatic SG value obtained from a chipped-off fragment was 2.72. Microscopic examination revealed some interesting, well-crystallised, monoclinic mineral inclusions (Figure 4). These were

specimens showing trapiche-like patterns, which have been fashioned as slices or flattened cabochons (see Krzemnicki & Laurs 2014; Wang & Song 2019).

Thanh Nhan Bui (tnhan93@gmail.com)
 Université catholique de Louvain
 Louvain-la-Neuve, Belgium

Aurélien Delaunay and Ugo Hennebois
 Laboratoire Français de Gemmologie
 Paris, France

Martin P. Steinbach
 Steinbach – Gems with a Star
 Idar-Oberstein, Germany

Prof. Jean-Pierre Gauthier
 Centre de Recherches Gemmologiques
 Nantes, France



Figure 3: This specimen (6 cm in maximum dimension), comprised of pale blue aquamarine and white albite from the Oceanview mine, California, USA, was examined for this study. Photo by T. Stephan.

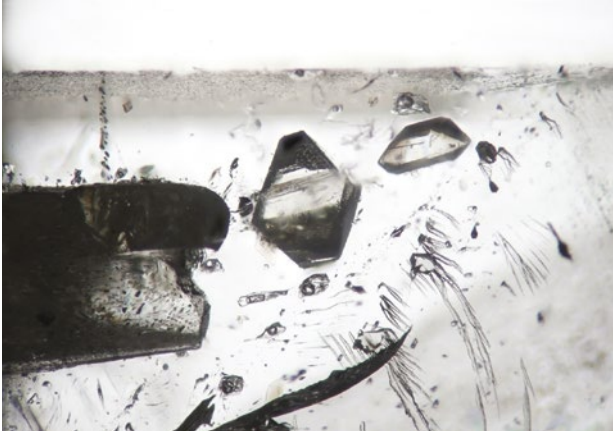


Figure 4: The angular, high-relief crystals in the aquamarine were identified as spodumene. They show well-developed {010} and {110} faces. Also present are two-phase (liquid-gas) fluid inclusions. Photomicrograph by T. Stephan, in paraffin oil with transmitted light; image width 4.1 mm.

analysed with confocal Raman spectroscopy (using a Renishaw inVia Raman microscope with 514.5 nm laser excitation), and after subtracting the contributions from the host beryl, the resulting spectrum matched that of spodumene ($\text{LiAlSi}_2\text{O}_6$) in the RRUFF database (Figure 5). Because it is rather unusual for spodumene to be associated with iron-bearing beryl (aquamarine) in gem-bearing pegmatites, we performed further analytical work to confirm the identity of these inclusions.

A small piece of the sample was broken off and polished until one of the spodumene inclusions was exposed on the surface. Prior to chemical analysis using laser ablation inductively coupled plasma mass spectrometry (LA-ICP-MS), the Si contents of both the spodumene inclusion and the beryl host were measured with electron probe micro-analysis (EPMA) in order to serve as internal standards for ICP-MS analysis. The SiO_2 content of the spodumene was 63.36 wt.% and that of the host beryl was 64.75 wt.%. LA-ICP-MS analyses of the spodumene and beryl were then conducted with an Agilent 7500c quadrupole spectrometer, using external standards NIST-SRM 610 and 612. Chemical data obtained for the inclusion confirmed its identity as spodumene, with 27.8 wt.% Al_2O_3 and 8.59 wt.% Li_2O . Deviations from ideal formula values of 27.4 wt.% Al_2O_3 and 64.58 wt.% SiO_2 were due to a slightly elevated Li_2O content and the presence of trace elements such as Na, Ca and others (Table I). Analyses of the aquamarine host revealed highly enriched amounts of Li (3713–4051 ppm) for iron-bearing beryl (cf. Viana *et al.* 2002), consistent with the presence of the syngenetic spodumene inclusions. A highly evolved composition of the pegmatitic fluids that formed the aquamarine is also indicated by the elevated alkali contents of this beryl (i.e. 7037–7816 ppm Na and 1886–4114 ppm Cs).

To the authors' knowledge, this is the first report

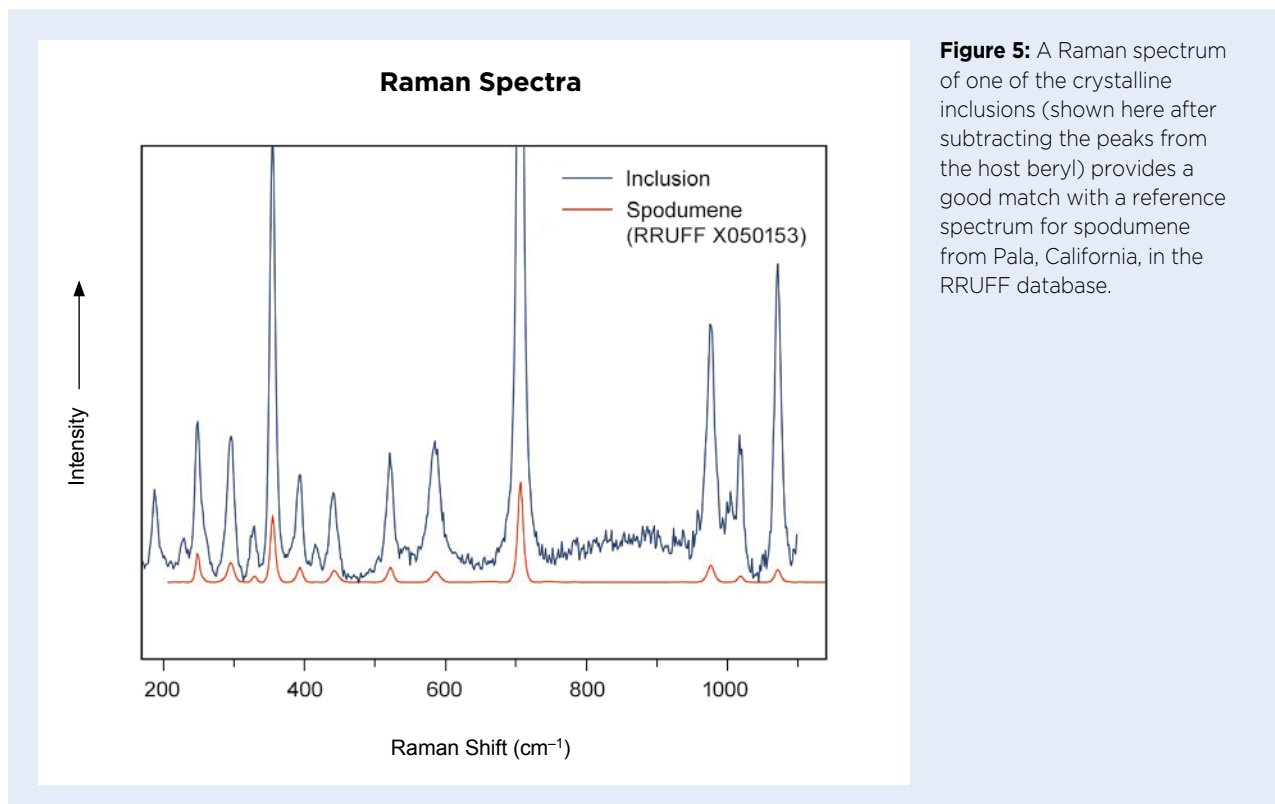


Figure 5: A Raman spectrum of one of the crystalline inclusions (shown here after subtracting the peaks from the host beryl) provides a good match with a reference spectrum for spodumene from Pala, California, in the RRUFF database.

Table I: Minor- and trace-element analysis by LA-ICP-MS of a spodumene inclusion and its aquamarine host from the Oceanview mine.^a

| Element (ppmw) | Spodumene inclusion | Aquamarine host ^b |
|----------------|---------------------|------------------------------|
| Li | 42112 | 3713–4051 (3910) |
| Na | 929.5 | 7037–7816 (7480) |
| Mg | bdl | 8.40–21.61 (9.63) |
| K | bdl | 364.9–390.1 (375.9) |
| Ca | 306.5 | 198.2–383.0 (270.1) |
| Ti | 44.17 | 12.10–16.80 (14.72) |
| Fe | nd | 1010–1555 (1455) |
| Zn | 40.06 | 568.3–622.8 (597.1) |
| Ga | 63.35 | 16.43–25.82 (20.04) |
| Rb | bdl | 260.8–302.6 (283.9) |
| Cs | bdl | 1886–4114 (2816) |

^a Fe was measured with EPMA and Sc was below the detection limit in all analyses. Abbreviations: bdl = below detection limit, nd = not determined, ppmw = parts per million by weight.

^b Range of 10 spots analysed in a line across the sample, with average values given in parentheses.

of spodumene inclusions in aquamarine (although spodumene is known to form inclusions in the morganite variety of beryl).

Acknowledgement: The authors thank Jeff Swanger of Oceanview Mines LLC for information on the mine.

Dr Fabian Schmitz

(schmitz@rheinmaingemconsulting.com)

Geomaterial and Gemstone Research Institute
Johannes Gutenberg-University Mainz, Germany

Stefan Müller

DSEF German Gem Lab
Idar-Oberstein, Germany

Tom Stephan

DGemG German Gemmological Association
Idar-Oberstein, Germany

Reference

Viana, R.R., Jordt-Evangelista, H., da Costa, G.M. & Stern, W.B. 2002. Characterization of beryl (aquamarine variety) from pegmatites of Minas Gerais, Brazil. *Physics and Chemistry of Minerals*, **29**(10), 68–79, <https://doi.org/10.1007/s00269-002-0278-y>.

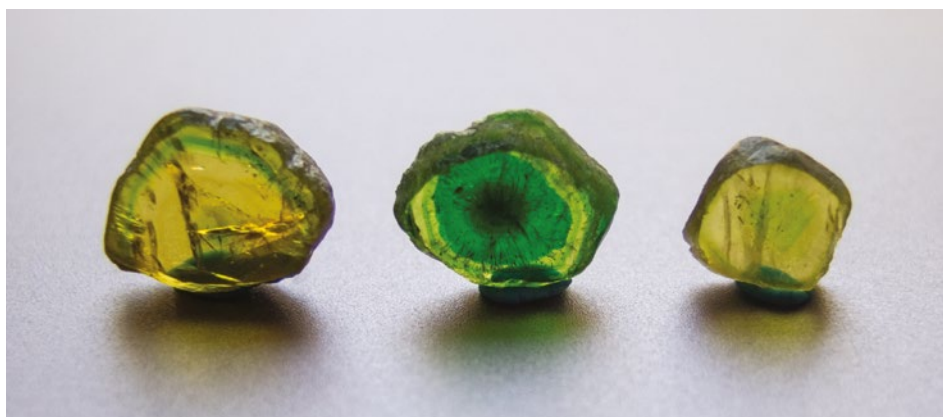
Demantoid/Andradite Slices from Iran

Colour-zoned demantoid/andradite from Kerman Province in southern Iran showing green/brown zones was first documented by Karamelas *et al.* (2007), who found that the green areas correlated to >0.7 wt.% Cr₂O₃. The two faceted stones examined for that report were specifically cut to display their brown-orange and green colour zoning.

During the February 2020 Tucson gem shows in Arizona, USA, demantoid/andradite from Iran was newly available as polished slices, which showed the colour

zoning more effectively than faceted stones. Three such slices (Figure 6) were kindly donated to Gem-A by Indra Man Sunuwar (Nepali Bazaar Co. Ltd, Tokyo, Japan); his supplier reportedly had cut about 450 carats of this material. Stone dealer Bradley J. Payne (The Gem Trader, Cave Creek, Arizona) also obtained some of the slices in Tucson, as well as faceted stones showing colour zoning (e.g. Figure 7). Some of the slices were trimmed into polygonal shapes, while others retained their natural

Figure 6: These colour-zoned slices of demantoid/andradite from Iran measure 5.7–8.5 mm wide. Gift of Indra Man Sunuwar; photo by B. M. Laurs.



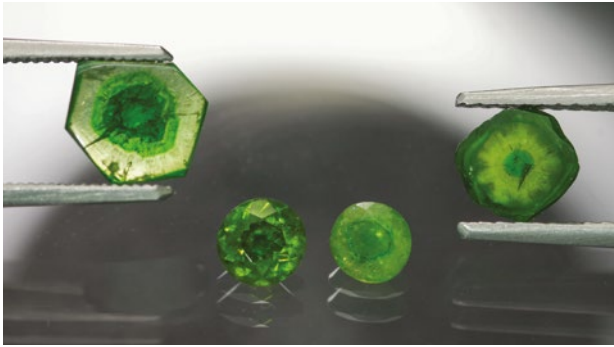


Figure 7: Attractive patterns are shown by these colour-zoned Iranian demantoid/andradite slices, which weigh 1.68 ct (left) and 1.08 ct (right). The faceted stones at the bottom centre were cut so that darker green colour zones are centred under their tables; they weigh 0.67 ct (left) and 0.52 ct (right). Photo by Bradley J. Payne.

Blue Diopside from Russia

Violane (or *violan*) is a term used for violet to blue diopside with a massive polycrystalline texture that mainly has been mined from the Praborna manganese deposit in St Marcel, Italy, and is coloured by Mn (Mottana *et al.* 1979). Although known for decades, this ornamental material is rarely mentioned in the gemmological literature (cf. Webster 1949). The term *violane* has also been applied to massive polycrystalline blue diopside from Russia, particularly by sellers on the Internet. In addition, similar material is known from Baffin Island, Canada, which is coloured by Fe^{2+} - Ti^{4+} intervalence charge transfer (Herd *et al.* 2000).

During the February 2020 Tucson gem shows, Rare Earth Mining Co. (Trumbull, Connecticut, USA) displayed some blue and blue/white cabochons represented as *violane*. According to Rare Earth's Bill Heher, the rough material came to market in around August 2018 and was mined from the Lake Baikal region of Russia. So far he has cut a few hundred cabochons that ranged up to about 50 mm in maximum dimension.

Ornamental blue diopside is known from three localities in Russia: the Khakassia area of eastern Siberia (Shil'tsina & Vereshchagin 2000) and two areas near Lake Baikal (Zadov *et al.* 2004; Simakin *et al.* 2019). According to D. Belakovskiy (pers. comm. 2020), the Lake Baikal deposits are hosted by (1) the Yoko-Dovyrenskiy (or Yoko-Dovyren) massif near the north end of the lake and (2) the Tazheranskiy (or Tazheran) massif near the lake's south end.

Heher loaned three samples for examination (Figure 8), and they were characterised by authors CW and

outer surfaces along their edges. The slices that Payne obtained ranged from 1 to 2 ct and the faceted stones weighed 0.15–1.25 ct.

Although demantoid/andradite from Iran has been known since 2001, this is the first time that this author is aware of this material being cut into polished slices to showcase its attractive colour zoning—as is commonly done with multicoloured tourmaline.

Brendan M. Laurs FGA

Reference

- Karampelas, S., Gaillou, E., Fritsch, E. & Douman, M. 2007. Gem News International: Color-zoned andradite from Iran, with calcite inclusions. *Gems & Gemology*, **43**(1), 65–67.

BW. They consisted of a blue oval cabochon weighing 17.88 ct (27.50 × 21.27 mm), and a matched pair of bicoloured blue and white/tan rectangular cabochons with a total weight of 35.71 ct (each measuring approximately 26 × 15 mm). All displayed an obvious polycrystalline structure that was fine- to coarse-grained and showed variable depth of blue colour between grains in the blue portions (Figure 9). A few sparkles seen as the samples were moved apparently corresponded to cleavage fractures in some of the diopside grains. Viewed with the microscope, the blue areas of the samples also exhibited variations in surface lustre between grains (again, see Figure 9). Although individual grains were somewhat transparent, the presence of abundant polycrystalline



Figure 8: These three cabochons containing blue diopside (17.57–17.88 ct) are from Russia's Lake Baikal region and were studied for this report. Photo by B. Williams.

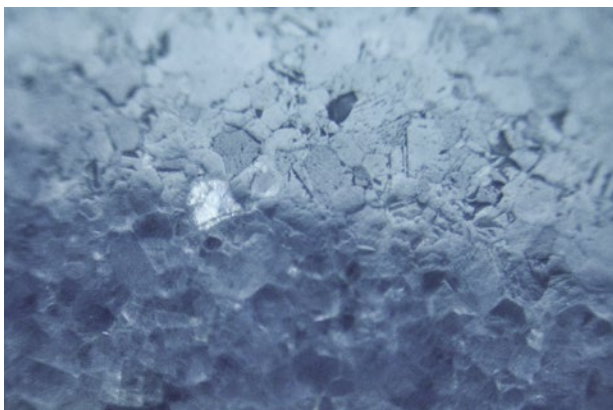


Figure 9: Microscopic examination of the blue diopside shows a polycrystalline texture with variations in surface lustre between grains and a reflection from a cleavage fracture (left centre). Photomicrograph by B. Williams and C. Williams, in reflected light; image width 9 mm.

grain boundaries created an overall semi-translucent appearance in the blue areas.

All three samples were confirmed as diopside in the blue areas by Raman analysis using a Magilabs Gemmo-Raman-532SG spectrometer. A Raman peak shift was observed in the white/tan area of the bicoloured stones, which might be due to the presence of additional mineral phases occurring with the diopside. Indeed, Simakin *et al.* (2019) reported that ‘bleached’ metasomatised zones associated with blue diopside from Lake Baikal consist of recrystallised white diopside and monticellite, while Zadov *et al.* (2004) indicated that the light-coloured zones consisted of foshagite and other minerals.

Spot RI readings of the cabochons could not be obtained due to the polycrystalline nature of the material. The hydrostatic SG value of the blue sample was 3.23, which is slightly lower than the typical range for diopside (3.24–3.33) but consistent with its polycrystalline structure. The stones were inert to long- and short-wave UV radiation. Energy-dispersive X-ray fluorescence (EDXRF) chemical analysis of the blue sample performed with an Amptek X123-SDD spectrometer showed traces of the chromophoric elements V, Fe and Cr (as well as very small amounts of Pt, consistent with blue diopside from the Yoko-Dovyren massif documented by Simakin *et al.* 2019).

Simakin *et al.* (2019) reported an average of 345 ppm V in blue diopside from the Lake Baikal area, and attributed its colouration to VO^{2+} . Visible-near infrared (Vis-NIR) absorption spectroscopy of the present blue cabochon with a Magilabs GemmoSphere spectrometer showed a large broad peak centred at about 630 nm and a smaller absorption at about 430 nm (Figure 10). This pattern is indeed consistent with colouration due

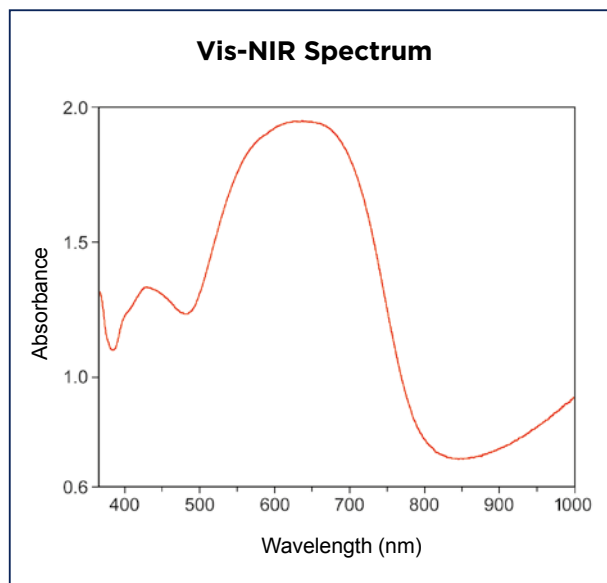


Figure 10: Vis-NIR spectroscopy of the blue diopside shows a large broad peak centred at about 630 nm and a smaller absorption at about 430 nm, consistent with colouration due to VO^{2+} .

to tetravalent vanadium in the form of the vanadyl ion (VO^{2+}), as seen for example in cavansite (Rossman 2014). Vanadium-doped synthetic diopside also shows distinct blue colouration and a similar absorption spectrum (see, e.g., sample GRR 510 at <https://minerals.gps.caltech.edu/FILES/Visible/pyroxene/Index.html>). Taken together, all of these aspects provide confirmation that the blue colouration of the Russian diopside studied for this report is due to VO^{2+} .

Acknowledgement: We thank Dmitriy Belakovskiy (curator of the Fersman Mineralogical Museum, Moscow) for providing information and references on blue diopside from Russia.

Cara Williams FGA and Bear Williams FGA
(info@stonegrouplabs.com)
Stone Group Laboratories
Jefferson City, Missouri, USA

Brendan M. Laurs FGA

References

- Herd, C.D.K., Peterson, R.C. & Rossman, G.R. 2000. Violet-colored diopside from southern Baffin Island, Nunavut, Canada. *Canadian Mineralogist*, **38**(5), 1193–1199, <https://doi.org/10.2113/gscanmin.38.5.1193>.
- Mottana, A., Rossi, G., Kracher, A. & Kurat, G. 1979. Violan revisited: Mn-bearing omphacite and diopside. *Tschermaks Mineralogische und Petrographische Mitteilungen*, **26**(3), 187–201, <https://doi.org/10.1007/bf01081845>.

Rossmann, G.R. 2014. Optical spectroscopy. *Spectroscopic Methods in Mineralogy and Materials Sciences*, Reviews in Mineralogy and Geochemistry, Vol. 78, Mineralogical Society of America, Chantilly, Virginia, USA, 371–398, <https://doi.org/10.2138/rmg.2014.78.9>.

Shil'tsina, A.D. & Vereshchagin, V.I. 2000. Ceramic tiles containing diopside and clay raw materials from Khakassia. *Glass and Ceramics*, 57(3–4), 87–90, <https://doi.org/10.1007/bf02681515>.

Simakin, A.G., Kislov, E.V., Salova, T.P., Shaposhnikova, O.Y. & Nekrasov, A.N. 2019. Reduced CO₂ fluid as

an agent of ore-forming processes: A case study of dolomite-replacement skarns at the Yoko-Dovyren massif. *Petrology*, 27(1), 1–16, <https://doi.org/10.1134/S086959111901003x>.

Webster, R. 1949. The identification of gemstones by colour. *The Gemmologist*, 18(215), 152–155.

Zadov, A.E., Pertsev, N.N., Belakovskiy, D.I., Chukanov, N.V. & Kuznetsova, O.Yu. 2004. Foshagite and hillebrandite from skarn xenoliths of Ioko-Dovyrensky massif. *Proceedings of the Russian Mineralogical Society*, 133(1), 73–83 (in Russian with English abstract).

A Collection of Cat's-Eye Emeralds from Colombia

Fine cat's-eye emeralds are quite rare, and have been documented mostly from Brazil (e.g. Laurs 2012 and references therein). However, flattened cabochons showing chatoyancy have been reported from Colombia—specifically the Coscuez mine in the Muzo region (Johnson & Koivula 1996). More recently, Weldon and McClure (2013) described the cutting of a fine matched pair of Colombian cat's-eye emeralds that weighed 75 ct by husband-and-wife gem cutters Misael Angel Rodríguez and Claudia Patricia Beltrán Rubiano.

During the February 2020 Tucson gem shows, the same emerald cutters showed this author an impressive collection of 24 cat's-eye emeralds from Colombia (Figure 11). The stones ranged from 0.49 to 3.81 ct and had a total weight of 37.90 carats. The collection was assembled during 2019 from polished stones that they obtained on the market in Colombia; all of them had undergone clarity enhancement with cedarwood oil. According to them, the stones showed characteristics consistent with being cut from trapiche rough material mined in the Muzo area.

The cat's-eye effect was best seen when the stones were displayed over a light-coloured reflective background. Moreover, the chatoyancy appeared to be caused by very fine-scale, parallel, transparent structures, which likely correspond to the dislocations that were documented by Pignatelli *et al.* (2015) in the 'arms' of Colombian trapiche emeralds. These bundles of straight dislocations are oriented perpendicular to $\{10\bar{1}0\}$ faces, commonly with parallel elongated voids and trains of fluid inclusions. As documented by Weldon and McClure (2013),

rough material obtained from the arms of trapiche crystals can be polished into attractive cat's-eye cabochons if it contains the appropriate structural properties and is suitably oriented. As awareness grows of the potential for cutting cat's-eyes from trapiche rough material, these rare chatoyant emeralds from Colombia may become more available in the future.

Brendan M. Laurs FGA



Figure 11: Cat's-eye emeralds from Colombia are quite rare. The 24 stones in this impressive collection weigh 0.49–3.81 ct. Photo by Jeff Scovil.

References

- Johnson, M.L. & Koivula, J.I. (eds) 1996. Gem News: Cat's-eye emerald from Colombia... *Gems & Gemology*, **32**(4), 284–285.
- Laurs, B.M. 2012. Gem News International: Cat's-eye emerald from the Belmont mine, Brazil. *Gems & Gemology*, **48**(1), 56.
- Pignatelli, I., Giuliani, G., Ohnenstetter, D., Agrosi, G., Mathieu, S., Morlot, C. & Branquet, Y. 2015. Colombian trapiche emeralds: Recent advances in understanding their formation. *Gems & Gemology*, **51**(3), 222–259, <https://doi.org/10.5741/gems.51.3.222>.
- Weldon, R. & McClure, S. 2013. Unveiling the cat's-eye effect in a 75 ct Colombian emerald pair. www.gia.edu/gia-news-research-unveiling-cats-eye-effect-in-colombia-emerald-pair, 12 July, accessed 25 May 2020.

Gem-quality Euchroite from Slovakia

Euchroite, ideally $\text{Cu}_2(\text{AsO}_4)(\text{OH}) \cdot 3\text{H}_2\text{O}$, is a supergene copper arsenate that was originally described by Breithaupt (1823) from the Svätodušná (Svätoduška) copper deposit near the village of Lubietová, Banská Bystrica Region, Slovakia. The mineral's name is derived from the Greek word *eyxroia* (eu = good and chros = colour), in reference to its beautiful deep green colour. It is orthorhombic and forms crystals typically up to 1 cm (exceptionally 3 cm) that are equant to short prismatic and transparent to translucent with vitreous lustre. Its hardness is rather low at 3.5–4 on the Mohs scale. The crystals range from bright 'emerald' green to darker yellow-green, and typically form supergene encrustations on fracture surfaces. The most commonly associated minerals are pseudomalachite $[\text{Cu}_5(\text{PO}_4)_2(\text{OH})_4]$, malachite $[\text{Cu}_2(\text{OH})_2(\text{CO}_3)]$, brochantite $[\text{Cu}_4(\text{SO}_4)(\text{OH})_6]$ and several other secondary copper minerals (see Figuschová 1977; Řídkošil & Medek 1981; and unpublished data of Martin Števkó and Jiří Sejkora).

Euchroite specimens were commonly found by hobbyists in the tailings piles of the Svätodušná mine from 1950 until recently, when all mineral collecting activities at the site were forbidden. Gem-quality euchroite is quite rare and such pieces are seldom faceted because they are prized as crystal specimens.

Recently, four euchroite gemstones (see, e.g., Figure 12) were faceted by Czech gem cutter Svatopluk Prchlík from damaged crystals that were collected in 1998 by a group organised by one of the authors (RH). The stones weighed 1.35 ct (round), 1.36 ct (octagon), 0.06 ct (octagon) and 0.04 ct (octagon); all four of them were examined for this report. Refractive indices were 1.695–1.733, with a birefringence of 0.038. The SG of each sample (measured with a pycnometer, as well as hydrostatically) was 3.45.

The authors' investigations of the euchroite rough material using powder X-ray diffraction and electron probe microanalysis (with an energy-dispersive spectrometer) revealed the presence of various mineral impurities, including olivenite, libethenite and pseudomalachite, as well as limonite and other secondary minerals ($\text{Fe} \pm \text{Mn} \pm \text{Ba}$ oxy-hydroxides). Microscopic examination of the faceted stones showed a texture composed of radiating aggregates of flat needles of euchroite with interstitial fillings of olivenite and libethenite. Pseudomalachite was present alongside individual crystals of the euchroite. Limonite and other secondary minerals were present as fillings in small cavities and as coatings along some mineral grains (especially libethenite).

Euchroite is a rare mineral and encountering gem-

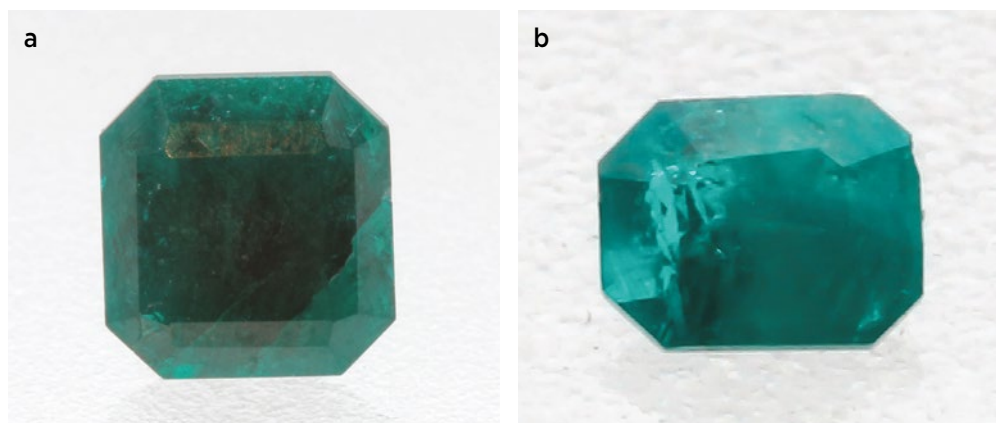


Figure 12: These euchroite gemstones were cut from rough material obtained at the Svätodušná copper deposit in Slovakia. The stones weigh (a) 1.36 ct and (b) 0.06 ct. Photos by R. Hanus.

quality material is even rarer. Euchroite is quite difficult to cut and polish due to the mineral's softness and its texture consisting of fibrous aggregates. Due to its extreme rarity in cut form, euchroite is unlikely to be encountered on the market, even as a collector's stone. Although its colour may closely resemble that of diopside, gems cut from diopside typically have better transparency. In addition, euchroite is commonly accompanied by inclusions of libethenite, which are emerald green show a high lustre.

References

- Breithaupt, A. 1823. Euchroit. In: *Vollständige Charakteristik des Mineral-Systems*. Arnoldischen Buchhandlung, Dresden, Germany, 292 pp. (see pp. 172, 266–267; in German).
- Figuschová, M. 1977. Secondary copper minerals from Lubietová. In: *Ložiskotvorné procesy Západných*

Dr Radek Hanus (hanusrdk@gmail.com)
Gemological Laboratory of e-gems.cz
Prague, Czech Republic

Dr Ján Štubňa (janstubna@gmail.com)
Gemological Laboratory, Constantine the
Philosopher University, Nitra, Slovakia

Kamila Jungmannová
Koněprusy Caves, Czech Republic

Karpát (Conference on Ore Forming Processes in the Western Carpathians), Bratislava, Slovakia, 135–137 (in Slovak).

Řídkošil, T. & Medek, Z. 1981. New finds of minerals at the locality Svätoduška near Lubietová in central Slovakia. *Časopis Pro Mineralogii a Geologii*, **26**, 91 (in Czech).

Properties of Green Fluorite from England Showing Daylight Fluorescence

A famous locality for fine-quality fluorite crystals is the historic Weardale mining district in County Durham, northern England. Weardale is the centre of the North Pennines Orefield, which has been a source of lead, iron, zinc, fluorite and other mineral commodities for the past millennium (Fisher 2013). In recent times, the most prolific source of fluorite specimens for collectors has been the Rogerley mine, which was first developed in the early 1970s by a team of local collectors. In 1999, the mine was taken over by a group of Americans and operated as UK Mining Ventures LLC (Fisher 2013). In the summer of 2017, the project changed ownership to Ian and Diana Bruce under the name UK Mining Ventures Ltd (www.ukminingventures.com/dianamaria.html). They opened the Diana Maria mine about 400 m west of the Rogerley main portal; both mines are currently being

worked throughout the year. The mineralised cavities are hosted by vertical veins and by metasomatic zones or 'flats' that extend laterally from the veins, subparallel to the limestone host-rock bedding. The fluorite is most commonly green, yellow or purple, and the crystals typically form penetration twins on {111} (Fisher 2004).

In 2017, one of the authors (JŠ) obtained some green fluorite samples from UK Mining Ventures Ltd that came from the Rogerley and Diana Maria mines. Author ZP recently faceted three Diana Maria fluorites, consisting of two matched square step cuts with dimensions of 4.50 × 4.50 × 3.29 (0.60 ct) each, and one rectangular step cut measuring 5.30 × 9.45 × 4.28 (2.07 ct; Figure 13). Their gemmological properties were comparable to those of fluorite, with a singly refractive RI varying from 1.425 to 1.445 (although this range is somewhat wider than

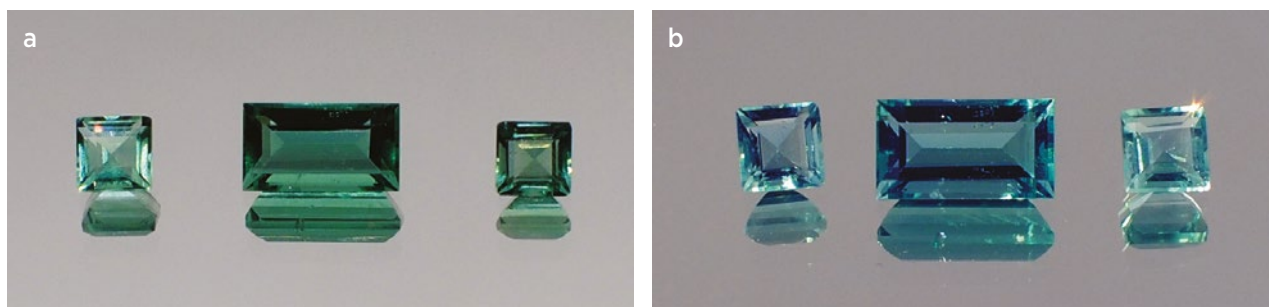


Figure 13: These faceted fluorites (from left to right: 0.60, 2.07 and 0.60 ct) are from the Diana Maria mine in the Weardale mining district of County Durham, northern England. (a) They are green when viewed with standard 'warm' or 'cool' white LED illumination, but (b) appear more blue in daylight-equivalent illumination due to their strong UV fluorescence. Photos by J. Štubňa.



Figure 14: Two-phase (liquid-gas) inclusions displaying various shapes occur in the Diana Maria fluorites. Photomicrographs by J. Štubňa; magnified 40 \times .

typically reported for fluorite) and a hydrostatic SG value of 3.17–3.19. They appeared pink to red under a Chelsea Colour Filter. Magnification revealed two-phase (liquid-gas) inclusions (Figure 14), which are characteristic of fluorite from various locations.

The most striking aspect of these green fluorites was their exceptionally strong violetish blue fluorescence to long-wave UV radiation (Figure 15), which was weaker under short-wave UV. This fluorescence behaviour is similar to that shown by fluorite from many other Weardale localities, and most of the green and purple fluorite from these deposits shows blue-to-violet overtones resulting from daylight fluorescence (Fisher *et al.* 2004). This colour effect was clearly seen in the faceted stones examined for this study (again, see Figure 13).

Ultraviolet-visible (UV-Vis) spectroscopy of our green fluorites revealed absorption bands at 376, 426, 444, 617 and 688 nm (Figure 16a). O'Donoghue (2006) reported similar absorption features in green fluorite, with bands at 427, 445, 582, 610 and 634 nm. Raman spectroscopy showed numerous peaks, including a Raman band at 322 cm^{-1} (Figure 16b). Čermáková *et al.* (2014) indicated that Raman bands at wavenumbers higher than 500 cm^{-1}

in fluorite are probably related to the presence of rare-earth elements (REE).

The cause of the vivid green colour shown by Weardale fluorite is still not clearly understood. However, modern analytical techniques and observations of the colour behaviour under different light sources suggest the fluorite's colouration is produced by colour centres resulting from lattice defects caused by the presence of REE (Fisher & Greenbank 2000). Weardale fluorite is enriched in light REE such as Y, Ce, La, Sm and Nd, and displays a strong negative Eu anomaly (Falster *et al.* 2001; Ixer 2003). Although the role of these elements in causing the green colour needs further study, they are apparently responsible for the fluorite's intense UV fluorescence (Falster *et al.* 2001; Fisher 2004).

*Drs Ján Štubňa (janstubna@gmail.com)
and Zuzana Pulišová*

*Gemmological Laboratory, Constantine the
Philosopher University, Nitra, Slovakia*

*Drs Jana Fridrichová and Peter Bačík
Comenius University, Bratislava, Slovakia*

Figure 15: Intense violetish blue fluorescence is seen with long-wave UV radiation in this Diana Maria fluorite. Note also the subtle zones displaying magenta fluorescence. Photomicrograph by J. Štubňa; magnified 7.5 \times .



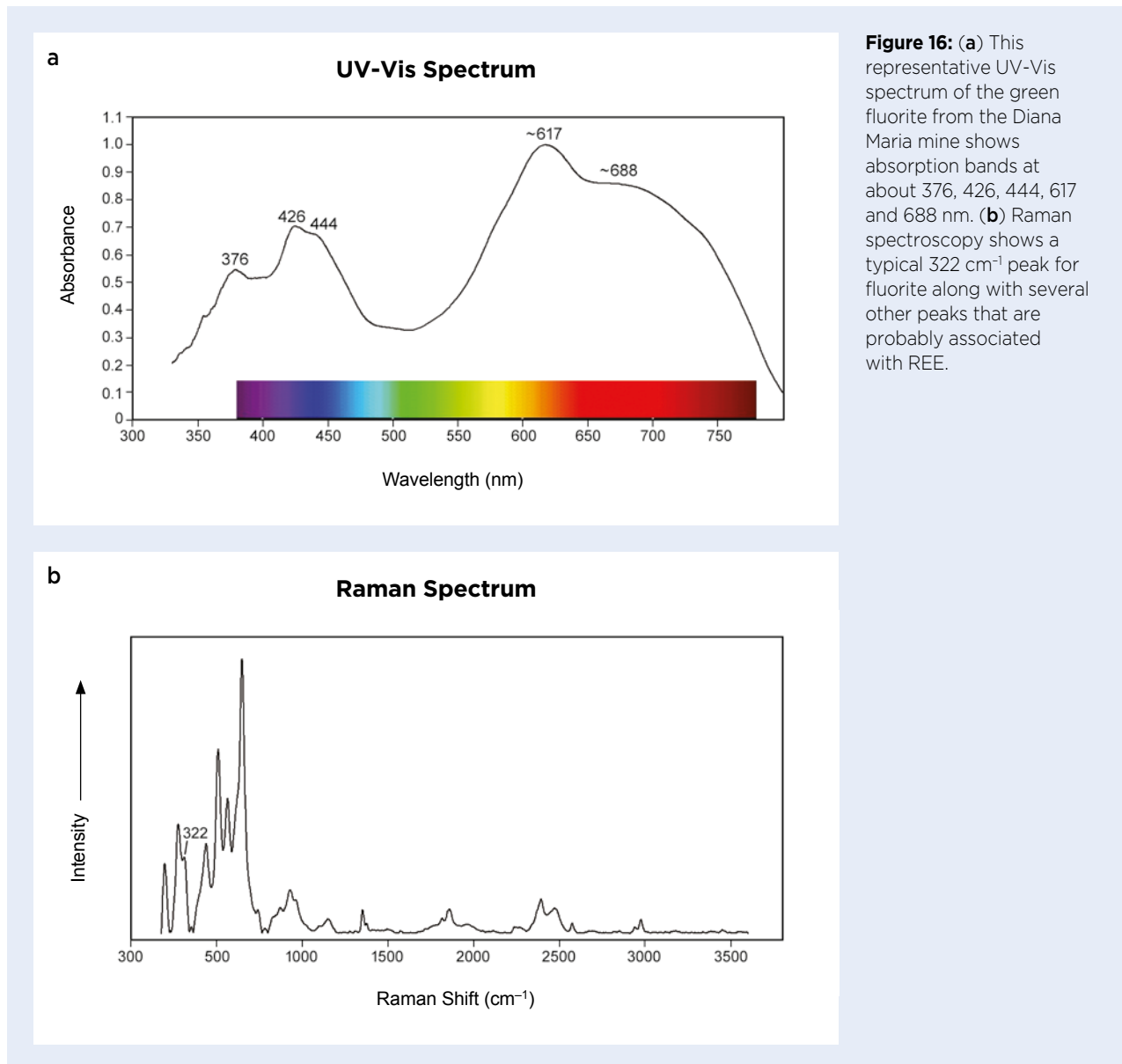


Figure 16: (a) This representative UV-Vis spectrum of the green fluorite from the Diana Maria mine shows absorption bands at about 376, 426, 444, 617 and 688 nm. (b) Raman spectroscopy shows a typical 322 cm⁻¹ peak for fluorite along with several other peaks that are probably associated with REE.

References

- Čermáková, Z., Bezdička, P., Němec, I., Hradilová, J., Šrein, V., Blažek, J. & Hradil, D. 2015. Naturally irradiated fluorite as a historic violet pigment: Raman spectroscopic and X-ray diffraction study. *Journal of Raman Spectroscopy*, **46**(2), 236–243, <https://doi.org/10.1002/jrs.4627>.
- Falster, A.U., Fischer, J. & Simmons, W.B. 2001. REE-content and fluorescence in fluorite from the Rogerley mine, Weardale, County Durham, England. *Rocks & Minerals*, **76**(4), 253–254, <https://doi.org/10.1080/00357520109603226>.
- Fisher, J. 2004. Properties of fluorite from the North Pennines England. *Rocks & Minerals*, **79**(6), 399–400, <https://doi.org/10.1080/00357529.2004.9925744>.
- Fisher, J. 2013. The Weardale giant: A large fluorite specimen recovered from the Rogerley mine, Weardale, northern England, July 2012. *Rocks & Minerals*, **88**(1), 12–19, <https://doi.org/10.1080/00357529.2013.747894>.
- Fisher, J. & Greenbank, L. 2000. The Rogerley mine, Weardale, County Durham, England. *Rocks & Minerals*, **75**(1), 54–61, <https://doi.org/10.1080/00357520009602577>.
- Ixer, R.A. 2003. The distribution of rare earth elements in North Pennine fluorspar and fluorite. *UK Journal of Mines & Minerals*, **23**, 21–26.
- O'Donoghue, M. 2006. *Gems*, 6th edn. Butterworth-Heinemann, Oxford, 873 pp.

Jewellery Set with Green Fluorite from England

Fluorite from the Rogerley and Diana Maria mines in the Weardale mining district, County Durham, northern England, is prized by mineral collectors who appreciate the well-formed crystal specimens. Particularly well known from these mines is green fluorite showing daylight fluorescence (see the previous Gem Note in this issue).

During the February 2020 Tucson gem shows, Diana Bruce (Crystal Classics, East Coker, Somerset) showed this author a new line of jewellery created with faceted fluorite that mainly comes from the Diana Maria mine (e.g. Figures 17 and 18). Cutting of this material started in late 2018 and the first batch yielded about 1,000 gemstones, of which 650 have been set into pendants and earrings (called the Viridis Gems collection), and the rest are being sold as loose stones. The vast majority of the fluorites are green, although some purple and yellow gems have been cut. The shapes include round, oval and trilliant, in concave or fantasy cuts that mostly range from 6 × 6 mm to 14 × 12 mm; there are three sizes available for earrings and four sizes for necklaces. The largest stone faceted so far weighs approximately 28 ct. The cutting styles employ relatively small tables so they are less susceptible to scratching. (Viridis Gems fluorite is accompanied by information on the care and cleaning of



Figure 18: These concave-cut fluorites from the Diana Maria mine weigh 4 ct (left, set in 18 ct gold) and 6 ct (right). Photo by Olga Kaspera, Crystal Classics.

this delicate stone.) The fluorite is set in rhodium-plated sterling silver, or in 14 or 18 ct gold. A few loose twinned crystals of the fluorite have also been set as pendants.

The attractive green colour, custom cutting styles and daylight fluorescence combine to make these fluorites interesting as loose stones and jewellery items.

Brendan M. Laurs FGA

Figure 17: Set in rhodium-plated sterling silver, these concave-cut fluorites from the Diana Maria mine range from 8 to 12 mm (approximately 2.0–6.8 ct for the rounds and 1.8–4.9 ct for the trilliants). Photo by Olga Kaspera, Crystal Classics.



Frankamenite as an Ornamental Gem Material

Frankamenite— $K_3Na_3Ca_5(Si_{12}O_{30})(F,OH)_4 \cdot H_2O$ —is a relatively new mineral (described in 1996) that occurs together with charoite from the Sakha Republic (formerly Yakutia), Russia. Frankamenite is a member of the canasite group and is the hydrated, fluorine-dominant analogue of canasite. It is triclinic and has a Mohs hardness of $5\frac{1}{2}$. It forms aggregates of prismatic crystals, with individuals usually measuring about 1 cm (rarely up to 10 cm) long. Its colour is typically grey but may also be yellow, violet or (rarely) light blue or green (Rozhdestvenskaya *et al.* 1996).

For this study, we examined a cabochon consisting of frankamenite together with other minerals (Figure 19), which came from the Sirenevyy Kamen charoite deposit, located near the confluence of the Chara and Tokko rivers in the Murunskii massif, Aldan Shield, Sakha Republic. The deposit covers an area of 12 km² and the estimated charoite resource is around 20,000 t (Ivanov *et al.* 2018). Although *charoite* is the name of a mineral, it also refers to a rock with a distinctive purple colour that is mostly comprised of charoite *sensu stricto* with various other minerals. Charoite's colour

and textural characteristics make it highly prized as an ornamental material.

The sample described here was purchased at the source locality many years ago. It was chosen for examination because its colouration is significantly different from that of charoite. The cabochon measures 43.3×34.5 mm and weighs 121.32 ct. It shows a coarse-grained interlocking texture, with individual crystals of about 15 mm long and 4 mm wide. With Raman microspectroscopy, the pale grey-green domains were identified as frankamenite. The following peaks were recorded and are typical of frankamenite: 461, 441, 386, 332, 266 and 187 cm⁻¹ with important maxima at 1121, 645 and 625 cm⁻¹ (charoite and quartz peaks were subtracted). The frankamenite crystals showed perfect cleavage, and they fluoresced intense pink to long-wave UV radiation and a weak, deep red to short-wave UV. Associated minerals (labelled in Figure 19) included charoite (purple), quartz (colourless), aegirine (black), tinaksite (orangey brown) and fedorite (as lamellar inclusions in tinaksite); these were identified by Raman spectroscopy of the cabochon or by powder X-ray diffraction analysis of samples taken from

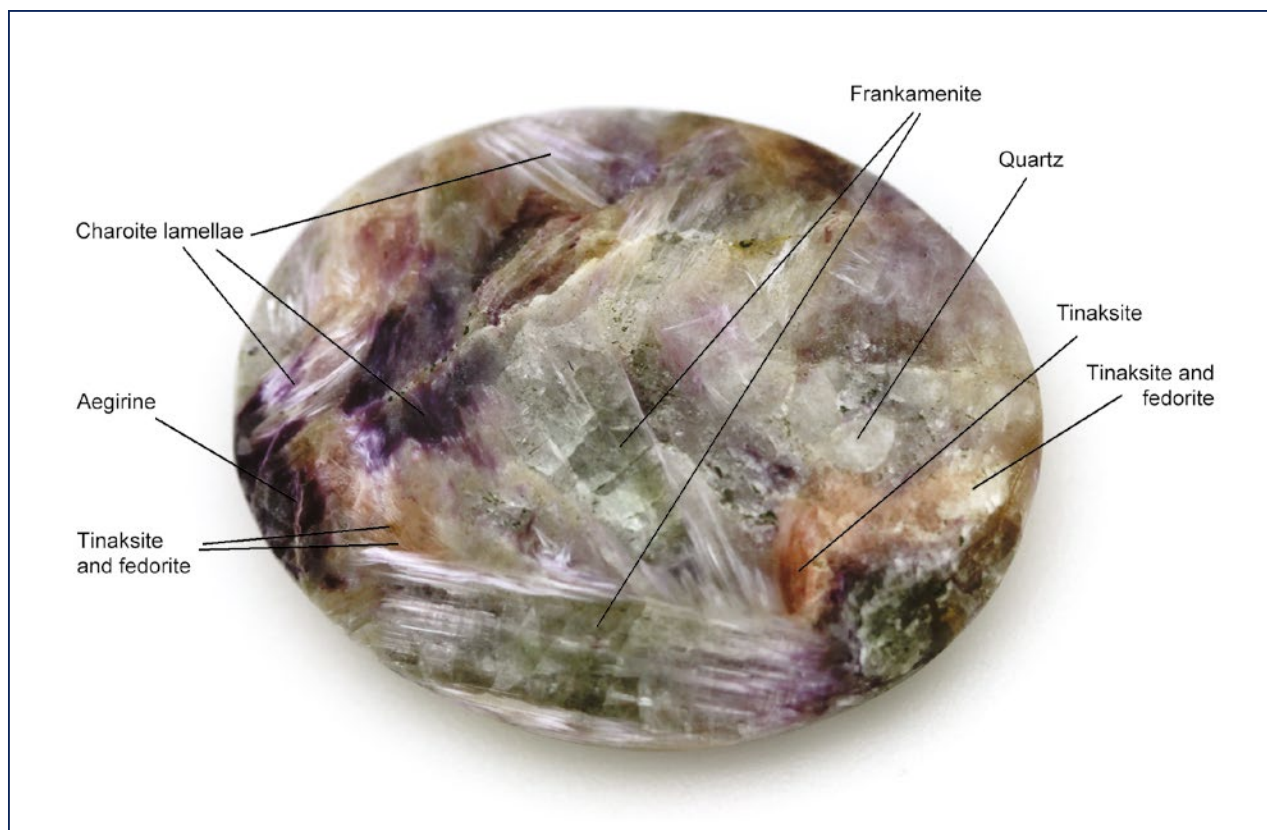


Figure 19: This 121.32 ct cabochon from the Sirenevyy Kamen charoite deposit in Russia consists of frankamenite (pale grey-green), charoite (purple), tinaksite (orangey brown) and aegirine (black), together with small amounts of quartz and fedorite. Photo by R. Hanus.

an offcut of the stone. While not identified in the present sample, celsian (barium feldspar) is also commonly found in association with charoite.

Although charoite is a better known and visually more appealing gem material, frankamenite is an unusual collector's stone and its presence together with the various associated minerals creates an interesting appearance.

*Dr Radek Hanus, Dr Ján Štubňa
and Kamila Jungmannová*

References

- Ivanov, A.V., Gorovoy, V.A., Gladkochub, D.P., Shevelev, A.S. & Vladykin, N.V. 2018. The first precise data on the age of charoite mineralization (eastern Siberia, Russia). *Doklady Earth Sciences*, **478**(2), 179–182, <https://doi.org/10.1134/s1028334x18020241>.
- Rozhdestvenskaya, I.V., Nikishova, L.V. & Lazebnik, K.A. 1996. The crystal structure of frankamenite. *Mineralogical Magazine*, **60**(403), 897–905, <https://doi.org/10.1180/minmag.1996.060.403.05>.

Colour-Change Garnet from Tanga, Tanzania

Colour-change garnets are well known from East Africa, and in Tanzania this material typically comes from the Umba River Valley and consists of pyrope-spessartine that can appear greenish blue in daylight and magenta in incandescent light (e.g. Jobbins *et al.* 1975). Recently, additional production of colour-change garnet reportedly occurred near Tanga, which is in the same region as Umba in north-eastern Tanzania. Gem dealer Dudley Blauwet (Dudley Blauwet Gems, Louisville, Colorado, USA) obtained the rough material at the February 2017 Tucson gem shows. He sent eight pieces of rough totalling 5.0 g to his cutting factory and they yielded eight faceted stones ranging from 0.66 to 2.03 ct (7.31 carats total weight).

Blauwet loaned three of the gems for examination (Figure 20), and they measured 8.47 × 6.97 × 4.37 mm (2.02 ct oval), 6.41–6.47 × 3.86 mm (1.09 ct round) and 6.87 × 6.76 × 3.48 mm (1.07 ct triangle). In daylight, the oval appeared dark reddish purple with flashes of deep purplish pink, and the round and triangular stones showed a strong, deep purple colour. All three changed to purplish red in incandescent light. The RIs of the oval, round and triangular samples were 1.759, 1.747 and 1.743, and their average hydrostatic SG values were 3.86, 3.77 and 3.76, respectively.

A prism spectroscopy revealed absorption in the violet and blue regions to about 460 nm. The oval specimen displayed an absorption band at about 540–610 nm. In the other two stones this absorption band was slightly narrower (around 550–590 nm). All three gems were inert to long- and short-wave UV radiation.

The oval and triangular stones were eye clean, but microscopic examination revealed some needle-like inclusions oriented in four different directions. The round sample was slightly included, containing a partially healed fissure and needles that were crystallographically oriented and in seemingly random orientations.

UV-Vis-NIR absorption spectra collected with an Ocean Optics HR2000+ spectrometer gave a more detailed picture of the features observed with the spectroscope. The round and triangular stones showed identical spectra consisting of pronounced bands at about 410 and 573 nm (with a shoulder at 505 nm; Figure 21). The most pronounced transmission windows were in the blue (at about 477 nm) and red regions. The spectrum of the oval stone was slightly different (again, see Figure 21): it showed a somewhat asymmetrical band at 572 nm, a feature at 484 nm, and weak shoulders at about 460 and 525 nm. Because of its relatively greater absorption in the blue region, in daylight this sample displayed slightly less of the blue component than in the other stones, and therefore its colour change was less distinct.

The absorption spectra resembled those of colour-change pyrope-spessartine described by Lind (2015) and Schmetzer *et al.* (2009). Those samples revealed a band at about 410 nm and a weaker feature at 484 nm due to Mn²⁺; (weak) features at 505 and 525 nm, plus a band at about 570 nm, due to Fe²⁺; and an intense band at 573 nm due to Cr³⁺ and V³⁺.

The RI values of the round and triangular stones were (1) considerably lower than those reported by Lind (2015)



Figure 20: The three faceted colour-change garnets from Tanga, Tanzania (2.02 ct oval, 1.09 ct round and 1.07 triangle) examined for this report are shown here in daylight-equivalent illumination. In incandescent light, all three stones appear purplish red. Photo by J. C. Zwaan.

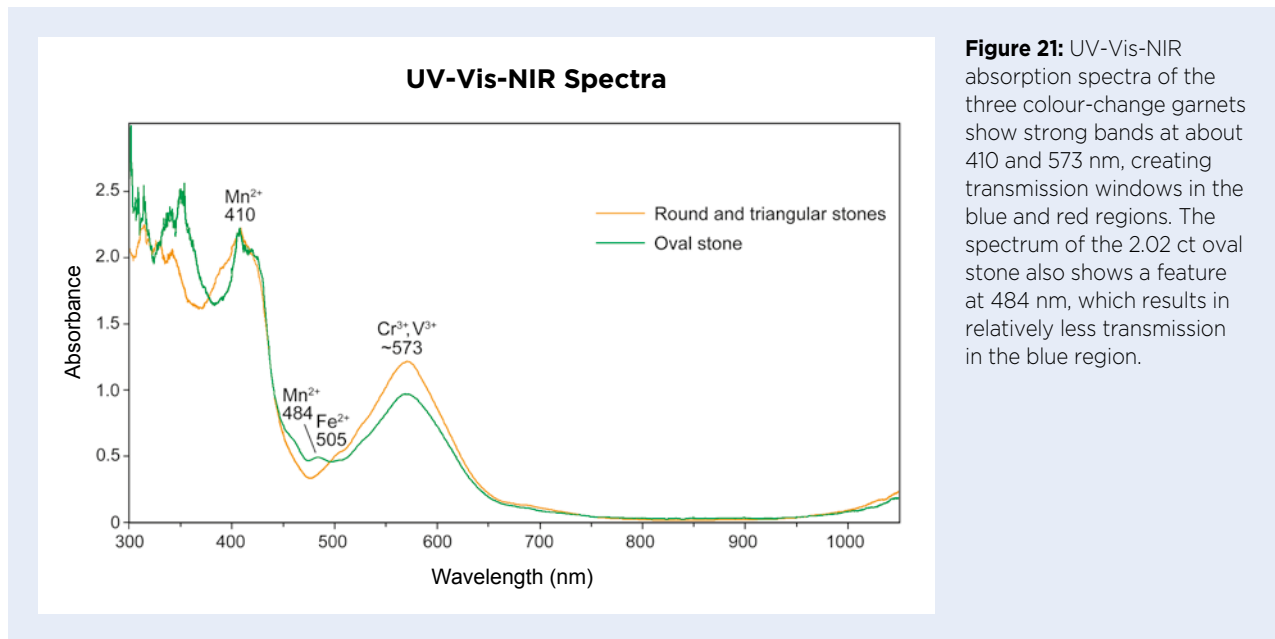


Figure 21: UV-Vis-NIR absorption spectra of the three colour-change garnets show strong bands at about 410 and 573 nm, creating transmission windows in the blue and red regions. The spectrum of the 2.02 ct oval stone also shows a feature at 484 nm, which results in relatively less transmission in the blue region.

for colour-change garnets (1.751–1.771); (2) considerably lower than those of V ± Cr-bearing pyrope-spessartine garnets from Umba (1.757; Jobbins *et al.* 1975) and from Tranoroa, Madagascar (1.768–1.773; Schmetzer *et al.* 2002); and (3) similar but still lower than those of colour-change garnets from Bekily, Madagascar (1.750–1.755; Schmetzer *et al.* 2002), indicating a higher pyrope content than is commonly present in colour-change garnets (pyrope-spessartine solid solution: pyrope dominant RI < 1.760 and spessartine dominant RI > 1.765; Lind 2015).

EDXRF spectroscopy obtained with an EDAX Orbis Micro-XRF Analyzer revealed major amounts of Mg, Mn, Al and Si (with Mg > Mn in all three stones), plus minor Ca and Fe, with traces of Cr, V and Zn (Table II). The 2.02 ct oval had a higher Mn content (about 13–14 wt.% MnO) than the other two stones (about 7–8 wt.% MnO). Comparison of the Cr₂O₃ + V₂O₃ concentrations to the spectra in Figure 21 indicates that only a slight increase in Cr³⁺ + V³⁺ can have a considerable impact on the intensity of the 573 nm band (Lind 2015).

Table II: Minor and trace elements by EDXRF in colour-change pyrope-spessartine from Tanga, Tanzania.

| Oxides (wt.%) | Oval (2.02 ct) | Round (1.09 ct) | Triangle (1.07 ct) |
|--|----------------|-----------------|--------------------|
| CaO | 3.6–3.9 | 2.5–2.6 | 1.8–1.9 |
| FeO | 1.9 | 3.4–3.5 | 2.5–2.6 |
| Cr ₂ O ₃ + V ₂ O ₃ | 0.40–0.42 | 0.60–0.64 | 0.64–0.67 |
| ZnO | 0.03 | 0.05–0.06 | 0.05 |

The extent of the colour change in the pyrope-spessartine samples described here could be described as moderate for the round and triangular stones, and faint for the oval stone, when compared to the overall range of colour change observed in garnets, some of which display a very strong change from green to bluish green in daylight to red-purple in incandescent light (Schmetzer *et al.* 2009).

Dr J. C. (Hanco) Zwaan FGA
(hanco.zwaan@naturalis.nl)

Netherlands Gemmological Laboratory
Naturalis Biodiversity Center
Leiden, The Netherlands

References

- Jobbins, E.A., Saul, J.M., Tresham, A.E. & Young, B.R. 1975. Blue colour-change gem garnet from East Africa. *Journal of Gemmology*, **14**(5), 201–208, <https://doi.org/10.15506/jog.1975.14.5.201>.
- Lind, T. 2015. Kristallchemie und Farbe von Granaten kommerzieller Edelsteinvorkommen [Crystal chemistry and colour of garnets from commercial gemstone deposits]. *Gemmologie: Zeitschrift der Deutschen Gemmologischen Gesellschaft*, **64**(1/2), 1–41.
- Schmetzer, K., Hainschwang, T., Bernhardt, H.-J. & Kiefert, L. 2002. New chromium- and vanadium-bearing garnets from Tranoroa, Madagascar. *Gems & Gemology*, **38**(2), 148–155, <https://doi.org/10.5741/gems.38.2.148>.
- Schmetzer, K., Bernhardt, H.-J., Bosshart, G. & Hainschwang, T. 2009. Colour-change garnets from Madagascar: Variation of chemical, spectroscopic and colorimetric properties. *Journal of Gemmology*, **31**(5), 235–282, <https://doi.org/10.15506/JoG.2009.31.5.235>.

Hessonite from Somaliland

Somaliland is an autonomous region of Somalia in East Africa, and has produced gem-quality garnet, opal, emerald, aquamarine and several other gem materials (Kinnaird & Jackson 2000). At the February 2020 Tucson gem shows, one of the authors (AMY) had some recent production of rough and cut orange garnets from Somaliland. According to his contacts in the mining area—including dealer Ahmed Shekh, a miner named Abdikarim and archaeologist Mohamed Abdi Allamagan—the garnet-bearing area is situated in an area measuring approximately 10 × 10 km that is located just south-west of the town of Daarbuduq (or Da'ar buduq), which is in between the capital city of Hargeisa and the coastal city of Berbera. Garnets have been mined from secondary deposits in this area since the 1990s, although some stones were collected from the surface before that time.

Both artisanal and mechanised methods have been used to recover the garnets. Artisanal miners work in groups of 3–5 persons and employ simple hand tools to dig shafts that are 1 m wide and average 4–6 m deep; sometimes three or four tunnels are interconnected. On average, each miner collects about 1 kg of garnet rough per day, although production may be greater during the rainy season. Mechanised mining takes place mainly along riverbanks, where about 50–100 persons work in screening operations. Depending on the capacity of the machinery used, the average daily production from each one ranges from about 15 to 40 kg.

The rough garnets consist of medium to dark orange broken fragments (rarely showing crystal faces) that typically range up to 5 g each, with the largest stones weighing 50 g. About 40% is of good quality and 60% is comprised of lower-grade material.

Author AMY donated some rough and cut garnets

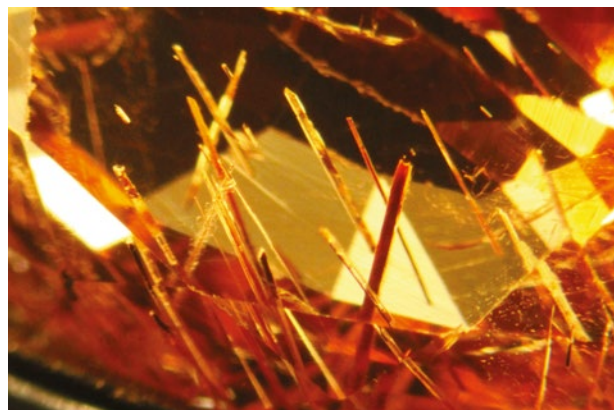


Figure 23: Etch tubes are prominent in this hessonite from Somaliland. Photomicrograph by B. Williams; image width 6 mm.

to Gem-A (Figure 22), and the five faceted stones were characterised by authors BW and CW. They weighed 5.66–8.16 ct and ranged from medium yellowish orange (6.13 ct) to deep orangey red (6.04 ct). The RI ranged from 1.740 (6.13 ct) to 1.749 (6.04 ct), and SG was measured hydrostatically at 3.61 (6.13 ct) to 3.64 (6.04 ct). These values are all within the expected range for grossular (hessonite), with those exhibiting a deeper, more reddish colouration—along with higher RI and SG values—inferred to contain greater amounts of iron. The identification of all the samples as grossular was confirmed by Raman spectroscopy using a Magilabs GemmoRaman-532SG spectrometer. Between crossed polarisers, some stones showed uneven, patchy, anomalous extinction while others exhibited a more striated and semi-parallel extinction pattern. Inclusions consisted of partially healed fluid-filled fissures, etch tubes (Figure 23) and colourless crystalline inclusions with a prismatic or rhomboid shape that appeared to be calcite and/or apatite. Absent was the roiled optical effect that is commonly seen in hessonite.

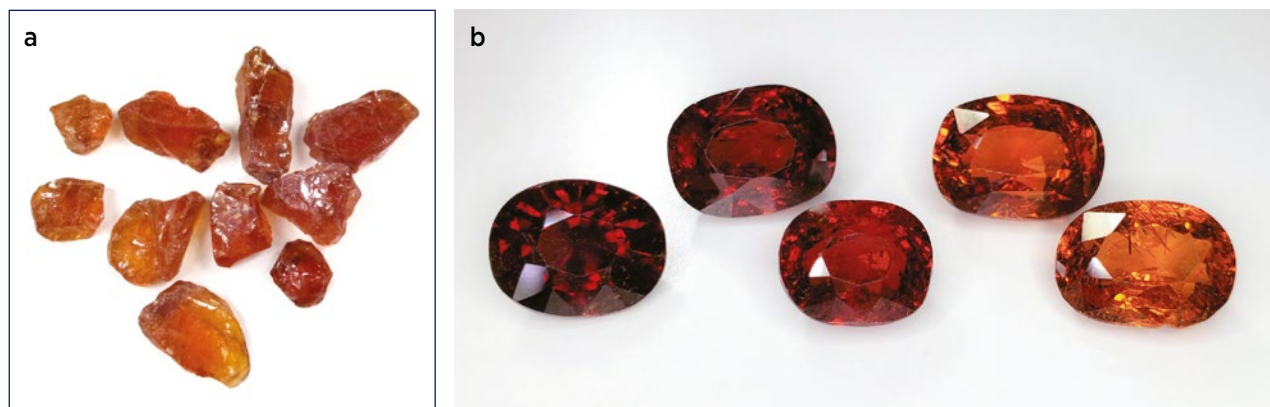


Figure 22: (a) These rough pieces of hessonite from Somaliland range from yellowish orange to reddish orange and weigh 0.70–2.47 g. (b) The five faceted hessonites examined for this report weigh 5.66–8.16 ct. Photos by (a) B. Williams and (b) C. Williams.

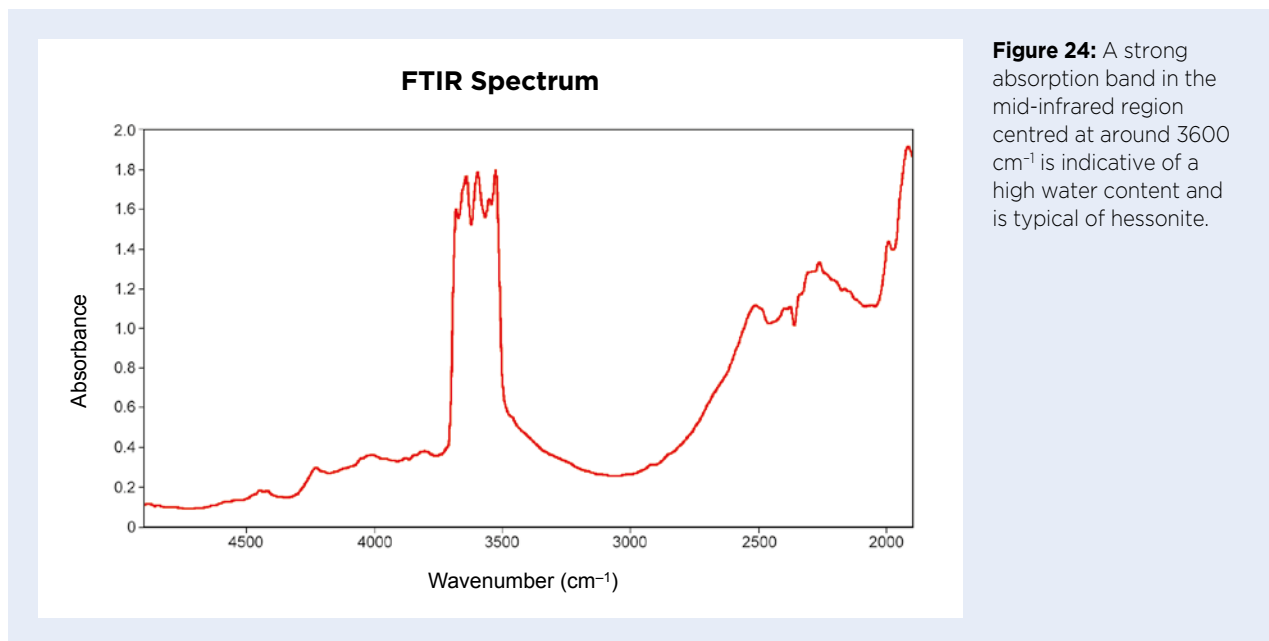


Figure 24: A strong absorption band in the mid-infrared region centred at around 3600 cm^{-1} is indicative of a high water content and is typical of hessonite.

Fourier-transform infrared (FTIR) spectroscopy using a Magilabs GemmoFtir showed a distinctive water absorption band centred at around 3600 cm^{-1} (Figure 24), which in these authors' experience is a consistent feature of hessonite.

Kinnaird and Jackson (2000) documented three different types of orange to red garnets from Somaliland: grossular, pyrope and almandine. The grossular was orange-red (i.e. hessonite) with a composition of $\text{Grs}_{86.9}\text{And}_{9.86}\text{Alm}_{2.57}$ (with traces of pyrope and spessartine components), and it contained a cluster of parallel, tubular, partially liquid-filled inclusions. Clark (2014) also documented a hessonite from Somalia, which was orange and had an RI of 1.741; it was described as containing small flake-like inclusions and transparent needle-like and tabular crystals, descriptions consistent with the inclusions noted in the present hessonites. In addition, as in the present samples, the stone examined by Clark (2014) lacked a roiled appearance.

The presence of hessonite in the Daarbuduq area is consistent with the geology of the region. According to

the geological map presented by Kinnaird and Jackson (2000), the area is underlain by Proterozoic marbles and other metamorphic rocks of the Mora complex that are intruded by granitic rocks of mainly Cambrian age (500–550 million years old). The interaction between marble and granitic rock is favourable for the formation of skarn, which is a common host rock for grossular.

Bear Williams FGA and Cara Williams FGA

*Abdiaziz Mohamed Yousuf
Addis Ababa, Ethiopia*

Brendan M. Laurs FGA

References

- Clark, B. 2014. Gem Notes: Hessonite from Somalia. *Journal of Gemmology*, **34**(4), 293.
- Kinnaird, J.A. & Jackson, B. 2000. Somaliland – A potential gem producer in the Mozambique Belt. *Journal of Gemmology*, **27**(3), 139–154, <https://doi.org/10.15506/jog.2000.27.3.139>.

Laurentthomasite, a New Gem Mineral

In March 2020, the GIT Gem Testing Laboratory (GIT-GTL) received two greenish blue faceted stones that weighed 0.98 and 1.67 ct for identification (Figure 25a). The stones' owner indicated that they reportedly consisted of a newly described mineral, laurentthomasite, named after the French mineral dealer Laurent Thomas of Polychrom France (www.mindat.org/min-53556.html). The mineral

was discovered in Madagascar's Toliara Province, and in April 2019 it was approved by the International Mineralogical Association as a new member of the milarite (osumilite) group—specifically the Mg analogue of milarite ($\text{KCa}_2\text{AlBe}_2\text{Si}_{12}\text{O}_{30} \cdot 0.5\text{H}_2\text{O}$)—with an ideal chemical formula of $\text{KMg}_2\text{AlBe}_2\text{Si}_{12}\text{O}_{30}$ and hexagonal symmetry (Ferraris *et al.* 2019).

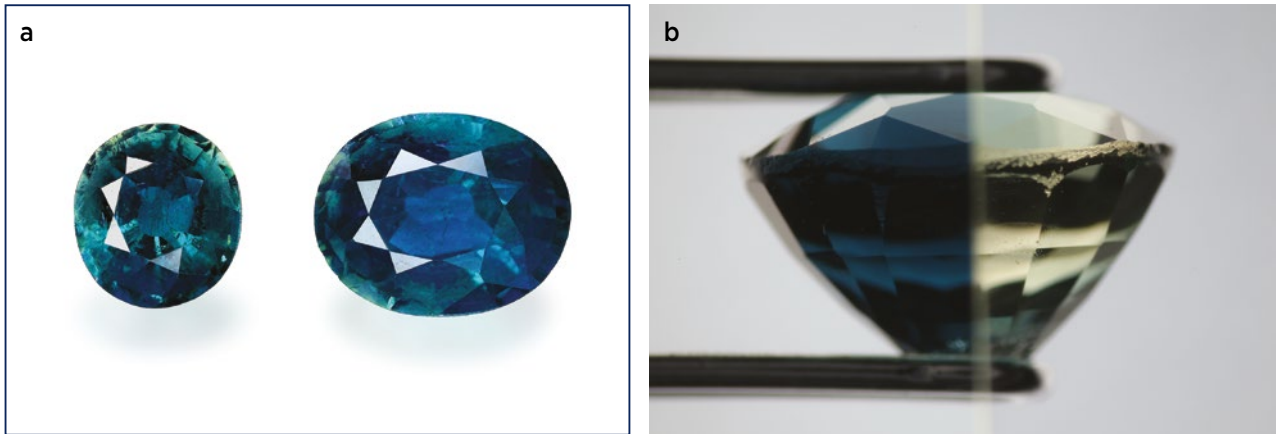


Figure 25: (a) The two laurentthomasite gemstones described here weigh 0.98 and 1.67 ct. (b) They exhibit strong dichroism in greenish blue and light greenish yellow, as shown here for the 0.98 ct stone. Photos by (a) C. Kamemaganon and (b) P. Ounorn.



Figure 26: Magnification of the laurentthomasite gems shows (a) 'fingerprints', (b) negative crystals and (c) primary two-phase (liquid-gas) inclusions. Photomicrographs by P. Ounorn and C. Suphan, using darkfield illumination; image widths 3.2 mm (a) and 2.8 mm (b and c).

Both gems consisted of oval mixed cuts. Standard gemmological testing showed the following properties: RIs—1.555–1.560, birefringence—0.005, optic character—doubly refractive and uniaxial positive, hydrostatic SG—2.59–2.63, and fluorescence—inert to long- and short-wave UV radiation. Their most distinct optical characteristic was strong dichroism in greenish blue and light greenish yellow (Figure 25b).

Magnification showed various features, such as 'fingerprints', negative crystals and primary two-phase (liquid and gas) fluid inclusions (Figure 26).

Polarised UV-Vis-NIR absorption spectra of the two samples in the range of 300–1500 nm, collected by a PerkinElmer Lambda 1050 spectrophotometer, showed features at 374, 407, 423, 441, 455 and 486 nm, along with a broad band at around 600–1400 nm (Figure 27).

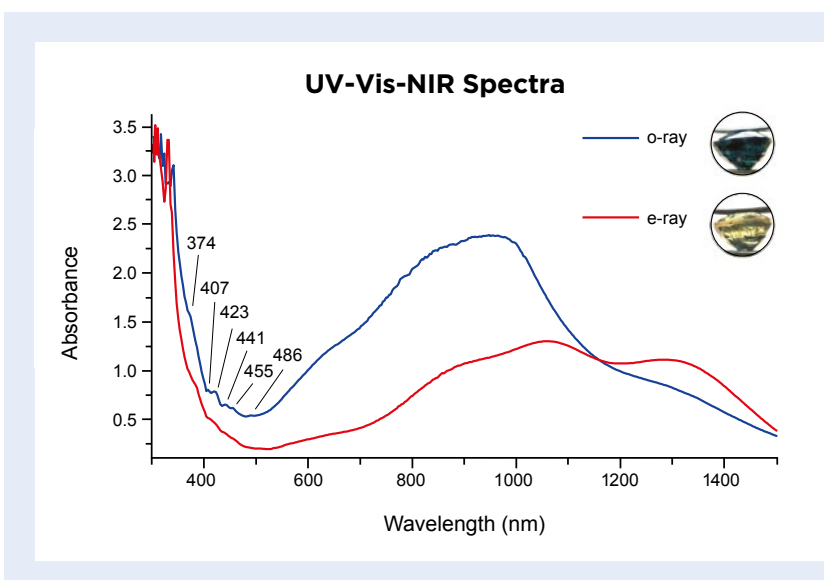


Figure 27: Representative polarised UV-Vis-NIR spectra (recorded here from the 0.98 ct stone) show broad bands centred at around 900 nm for the o-ray and 1040 nm for the e-ray, which are responsible for the strong dichroism of laurentthomasite. The path length of the beam was about 5–6 mm.

The strong dichroism corresponded to differences in the intensity and position of this broad band, which for the o-ray was centred at around 900 nm and for the e-ray was centred at around 1040 nm (and relatively weaker). As such, a distinct spectral window transmits in the blue region for the o-ray, while relatively weaker blue-green-yellow transmission is present in the e-ray direction (again, see Figure 27). (*Editor's note:* Raw data for the UV-Vis-NIR spectra are available in *The Journal's* online data depository.)

The mid-infrared spectra of both samples, recorded with a Thermo Nicolet 6700 FTIR spectrometer, showed broad transmission in the 7000–2000 cm^{-1} range along with weak absorption features at approximately 5000, 3550, 3447 and 3253 cm^{-1} (Figure 28a). Raman spectra, collected with a Renishaw inVia spectrometer using 532 nm laser excitation, showed dominant peaks (Raman shifts) at 287, 380, 490 and 566 cm^{-1} (Figure 28b). The overall pattern was similar to the reference spectrum of milarite but showed somewhat different positions for some peaks.

Semi-quantitative EDXRF chemical analyses of both stones obtained with an Eagle III spectrometer revealed enriched Si contents, minor amounts of Al, Mg, K, Fe, Sc and Mn, and traces of Rb and Y (Table III). In addition, a significant amount of Be was detected by laser-induced breakdown spectroscopy (LIBS). The data obtained by EDXRF were normalised to 100 wt. % but do not include

Table III: Semi-quantitative normalised EDXRF chemical data for laurentthomasite.*

| Oxides (wt.%) | 0.98 ct | 1.67 ct |
|--------------------------------|---------|---------|
| SiO ₂ | 83.08 | 80.72 |
| Al ₂ O ₃ | 3.70 | 4.38 |
| Sc ₂ O ₃ | 2.40 | 2.21 |
| Y ₂ O ₃ | 0.54 | 0.56 |
| Fe ₂ O ₃ | 2.37 | 2.87 |
| MnO | 1.26 | 1.66 |
| MgO | 3.39 | 3.97 |
| K ₂ O | 2.87 | 3.21 |
| Rb ₂ O | 0.39 | 0.42 |
| Sum | 100.00 | 100.00 |

* Be cannot be detected by EDXRF, so the Si data shown here are believed to be too high.

Be, so the actual content of Si (by far the most abundant element) is expected to be somewhat lower than the amount shown in Table III. Overall, the compositions we obtained are consistent with the chemical formula of an Al-Mg-K-Be silicate mineral (i.e. laurentthomasite) containing minor amounts of Fe, Sc and Mn.

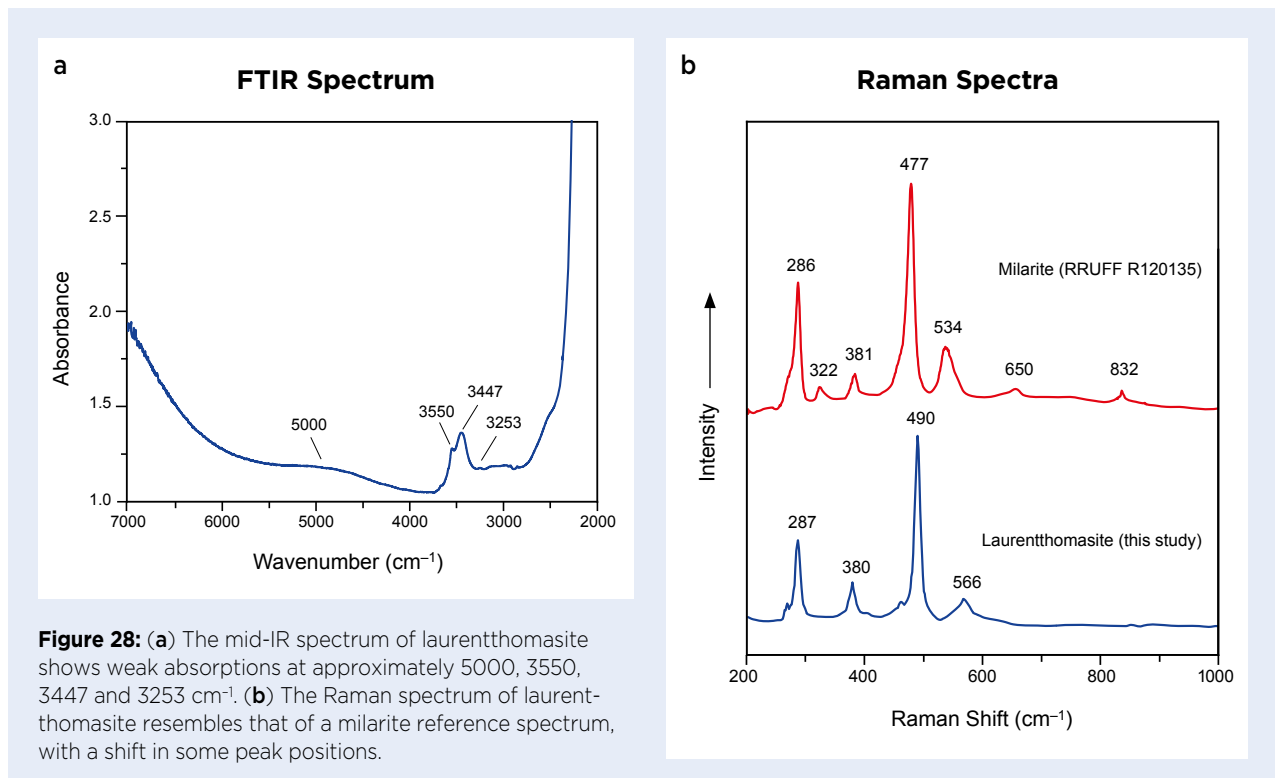


Table IV: Properties of laurenthomasite.

| Property | This study | C. Ferraris (pers. comm. 2020) |
|----------------------|--|---|
| Colour | Greenish blue | Greenish blue |
| Pleochroism | Very strong, in greenish blue and light greenish yellow | Very strong, in 'cobalt' blue and greenish yellow |
| Optic character | Doubly refractive (uniaxial +) | Doubly refractive (uniaxial +) |
| RI | 1.555-1.560 (birefringence 0.005) | 1.540-1.545 (birefringence 0.005) |
| SG | 2.59-2.63 | 2.66 |
| Hardness (Mohs) | Not determined | Approximately 6 |
| Cleavage | Not observed | Poor |
| Fluorescence | Inert to both long- and short-wave UV | Inert to both long- and short-wave UV |
| Inclusions | Negative crystals, 'fingerprints', primary two-phase (liquid-gas) inclusions | Dark elongated crystals (Fe-rich oxides) |
| UV-Vis-NIR spectrum | Absorption peaks at 374, 407, 423, 441, 455 and 486 nm with a broad absorption band at around 600-1400 nm | Not reported |
| FTIR spectrum | Broad transmission in the 7000-2000 cm ⁻¹ range with weak absorption features at about 5000, 3550, 3447 and 3253 cm ⁻¹ | Not reported |
| Raman spectrum | Peaks at 287, 380, 490 and 566 cm ⁻¹ | Not reported |
| Chemical composition | Al-Mg-K-Be-Fe-Sc-Mn silicate | (K,Na,Y,Ca)(Mg,Sc,Fe ²⁺ ,Mn) ₂ [(Be,Al,Mg,Fe ³⁺) ₂ (Si,Al) ₁₂ O ₃₀] |

A summary of the properties obtained for the laurenthomasite samples we examined is presented in Table IV and compared to data supplied by C. Ferraris (pers. comm. 2020; further information to be published in a future mineralogical article). The gemmological characteristics are similar except for somewhat higher RI and lower SG values shown by the two stones examined in the present study. Furthermore, the chemical data we obtained by EDXRF and LIBS analyses are consistent with the formula of laurenthomasite. Moreover, the Raman spectrum indicates a close association with milarite. Although the gemmological properties of laurenthomasite are similar to those of milarite (cf. www.gemdat.org/gem-2710.html), laurenthomasite has distinctly different colour/pleochroism than milarite, which is colourless to pale yellow or green.

Acknowledgements: The authors would like to thank Gemshoppe Co. Ltd for supplying the samples examined for this study. We also thank GIT-GTL deputy director

Thanong Leelawatanasuk and GIT advisory team members Dr Visut Pisutha-Arnond, Prof. Dr Chakkaphan Sutthirat and Wilawan Atichat for reviewing this article, as well as Dr Cristiano Ferraris (National Museum of Natural History, Paris, France) for providing some unpublished data on laurenthomasite.

*Papawarin Ounorn (opapawarin@git.or.th),
Budsabakorn Srisataporn and
Cheewaporn Suphan
GIT Gem Testing Laboratory
Bangkok, Thailand*

Reference

- Ferraris, C., Pignatelli, I., Cámara, F., Ponti, S., Schreyer, M., Parodi, G.C. & Wei, F. 2019. CNMNC Newsletter No. 49: Laurentthomasite, IMA 2018-157. *Mineralogical Magazine*, **83**, 480, <https://doi.org/10.1180/mgm.2019.35>.

Green Orthoclase with Chatoyancy from Vietnam

Gem-quality green feldspar from Vietnam is commonly traded as amazonite, but rather than being a variety of microcline it is actually orthoclase (Ponahlo *et al.* 2001; Laurs *et al.* 2005; Huong *et al.* 2012). Most of this material has limited transparency and is therefore suitable for cabochons or carvings, although rare transparent material has been faceted into attractive gemstones. In 2008, one of the present authors (RH) obtained some samples of green orthoclase from the Minh Tien pegmatites during fieldwork in the Luc Yen District of Yen Bai Province in northern Vietnam. These pegmatites are also known as a source of colourful tourmaline, as well as smoky quartz and citrine (Nguyen *et al.* 2010).

Some of the samples obtained by author RH displayed a sheen effect that suggested they could show chatoyancy when polished as cabochons, and cutting of this material yielded two cat's-eye orthoclase gems weighing 13.18 ct (22.50 × 12.80 mm) and 47.61 ct (26.10 × 19.50 mm; see Figure 29). Their RIs were 1.519–1.524 (birefringence of 0.005) and SG values were 2.45 and 2.51. The stones were inert to long-wave UV radiation, but showed strong blue-white fluorescence to short-wave UV. The chatoyancy displayed by both cabochons was caused by aligned voids and channels (e.g. Figure 30).

The previously known occurrences of green orthoclase in the Minh Tien area have been exhausted and nowadays this material is only rarely encountered in the trade. However, light green orthoclase imitations are sometimes offered at the local gem market in Luc Yen, including transparent fluorite and included pieces of glass.

Drs Radek Hanus and Ján Štubňa



Figure 30: The cat's-eye effect in the Vietnamese orthoclase is caused by linear arrays of voids and channels. Photomicrograph by R. Hanus; image width 2.8 mm.

References

- Huong, L.T., Häger, T., Hofmeister, W., Hauzenberger, C., Schwarz, D., Van Long, P., Wehrmeister, U. *et al.* 2012. Gemstones from Vietnam: An update. *Gems & Gemology*, **48**(3), 158–176, <https://doi.org/10.5741/gems.48.3.158>.
- Laurs, B.M., Rossman, G.R. & Shigley, J.E. 2005. Gem News International: Green orthoclase feldspar from Vietnam. *Gems & Gemology*, **41**(4), 354–355.
- Nguyen, T.M.T., Nguy, T.N., Hofmeister, W. & Häger, T. 2010. Amazonite from Luc Yen mining, Yen Bai, Vietnam. *Fifth International Workshop on Provenance and Properties of Gem and Geo-Materials*, Hanoi, Vietnam, 17–24 October, 40–52.
- Ponahlo, J., Tam, T.T., Brandstätter, F. & Wilder, M. 2001. Transparent green orthoclase, a new ornamental stone from North Vietnam. *28th International Gemmological Conference*, Madrid, Spain, 71–75.



Figure 29: These two cabochons of orthoclase from Vietnam display chatoyancy. The stones weigh (a) 13.18 ct and (b) 47.61 ct. Photos by J. Štubňa.

Faceted Proustite from Chañarcillo, Chile

Proustite (Ag_3AsS_3), and its antimony analogue pyrargyrite (Ag_3SbS_3), are commonly known as *ruby silver*. They both are deep red and display an adamantine to submetallic lustre, although proustite tends to be more transparent and a lighter red than pyrargyrite. Proustite forms particularly attractive crystal clusters that are highly prized by mineral collectors, but they are very difficult to obtain:

Good proustites are almost impossible to field collect and are typically available only from old collections or once-a-century type finds in operating silver mines. Consequently, this much-revered mineral...exemplifies one of the truly difficult-to-acquire collectible species. (Cook 1996, p. 345)

According to Cook (1996), collectible proustite crystals are found in Canada, USA, Mexico, Peru, Chile, Czech Republic, Germany, France, Italy (Sardinia) and Russia (Siberia). More recently, Morocco has also produced high-quality specimens. The finest proustites are widely regarded as coming from the Dolores silver mine in the Chañarcillo District of northern Chile. The district was discovered in 1832, reached maximum production during approximately 1860–1880, and continued to be mined in underground workings until the early 20th century (Sillitoe 2007). Proustite specimens from Chañarcillo have found their way into private and museum collections worldwide, and although faceted gemstones are very rare, Hyršl (2003) indicated that gems from this locality are known to weigh up to 55.48 ct.

Given the scarcity of fine-quality proustite today—as either specimen- or facet-grade material—this author was surprised to see a recently faceted 43.21 ct Chañarcillo proustite at the booth of Pala International (Fallbrook, California, USA) during the February 2020 Tucson gem shows. According to Bill and Carl Larson, the original rough piece was traded out of an old museum collection

and then passed through another dealer before they acquired it. Since it consisted of a broken piece that was not very desirable as a mineral specimen (Figure 31a), the Larsons assessed its potential gem value and determined that it contained a large area that was transparent enough for faceting. The piece was entrusted to Tim Condrón (InOro Gems and Jewels, Sedona, Arizona, USA). Performing the rough (Figure 31b, c) was challenging due to the brittle nature of proustite (which is also quite soft, having a Mohs hardness of about $2\frac{1}{2}$) and the difficulty of seeing inside the piece. Other factors that make proustite difficult to facet are its distinct cleavage on $\{10\bar{1}1\}$ and the common occurrence of twinning. In addition, proustite is photochromic, so prolonged exposure to bright light will cause it to darken and acquire a dull tarnish on the surface.

Despite the challenges of working with this material, Condrón obtained the 43.21 ct stone shown in Figure 32, along with a 2.49 ct round brilliant. A very light touch was needed when cutting the gems, and Condrón used a homemade wax lap for the final polish. The stones contained some feathers, partially healed fractures and growth tubes, and the larger gem also hosted a surface-reaching channel with an angular cross-section.

The red colouration of proustite is best appreciated by passing some transmitted light through the gem (again, see Figure 32). According to Loeffler and Burns (1976), proustite is red because it is a semiconductor material with a band gap of $\sim 16,000\text{ cm}^{-1}$ (or 625 nm). Light wavelengths with energies greater than the band gap are absorbed, while lower-energy wavelengths are transmitted. The band gap of proustite at 625 nm is in the orange region of the spectrum, so only the lower-energy red wavelengths are transmitted.

This instance shows the value of examining rough samples of proustite (or other rare collector's stones) for

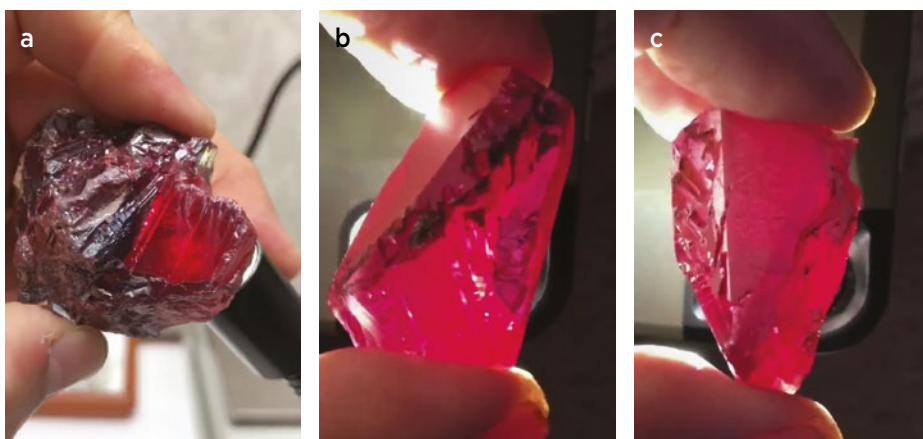


Figure 31: These images (taken from video clips) show (a) the original specimen before cutting, and (b, c) two views of the facetable portion of the proustite during the preforming process. Photos courtesy of Tim Condrón.

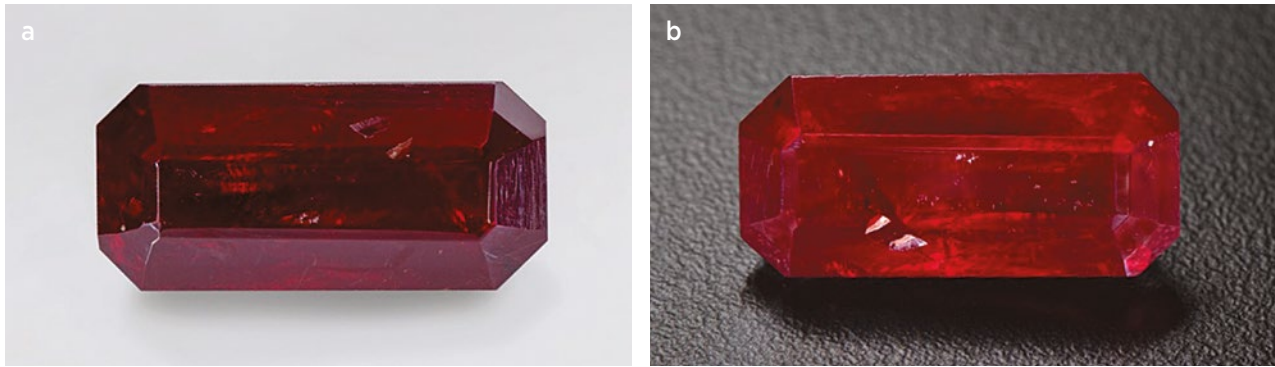


Figure 32: The finished 43.21 ct proustite is shown here (a) under diffuse illumination and (b) with partially transmitted light. Photos by Orasa Weldon.

their gem potential, particularly when they consist of broken pieces that are undesirable as crystal specimens.

Brendan M. Laurs FGA

References

Cook, R.B. 1996. Connoisseur's Choice: Proustite—Delores [sic] mine, Chañarcillo, Chile. *Rocks & Minerals*, **71**(5), 344–346, <https://doi.org/10.1080/00357529.1996.11761555>.

Hyršl, J. 2003 Gem News International: Some rare faceted gem materials. *Gems & Gemology*, **39**(4), 334–336.

Loeffler, B.M. & Burns, R. 1976. Shedding light on the color of gems and minerals. *American Scientist*, **64**, 636–647, www.jstor.org/stable/27847555.

Sillitoe, R.H. 2007. Hypogene reinterpretation of supergene silver enrichment at Chañarcillo, northern Chile. *Economic Geology*, **102**(5), 777–781, <https://doi.org/10.2113/gsecongeo.102.5.777>.

Visit to a New Blue Spinel Mining Area in Vietnam

In July 2019, this author heard rumours about a major find of blue spinel—supposedly including some fine-quality cobalt-coloured material—that occurred at a new deposit in the Luc Yen District of northern Vietnam. The mine is known as Bai Boui, which means ‘Pomelo mine’ in Vietnamese. It is located north-west of Thac Ba Lake, about 43 km north of the town of Yen Bai. The initial discovery took place in June 2019 and was soon followed by a mining rush, with up to 500 people digging in the area. This lasted for several weeks until government officials sent police to clear the area. (In recent years, Vietnam has become more restrictive in allowing people to mine, even on their own property.) Local dealers estimated that during July–August 2019, rough and cut blue spinel from this find sold for around USD500,000 at the local gem market in Luc Yen. Some of the production was obtained by Vietnamese dealers and most of the remainder was purchased by gem merchants from Bangkok.

In November 2019, this author and his wife, Darunee (Muy) Pisutadamongkol, went on a buying trip to Vietnam. From the capital city of Hanoi it took 4½–5 hours to drive to Luc Yen. There we visited the gem market, and saw some rough blue to violet spinel represented as being from Bai Boui that was mostly dark coloured, had grey tones and showed a colour shift to purple-grey in incandescent

light. When viewed with a Chelsea Colour Filter, most of the spinel showed no reaction, or appeared ‘murky’ pink in the filter. Also, the spinel displayed almost no fluorescence when viewed with a 380 nm UV laser pointer. By contrast, fine ‘cobalt spinel’ appears bright red with the Chelsea filter and it fluoresces intense red to long-wave UV radiation. Therefore, it seemed likely that the blue colour of most of the samples examined was due mainly to iron rather than cobalt.

With the help of our local contacts, we arranged a trip to the Bai Boui spinel mine. From Luc Yen we travelled by motorbike for about 40 minutes to where steep karst formations blocked further wheeled travel. We then hiked to the site of the initial mining rush, which was marked by pits of 1–2+ m deep in the alluvial soil between the karst outcrops. Further examination showed that the soil had been removed from almost every spot of the karst that was wide enough for a person to enter. We continued climbing through challenging karst terrain, sometimes crossing bamboo bridges that traversed deep gaps between fins of weathered marble. We passed several scattered areas where digging was evident amongst the jungle growth. After proceeding about 300 m we entered an area that was about 75–100 m wide, spanning an elevation of 30–40 m, which had been cleared of most vegetation and was



Figure 33: (a) The Bai Boui spinel mining area is situated in karst terrain. (b) Gravels containing blue spinel are mined from narrow ravines in the weathered marble. Photos by (a) D. Pisutadamongkol and (b) D. Blauwet.

being actively worked (e.g. Figure 33). A mining camp consisted of a large tarpaulin with open sides where the miners slept and prepared food. Near the top of the area was a large tarpaulin tank for capturing and storing water, both for drinking and for washing the alluvial gravels. The highest worked area was at an elevation of 475 m and was located at coordinates 22°05.296'N, 104°47.271'E.



Figure 34: The spinel-bearing gravels are hand washed in a small pond using shallow baskets. Photo by D. Blauwet.

Approximately 20 people were working in the area, and most of the digging took place in narrow ravines that were 0.5–2 m wide where alluvial gravels had been deposited. The gravels were washed in a makeshift pond using wide, flat, woven bamboo baskets (Figure 34). We also saw a small hand-turned trommel at the site.

Nevertheless, only small amounts of spinel had been recovered recently. Although most of the material we saw was not transparent enough for cutting, it could be sold to artisans in Luc Yen for use in making gem 'paintings'. The asking prices at the mine were too high to even consider starting the bargaining process.

The following day, we returned to the gem market and bought a parcel of small Bai Boui rough spinel for a reasonable price. We also obtained a larger fragment of Bai Boui spinel from our regular supplier that had a redder appearance under the Chelsea filter and also fluoresced, as well as showed a significant colour change. Cutting of this piece in Sri Lanka yielded a 1.15 ct stone, and some smaller gems were also cut from the other rough material (e.g. Figure 35).

Additional blue spinel from Bai Boui will probably enter the market in the future as more of the rough is cut. It is also likely that other small deposits of blue spinel will continue to be found in Vietnam in the future.

Dudley Blauwet (DudleyBlauwet@gmail.com)

*Dudley Blauwet Gems
Louisville, Colorado, USA*



Figure 35: Cutting of some of the rough Bai Boui spinel obtained at the Luc Yen gem market yielded these blue to violet gems (0.42–0.66 ct). Photo by D. Blauwet.

Gemmological and Spectroscopic Characteristics of Different Varieties of Amber from the Hukawng Valley, Myanmar

Xinran Jiang, Zhiqing Zhang, Yamei Wang and Fanli Kong

ABSTRACT: With its broad range of varieties, Burmese amber may show various optical effects, including ‘oil gloss’ (a red or green surface fluorescence effect) and phosphorescence phenomena. Samples representing golden, brown, red (‘blood’), ‘beeswax’ and ‘root’ ambers were characterised, as well as those showing red or green ‘oil gloss’; many of these also displayed phosphorescence. Common internal features seen with optical microscopy include reddish brown dot-like inclusions in brown amber and flow-banded concentrations of bubbles in ‘beeswax’ and ‘root’ ambers (the latter displaying patterns comprised of opaque light- and dark-coloured layers). SEM imagery revealed various scaly or layered structures on freshly broken surfaces, micro-bubbles in some samples and distinctive hollow micro-channels in ‘root’ amber. Fluorescence spectra recorded luminescence centres at 432 and 470 nm in all samples, and additionally at 650 nm (\pm 625 nm) in red ‘oil gloss’ amber. The ‘oil gloss’ appearance is caused by a mixture of surface fluorescence and the amber’s body colour. Phosphorescence spectroscopy showed that the effect was strongest at 525 nm, and the phosphorescence lifetime measured at this emission wavelength ranged from 0.134 to 1.396 seconds.

The Journal of Gemmology, 37(2), 2020, pp. 144–162, <https://doi.org/10.15506/JoG.2020.37.2.144>
© 2020 Gem-A (The Gemmological Association of Great Britain)

Myanmar is a major source of Asian amber (e.g. Figure 1), and Burmese amber (or Burmite) has the longest geological history (about 98 million years old: Shi *et al.* 2012) and most complicated formational patterns compared to material from other localities around the world (Edwards *et al.* 2007; Dutta *et al.* 2011; Zong *et al.* 2014). For millennia, Burmese amber has been highly valued for producing art objects and jewellery (Zherikhin & Ross 2000), and according to the authors’ research it currently represents 10%–20% of China’s amber market. Burmese amber is also well known for its diversity of inclusions, including invertebrates and plant materials (Lauris 2012; Lu *et al.* 2014), which have multidisciplinary importance to fields such as geology, biology and palaeontology (e.g. Xing *et al.*

2016). Most Burmese amber comes from the Hukawng Valley in northern Myanmar (e.g. Cruickshank & Ko 2003), although other deposits are known near Khamti in the Sagaing Region of northern Myanmar (Liu 2018) and near Hti Lin in the central part of the country (Tay *et al.* 2015).

Several distinctive types of amber are recognised from Myanmar, and some of them have not been found elsewhere. However, their gemmological properties and fluorescence characteristics have not been studied systematically until fairly recently (see Jiang *et al.* 2017, 2018, 2019; Xie *et al.* 2017; Xiao & Kang 2018—all in Chinese). In this study, we characterise different types of Burmese amber by observing their micro-structures as well as fluorescence and phosphorescence spectra to explain their appearance and optical effects.



Figure 1: This large faceted Burmese amber weighs 42.33 ct and shows the attractive appearance of golden amber from Myanmar. Photo by Mark Smith, Thai Lanka Trading Ltd. Part., Bangkok, Thailand.

Types of Burmese Amber

Burmese amber can be broadly divided into two main groups, according to whether it is mostly transparent or opaque. The mostly transparent ambers are classified according to their colour into golden, brown and red (or 'blood') varieties (Figures 2a–c), with brown being the most common. The red colour of 'blood' amber is caused by oxidation and is concentrated near the surface; when such material is sliced, the golden colour of the interior becomes visible (Figure 2d). If the coloured layer is particularly dark, it is called 'black' amber (Xiao *et al.* 2014; Zhang *et al.* 2017).

There are two main opaque types of amber found in Myanmar: 'beeswax' amber, which is a mixture of opaque and transparent ambers displaying flow patterns (Figure 3a); and 'root' amber, which shows a mixture of colours (e.g. white, yellow, brownish yellow, orange and/or brown) in patterns that resemble wood or tree roots (Figure 3b).

Some transparent ambers display an 'oil gloss' surface fluorescence effect when observed in sunlight and under some artificial light sources. These samples may show various body colours when viewed over a white background (yellow, greenish yellow, brown and brownish

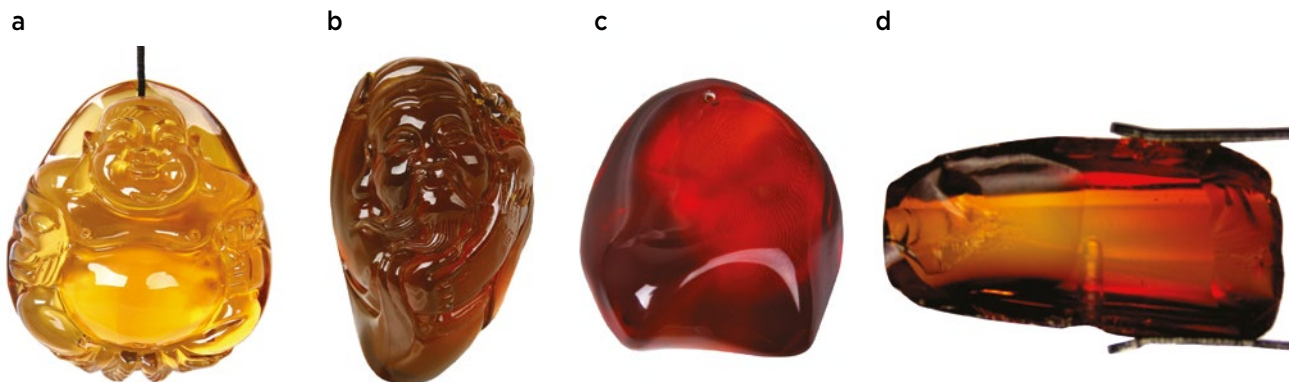


Figure 2: Transparent Burmese amber may be divided into various colour categories, such as (a) golden, (b) brown, which is the most common colour variety, and (c) 'blood' or red amber. (d) When 'blood' amber is sliced, the golden colour of the interior becomes visible, since the red colouration is only present near the surface. The samples weigh (a) 156.15 ct, (b) 146.60 ct, (c) 105.60 ct and (d) 2.83 ct. Photos a–c reprinted with permission from Wang (2018); image d by X. Jiang.

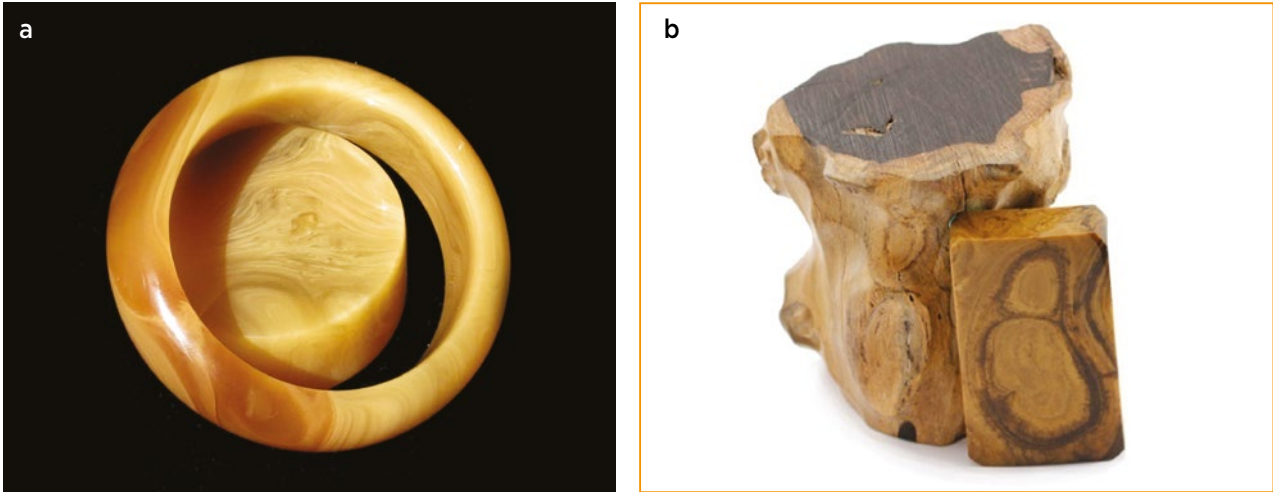


Figure 3: The two types of opaque Burmese amber consist of (a) ‘beeswax’ and (b) ‘root’ varieties. The total weight of the samples is (a) 78.77 g and (b) 25.20 g. Photos reprinted with permission from Wang (2018).

red), but appear to exhibit different surface hues over a black background. For example, amber with a greenish yellow body colour may show a reddish surface appearance when viewed against a black background (Figure 4a, b). Also, reddish brown amber can show a greenish surface appearance against a black background (Figure 4c), and is therefore sometimes known colloquially as ‘chameleon’ amber. Such amber is often referred to in

China as having ‘machine-oil gloss’ because its appearance may resemble that of machine oil.

Burmese amber may also show phosphorescence. After being illuminated by bright light for a certain time period (typically at least several seconds), the exposed area will display greenish yellow phosphorescence for a short time (typically 0.5–1 s; see Figure 4d). This phenomenon may occur in various types of transparent



Figure 4: Some Burmese amber displays an ‘oil gloss’ effect, in which the stone’s true body colour is seen against a light background, but a different colour appearance due to a surface fluorescence effect is observed when the amber is viewed against a dark background. (a) This 81.75 ct sample has a greenish yellow body colour visible against a white background, but (b) it appears reddish against a dark background. (c) The 13.75 ct amber in this pendant has a reddish brown body colour, but it appears green when viewed over a dark background. (d) Transparent Burmese amber (here, 96.35 ct) also commonly displays greenish yellow phosphorescence. Photos a–c reprinted with permission from Wang (2018); image d by X. Jiang.



Figure 5: This light yellow Burmese amber (a) appears greenish in daylight-equivalent lighting (b) due to its blue long-wave UV fluorescence (c). The sample weighs 20.21 ct; photos by X. Jiang.

Burmese amber and is commonly known as a ‘glow-in-the-dark’ effect.

Pale-coloured Burmese amber with blue fluorescence may appear green (from the combination of blue luminescence and yellow body colour; see Figure 5) or

even blue when viewed in daylight, and is therefore sometimes called ‘blue’ amber; such material is known from various world localities and has been well documented (e.g. Chekryzhov *et al.* 2014; Jiang *et al.* 2017), so it is not included in the present article.

MATERIALS AND METHODS

Samples

Nine representative amber samples from the Hukawng Valley in Myanmar were studied for this report (see Table I and Figure 6). These included three pieces of transparent amber (golden, brown and ‘blood’), both types

of opaque amber (one ‘beeswax’ piece and two ‘root’ samples) and three ‘oil gloss’ ambers (two showing red ‘oil gloss’ and one with green ‘oil gloss’). Phosphorescence was exhibited by most samples, but not by the three opaque pieces or the ‘blood’ amber.

Table I: General gemmological characteristics of the nine Burmese amber samples.

| Type | Sample ID | Body colour | Optical effects | Transparency | SG | Internal features |
|-------------------|-----------|-------------------------------------|---|------------------------------------|------|--|
| Golden amber | JP | Golden | Phosphorescence | Transparent | 1.04 | Reddish brown impurities and calcite-filled fissures |
| Brown amber | ZP | Reddish brown | Phosphorescence | Mostly transparent | 1.04 | Reddish brown dot-like inclusions directionally arranged along flow patterns |
| ‘Blood’ amber | XP | Red (surface) | — | Transparent | 1.05 | No features seen |
| ‘Beeswax’ amber | ML | Yellowish white | — | Opaque | 1.04 | Yellowish white flow patterns, black inclusions |
| ‘Root’ amber | GP-1 | Yellowish white and yellowish brown | — | Mostly opaque | 1.02 | Conspicuous yellowish white flow patterns with opaque and transparent zones |
| | GP-2 | Yellowish white | — | Opaque | 1.04 | Mottled structure |
| ‘Oil gloss’ amber | GX-1 | Reddish brown | Red ‘oil gloss’, phosphorescence | Transparent | 1.03 | Fissures resembling a bird feather or displaying iridescence |
| | GX-2 | Greenish yellow | Red ‘oil gloss’, phosphorescence | Transparent | 1.03 | Nearly free of inclusions |
| | GX-3 | Reddish brown | Green ‘oil gloss’ (or ‘chameleon’), phosphorescence | Transparent with opaque impurities | 1.05 | Dark opaque impurities (foreign objects) |



Figure 6: Burmese amber samples studied for this report include (a) golden, (b) brown, (c) 'blood', (d) 'beeswax', (e and f) 'root', (g and h) red 'oil gloss' and (i) green 'oil gloss' varieties. The colour appearance of the 'oil gloss' varieties is shown against both white and black backgrounds. Photos by X. Jiang.

Experimental Methods and Test Conditions

Internal features in all samples were examined with a gemmological microscope. In addition, the structural characteristics in five of the samples—consisting of the golden, brown and ‘beeswax’, as well as the two ‘root’ ambers—were studied with scanning electron microscopy (SEM), which was performed at the State Key Laboratory of Geological Processes and Mineral Resources, China University of Geosciences, Wuhan. The samples were fractured and gold coated to provide surfaces suitable for SEM examination (cf. Zhang & Li 2010). We used an FEI Quanta 200 environmental SEM operating under low vacuum with the following conditions: 20 kV acceleration voltage, 3.5 nm electron beam spot diameter, 1024 × 884 pixels resolution and 12.5–18.3 mm working distance.

Infrared spectroscopy of all samples was performed at the Guangzhou laboratory of the Gemmological Institute, China University of Geosciences. The specular reflection method was used (Kramers-Kronig transformation) with a Bruker Tensor 27 Fourier-transform infrared (FTIR) spectrometer under the following conditions: 220 V scanning voltage, 6 mm raster, 10 kHz scanning rate, 32 scans, 4000–400 cm⁻¹ range and 4 cm⁻¹ resolution.

The fluorescence of all samples was checked with a standard 4 W long-wave UV lamp. Three-dimensional fluorescence spectroscopy was performed on the five samples showing fluorescence (JP, ZP, GX-1, GX-2 and GX-3) with a Jasco FP-8500 spectrofluorometer at the Gem Testing Center, China University of Geosciences, Wuhan. The parameters included a bandwidth excitation of 5 nm and emission of 5 nm, response time of 10 ms, excitation range of 220–500 nm (5 nm interval), emission range of 240–750 nm (1 nm interval) and scanning velocity of 2,000 nm/min. The data were plotted according to excitation wavelength, emission wavelength and fluorescence intensity, and in addition we generated two-dimensional fluorescence spectra (emission wavelength vs. intensity) for the optimum excitation wavelength of 365 nm and for other excitations (400 and 460 nm). For comparison, we also obtained two-dimensional fluorescence spectra for samples GX-1 and GX-2 with another instrument, a Qspec photoluminescence microspectrometer (405 nm excitation), at the Guangzhou laboratory of the Gemmological Institute, China University of Geosciences.

Transient phosphorescence time-resolved spectroscopy was performed on the same five samples at the Hubei Key Laboratory of Low Dimensional

Optoelectronic Materials and Devices, Xiangyang, using an Edinburgh Instruments FLS980 steady-state and transient fluorescence spectrometer with a 60 W xenon lamp (365 nm) as the excitation source. We measured the time-resolved phosphorescence spectra and the phosphorescence lifetime of each sample. The parameters included an emission range of 420–650 nm, test frequency of 100 Hz, monochromatic bandwidth excitation of 20 nm, luminous flux of 1,000, test time-frame of 8 s, trigger delay time of 0.1 ms, step size of 5 nm and a test time at each fixed wavelength of 1 min. The optimum monitoring wavelength for each sample was determined from the results of the transient phosphorescence time-resolved spectra, and the phosphorescence lifetime was then measured at that wavelength (525 nm). Each phosphorescence lifetime test had a frequency of 100 Hz, monochromatic bandwidth excitation of 20 nm, luminous flux of 1,000, test time frame of 4 s and trigger delay time of 0.1 ms. Each test utilised a total of 5,000 photons.

RESULTS

Optical Microscopy: Internal Features

The golden amber showed reddish brown impurities (Figure 7a) and surface-reaching fissures that were filled with a white mineral showing good cleavage (probably calcite; Figure 7b). The brown amber contained concentrations of reddish brown dots that were directionally arranged, resulting in dark flow patterns (Figure 7c). The ‘blood’ amber sample did not contain any inclusions, and there was no evidence that its red colour was created artificially by heating in the laboratory.

The ‘beeswax’ amber showed obvious flow patterns, with lighter-coloured bands containing large amounts of bubbles (Figure 7d; cf. Wang *et al.* 2016), as well as black inclusions (Figure 7e). The ‘root’ amber showed two different types of features: (1) distinctive yellowish white flow patterns that were locally concentric, with well-defined borders between transparent and opaque zones (sample GP-1; see Figure 7f), and (2) a mottled structure (sample GP-2; see Figure 7g).

Of the three samples showing the ‘oil gloss’ effect, GX-1 contained fissures that in one case resembled a bird feather (Figure 7h) or locally displayed iridescence. Sample GX-2 was nearly free of inclusions, while GX-3 contained some dark impurities (Figure 7i) but lacked the reddish brown dot-like inclusions.

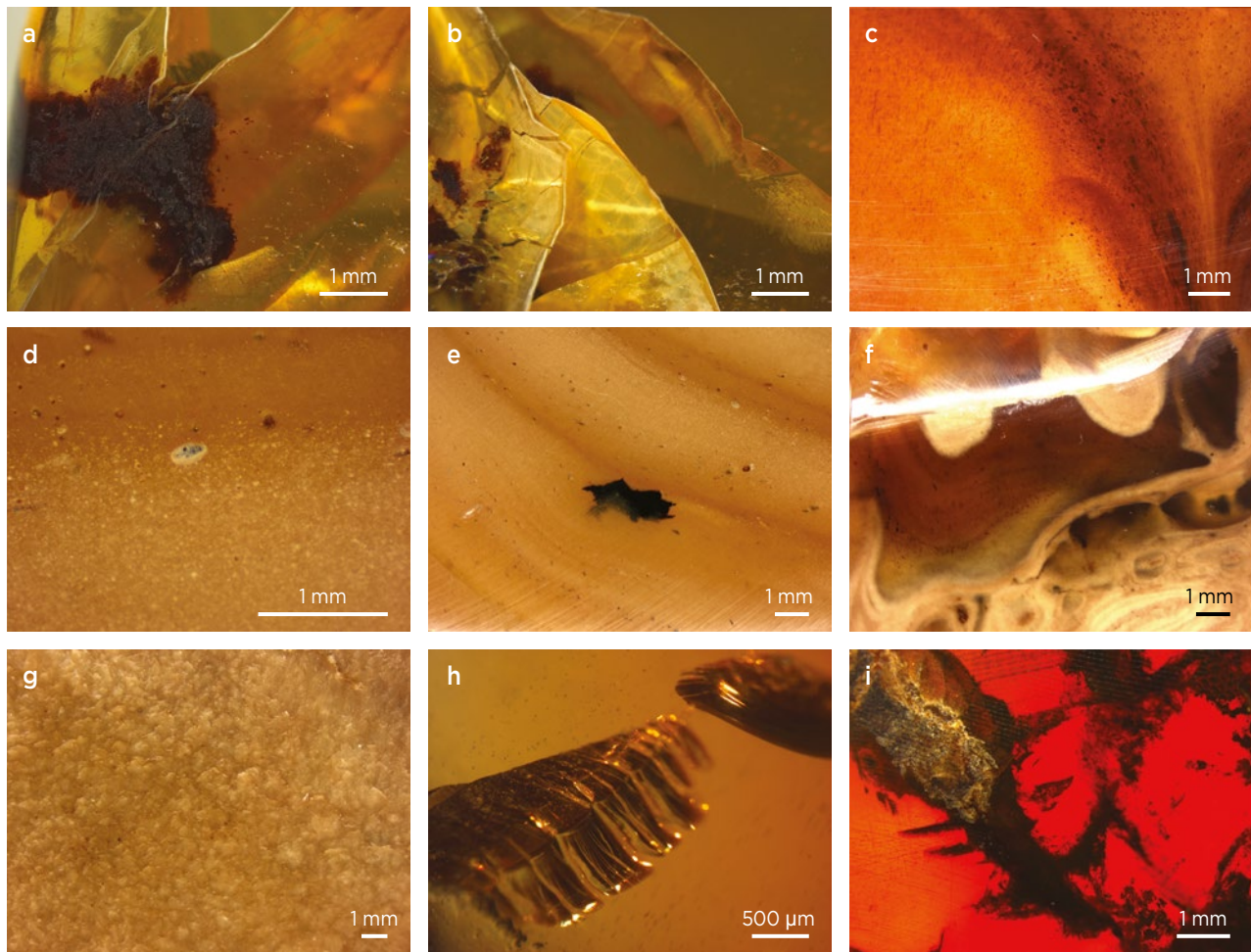


Figure 7: Various types of internal features are seen in the Burmese amber samples examined for this report. The golden amber contains (a) reddish brown impurities and (b) fractures that are probably filled with calcite. (c) The brown amber shows abundant reddish brown dot-like inclusions in a flow-banded arrangement. Internal features in ‘beeswax’ amber consist of (d) abundant bubbles or (e) flow patterns and dark inclusions. ‘Root’ amber may display (f) conspicuous flow patterns or (g) a mottled structure. (h) ‘Oil gloss’ sample GX-1 contains a fissure resembling a bird feather, while (i) GX-3 contains dark impurities. Photomicrographs by X. Jiang.

**Electron Microscopy:
Structural Characteristics**

SEM examination of the golden amber showed a scaly, layered appearance with no bubbles (Figure 8). The surface of the brown amber was smoother, and the dot-like inclusions (which appeared reddish brown with optical microscopy; see Figure 7c) were directionally oriented along flow patterns. The individual dot-like inclusions had oval shapes (Figure 9a) and were of various sizes. Higher magnification of these inclusions revealed that they commonly contained an inhomogeneous texture (Figure 9b), consisting of smooth oval areas within a slightly more scaly-appearing matrix (Figure 9c, d).

The ‘beeswax’ amber contained locally abundant bubbles along flow layers that corresponded to the lighter-coloured, more opaque bands (Figure 10a, b). The flow layers were probably caused by external

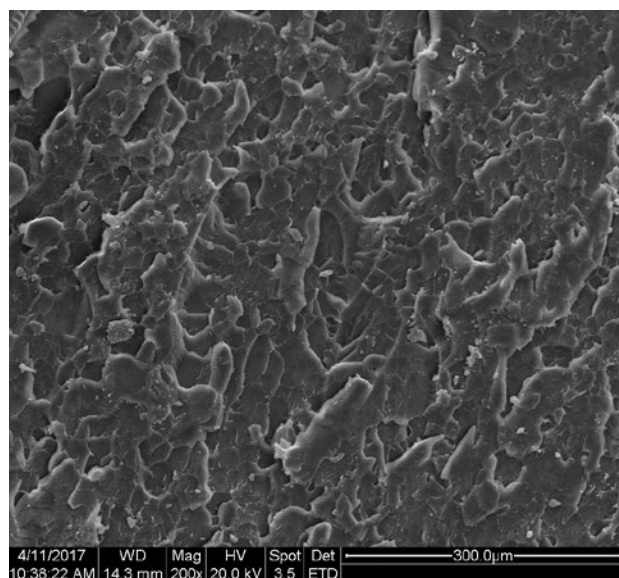


Figure 8: SEM imagery of the golden amber sample reveals a scaly, layered structure. Image by X. Jiang.

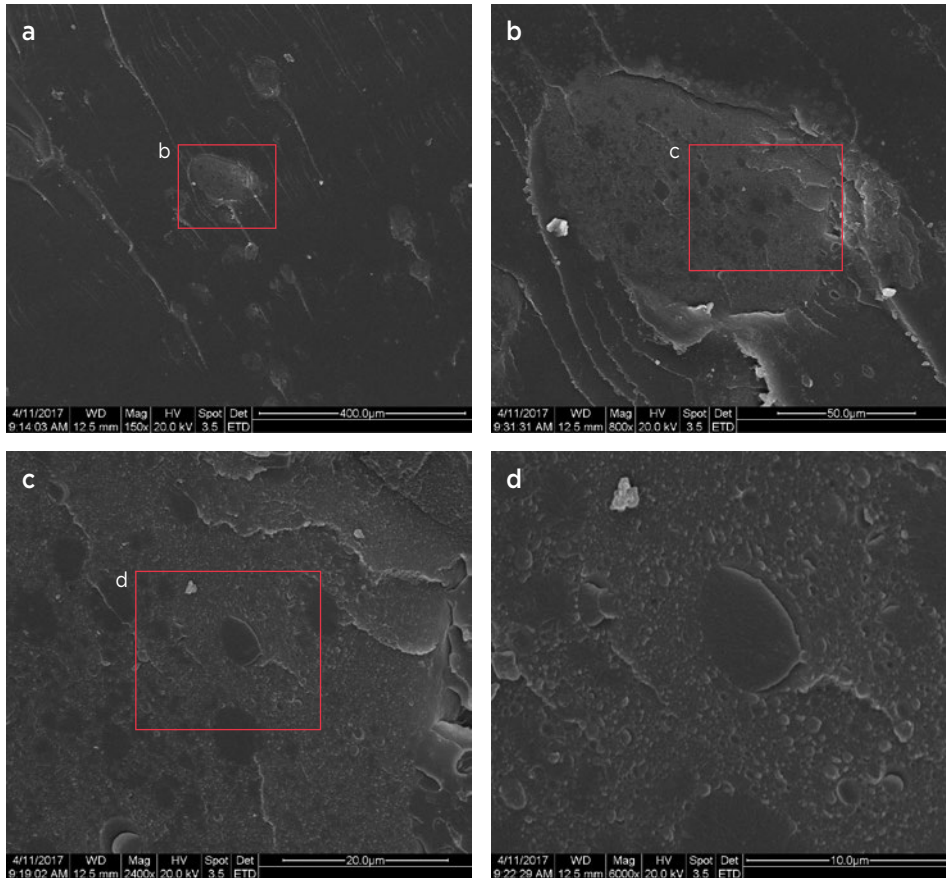


Figure 9: The structure of the reddish brown dot-like inclusions in the brown amber is shown in these successively higher-magnification SEM images, taken at (a) 150×, (b) 800×, (c) 2,400× and (d) 6,000×. Images by X. Jiang.

temperature and pressure during burial of the amber, which led to mutual extrusions between adjacent bubbles. The darker, more transparent layers in the ‘beeswax’ amber lacked bubbles but still showed some evidence of flow layering (Figure 10c).

The two samples of ‘root’ amber revealed different characteristics. A lighter-coloured, opaque area of sample GP-1 (Figure 11a) contained micro-bubbles showing various shapes and sizes, along with thin, curved, hollow micro-tubes (Figure 11b, right side of

image). In some cases, the bubbles occurred alongside the tubes. A layered structure was also observed in the areas containing the bubbles and tubes. An adjacent, more transparent area of this sample appeared mostly featureless in the SEM (Figure 11b, left side). ‘Root’ amber sample GP-2 was examined in a mottled area that was free of consistent flow patterns (Figure 12). The SEM images showed a fine-grained scaly appearance along with elliptical bubbles of various size, although they were significantly less abundant than in GP-1.

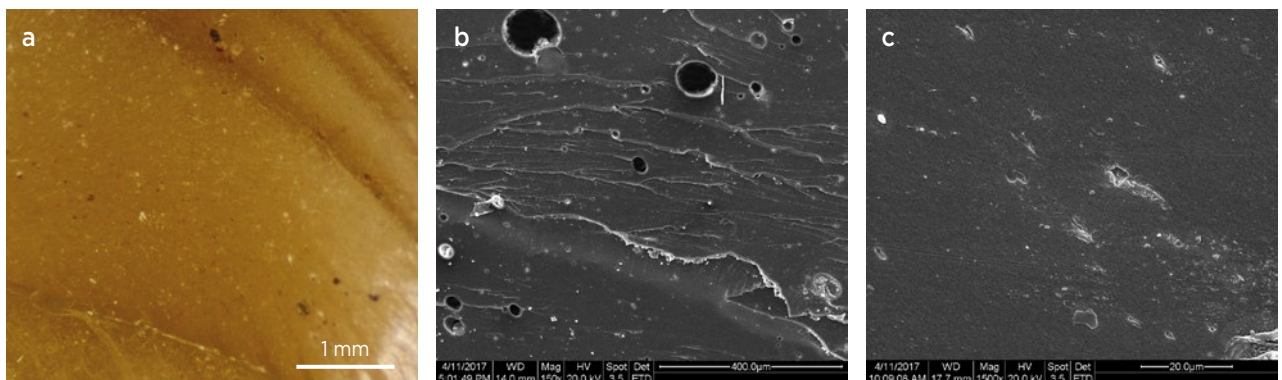


Figure 10: A closer look at the ‘beeswax’ amber (a) with the SEM reveals the microstructure of an opaque zone (b), which contains bubbles of various size, and a transparent zone (c), which has a more featureless structure. Both areas show flow patterns. Photomicrograph and SEM images by X. Jiang.

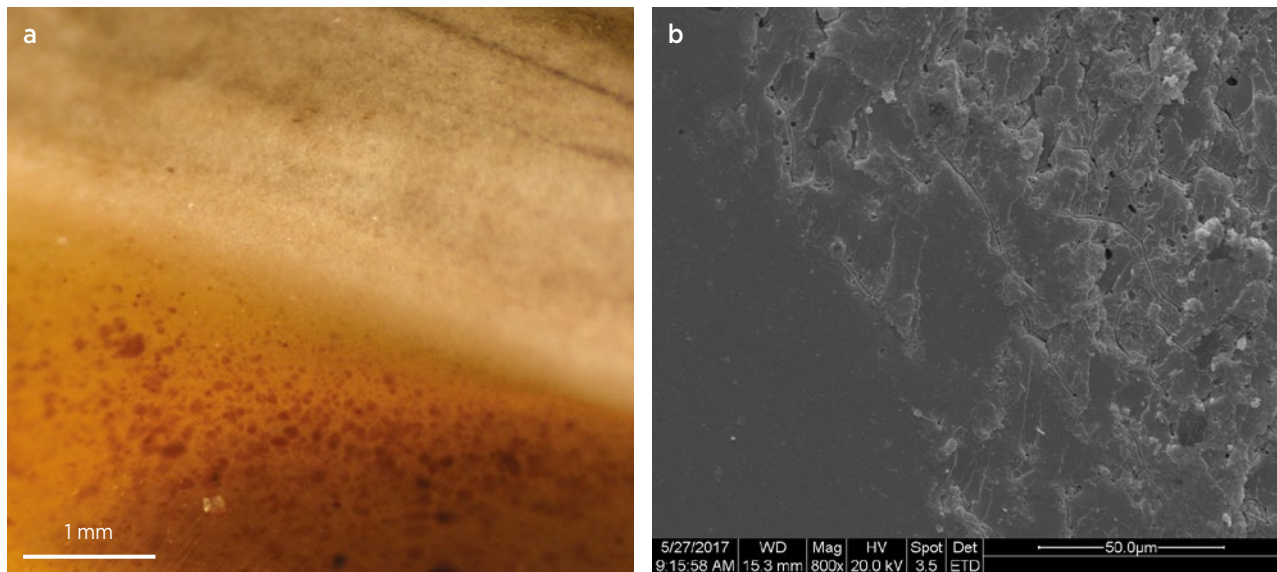


Figure 11: The transitional zone between transparent (lower left) and opaque (upper right) areas of ‘root’ amber sample GP-1 (a) is shown in this SEM image (b). The transparent portion appears smooth and featureless, while the opaque zone displays a layered structure with curved hollow micro-tubes between the layers that are locally associated with bubbles. Photomicrograph and SEM image by X. Jiang.

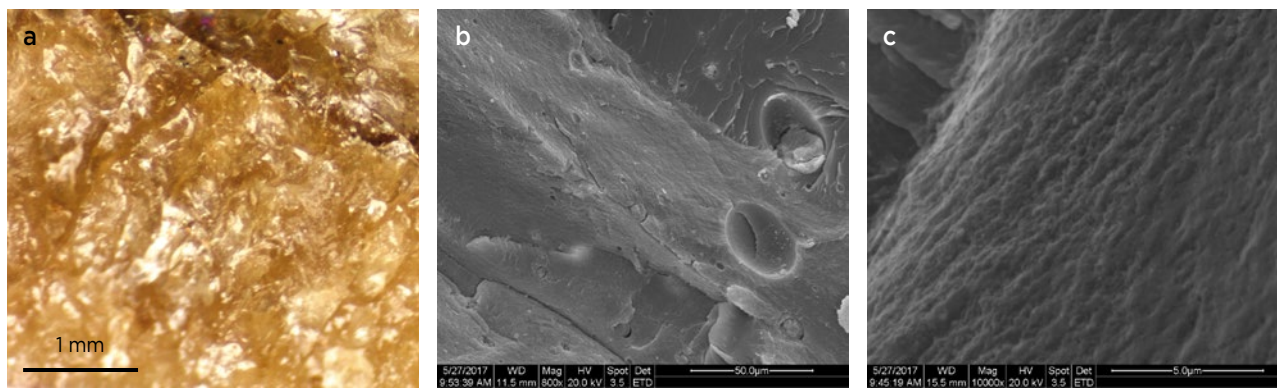


Figure 12: Examination of the mottled area of ‘root’ amber sample GP-2 (a) with the SEM reveals (b) heterogeneous surface features with elliptical bubbles of various size and (c) a fine-scaly microstructure. Photomicrograph and SEM images by X. Jiang.

Infrared Spectroscopy

The FTIR spectra were highly consistent among the different types of Burmese amber samples that were analysed (Figure 13). Strong bands at around 2928–2930 cm^{-1} and at 2862 cm^{-1} were caused by asymmetric C–H stretching vibrations. Stretching vibrations of the carbonyl (C=O) functional group caused a band at around 1719–1722 cm^{-1} . The bands at 1458 and 1375 cm^{-1} were caused by $\text{CH}_2\text{--CH}_3$ and symmetric deformation vibrations, respectively. Thus, the amber was confirmed to be an aliphatic compound, and the bands at 1027–1034 and 972 cm^{-1} were caused by lipid C–O–C and C–O stretching vibrations, respectively (Marrison 1951; Lambert & Frye 1982; Abduriyim *et al.* 2009; Wang *et al.* 2015, 2017; Lan *et al.* 2017).

Fluorescence and Phosphorescence

The golden and brown ambers displayed violetish blue long-wave UV fluorescence (Figure 14a, b), which is the most common luminescence colour in Burmese amber. The two samples displaying a red ‘oil gloss’ effect showed a peculiar magenta or violetish purple fluorescence (Figure 14c, d), while the amber displaying green ‘oil gloss’ showed whitish blue luminescence (Figure 14e).

The ‘blood’ amber and the opaque samples were inert to long-wave UV radiation, and they were also inert to the 220–500 nm excitation range utilised for fluorescence spectroscopy. Greenish yellow phosphorescence was noted in all of the transparent samples except for the ‘blood’ amber.

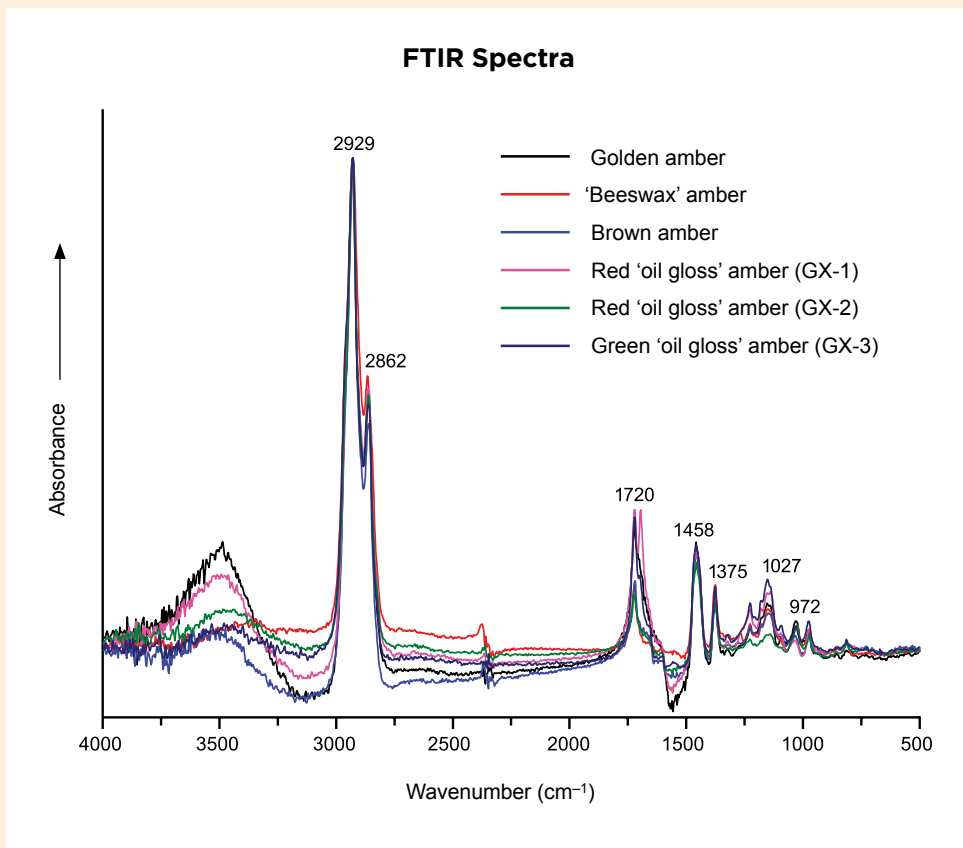


Figure 13: FTIR spectra of the six analysed specimens of Burmese amber show similar features.

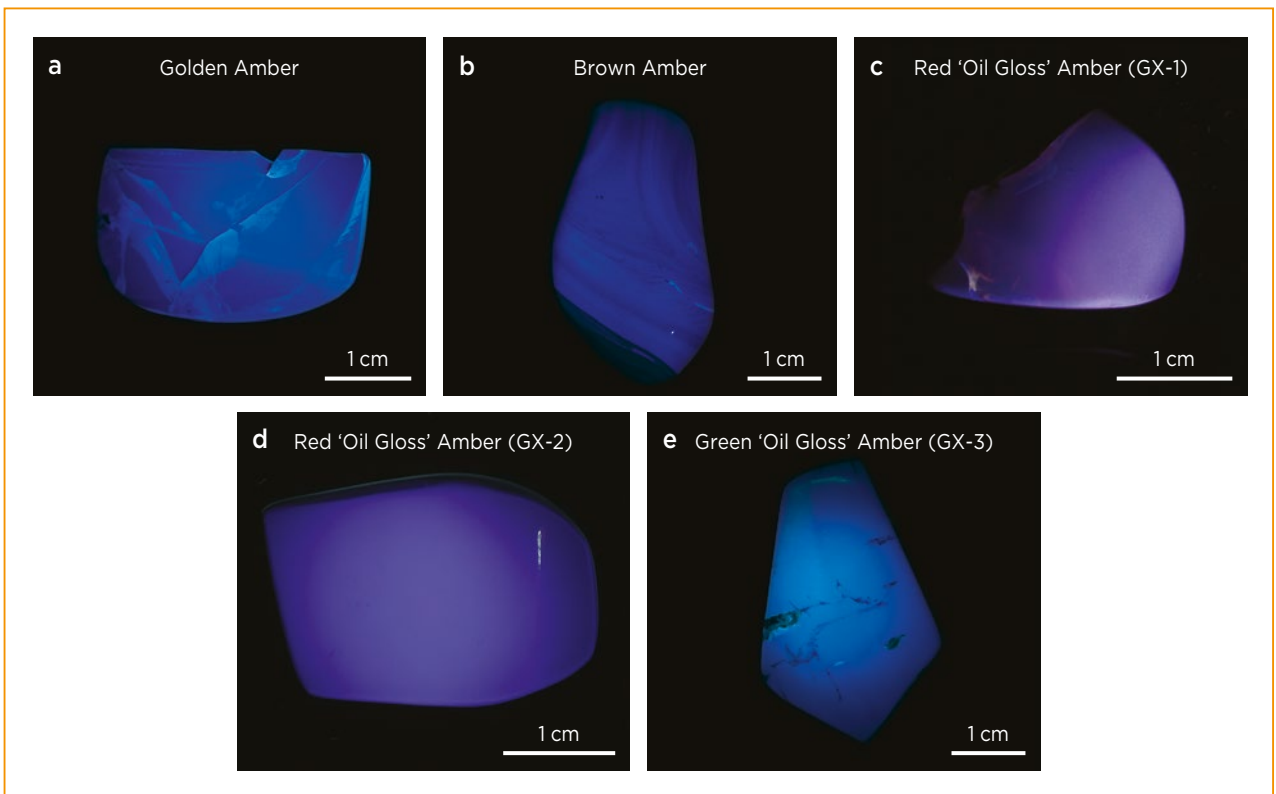


Figure 14: Viewed with long-wave UV fluorescence, Burmese amber typically fluoresces violetish blue (**a** and **b**). Less commonly, it displays magenta (**c**), violetish purple (**d**) or whitish blue (**e**) luminescence. Photos by X. Jiang.

Fluorescence Spectroscopy. Fluorescence spectra obtained for the golden and brown samples, as well as the three ambers showing the ‘oil gloss’ effect, recorded various luminescence centres (Figures 15–18 and Table II). Two luminescence centres in the 320–350 nm range fell outside the range of visible light. Other luminescence

centres at 390 (± 3) nm, 410 (± 2) nm, 432 (± 3) nm and 470 (± 4) nm in the violet-to-blue region of the spectrum were recorded in all samples except for the amber displaying green ‘oil gloss’. By contrast, the green ‘oil gloss’ sample showed emissions in the green region with increasing excitation wavelength (Figure 15e).

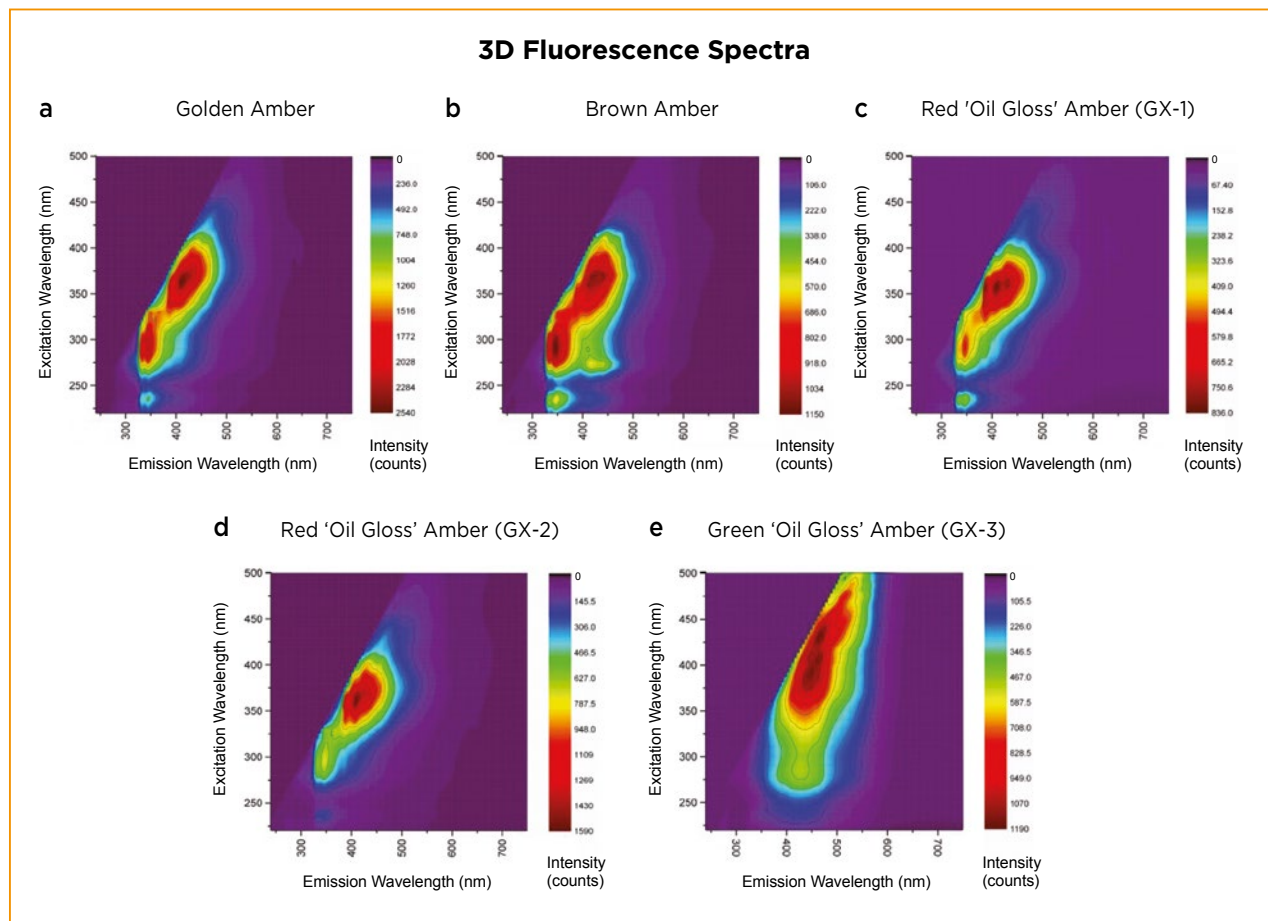
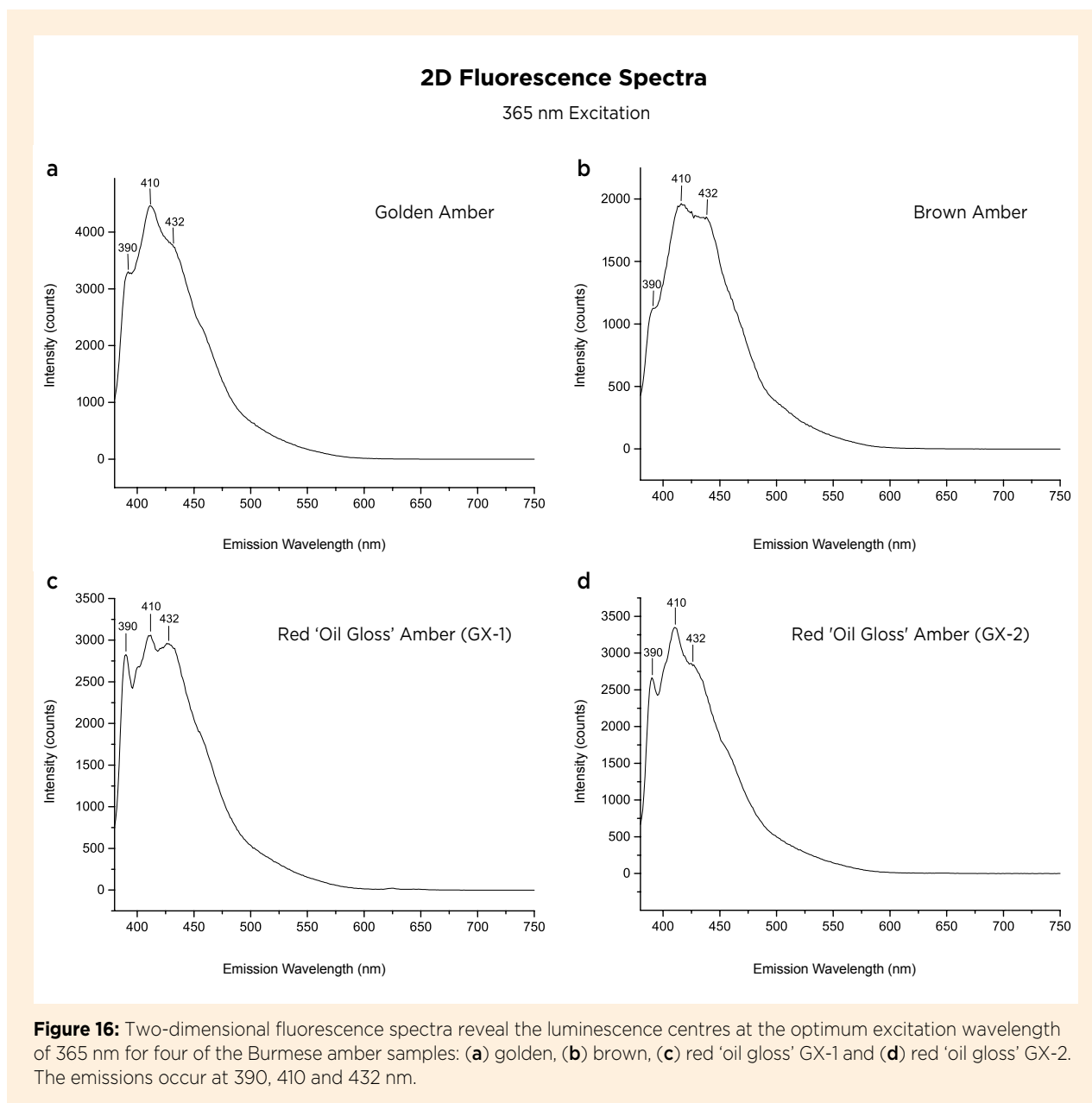


Figure 15: Three-dimensional fluorescence spectra are shown for the five Burmese amber samples in Figure 14: (a) golden, (b) brown, (c) red ‘oil gloss’ GX-1, (d) red ‘oil gloss’ GX-2 and (e) green ‘oil gloss’ GX-3. The spectra reveal luminescence centres at various wavelengths (see Table II for specific centres in each sample).

Table II: Long-wave UV fluorescence, luminescence centres (in the visible range) and phosphorescence lifetimes of Burmese amber.

| Sample ID | Type | Long-wave UV fluorescence | Luminescence centres (nm) | Phosphorescent lifetimes (s) |
|-----------|------------------------------------|---------------------------|---------------------------|------------------------------|
| JP | Golden amber | Violetish blue | 410, 432, 470 | $t_1 = 0.375, t_2 = 1.396$ |
| ZP | Brown amber | Violetish blue | 410, 432, 470 | $t_1 = 0.265, t_2 = 1.059$ |
| GX-1 | Red ‘oil gloss’ | Magenta | 410, 432, 470, 625, 650 | $t_1 = 0.134, t_2 = 0.447$ |
| GX-2 | Red ‘oil gloss’ | Violetish purple | 410, 432, 470, 650 | $t_1 = 0.154, t_2 = 0.607$ |
| GX-3 | Green ‘oil gloss’ (or ‘chameleon’) | Whitish blue | 432, 470, 503, 532 | $t_1 = 0.134, t_2 = 0.706$ |



Two-dimensional fluorescence spectra were generated for the optimum excitation wavelength, which was 365 nm for all samples except for the amber showing green 'oil gloss' (which had an optimum excitation of 400 nm). With 365 nm excitation, the spectra showed luminescence centres at about 390, 410 and 432 nm (Figure 16). When the excitation wavelength was increased to 400 nm (i.e. in the visible range), a luminescence centre in the blue region at 470 nm appeared (Figure 17). Moreover, with 400 nm excitation the two red 'oil gloss' ambers also showed luminescence in the red region at 650 nm (± 2 nm) and also at 625 nm for sample GX-1. For the green 'oil gloss' amber, the optimum excitation wavelength of 400 nm generated emissions at about 432 and 470 nm

(Figure 18a). At a higher excitation wavelength of 460 nm (i.e. further into the visible region), the luminescence centres shifted to the 500–550 nm range in the green portion of the spectrum (Figure 18b).

Phosphorescence Spectroscopy. Transient time-resolved phosphorescence spectroscopy showed that the strongest phosphorescence occurred at 525 nm (Figure 19) for all samples. Thus, the phosphorescence lifetime was measured for an emission wavelength of 525 nm and calculated using the decay function of Wang (2015). The results revealed two phosphorescence lifetimes for all the samples, with t_1 ranging from 0.134 to 0.375 s and t_2 ranging from 0.447 to 1.396 s (Figure 20; see Table II for details).

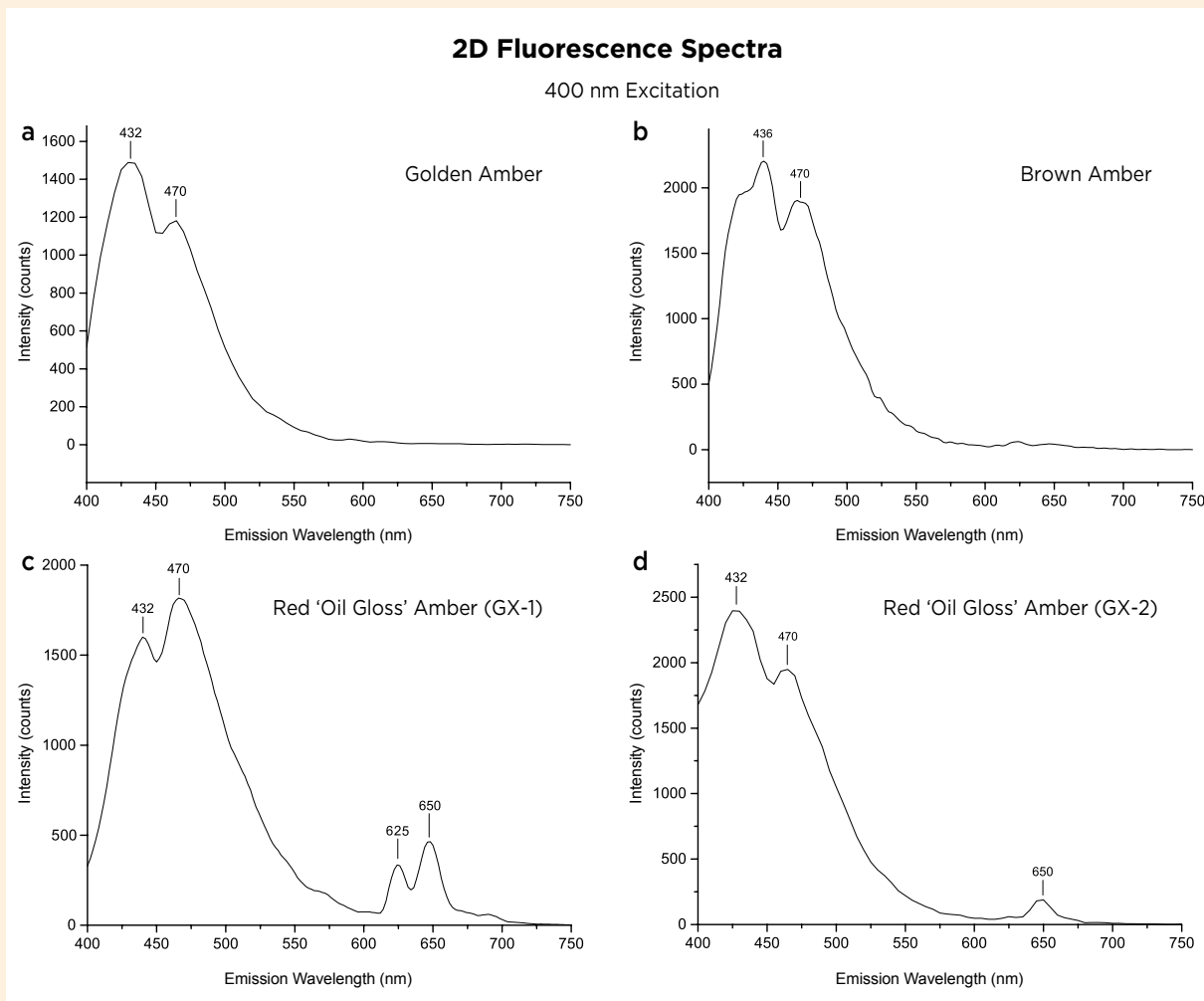


Figure 17: Two-dimensional fluorescence spectra of the same samples as in Figure 16 with 400 nm excitation show luminescence centres at 432 and 470 nm. In addition, red 'oil gloss' samples GX-1 and GX-2 have emission(s) in the red region at 650 nm ± 625 nm.

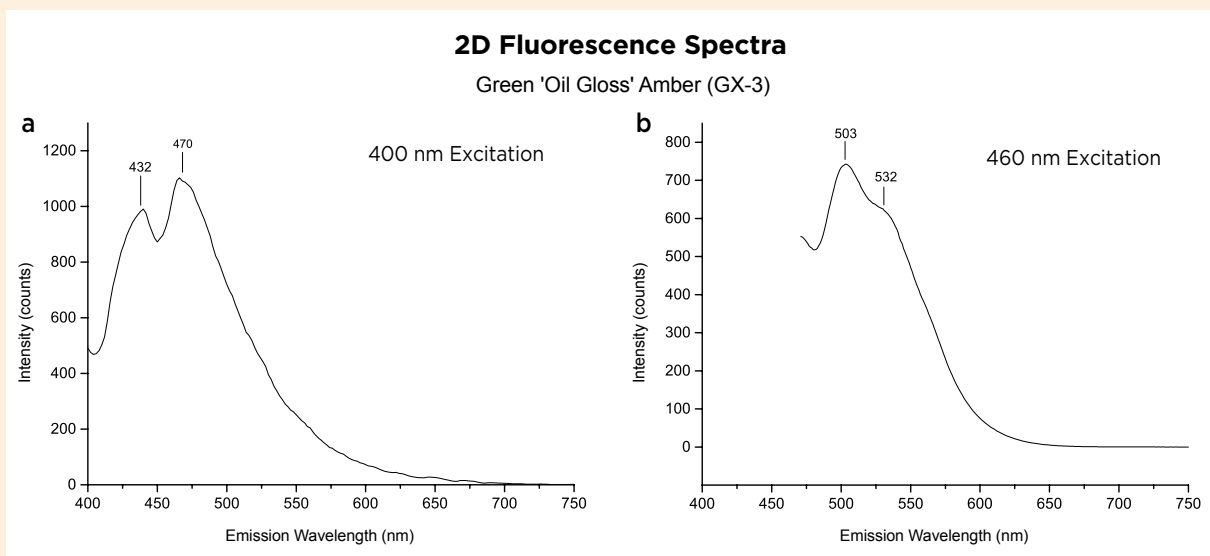


Figure 18: Two-dimensional fluorescence spectra are shown for green 'oil gloss' amber GX-3. (a) At the optimum excitation wavelength of 400 nm, the luminescence centres occur only at 432 and 470 nm in the violet-to-blue region. (b) With 460 nm excitation, luminescence centres are revealed in the green region at 503 and 532 nm.

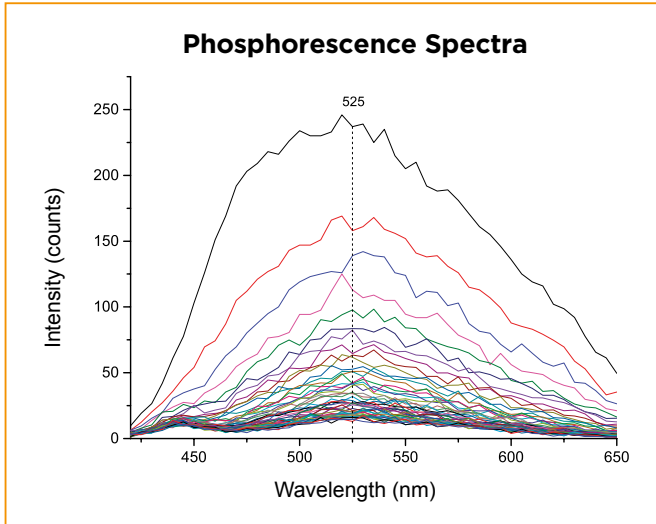


Figure 19: Time-resolved phosphorescence spectra demonstrate that the strongest phosphorescence occurred at 525 nm in all the Burmese amber samples. Each line refers to a different excitation wavelength.

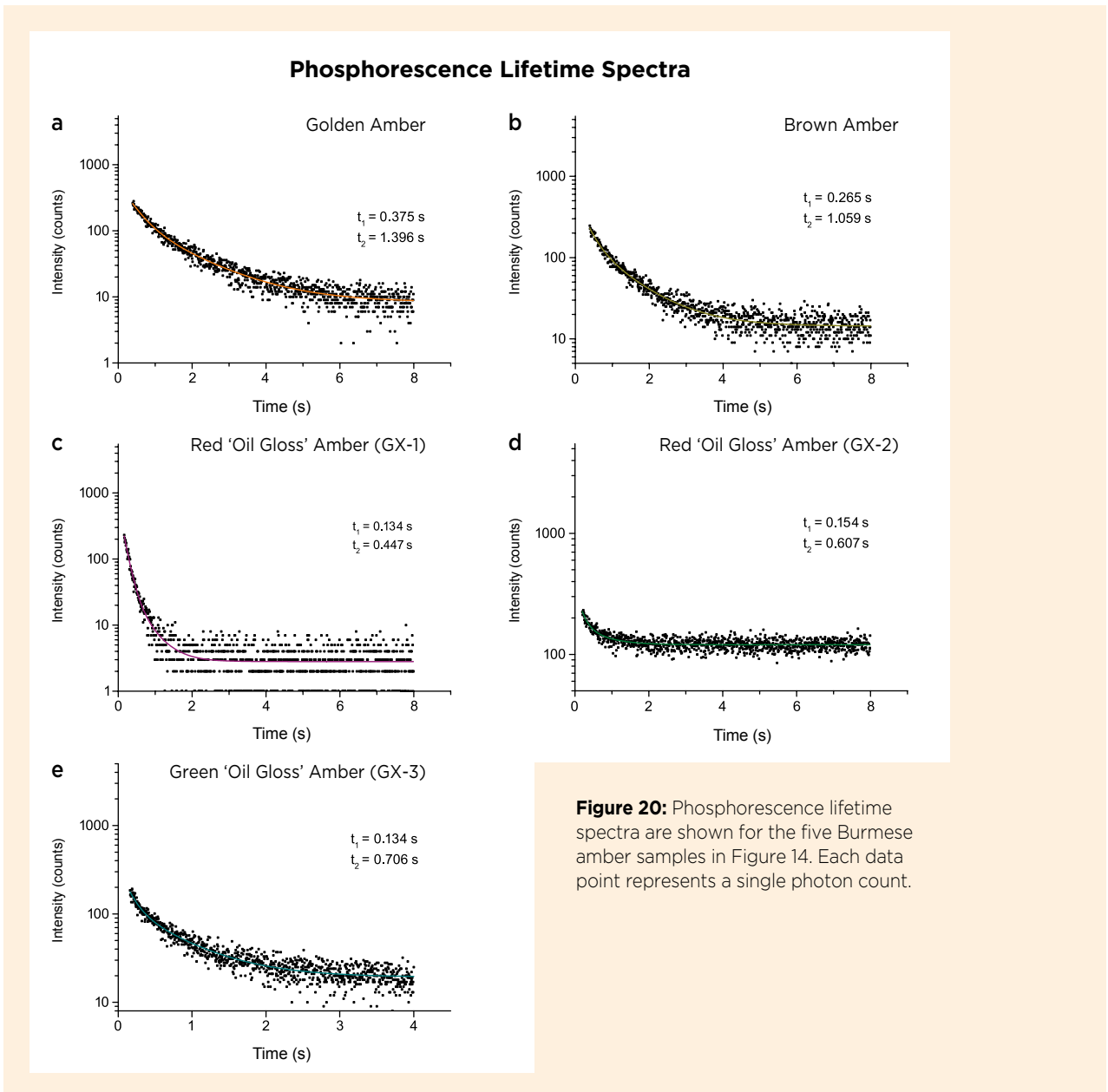


Figure 20: Phosphorescence lifetime spectra are shown for the five Burmese amber samples in Figure 14. Each data point represents a single photon count.

DISCUSSION

Formation of the Reddish Brown Dot-like Inclusions

The reddish brown dot-like inclusions in the brown amber (Figure 7c) showed a scaly structure in SEM images (Figure 9) that was clearly different from that of the surrounding amber. We speculate that these inclusions are related to some type of organic matter contained in the amber (especially volatile substances), rather than inorganic foreign material. Specifically, the inclusions may correspond to devolatilised sporopollen (chemically inert biological polymers) that were subjected to oxidation, thereby leading to a reddish brown appearance.

Structure of ‘Root’ Amber

According to our observations with the SEM, the diameter of the bubbles in the Burmese ‘root’ amber samples was micron-sized, typically ranging from 1 to 5.5 μm . In sample GP-1, an opaque region measuring 0.03 mm^2 contained 435 bubbles which took up 4.9% of the area. In the same region, hollow tubes occupied 257.1 μm^2 . In the transitional zone leading into a transparent area, another 0.03 mm^2 region contained 149 bubbles of 0.9–5.5 μm diameter, which accounted for 3.1% of the area, and the hollow micro-tubes occupied 56.7 μm^2 . Bubbles and hollow tubes were not present in the transparent zone. For sample GP-2, a 0.03 mm^2 region contained 47 bubbles which took up 1.8% of the area, but no hollow tubes. Thus, ‘root’ amber samples GP-1 and GP-2 differed considerably in their microscopic structural characteristics, and we attribute the distinctive textures seen in ‘root’ amber to variations in these structures.

The hollow micro-tubes accompanying the bubbles in ‘root’ amber GP-1 might represent escape channels for volatile components. The empty bubbles visible at the ends of the hollow tubes could have been left over when volatile components escaped along the tubes. The lack of bubbles visible at the ends of some tubes does not necessarily indicate an absence of bubbles, but may simply be due to the single plane being observed. The hollow tubes could also be related to cracks that appeared as the resin was exuded. The resin that formed Burmese amber was highly viscous, and as it was secreted in stages, small cracks could have resulted from more rapid hardening at the surface. However, the cracks could not continue to spread owing to rapid coverage by newly exuded resin. The ‘internal’ cracks were subsequently subjected to geological processes during burial of the host sediments. During this process, the healed fissures could

have become channelways for escaping volatile components. Bubbles that remained after the volatiles escaped were mostly found along the curving, hollow tubes.

Origin of the ‘Oil Gloss’ Effect

The ‘oil gloss’ appearance of the Burmese amber is caused by a mixture of surface fluorescence and body colour, as seen in samples GX-1, GX-2 and GX-3. The effect is best seen against a black background because it reduces the influence of a sample’s body colour on colour perception. The different appearances of this effect (red vs. green) depend on the luminescence centres present in the amber.

Amber with Red ‘Oil Gloss’. Red surface fluorescence was noted on reddish brown and greenish yellow samples GX-1 and GX-2, respectively, when they were viewed against a black background. As expected, both showed emission in the red region at 650 nm (and also at 625 nm in GX-1) with 400 nm excitation (Figure 17c, d). Although this red emission was not recorded at the optimum excitation wavelength of 365 nm, it was present at a higher excitation wavelength in the range of visible light (i.e. 400 nm), and therefore we suggest that the red surface fluorescence of Burmese amber is related to these luminescence centres.

Nevertheless, the two samples showing the red ‘oil gloss’ effect also had strong luminescence centres in the violet-to-blue region at 432 and 470 nm, raising the question of how the 625 and 650 nm luminescence centres contribute to the red fluorescence. However, two-dimensional fluorescence spectroscopy of these samples using the Qspec micro-PL spectrometer (405 nm excitation) revealed that the red luminescence centres at 625 and 650 nm in GX-1 were stronger than the blue luminescence centres, and an additional red luminescence centre was also present at 690 nm (Figure 21a). In GX-2, the luminescence centres in the red region were nearly the same strength as those in the violet-to-blue region (Figure 21b). Therefore, it appears that different instruments have different sensitivities according to various emission wavelengths.

Amber with Magenta or Violetish Purple Fluorescence. Burmese amber commonly fluoresces violetish blue to long-wave UV radiation (e.g. Figure 14a). However, samples showing red ‘oil gloss’ showed magenta or violetish purple fluorescence under long-wave UV radiation (Figure 14c, d). Therefore, the luminescent centre(s) in the red region are not only responsible for the red ‘oil gloss’ effect, but they also contribute to the

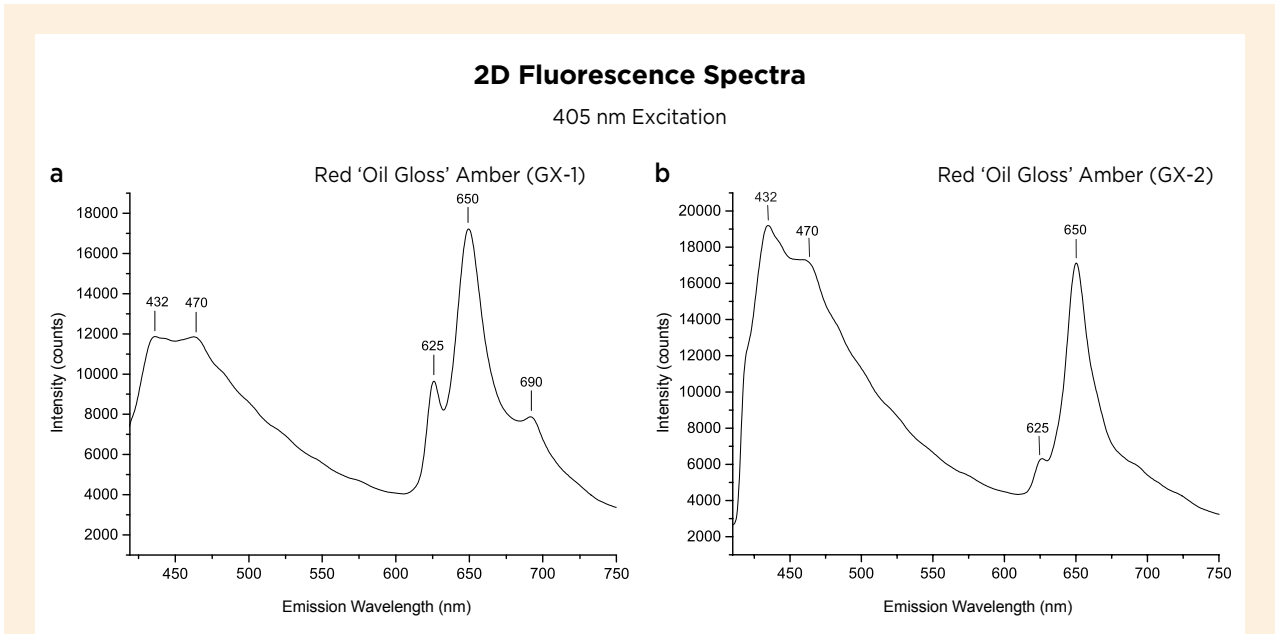


Figure 21: Two-dimensional fluorescence spectroscopy using the Qspec micro-PL instrument (405 nm excitation) shows luminescence centres in (a) red ‘oil gloss’ sample GX-1, which are much stronger in the red region at 625–690 nm than in the violet-to-blue region at 432 and 470 nm. (b) Red ‘oil gloss’ sample GX-2 shows strong emissions in both the violet-to-blue and red regions, but lacks a well-defined luminescence centre at 690 nm.

magenta or violetish purple fluorescence seen under long-wave UV radiation. The combination of luminescence centres in the red and violet-to-blue regions appears to be responsible for the distinctive magenta or violetish purple fluorescence of those samples seen under long-wave UV radiation.

Amber with Green ‘Oil Gloss’. Reddish brown amber sample GX-3 displayed green surface fluorescence when viewed on a black background. In addition to the luminescence centres at 432 and 470 nm, fluorescence spectroscopy also revealed emissions in the green region (again, see Figure 18b). The spectral data were converted into Commission Internationale de L’Eclairage (CIE) chromaticity coordinate points, but the corresponding fluorescence did not plot in the green area—rather it plotted in the blue region (Figure 22). This suggests that the green ‘oil gloss’ of sample GX-3 is not only derived from green luminescence centres, but is also enhanced by the mixture of blue fluorescence and the amber’s reddish brown body colour.

Phosphorescent Amber

‘Glow in the dark’ Burmese amber shows phosphorescence. With an excitation wavelength of 365 nm (typical long-wave UV radiation), the phosphorescent luminescence centre with the highest intensity was at 525 nm (yellowish green area of the spectrum), which is similar

to the visually observed greenish yellow phosphorescent colour of Burmese amber. Thus, we measured the phosphorescence lifetime at 525 nm.

Phosphorescence lifetime is defined as the time it takes for the phosphorescence to decrease to 36.8% of the maximum strength (i.e. one lifetime), rather than the

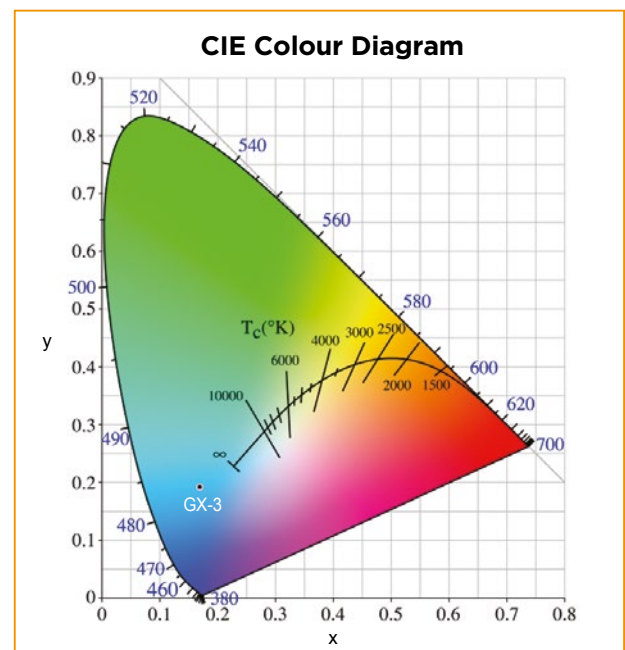


Figure 22: The CIE coordinate point calculated from the spectral data for green ‘oil gloss’ amber sample GX-3 confirmed the fluorescence colour as blue.

time to disappearance (when it becomes invisible to the naked eye; for more information, see Díaz García & Badía 2006). After phosphorescent amber is exposed to bright light, a large number of photons are emitted, leading to luminescence. The higher the intensity of the excitation source and the longer the exposure time, the more photons are excited in this process, resulting in longer times of luminescent energy emission. Hence, longer duration and higher intensity of irradiation contribute to longer ‘luminescence times’ (Xia 1992). However, after sufficient exposure time, regardless of how much longer the excitation lasts, the phosphorescence lifetime will remain nearly the same. This indicates a threshold inherent in the amber phosphorescence phenomenon. Once the quantity of excited photons reaches the threshold, the total number of active photons does not increase. At that point, the absorption and release of luminescent energy strike a dynamic balance.

Among the large number of organic compounds that are known to occur in amber, only a few can emit strong fluorescence, which is closely associated with their structures. Amber is a mixture of organic compounds, and may display fluorescence and sometimes phosphorescence when it contains the appropriate natural fluorescent impurities (e.g. Chekryzhov *et al.* 2014). Although Burmese amber is commonly thought to be the only fossil resin that displays the ‘glow-in-the-dark’ phenomenon, in fact amber from many origins may emit phosphorescence (e.g. Dominican amber; see Liu *et al.* 2014). The results of the authors’ investigations of phosphorescence in ambers from various localities will be published in the future.

Figure 23: This Burmese amber carving depicts a *lohan* from traditional Chinese mythology. The amber displays a green ‘oil gloss’ effect in the transparent part, whereas the opaque areas consist of ‘root’ amber. The amber is 20.5 cm wide and rests on a carved wooden stand.
Photo courtesy of Tengchong Huo Ren Carving Studio.

CONCLUSIONS

We characterised various types of Burmese amber, including golden, brown, ‘blood’, ‘beeswax’ and ‘root’ varieties, as well as those showing ‘oil gloss’ surface fluorescence effects and phosphorescence. Differences in the original resin secretions are responsible for the different amber types, as evidenced by the layered structure of some specimens and the characteristics of bubbles of various sizes and concentrations. It is also possible for multiple types/phenomena to occur within a single piece of Burmese amber (e.g. Figure 23).

The reddish brown dot-like inclusions in brown Burmese amber are possibly related to reactions involving volatile substances. The association of these inclusions with flow patterns suggests they may be related to the escape of volatile components. The opaque appearance



of Burmese ‘root’ amber is primarily attributed to its layered microscopic structure, as well as the abundance of bubbles and microscopic hollow tubes in certain areas of this material. The micro-tubes may have formed as escape channels for volatile components or they may be related to small cracks that formed during more rapid hardening of the outer surface of the resin and were then covered by successive resin exudations.

Red or green ‘oil gloss’ effects in Burmese amber are produced by a mixture of surface fluorescence and body colour, while the ‘glow-in-the-dark’ phenomenon is produced by phosphorescence. Generally, Burmese

amber has two luminescence centres in the violet-to-blue region (at 432 and 470 nm), and those samples displaying red ‘oil gloss’ show additional emission(s) in the red region at 625–690 nm.

An important challenge facing amber researchers is the identification of specific components and structural formulas in these materials, and this investigation of the fluorescence and phosphorescence of Burmese amber not only explains various distinctive appearances shown by this material, but also provides further information for future research on the organic components in amber.

REFERENCES

- Abduriyim, A., Kimura, H., Yokoyama, Y., Nakazono, H., Wakatsuki, M., Shimizu, T., Tansho, M. & Ohki, S. 2009. Characterization of “green amber” with infrared and nuclear magnetic resonance spectroscopy. *Gems & Gemology*, **45**(3), 158–177, <https://doi.org/10.5741/gems.45.3.158>.
- Chekryzhov, I.Y., Nechaev, V.P. & Kononov, V.V. 2014. Blue-fluorescing amber from Cenozoic lignite, eastern Sikhote-Alin, Far East Russia: Preliminary results. *International Journal of Coal Geology*, **132**, 6–12, <https://doi.org/10.1016/j.coal.2014.07.013>.
- Cruikshank, R.D. & Ko, K. 2003. Geology of an amber locality in the Hukawng Valley, northern Myanmar. *Journal of Asian Earth Sciences*, **21**(5), 441–455, [https://doi.org/10.1016/s1367-9120\(02\)00044-5](https://doi.org/10.1016/s1367-9120(02)00044-5).
- Díaz García, M.E. & Badía, R. 2006. Phosphorescence measurements, applications of. In: Meyers, R.A. (ed), *Encyclopedia of Analytical Chemistry*, John Wiley & Sons Ltd, New York, New York, USA, 14 pp., <https://doi.org/10.1002/9780470027318.a5411>.
- Dutta, S., Mallick, M., Kumar, K., Mann, U. & Greenwood, P.F. 2011. Terpenoid composition and botanical affinity of Cretaceous resins from India and Myanmar. *International Journal of Coal Geology*, **85**(1), 49–55, <https://doi.org/10.1016/j.coal.2010.09.006>.
- Edwards, H.G.M., Farwell, D.W. & Villar, S.E.J. 2007. Raman microspectroscopic studies of amber resins with insect inclusions. *Spectrochimica Acta Part A: Molecular and Biomolecular Spectroscopy*, **68**(4), 1089–1095, <https://doi.org/10.1016/j.saa.2006.11.037>.
- Jiang, W., Nie, S. & Wang, Y. 2017. Fluorescence spectral characteristic of blue amber from Dominican Republic, Mexico and Myanmar. *Journal of Gems and Gemmology*, **19**(2), 1–8 (in Chinese with English abstract).
- Jiang, X., Wang, Y. & Kong, F. 2018. Microstructure characteristic of amber from Myanmar. *Journal of Gems and Gemmology*, **20**(6), 18–30 (in Chinese with English abstract).
- Jiang, X., Zhang, Z., Wang, Y. & Kong, F. 2019. Special optical effect of amber from Myanmar. *Journal of Gems and Gemmology*, **21**(5), 1–17 (in Chinese with English abstract).
- Lambert, J.B. & Frye, J.S. 1982. Carbon functionalities in amber. *Science*, **217**(4554), 55–57, <https://doi.org/10.1126/science.217.4554.55>.
- Lan, J., Lan, Y., Hu, C. & Li, X. 2017. Application of GC-MC and FTIR in identification of amber and copal resin. *Journal of Gems and Gemmology*, **19**(2), 9–19 (in Chinese with English abstract).
- Laurs, B.M. 2012. Gem News International: Burmese amber update. *Gems & Gemology*, **48**(2), 142–155, <https://doi.org/10.5741/gems.48.2.142>.
- Levinson, A.A. 2001. Gem News International—Amber (“Burmite”) from Myanmar: Production resumes. *Gems & Gemology*, **37**(2), 142–143.
- Liu, S.I. 2018. Gem Notes: Burmese amber from Khamti, Sagaing region. *Journal of Gemmology*, **36**(2), 107–110.
- Liu, Y., Shi, G. & Wang, S. 2014. Color phenomena of blue amber. *Gems & Gemology*, **50**(2), 134–140, <https://doi.org/10.5741/gems.50.2.134>.
- Lu, B., Yang, D., Fang, H. & Shi, G. 2014. A preliminary study of inclusions in the burmite (Myanmar amber) and their significance. *Acta Petrologica et Mineralogica*, **33**(Supp. 2), 117–122 (in Chinese with English abstract).
- Marrison, L.W. 1951. Characteristic absorption bands in the 10- μ region of the infra-red spectra of cycloParaffin derivatives. *Journal of the Chemical Society (Resumed)*, 1614–1617, <https://doi.org/10.1039/jr9510001614>.

- Shi, G., Grimaldi, D.A., Harlow, G.E., Wang, J., Wang, J., Yang, M., Lei, W., Li, Q. *et al.* 2012. Age constraint on Burmese amber based on U–Pb dating of zircons. *Cretaceous Research*, **37**, 155–163, <https://doi.org/10.1016/j.cretres.2012.03.014>.
- Tay, T.S., Kleiřmantas, A., Nyunt, T.T., Minrui, Z., Krishnaswamy, M. & Ying, L.H. 2015. Burmese amber from Hti Lin. *Journal of Gemmology*, **34**(7), 606–615, <https://doi.org/10.15506/JoG.2015.34.7.606>.
- Wang, P. 2015. Process the experimental data of time-resolved photoluminescence lifetime spectra of Cu₂O nanowires by origin. *Physical Experiment of College*, **28**(3), 80–83 (in Chinese with English abstract).
- Wang, Y. 2018. *Amber Gemology*. China University of Geosciences Press, Beijing, China, 244 pp. (in Chinese).
- Wang, Y., Shi, G., Shi, W. & Wu, R. 2015. Infrared spectral characteristics of ambers from three main sources (Baltic, Dominica and Myanmar). *Spectroscopy and Spectral Analysis*, **35**(8), 2164–2169 (in Chinese with English abstract).
- Wang, Y., Wang, Q. & Nie, S. 2016. Gas bubble characteristic of translucent to opaque amber and its relationship to quality assessment. *Journal of Gems & Gemmology*, **18**(5), 20–27 (in Chinese with English abstract).
- Wang, Y., Yang, M., Nie, S. & Liu, F. 2017. Gemmological and spectroscopic features of untreated vs. heated amber. *Journal of Gemmology*, **35**(6), 530–542, <https://doi.org/10.15506/JoG.2017.35.6.530>.
- Xia, J. 1992. *Practical Fluorescence Analysis*. Chinese People's Public Security University Press, Beijing, China, 335 pp. (in Chinese).
- Xiao, R. & Kang, J. 2018. Characteristics of Burma blood amber and other colours of ambers. *Superhard Material Engineering*, **30**(2), 54–58 (in Chinese with English abstract).
- Xiao, Y., Guo, Y. & Chen, D.P. 2014. The influences of lightness variation of the non-color background on the color of the blood amber. *Key Engineering Materials*, **633**, 524–535, <https://doi.org/10.4028/www.scientific.net/KEM.633.524>.
- Xie, X., Di, J. & Wu, X. 2017. Type of amber from Myanmar and its gemmological characteristic. *Journal of Gems and Gemmology*, **19**(5), 48–59 (in Chinese with English abstract).
- Xing, L., McKellar, R.C., Wang, M., Bai, M., O'Connor, J.K., Benton, M.J., Zhang, J., Wang, Y. *et al.* 2016. Mummified precocial bird wings in mid-Cretaceous Burmese amber. *Nature Communications*, **7**(1), article 12089 (7 pp.), <https://doi.org/10.1038/ncomms12089>.
- Zhang, X. & Li, R. 2010. Principle of SEM and application in TFT-LCD production. *Advanced Display*, **21**(1), 10–15 (in Chinese with English abstract).
- Zhang, Z., Lin, Q. & Shen, A. 2017. Characteristic of oxygen content in black amber from Myanmar. *Journal of Gems & Gemmology*, **19**(1), 17–21 (in Chinese with English abstract).
- Zherikhin, V.V. & Ross, A.J. 2000. A review of the history, geology and age of Burmese amber (Burmite). *Bulletin of the Natural History Museum [London], Geology Series*, **56**(1), 3–10.
- Zong, P., Xue, J. & Tang, B. 2014. Tracing the most ancient amber: The origin and evolution of resin-producing plants. *Acta Petrologica et Mineralogica*, **33**(S2), 111–116 (in Chinese with English abstract).

The Authors

Xinran Jiang, Zhiqing Zhang and Dr Yamei Wang

Gemmological Institute, China University of Geosciences, No. 388 Lumo Rd., 430074 Wuhan, China
Email: wangym@cug.edu.cn

Fanli Kong

Century Amber Museum, 1 Songrui Road, Songgang, Baoan District, Shenzhen, China

Acknowledgements

The authors are grateful to all who contributed to the project, especially to various companies for their great support and fruitful discussions. The thoughtful and constructive comments by reviewers and technical editors are gratefully acknowledged. This research was financially supported by the National Key R&D Program of China (grant no. 2018YFF0215403). In addition, the project was partially supported by the Fundamental Research Funds for the Central Universities (no. CUG170677), China University of Geosciences, Wuhan.

An innovator in gemstone reporting

- Identification of colored gemstones • Country of origin determination • Full quality and color grading analysis



AMERICAN GEMOLOGICAL LABORATORIES



580 5th Ave • Suite 706 • New York, NY 10036, USA
www.aglgemlab.com • +1 (212) 704 - 0727



Saltwater Cultured Pearls from *Pinctada radiata* in Abu Dhabi (United Arab Emirates)

Abeer Al-Alawi, Zainab Ali, Zainab Rajab, Fatema Albedal and Stefanos Karampelas

ABSTRACT: Since late 2007, *Pinctada radiata* molluscs have been used to produce bead-cultured saltwater pearls in the Al Dhafra region of Abu Dhabi, United Arab Emirates (UAE). This bivalve is seldom used for cultivation. The cultured pearls are harvested after two years, and some non-bead-cultured by-products are also produced. The bead-cultured pearls average 5–8 mm in diameter and show a range of body colours (principally white to yellow, and rarely grey or brown). An examination of 113 bead-cultured and 33 non-bead-cultured samples by X-ray imaging revealed classic structures associated with both types of cultured pearls, sometimes with significant overgrowth and radial-like structures rich in organic matter. Raman, photoluminescence and UV-Vis-NIR spectroscopy indicated that a series of partially substituted (i.e. partially methylated) polyenes, sometimes together with a type of porphyrin, contribute to the various body colours.

The Journal of Gemmology, 37(2), 2020, pp. 164–179, <https://doi.org/10.15506/JoG.2020.37.2.164>
© 2020 Gem-A (The Gemmological Association of Great Britain)

Figure 1: This selection of finer-quality bead-cultured pearls (4.85–8.50 mm) are from *P. radiata* molluscs farmed off Abu Dhabi. They include some of the samples that were studied for this report. Photo by Hasan Abdulla, DANAT.



P*inctada radiata* (*P. radiata*) is the native mollusc of the Arabian Gulf region, and most of the natural pearls fished there are obtained from this relatively small mollusc. Although this bivalve has rarely been used for pearl cultivation, recently gem-quality bead-cultured pearls (Figure 1) were produced from *P. radiata* in the Al Dhafra region of Abu Dhabi, UAE. Pearl cultivation is allowed in the UAE, in contrast to the Kingdom of Bahrain, where strict laws prohibit the trade (import and sale) of cultured pearls.

In late 2007, the Abu Dhabi Pearls project was initiated as a pilot study to assess the feasibility of producing gem-quality cultured pearls in the warm waters of the Arabian Gulf. Since its inception, the project has been managed by the Environment Agency – Abu Dhabi. Pearl cultivation has taken place at two sites in the Al Dhafra region: Al Mirfa (24°06'21''N, 53°28'01''E) and

Al Mughirah (24°03'46''N, 53°34'07''E; see Figure 2). Other, smaller-scale farms using the same mollusc are operating in the Arabian Gulf, but no specific information on them is publicly available.

The feasibility of culturing pearls using *P. radiata* was confirmed with the Abu Dhabi Pearls project's first harvest in January 2010. To date, approximately 150,000 cultured pearls have been produced, with around 25% being of very good to excellent quality. They typically range from 5 to 8 mm in diameter, and come in a wide range of shapes and colours. No post-harvest treatment is applied. For this study, representative medium- to excellent-quality cultured pearls (both bead-cultured and non-bead-cultured) were studied using various imaging, spectroscopic and chemical methods. This is the first published scientific documentation of cultured pearls from *P. radiata*.



Figure 2: (a) The Abu Dhabi Pearls project is located in the Arabian Gulf, off the coast of UAE. The inset shows the location of the Abu Dhabi Pearls project within the Al Dhafra region in the Emirate of Abu Dhabi. (b) The project's two pearl-cultivation sites of Al Mirfa and Al Mughirah can be seen in this aerial photo (scale 1:130,000; courtesy of the Abu Dhabi Pearls project).

PEARL CULTURING PROCESS

The cultivation process (Figure 3) employs methodology that is similar to that used for akoya cultured pearls (*Pinctada fucata*; see Otter *et al.* 2017). The mantle

tissue graft is obtained from a donor mollusc that is carefully selected based on the colour and quality of the nacre on the shell's interior. The outer epithelium layer of the mantle tissue is removed from the darker part of the mantle and then cut into the square pieces



Figure 3: The culturing process employed by the Abu Dhabi Pearls project using *P. radiata* molluscs consists of several steps. (a) A *P. radiata* donor mollusc displaying colourful shell nacre provides mantle tissue that will be used for the graft accompanying the bead nucleus. (b) The outermost part of mantle epithelium layer cut from the donor mollusc is laid out in strips (top), which are then cut into squares of about 2 × 2 mm each to create tissue grafts (bottom). The orange-red colour of the grafts shows that they have been treated with antibiotics. (c) Unionidae shell beads are used as cultured pearl nuclei; their yellow colour shows that they have been coated with antibiotics. (d) A technician prepares a host mollusc for insertion of the bead and tissue graft. (e) The technician makes an incision in the gonad area of the mollusc where the bead and tissue will be inserted. (f) The bead with the tissue graft (red) are seen in the host mollusc after insertion. Photos by A. Al-Alawi.



Figure 4: (a) The implanted molluscs are placed in cages to be immersed in the water. (b) The molluscs are removed from the ocean on a regular basis for cleaning. Photos by A. Al-Alawi.

used for graft material (or *saibo*, sometimes also spelled *seibo* in Japanese), each measuring approximately 2×2 mm. The valves of the acceptor molluscs are partially opened using a special tool, and a small incision is made in the gonad to allow the bead to be inserted together with the graft (with the nacre-producing side facing the bead). Cellular proliferation then rapidly forms a so-called *pearl sac*, depositing nacre on the bead. Both donor and acceptor molluscs are obtained from spat that are grown to an age of less than three years before they are used for pearl culture.

The bead nuclei range from 4 to 7 mm in diameter and are derived from freshwater mollusc shells (Unionidae) from the USA. Two types are used: normal white beads, and yellow beads that have been coated with antibiotics to decrease the possibility of the acceptor ‘oysters’ being infected by pathogens. The molluscs are conditioned before the operation, and this process is adjusted according to the developmental status of the mollusc’s gonad. Bead insertion (simultaneously with tissue graft transplantation) takes place from November to April, using host molluscs that measure approximately 5.5 cm, which are then returned to the water (Figure 4a). The water temperature in Abu Dhabi varies throughout the year, ranging from 16°C to 37°C, and the salinity changes from 44‰ to 49‰ depending on seasonal rainfall.

For successful pearl cultivation, the farm technicians must keep track of the age of the molluscs, monitor their health and ensure that the waters are not overcrowded.

In addition, to facilitate nacre growth, the molluscs are cleaned by hand (Figure 4b) or with a high-pressure sprayer to remove algae and other growths from their shells. This is done weekly, except during August and September when the water temperature is relatively high; cleaning is then performed less often (i.e. biweekly) to minimise stress on the ‘oysters’ since they become weaker in the warmer water. The percentage of rejected beads is still relatively high (about 30%).

Various experiments have been conducted to assess the optimal bead size range and cultivation time. For typical bead sizes of 4–7 mm in diameter, harvesting of the cultured pearls takes place after two years (Figure 5). Longer cultivation times (four years) were attempted for larger-sized beads of 7–8 mm in an effort to maintain high quality and sufficient nacre thickness, but the results were unsatisfactory. Experiments were also done to test the effect of cultivation time on final cultured pearl size. Regardless of the size of the bead used, the implanted ‘oysters’ were kept for either two years or four years. However, in both cases the nacre thickness was almost identical, and the ones that were cultivated for four years actually had lower lustre and quality.

After harvesting, the cultured pearls are sorted, cleaned and graded. The number of molluscs harvested is currently slightly more than 100,000 per year, which is a relatively low amount when compared to commercial akoya cultured pearl farms such as Mikimoto (1,000,000 molluscs), Kamimura (6,000,000 molluscs)



Figure 5: After a period of two years, the molluscs are opened to remove the cultured pearls. Photo by A. Al-Alawi.

and Kitamura (10,000,000 molluscs). Around 10,000 *P. radiata* cultured pearls of very good to excellent quality are produced annually. A trademark for the term *Abu Dhabi Pearls* was recently registered, and these cultured pearls will become commercially available in the near future. Currently, some of them have been given to the School of Design in Abu Dhabi to use in their future jewellery designs.

MATERIALS AND METHODS

For this study, we examined 113 *P. radiata* bead-cultured pearls from the Abu Dhabi Pearls project weighing 0.83–5.88 ct and ranging from 4.87×4.81 to 15.07×11.51 mm. We also examined 33 non-bead-cultured pearls found in the gonad after bead rejection (these by-products are sometimes referred to as ‘keshi’ cultured pearls); these weighed 0.34–1.31 ct and measured from 4.44×3.14 to 7.06×5.19 mm.

All samples were examined macroscopically, and with a binocular gemmological microscope using magnifications of $10\times$ – $70\times$ and fibre-optic illumination, as well as 3 W long-wave (365 nm) and short-wave (254 nm) UV lamps. X-ray luminescence was tested for all samples with a PXI GenX-100 unit set to 100 kV and 5 mA (500 W), and recorded with a Nikon D810 camera using an exposure time of 8 seconds with F6.3 aperture and ISO Hi 0.7; samples were placed about 20 cm from the X-ray tube. X-ray microradiographs were acquired for all samples in three directions perpendicular to each other using a PXI GenX-90P instrument set to 90 kV and 80 μ A, 100–120 milliseconds exposure time per frame and 128 frames. X-ray computed microtomography

(micro-CT) scans were acquired on 46 samples (13 of the bead-cultured and all non-bead-cultured pearls) using a ProCon X-ray CT-Mini instrument with 800 projection views in 360° (i.e. 0.45° increments), seven frames, 100 kV, 120 mA and 250 milliseconds/frame exposure time.

Raman spectra were obtained for all samples using a Renishaw inVia spectrometer coupled with a microscope. We used a laser excitation wavelength of 514 nm (diode-pumped solid-state laser). Spectra were collected from 200 to 2000 cm^{-1} with a resolution of around 2 cm^{-1} , using a grating of 1,800 grooves/mm, 40 μm slit, laser power of 5 mW on the sample (to avoid any destruction of the fragile organic material), $50\times$ long-distance objective, acquisition time of 30 seconds and seven accumulations. The instrument was calibrated using the diamond Raman line at 1331.8 cm^{-1} . Photoluminescence (PL) spectra were acquired for all samples using a mobile Raman spectrometer (GemmoRaman-532) with 532 nm excitation and a laser power of about 1 mW on the sample. Spectra were collected from 540 to 700 nm with a resolution of about 1 nm, acquisition time of 50–700 milliseconds and 30 accumulations; calibration was likewise performed using the 1331.8 cm^{-1} diamond Raman line.

Diffuse reflectance ultraviolet-visible-near infrared (UV-Vis-NIR) spectra were acquired for all samples using a Cary 60 spectrophotometer with an external Harrick diffuse reflectance accessory. Spectra were acquired from 250 to 1000 nm, and the data sampling interval and spectral bandwidth were set at 1 nm using a 100 nm/minute scan rate. Black sample holders with a 2-mm-diameter hole were used, and background spectra were acquired using a white MgO reference (for 100% reflectance) and with nothing (for 0% reflectance).

Chemical analysis of all samples was performed using energy-dispersive X-ray fluorescence (EDXRF) spectroscopy with a Thermo Scientific ARL Quant’X instrument using various energies and filters. In addition, the trace-element content of all samples was measured using laser ablation inductively coupled plasma mass spectrometry (LA-ICP-MS) using instrumentation and analytical conditions that were identical to those presented by Karampelas *et al.* (2019b). Several isotopes were measured, but in this article only data for ^{23}Na , ^{24}Mg , ^{55}Mn , ^{88}Sr and ^{137}Ba are presented. Three spots were analysed on each sample, on areas consisting of aragonite with nacreous microstructure (checked with Raman spectroscopy and optical microscopy).

The exact taxonomy of *P. radiata* is still under discussion, and in this article we use the terminology listed by WoRMS (World Register of Marine Species; <http://marinespecies.org>).

RESULTS AND DISCUSSION

Physical Characteristics

The 113 bead-cultured pearl samples had a range of colours (14 white, 29 light cream, 22 cream, six light yellow, two yellow, 36 grey and four brown) and various shapes (50 round, 13 near-round, eight near-button, 10 near-drop, three near-oval and 29 near-baroque). Half the bead-cultured pearl samples were of high quality—possessing high lustre, homogeneous colouration and a surface free from blemishes that exhibited pink overtones and iridescence—while others were of medium quality and had minor surface blemishes.

The 33 non-bead-cultured pearl samples also showed a range of colours (four white, 12 light cream, eight cream, three light grey and six grey) and various shapes (one near-round, one button, 11 near-button, one oval, five near-oval and 14 near-baroque). They were of relatively medium quality—possessing low to moderate lustre, sometimes non-homogeneous colouration and minor to moderate blemishes on the surface.

Viewed with the microscope, all samples presented typical nacreous overlapping layers of aragonite (Figure 6a, b) and some showed surface blemishes (Figure 6c).

UV and X-ray Luminescence

Most of the bead-cultured pearls (110) and all of the non-bead-cultured pearls luminesced green to greenish yellow to yellow under short-wave UV radiation, and yellow to green under long-wave UV (all of moderate intensity). Only two samples presented a different reaction: moderate light brown under short-wave UV radiation and moderate red under long-wave UV. In addition, one cultured pearl luminesced moderate yellowish orange under short-wave UV radiation and moderate orangey yellow under long-wave UV. There were no systematic variations in UV fluorescence according to body colour. Greenish yellow phosphorescence of low intensity was observed for 1–2 seconds

in 35 of the bead-cultured and 30 of the non-bead-cultured pearls.

When exposed to X-rays, most of the bead-cultured pearls displayed yellow-green luminescence, which varied from strong (58 samples) to moderate (22 samples) to weak (13 samples). This luminescence most likely originated from the underlying freshwater shell bead (cf. Hänni *et al.* 2005; Karampelas *et al.* 2019b). The other 20 samples were inert, probably due to their greater nacre thickness (>1.5 mm). All of the non-bead-cultured pearls were inert to X-rays.

X-ray Imaging: Bead-Cultured Samples

X-ray microradiographs and micro-CT slices of selected bead-cultured pearls are presented in Table I. All of the images are in greyscale; lighter tones indicate materials with higher density, such as calcium carbonate (usually aragonite in most natural and cultured pearls), while darker tones represent lower-density materials (usually organic matter, cracks, cavities or voids).

Most of the bead-cultured pearls showed a slightly lighter central region (corresponding to the bead) that was surrounded by a typical demarcation line (which appears dark due to organic-rich material; see, e.g., the micro-CT scans of samples XR-5132 and XR-5136). Some of the cultured pearls showed pronounced demarcation lines around the bead, with multiple growth lines or layers (e.g. XR-5190)—sometimes displaying radial-like structures—along with thick organic-rich layers of deposition. These radial structures appeared close to those observed in cultured pearls from other bivalves, supporting the idea that cultured pearls are formed by a process similar to shell regeneration and not to a reverse-shell mechanism as previously believed (see Cuif *et al.* 2011; Sato & Komaru 2019).

Some samples showed small (<2 mm) round features that looked like ‘seed pearls’ within organic-rich matter in layers following the demarcation lines around the bead (e.g. XR-5189); these need further study to



Figure 6: The typical appearance of overlapping layers of nacre is shown on the surface of (a) bead-cultured and (b) non-bead-cultured pearls. (c) Small bumps form blemishes on a bead-cultured pearl. Photomicrographs by Z. Ali; image widths 2.1 mm.

Table I: Characteristics, X-ray microradiographs and micro-CT slices of selected samples of bead-cultured pearls from Abu Dhabi.*


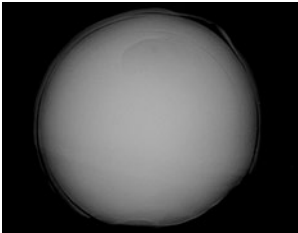



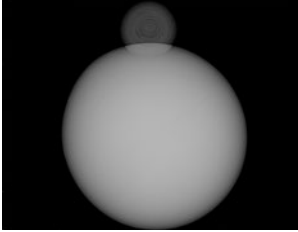
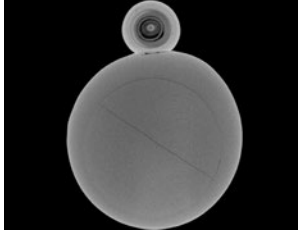

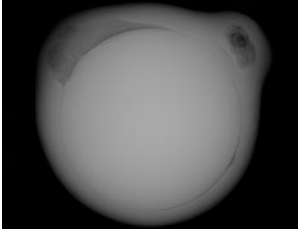
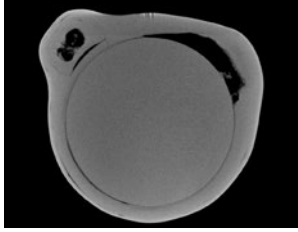

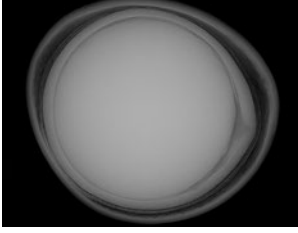
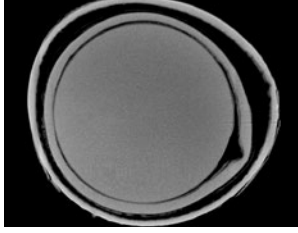


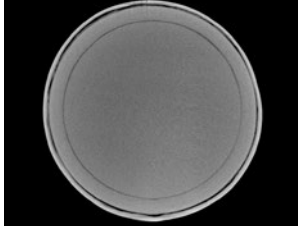


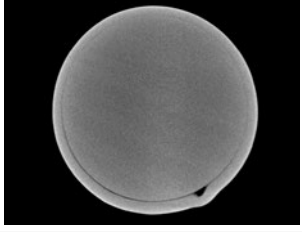

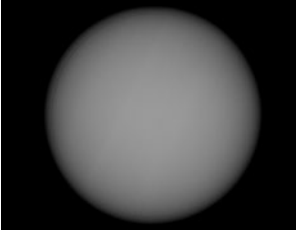
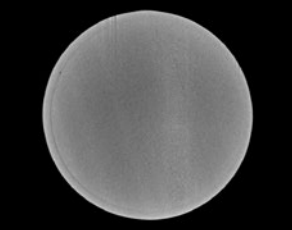



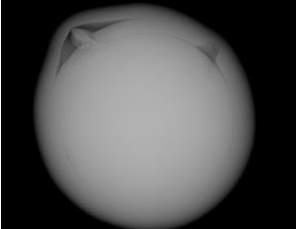
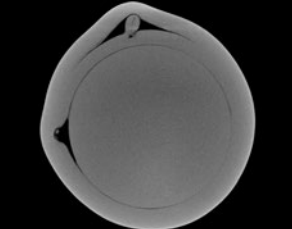

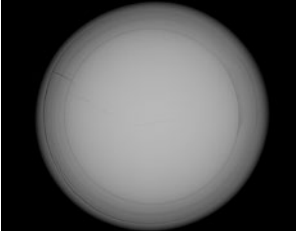
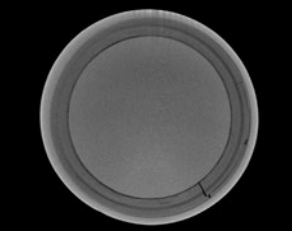

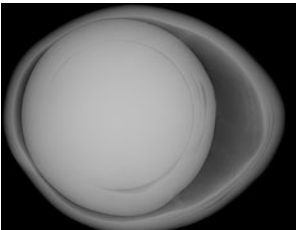
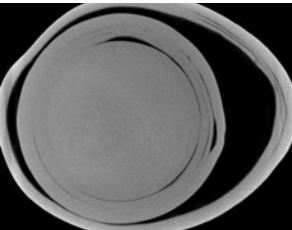

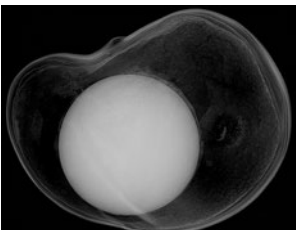
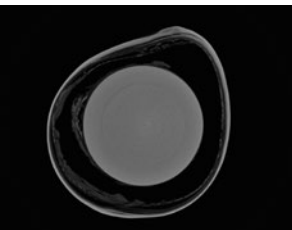
| Sample | Description | Photograph | X-ray microradiograph | Micro-CT slice |
|---------|--|---|--|---|
| XR-5093 | Weight: 1.90 ct Shape: Near baroque Colour: White and light cream Dimensions: 6.56 × 6.38 mm Nacre thickness: up to 0.60 mm |  |  | N/A |
| XR-5096 | Weight: 2.07 ct Shape: Near baroque Colour: Light cream and cream Dimensions: 6.60 × 6.37 mm Nacre thickness: up to 0.65 mm |  |  | N/A |
| XR-5104 | Weight: 2.30 ct Shape: Near baroque Colour: Light cream Dimensions: 8.71 × 6.62 mm Nacre thickness: up to 1.55 mm |  |  |  |
| XR-5106 | Weight: 2.02 ct Shape: Near baroque Colour: Light cream and orangey cream Dimensions: 7.47 × 6.36 mm Nacre thickness: up to 1.05 mm |  |  |  |
| XR-5114 | Weight: 1.89 ct Shape: Near baroque Colour: Brown and grey Dimensions: 7.26 × 6.19 mm Distance from the bead's edge to the cultured pearl's surface: up to 1.05 mm |  |  |  |
| XR-5119 | Weight: 1.97 ct Shape: Near round Colour: Grey Dimensions: 6.61 × 6.46 mm Nacre thickness: 0.60 mm |  |  |  |
| XR-5132 | Weight: 0.90 ct Shape: Near round Colour: Brownish cream Dimensions: 5.02 × 4.95 mm Nacre thickness: 0.25 mm |  |  |  |

Table I: (continued)

| Sample | Description | Photograph | X-ray microradiograph | Micro-CT slice |
|---------|---|---|--|---|
| XR-5136 | Weight: 0.83 ct Shape: Round Colour: Yellow Dimensions: 4.87 × 4.81 mm Nacre thickness: 0.15 mm |  |  |  |
| XR-5163 | Weight: 3.37 ct Shape: Round Colour: Light cream Dimensions: 7.78 × 7.70 mm Nacre thickness: 1.30 mm |  |  | N/A |
| XR-5189 | Weight: 3.79 ct Shape: Near baroque Colour: White Dimensions: 8.60 × 8.04 mm Nacre thickness: up to 1.10 mm |  |  |  |
| XR-5190 | Weight: 3.67 ct Shape: Round Colour: Cream Dimensions: 8.05 × 8.01 mm Nacre thickness: 0.95 mm |  |  |  |
| XR-5191 | Weight: 5.65 ct Shape: Near drop Colour: Grey Dimensions: 11.39 × 9.78 mm Distance from the bead's edge to the cultured pearl's surface: up to 1.75 mm |  |  |  |
| XR-5195 | Weight: 5.88 ct Shape: Baroque Colour: Cream and grey Dimensions: 15.07 × 11.51 mm Distance from the bead's edge to the cultured pearl's surface: up to 3.60 mm |  |  |  |

*Note: The X-ray microradiographs and micro-CT slices do not necessarily show the same sample positions. Abbreviation: N/A = not acquired. Photos by Ghadeer Abdali, DANAT.

determine the nature of the round features. Some of the samples (e.g. XR-5104) had ‘satellite pearls’ containing pronounced concentric growth structures (particularly visible with micro-CT imaging), which were similar to those observed for some bead-cultured pearls with attached non-bead-cultured pearls (by-products) from *Pinctada maxima* (Krzemnicki *et al.* 2010).

The higher-quality cultured pearls ranged in size from 7.00 to 8.50 mm, with beads of 5–7 mm and nacre thicknesses of 0.50–1.50 mm; more than half had a nacre thickness exceeding 0.90 mm. The largest samples (>9 mm) were baroque shaped and presented large areas of organic-matter deposition. For example, sample XR-5195, with an 8 mm bead, contained large amounts of organic material; the maximum distance from the bead’s edge to the cultured pearl’s surface was 3.60 mm. The cultured pearl with the thinnest nacre was XR-5136, with a thickness of 0.15 mm. Some medium-quality cultured pearl samples (e.g. XR-5114, XR-5191 and XR-5195) had thick organic-matter deposition with multiple growth structures; they also showed mostly grey to

brown body colours. Micro-CT slices of sample XR-5195 presented dark areas that are most probably associated with voids; the sound of the bead moving inside a hollow area could be heard when shaken.

Fourteen of the samples consisted of bead-cultured blister pearls (e.g. XR-5093 and XR-5096) that had a point of attachment to the inner shell of the mollusc. The nacre thickness of these samples varied from 0.15 to 2.00 mm, and in a few larger samples the distance from the bead’s edge to the cultured pearl’s surface was up to 3.60 mm.


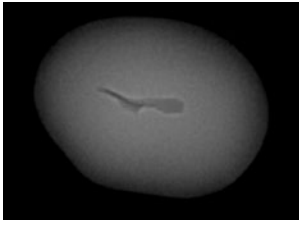
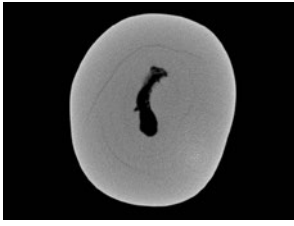

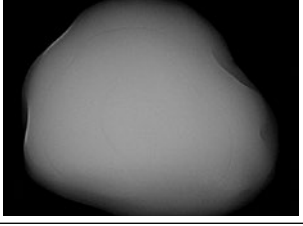


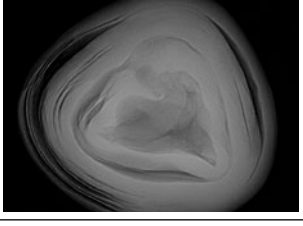
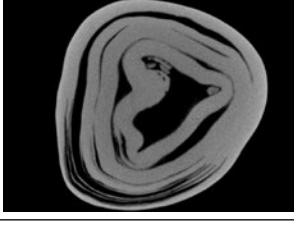

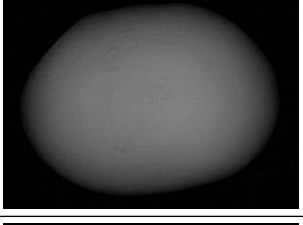
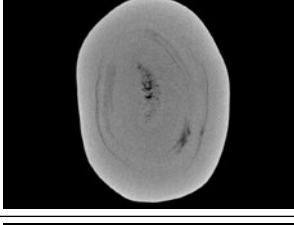


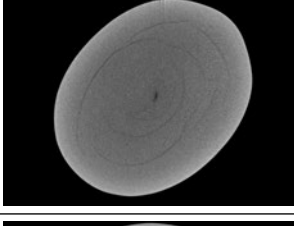


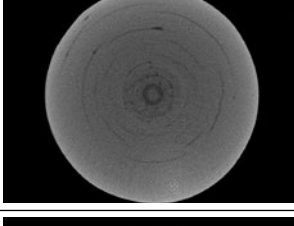

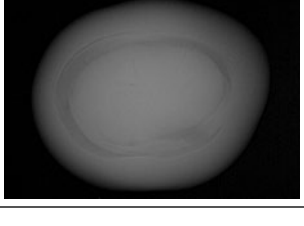
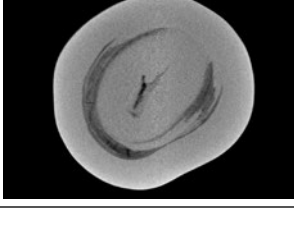
X-ray Imaging: Non-Bead-Cultured Samples

The 33 non-bead-cultured pearl by-products examined by the authors were also X-rayed and studied using micro-CT imaging (see some selected examples in Table II). These samples revealed diverse types of voids, which were in some cases linear in structure and of variable dimension. They were similar to those observed in non-bead-cultured pearls from other molluscs, and different from those documented in natural pearls (see Sturman 2009; Karampelas *et al.* 2010, 2017; Krzemnicki *et al.* 2010).

Table II: Characteristics, X-ray microradiographs and micro-CT slices of selected samples of non-bead-cultured pearls from Abu Dhabi.*

| Sample | Description | Photograph | X-ray microradiograph | Micro-CT slice |
|--------|---|------------|-----------------------|----------------|
| 1-2-2 | Weight: 0.68 ct Shape: Near baroque Colour: Light cream and cream Dimensions: 5.16 × 4.71 mm | | | |
| 1-2-4 | Weight: 0.54 ct Shape: Near baroque Colour: Light cream Dimensions: 5.43 × 4.33 mm | | | |
| 1-2-7 | Weight: 0.73 ct Shape: Near button Colour: Cream Dimensions: 5.84 × 4.40 × 4.10 mm | | | |
| 1-2-9 | Weight: 0.53 ct Shape: Near baroque Colour: Cream Dimensions: 4.86 × 4.18 mm | | | |

Table II: (continued)

| Sample | Description | Photograph | X-ray microradiograph | Micro-CT slice |
|--------|--|---|--|---|
| 1-2-13 | Weight: 0.52 ct Shape: Near oval Colour: Light cream Dimensions: 4.74 × 4.06 × 3.58 mm |  |  |  |
| 3-0-2 | Weight: 0.64 ct Shape: Near button Colour: Light cream Dimensions: 5.43 × 4.52 × 3.57 mm |  |  |  |
| 3-1-1 | Weight: 0.52 ct Shape: Near baroque Colour: Light cream and grey Dimensions: 4.79 × 4.44 mm |  |  |  |
| 3-1-3 | Weight: 0.34 ct Shape: Near oval Colour: Light cream Dimensions: 4.44 × 3.29 × 3.14 mm |  |  |  |
| 3-1-4 | Weight: 0.38 ct Shape: Oval Colour: Light cream Dimensions: 4.41 × 3.44 × 3.43 mm |  |  |  |
| 3-2-3 | Weight: 0.49 ct Shape: Near round Colour: Light cream Dimensions: 4.23 × 4.03 mm |  |  |  |
| 3-4-1 | Weight: 0.46 ct Shape: Near baroque Colour: Cream Dimensions: 4.63 × 3.87 mm |  |  |  |

*Note: The X-ray microradiographs and micro-CT slices do not necessarily show the same sample positions. In some of the micro-CT images, an off-centre lighter-coloured patch (e.g. near the bottom of sample 3-2-3) is an artefact related to the rotation axis of the sample during measurement. Photos by Ghadeer Abdali, DANAT.

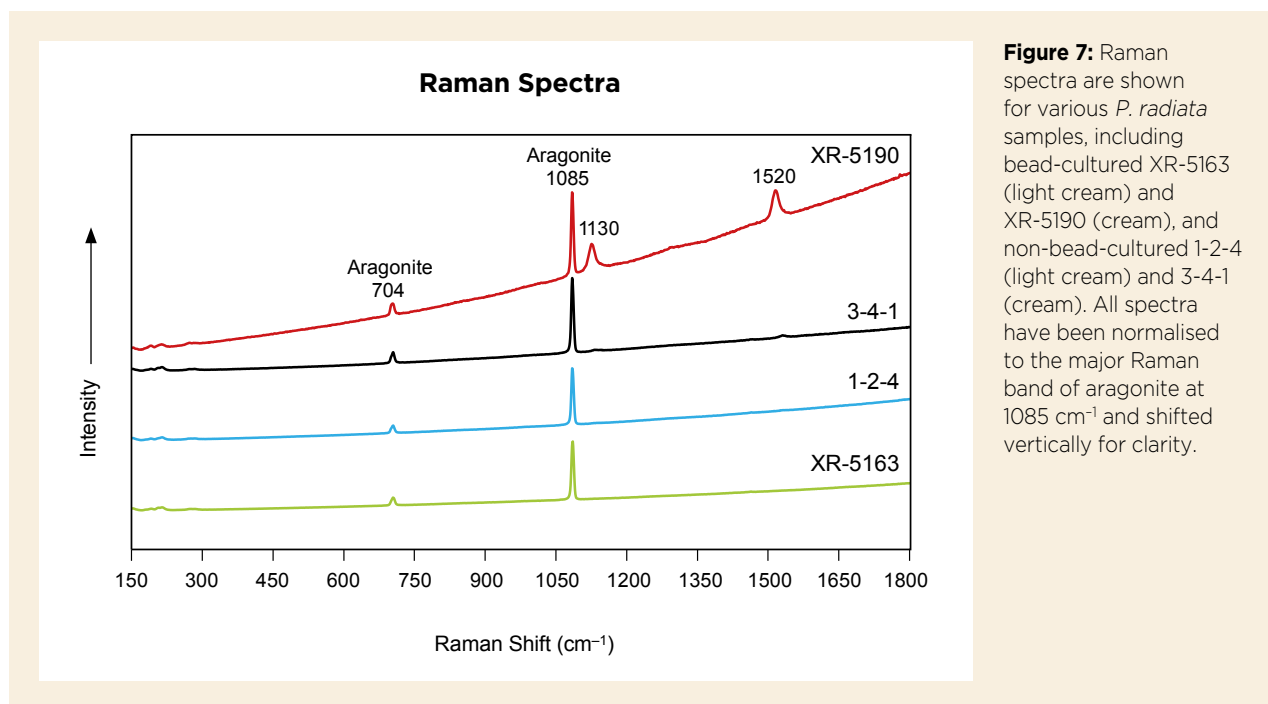


Figure 7: Raman spectra are shown for various *P. radiata* samples, including bead-cultured XR-5163 (light cream) and XR-5190 (cream), and non-bead-cultured 1-2-4 (light cream) and 3-4-1 (cream). All spectra have been normalised to the major Raman band of aragonite at 1085 cm^{-1} and shifted vertically for clarity.

The linear structures observed in our non-bead-cultured samples were related to some extent to their exterior shape, and often had a thick and dense appearance in the X-ray images (again, see Table II). These structures were revealed in considerably greater detail in the micro-CT images. In sample 3-1-1, a large irregular central cavity is visible with white spots on the sides. The organic material has a somewhat darker appearance than in the X-ray microradiographs and is surrounded by dark growth layers. An important factor to note is that the voids observed in all saltwater non-bead-cultured pearls do not change contrast significantly in different directions, and they frequently show an abrupt transition from darker to lighter colour (i.e. without intermediate shades of grey). In sample 3-2-3, a lighter core (most likely calcium-carbonate rich) is visible in the centre—particularly with micro-CT imaging—and is surrounded by fine concentric growth lines; this appearance could easily be confused with the growth pattern seen in saltwater natural pearls. However, natural pearls typically have a darker core (richer in organic matter; cf. Krzemnicki *et al.* 2010). Also noted in a few samples was a very small, fine, irregular central hairline feature surrounded by growth lines, such as in sample 3-0-2 (see also Sturman 2009). After being drilled, such cultured pearls might be challenging to identify. Moreover, in a few samples, the central cavity was not clearly visible by typical X-ray microradiography but was only seen in the micro-CT images (again, see Table II).

Raman Spectroscopy

Raman spectra of all samples presented bands at around 1085 and 704 cm^{-1} (Figure 7) due to the symmetric and in-plane bending modes, respectively, of carbonate molecules in aragonite. Also present was a series of weak bands below 400 cm^{-1} due to the lattice modes of carbonate in aragonite (Urmos *et al.* 1991). The vast majority of the studied samples (light cream, cream, light yellow and light grey) had peaks at about 1130 and 1520 cm^{-1} due to C–C and C=C stretching vibrations of partially substituted (i.e. partially methylated) polyenic pigments (Karampelas *et al.* 2019a). Similar Raman bands are known in pearls from various molluscs, including akoya cultured pearls (Fritsch *et al.* 2012; Otter *et al.* 2017; Karampelas *et al.* 2019a). Only 10 white-to-light cream coloured samples showed solely bands linked to aragonite without the presence of those related to pigments (e.g. the spectra for samples XR-5163 and 1-2-4 in Figure 7).

PL Spectroscopy

The PL spectra of the samples showed various apparent maxima. Bands centred at 565 nm and at around 590 nm are both possibly due to organic compounds present in the nacre. A band at 620 nm accompanied by two other bands at 650 and 680 nm are probably due to a type of porphyrin (Miyoshi *et al.* 1987; Hainschwang *et al.* 2013; see 3-4-1 in Figure 8). Overall, the apparent maximum in the PL spectra (as labelled in Figure 8) was due to the relative intensity of the three bands

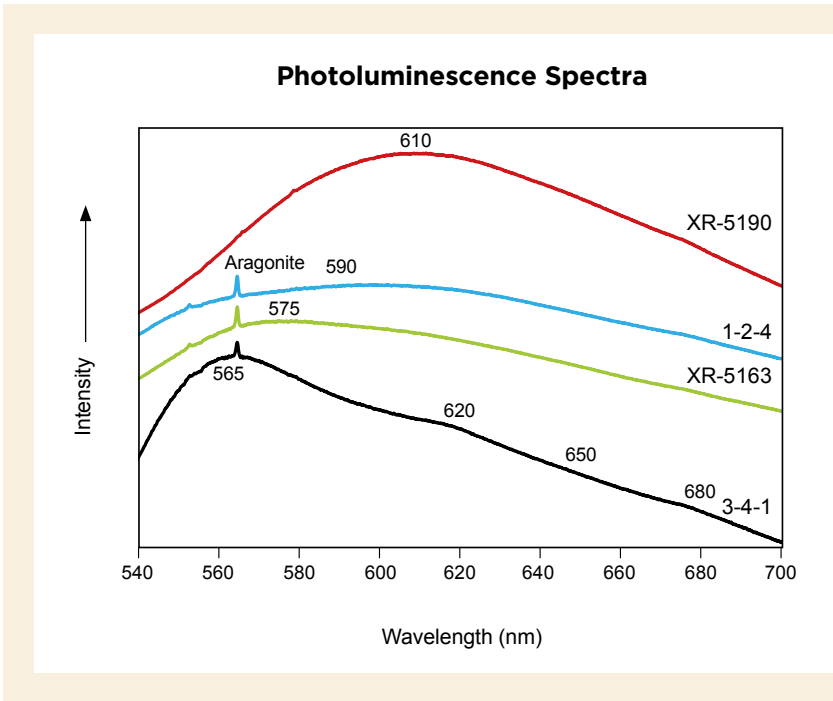


Figure 8: PL spectra are shown for the same *P. radiata* bead-cultured pearls (XR-5163 and XR-5190) and non-bead-cultured pearls (1-2-4 and 3-4-1) as in Figure 7. Three of the spectra (XR-5163, 1-2-4 and 3-4-1) have been normalised to the major Raman band of aragonite (appearing as a sharp band slightly above 560 nm, i.e. at 1085 cm⁻¹) and shifted vertically for clarity.

at 565, 590 and 620 nm. For the vast majority of the studied samples (110), the apparent PL maxima were in the orange to red region at 605–625 nm (e.g. XR-5190 in Figure 8); for 27 samples the maxima were positioned in the yellow to orange region at 580–600 nm (e.g. 1-2-4 in Figure 8); and nine cultured pearls showed maxima in the green to yellow region at 555–575 nm (e.g. XR-5163 in Figure 8).

UV-Vis-NIR Spectroscopy

The UV-Vis-NIR spectra of all the studied samples presented bands (appearing as minima in diffuse reflectance; Figure 9) in the visible range at around 410, 435 and 460 nm—possibly related to partially substituted (i.e. partially methylated) polyenic pigments—similar to those observed for freshwater cultured pearls (Karampelas *et al.* 2009). Some samples (of no particular colour)

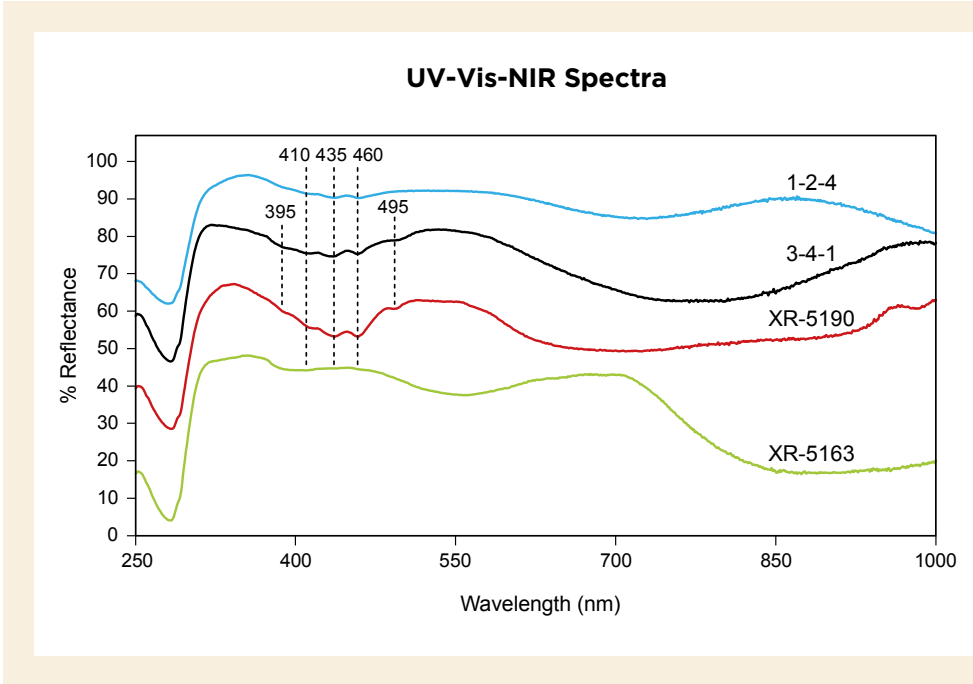


Figure 9: UV-Vis-NIR spectra for the same *P. radiata* bead-cultured pearls (XR-5163 and XR-5190) and non-bead-cultured pearls (1-2-4 and 3-4-1) as in Figures 7 and 8 are shown here for comparison. The spectra have been shifted vertically for clarity (-20% for XR-5163, +10% for 1-2-4 and +15% for 3-4-1).

displayed an additional band at 495 nm, possibly linked to a type of porphyrin (Nilpetpoy *et al.* 2018; Karampelas *et al.* 2019a). Taken together, the series of bands recorded here differ from those of saltwater cultured pearls from other species (*P. maxima*, *P. margaritifera*, *P. maculata* and *Pteria* sp.; cf. Karampelas *et al.* 2011a, b; Karampelas 2012; Otter *et al.* 2017; Nilpetpoy *et al.* 2018). Those at 435 and 460 nm have been observed in akoya cultured pearls (i.e. from *P. fucata*). However, those at 410 and 495 nm, along with another band at around 395 nm, have only been observed in *P. radiata* samples.

Chemical Analysis

The chemical composition of the cultured pearls from Abu Dhabi is presented in Table III and compared to previously published data on natural pearls from *P. radiata* fished off Bahrain, as well as bead-cultured pearls from *P. fucata* cultivated off Vietnam (Karampelas *et al.* 2019b) and Japan (from the DANAT reference collection).

All studied samples from Abu Dhabi presented low concentrations of Mn (always below the detection limit of EDXRF and sometimes below the quantification limit for LA-ICP-MS) and relatively high concentrations of Sr. The cultured pearls from *P. fucata* presented relatively higher amounts of Mn (>10 ppmw Mn) compared to the other samples. It was suggested by Gordon *et al.* (1970) that the water's Mn content is the most important factor affecting the Mn composition of molluscs, shells and possibly natural and cultured pearls. On the other

hand, the Sr content of the inner part of saltwater aragonitic bivalves is influenced by the animal's growth rate (possibly linked to water temperature), as well as physiological processes (Stecher *et al.* 1996; Poulain *et al.* 2015; Wanamaker & Gillikin 2019). Some of the studied samples from Abu Dhabi had slightly lower Sr values than the other two types. Sodium was present in relatively high amounts in all samples, and in biogenic carbonate this element is related to water salinity and pH (Gordon *et al.* 1970). The Na concentrations were similar in the cultured pearls from Abu Dhabi and natural pearls from Bahrain; however, Na was slightly lower in the cultured pearls from Japan and Vietnam.

It has been suggested that Mg in aragonitic shells is related to physiological processes (Foster *et al.* 2008; Poulain *et al.* 2015). All samples in Table III presented somewhat similar Mg contents; only nine of the 146 cultured pearls from Abu Dhabi contained >500 ppmw Mg. Barium in biogenic aragonite shows a strong inverse correlation with water salinity and food supply; shell growth and an as-yet undetermined environmental factor are also thought to influence Ba content (Gillikin *et al.* 2008; Poulain *et al.* 2015). All the samples in Table III contained very low Ba (sometimes below the quantification limit). Natural pearls from *P. radiata* fished off Bahrain showed slightly higher Ba, with 23 of the 248 samples having >1.5 ppmw Ba. Figure 10 presents a plot of Sr vs. Ba, suggesting an overall positive correlation between these elements; this apparent trend needs further investigation.

Table III: Chemical analysis by LA-ICP-MS (in ppmw) of *P. radiata* bead-cultured and non-bead-cultured pearls from Abu Dhabi, *P. radiata* natural pearls from Bahrain, and *P. fucata* cultured pearls from Japan and Vietnam.^a

| Samples | Element | Range | Average (SD) | Median |
|--|-----------------|-----------|--------------|--------|
| <i>P. radiata</i> (Abu Dhabi, cultured), 146 samples, 438 analyses | Na | 3440–7290 | 5200 (660) | 4910 |
| | Mg | 55.2–1280 | 265 (166) | 181 |
| | Mn | BQL–5.96 | 1.03 (1.02) | 0.48 |
| | Sr ^b | 448–1270 | 769 (186) | 670 |
| | Ba | BQL–0.85 | 0.22 (0.13) | 0.15 |
| <i>P. radiata</i> (Bahrain, natural), 248 samples, 248 analyses | Na | 3340–7270 | 5250 (801) | 5250 |
| | Mg | 29.5–477 | 147 (88.2) | 131 |
| | Mn | BQL–7.62 | 0.79 (1.38) | BQL |
| | Sr | 518–1650 | 944 (219) | 902 |
| | Ba | BQL–4.32 | 0.78 (0.60) | 0.58 |
| <i>P. fucata</i> (Japan and Vietnam, cultured), 17 samples, 51 analyses | Na | 2370–4950 | 4090 (502) | 4150 |
| | Mg | 116–950 | 292 (165) | 244 |
| | Mn | 0.48–18 | 6.35 (4.92) | 4.70 |
| | Sr | 888–1860 | 995 (222) | 933 |
| | Ba | 0.06–1.47 | 0.28 (0.34) | 0.14 |

^a The quantification limits of Mn were 0.26–1.28 and Ba were 0.02–0.17. Abbreviations: BQL = below quantification limit, SD = standard deviation.

^b As measured by EDXRF spectroscopy, the contents of Sr in the same bead-cultured and non-bead-cultured pearls from Abu Dhabi were 734–1660 ppmw (average 1000 ppmw). Mn was below the EDXRF detection limit.

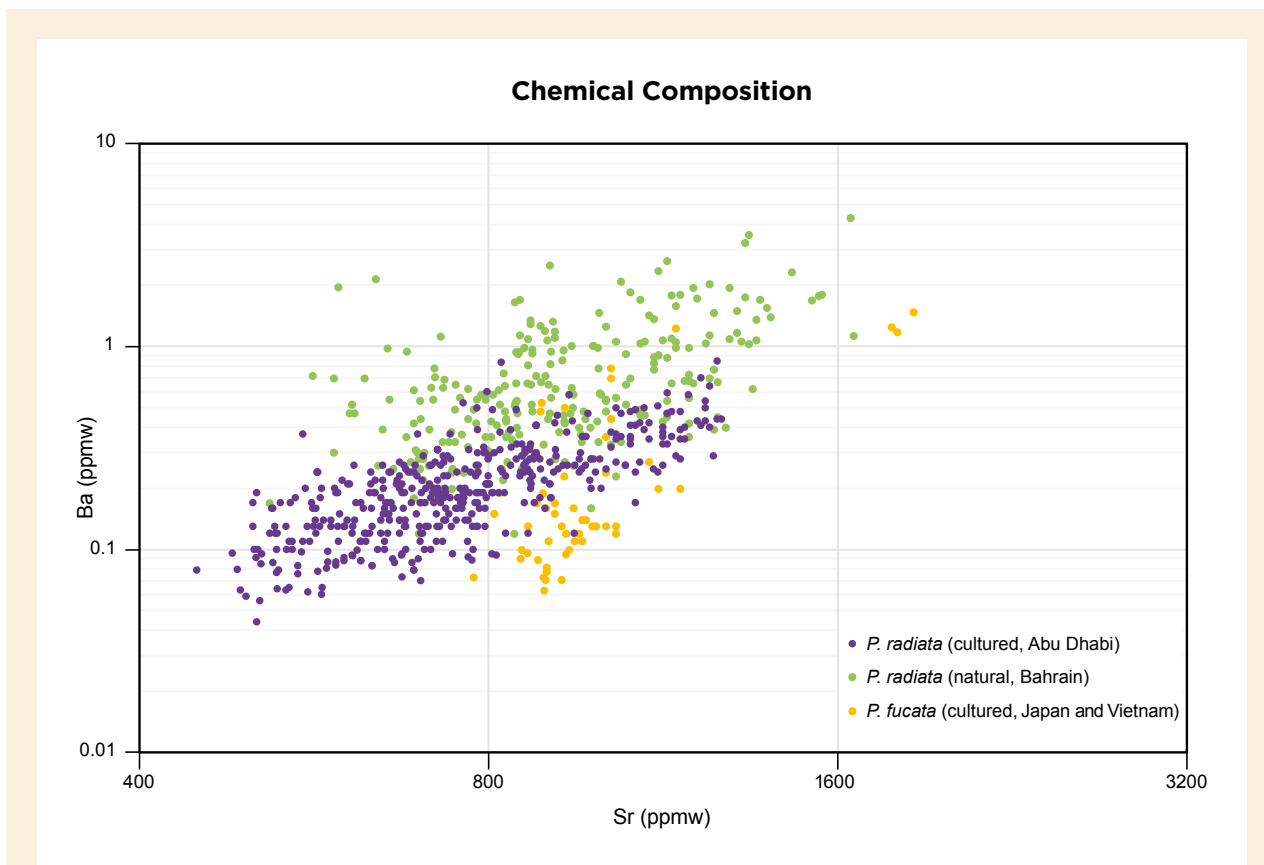


Figure 10: This binary plot compares the Sr and Ba contents of the *P. radiata* cultured pearl samples from Abu Dhabi with *P. radiata* natural pearls fished off Bahrain and *P. fucata* cultured pearls from Japan and Vietnam. Some of the studied samples from Abu Dhabi have lower Ba and Sr than the other two sample types.

CONCLUSION

This study of bead-cultured and non-bead-cultured products from the Abu Dhabi Pearls project in the UAE offers a complete gemmological analysis of cultured pearls from *P. radiata*. They showed a vast range of colours, from white to cream, light yellow to yellow, brown and various tones of grey with pink overtones, and some with iridescence. The vast majority of the cultured pearls luminesced green to greenish yellow under short-wave UV radiation and yellow to green under long-wave UV. With X-microradiography and micro-CT imaging, the bead-cultured pearls showed typical strong demarcation lines around the nuclei and sometimes large voids and calcium carbonate-rich areas with radial-like structures. Most of the non-bead-cultured pearls contained voids of variable dimension, similar to those observed in non-bead-cultured pearls from other molluscs, and different from those documented in natural pearls. Raman bands due to partially substituted (i.e. partially methylated) polyenes were recorded

at around 1130 and 1520 cm^{-1} for most of the samples. Samples from *P. radiata* and *P. fucata* (i.e. akoya cultured pearls) are the only nacreous saltwater-cultured pearls found to date presenting such bands. UV-Vis spectroscopy revealed bands at 410, 435 and 460 nm in all samples, and these are also linked to the same partially substituted (i.e. partially methylated) polyenic pigments indicated by Raman spectroscopy. Some samples yielded an additional band at around 495 nm, possibly linked to a type of porphyrin. These bands differ from those recorded for cultured pearls from other species (*P. maxima*, *P. margaritifera*, *P. maculata* and *Pteria* sp.), and those at 410 and 495 nm are different from bands recorded for akoya samples (i.e. *P. fucata*). Chemical analyses of the most important trace elements in the studied cultured pearls from Abu Dhabi show results similar to those for *P. radiata* natural pearls fished off Bahrain.

Work is ongoing at the Abu Dhabi Pearls project to decrease the rate of bead rejection and improve the

percentage of gem-quality cultured pearls. A trademark for the term *Abu Dhabi Pearls* was recently registered, and these cultured pearls (Figure 11) will be commercially produced in the near future. In addition, further studies are needed of the non-bead-cultured pearl by-products to characterise their internal structures, as well as their chemical and spectroscopic features, in order to properly separate them from natural pearls from *P. radiata* fished off Bahrain and other regions in the Arabian Gulf.

Figure 11: These white-to-cream bead-cultured pearls were produced from the Abu Dhabi Pearls project. They range from 5.5 to 8.5 mm in diameter. Courtesy of the Abu Dhabi Pearls project.



REFERENCES

- Cuif, J.-P., Dauphin, Y., Howard, L., Nouet, J., Rouzière, S. & Salomé, M. 2011. Is the pearl layer a reversed shell? A re-examination of the theory of pearl formation through physical characterizations of pearl and shell developmental stages in *Pinctada margaritifera*. *Aquatic Living Resources*, **24**(4), 411–424, <https://doi.org/10.1051/alr/2011149>.
- Foster, L.C., Finch, A.A., Allison, N., Andersson, C. & Clarke, L.J. 2008. Mg in aragonitic bivalve shells: Seasonal variations and mode of incorporation in *Arctica islandica*. *Chemical Geology*, **254**(1–2), 113–119, <https://doi.org/10.1016/j.chemgeo.2008.06.007>.
- Fritsch, E., Rondeau, B., Hainschwang, T. & Karampelas, S. 2012. Raman spectroscopy applied to gemmology. In: Dubessy, J., Caumon, M.-C. & Rull, F. (eds) *Raman Spectroscopy Applied to Earth Sciences and Cultural Heritage*. EMU Notes in Mineralogy, European Mineralogical Union and the Mineralogical Society of Great Britain and Ireland, Twickenham, **12**, 455–489, <https://doi.org/10.1180/EMU-notes.12.13>.
- Gillikin, D.P., Lorrain, A., Paulet, Y.-M., André, L. & Dehairs, F. 2008. Synchronous barium peaks in high-resolution profiles of calcite and aragonite marine bivalve shells. *Geo-Marine Letters*, **28**(5–6), 351–358, <https://doi.org/10.1007/s00367-008-0111-9>.
- Gordon, C.M., Carr, R.A. & Larson, R.E. 1970. The influence of environmental factors on the sodium and manganese content of barnacle shells. *Limnology and Oceanography*, **15**(3), 461–466, <https://doi.org/10.4319/lo.1970.15.3.0461>.
- Hainschwang, T., Karampelas, S., Fritsch, E. & Notari, F. 2013. Luminescence spectroscopy and microscopy applied to study gem materials: A case study of C centre containing diamonds. *Mineralogy and Petrology*, **107**(3), 393–413, <https://doi.org/10.1007/s00710-013-0273-7>.
- Hänni, H.A., Kiefert, L. & Giese, P. 2005. X-ray luminescence, a valuable test in pearl identification. *Journal of Gemmology*, **29**(5), 325–329, <https://doi.org/10.15506/JoG.2005.29.5.325>.
- Jochum, K.P., Scholz, D., Stoll, B., Weis, U., Wilson, S.A., Yang, Q., Schwalb, A., Borner, N. *et al.* 2012. Accurate trace element analysis of speleothems and biogenic calcium carbonates by LA-ICP-MS. *Chemical Geology*, **318–319**, 31–44, <https://doi.org/10.1016/j.chemgeo.2012.05.009>.
- Karampelas, S. 2012. Spectral characteristics of natural-color saltwater cultured pearls from *Pinctada maxima*. *Gems & Gemmology*, **48**(3), 193–197, <https://doi.org/10.5741/gems.48.3.193>.

- Karampelas, S., Fritsch, E., Mevellec, J.-Y., Sklavounos, S. & Soldatos, T. 2009. Role of polyenes in the coloration of cultured freshwater pearls. *European Journal of Mineralogy*, **21**(1), 85–97, <https://doi.org/10.1127/0935-1221/2009/0021-1897>.
- Karampelas, S., Michel, J., Zheng-Cui, M., Schwarz, J.-O., Enzmann, F., Fritsch, E., Leu, L. & Krzemnicki, M.S. 2010. X-ray computed microtomography applied to pearls: Methodology, advantages, and limitations. *Gems & Gemology*, **46**(2), 122–127, <https://doi.org/10.5741/gems.46.2.122>.
- Karampelas, S., Fritsch, E., Gauthier, J.-P. & Hainschwang, T. 2011a. UV-Vis-NIR reflectance spectroscopy of natural-color saltwater cultured pearls from *Pinctada margaritifera*. *Gems & Gemology*, **47**(1), 31–35, <https://doi.org/10.5741/gems.47.1.31>.
- Karampelas, S., Fritsch, E., Hainschwang, T. & Gauthier, J.-P. 2011b. Spectral differentiation of natural-color saltwater cultured pearls from *Pinctada margaritifera* and *Pteria sterna*. *Gems & Gemology*, **47**(2), 117.
- Karampelas, S., Al-Alawi, A. & Al-Attawi, A. 2017. Real-time microradiography of pearls: A comparison between the detectors used in two RTX units. *Gems & Gemology*, **53**(4), 452–456, <https://doi.org/10.5741/GEMS.53.4.452>.
- Karampelas, S., Fritsch, E., Makhloq, F., Mohamed, F. & Al-Alawi, A. 2019a. Raman spectroscopy of natural and cultured pearls and pearl producing mollusc shells. *Journal of Raman Spectroscopy*, 9 pp., <https://doi.org/10.1002/jrs.5670>.
- Karampelas, S., Mohamed, F., Abdulla, H., Almahmood, F., Flamarzi, L., Sangsawong, S. & Alalawi, A. 2019b. Chemical characteristics of freshwater and saltwater natural and cultured pearls from different bivalves. *Minerals*, **9**, article 357 (20 pp.), <https://doi.org/10.3390/min9060357>.
- Krzemnicki, M.S., Friess, S.D., Chalus, P., Hänni, H.A. & Karampelas, S. 2010. X-ray computed microtomography: Distinguishing natural pearls from beaded and non-beaded cultured pearls. *Gems & Gemology*, **46**(2), 128–134, <https://doi.org/10.5741/gems.46.2.128>.
- Miyoshi, T., Matsuda, Y. & Komatsu, H. 1987. Fluorescence from pearls to distinguish mother oysters used in pearl culture. *Japanese Journal of Applied Physics*, **26**(4), 578–581, <https://doi.org/10.1143/jjap.26.578>.
- Nilpetploy, N., Lawanwong, K. & Kessrapong, P. 2018. The gemological characteristics of pipi pearls reportedly from *Pinctada maculata*. *Gems & Gemology*, **54**(4), 418–427, <https://doi.org/10.5741/gems.54.4.418>.
- Otter, L.M., Agbaje, O.B.A., Huong, L.T.-T., Hager, T. & Jacob, D.E. 2017. Akoya cultured pearl farming in eastern Australia. *Gems & Gemology*, **53**(4), 423–437, <https://doi.org/10.5741/gems.53.4.423>.
- Poulain, C., Gillikin, D.P., Thébault, J., Munaron, J.M., Bohn, M., Robert, R., Paulet, Y.M. & Lorrain, A. 2015. An evaluation of Mg/Ca, Sr/Ca, and Ba/Ca ratios as environmental proxies in aragonite bivalve shells. *Chemical Geology*, **396**, 42–50, <https://doi.org/10.1016/j.chemgeo.2014.12.019>.
- Sato, Y. & Komaru, A. 2019. Pearl formation in the Japanese pearl oyster (*Pinctada fucata*) by CaCO₃ polymorphs: Pearl quality-specific biomineralization processes and their similarity to shell regeneration. *Aquaculture Research*, **50**(6), 1710–1717, <https://doi.org/10.1111/are.14057>.
- Stecher, H.A., Krantz, D.E., Lord, C.J., Luther, G.W. & Bock, K.W. 1996. Profiles of strontium and barium in *Mercenaria mercenaria* and *Spisula solidissima* shells. *Geochimica et Cosmochimica Acta*, **60**(18), 3445–3456, [https://doi.org/10.1016/0016-7037\(96\)00179-2](https://doi.org/10.1016/0016-7037(96)00179-2).
- Sturman, N. 2009. The microradiographic structures of non-bead cultured pearls. GIA News from Research, Gemological Institute of America, Bangkok, Thailand, 23 pp., www.gia.edu/doc/microradiographic-structures-in-NBCP.pdf, 20 August, accessed 7 December 2019.
- Urmos, J., Sharma, S.K. & Mackenzie, R.T. 1991. Characterization of some biogenic carbonates with Raman spectroscopy. *American Mineralogist*, **76**(3–4), 641–646.
- Wanamaker, A.D. & Gillikin, D.P. 2019. Strontium, magnesium, and barium incorporation in aragonitic shells of juvenile *Arctica islandica*: Insights from temperature controlled experiments. *Chemical Geology*, **526**, 117–129, <https://doi.org/10.1016/j.chemgeo.2018.02.012>.

The Authors

Abeer Al-Alawi, Zainab Ali FGA, Zainab Rajab FGA, Fatema Albedal FGA and Dr Stefanos Karampelas

Bahrain Institute for Pearls & Gemstones (DANAT), WTC East Tower, Manama, Bahrain
Email: Stefanos.Karampelas@danat.bh

Acknowledgements

The authors thank the following personnel from the UAE's Environment Agency – Abu Dhabi for providing the study samples: Mohamed Almarzooqi (Aquaculture Section Manager), Hamad Almansoori (Aquaculture Specialist), Koshi Hamada (Technical Site Supervisor) and Ayesha Alhammadi (Technician). Special thanks to Hasan Abdulla and Ghadeer Abdali for photographs, as well as Husna Alderazi and Fatima Mohamed from DANAT for their help with data reduction.

Diamonds from the Nassau Mountains, Suriname

Renoesha Naipal, J. C. (Hanco) Zwaan, Salomon B. Kroonenberg, Leo M. Kriegsman and Paul R. D. Mason

ABSTRACT: Alluvial diamonds have been found in Suriname since the late 19th century, but to date the details of their origin remain unclear. Here we describe diamonds from Paramaka Creek (Nassau Mountains area) in the Marowijne greenstone belt, Guiana Shield, north-eastern Suriname. Thirteen samples were studied, consisting mainly of euhedral crystals with dominant octahedral and dodecahedral habits. They had colourless to brown to slightly greenish body colours, and some showed green or (less commonly) brown irradiation spots. Surface features showed evidence of late-stage resorption that occurred during their transport to the earth's surface. The studied diamonds were predominantly type IaAB, with nitrogen as both A and B aggregates. In the DiamondView most samples displayed blue and/or green luminescence and concentric growth patterns. Their mineral inclusion assemblages (forsterite and enstatite) indicate a peridotitic (possibly harzburgitic) paragenesis.

The Journal of Gemmology, 37(2), 2020, pp. 180–191, <https://doi.org/10.15506/JoG.2020.37.2.180>
© 2020 Gem-A (The Gemmological Association of Great Britain)

Since 1880, diamonds from Suriname (e.g. Figure 1) have been collected from alluvial deposits situated within the Marowijne greenstone belt. The initial finds took place in the Rosebel area, which later became part of the Rosebel Gold Mines concession (van Kooten 1954; Schönberger & de Roever 1974; Schönberger 1975; de Vletter 1998). A second occurrence was reported from the Paramaka Creek area of the Nassau Mountains (Headley 1913; see Figure 2), located about 85 km south-east of Rosebel. The creek has been worked extensively by artisanal gold miners, and in early 2018 diamonds were accidentally discovered in their tailings. There is currently no diamond mine in the area, but recently systematic diamond exploration was initiated there.

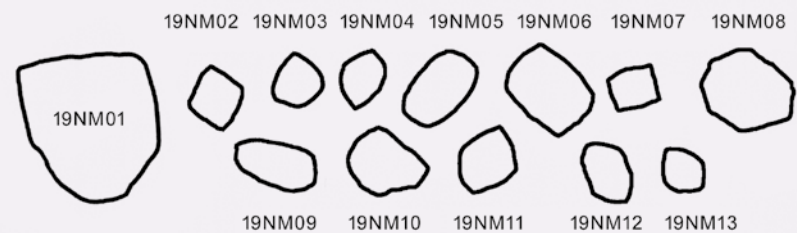
Although the geology of the Marowijne greenstone belt is fairly well known (see below), the original source of the alluvial diamonds remains unclear. Moreover, despite the rather long period that diamonds have been sourced from Suriname, they have not been previously studied in detail, and data on their mineral inclusions have also been lacking. This article characterises the external crystal morphology, mineral inclusions and other features of diamonds from Paramaka Creek in order to elucidate their source-rock environment and subsequent alluvial processes involved in their deposition.

GEOLOGY AND SOURCE OF THE DIAMONDS

The Marowijne greenstone belt of Suriname (Figure 3) forms part of a 1,500-km-long granite-greenstone terrane extending along the northern portion of the Guiana Shield from north-eastern Venezuela to Brazil's Amapá State. According to Kroonenberg *et al.* (2016), it formed during the Trans-Amazonian Orogeny (about 2,180–1,950 million years ago [Ma]) by the north-south convergence and eventual collision of the Amazonian and West African cratons. The dominant rock types are tholeiitic ocean-floor metabasalts, island arc meta-andesites and associated sediments of the Paramaka Formation, which are intruded by various types of igneous bodies (tonalite, trondhjemite and granodiorite). The area is overlain by metaturbidites of the Armina Formation and is intruded by two-mica granites. Unconformably overlying the earlier formations are epicontinental low-grade-metamorphosed fluvial sandstones and conglomerates of the Rosebel Formation. Small mafic to ultramafic plutons are scattered throughout the area, and the latter are typically metamorphosed into talc-chlorite-tremolite schists (Veenstra 1983; Naipal *et al.* 2019).



Figure 1: Thirteen diamonds (0.10–2.12 ct), typical of those recovered in Suriname since the late 19th century, were analysed for this study. The sample numbers are given in the key; see Table I for individual weights and sizes. Photo by J. C. Zwaan.



The Nassau Mountains form a horseshoe-shaped range that is mainly underlain by Paramaka Formation metabasalts (Figure 3) and associated rocks, and is covered by bauxite caps up to 500 m above sea level. Paramaka Creek (a tributary of the Marowijne [or Maroni] River) drains the mountains towards the east.

To date, gem-quality diamonds have been found in three known geological settings in the Guiana Shield: (1) in komatiitic volcanoclastic rocks (about 2,011 Ma) of the Inini greenstone belt in French Guiana (Capdevila *et al.* 1999); (2) in conglomerates of the Roraima Formation (about 1,843 Ma) in Venezuela (Santos *et al.* 2003) and Guyana (Tan *et al.* 2016), and (3) in kimberlite sills (about 730 Ma) in Guaniamo, Venezuela (Channer *et al.* 1998; Kaminsky *et al.* 2000). The source rocks of the alluvial diamond occurrences in Suriname (i.e. both the Rosebel and Paramaka Creek localities) are unknown.

MATERIALS AND METHODS

Thirteen diamonds from Paramaka Creek (Figure 1) were loaned to the authors from a collection of around 100 diamonds that were found by artisanal gold miners. They were studied at the Netherlands Gemmological Laboratory of the Naturalis Biodiversity Center, Leiden, the Netherlands. The diamonds were visually examined with a standard gemmological microscope and a Nikon Eclipse E600 POL polarising microscope to observe internal and external morphological and surface features.

The concentrations and aggregation states of nitrogen

impurities in the diamonds were determined by Fourier-transform infrared (FTIR) spectroscopy, using a Thermo Nicolet iS50 FTIR spectrometer equipped with a 5× beam condenser. Measurements were obtained for the mid-infrared range in transmission mode with a resolution of 4 cm⁻¹ and 200 scans per spectrum, using a KBr beam splitter and a DTGS KBr detector. The spectra were normalised to type IIa diamond (i.e. without any defect-induced absorption in the single-phonon region). Spectral deconvolution was performed using a spreadsheet provided by D. Fisher (De Beers Research Centre). Nitrogen abundances and type IaB aggregation states were estimated from the A- and B-defect components of the spectra using the IaA and IaB nitrogen absorption coefficients of Boyd *et al.* (1994, 1995).



Figure 2: The authors' team pans sediments from Paramaka Creek in search of diamonds. Photo by S. B. Kroonenberg.

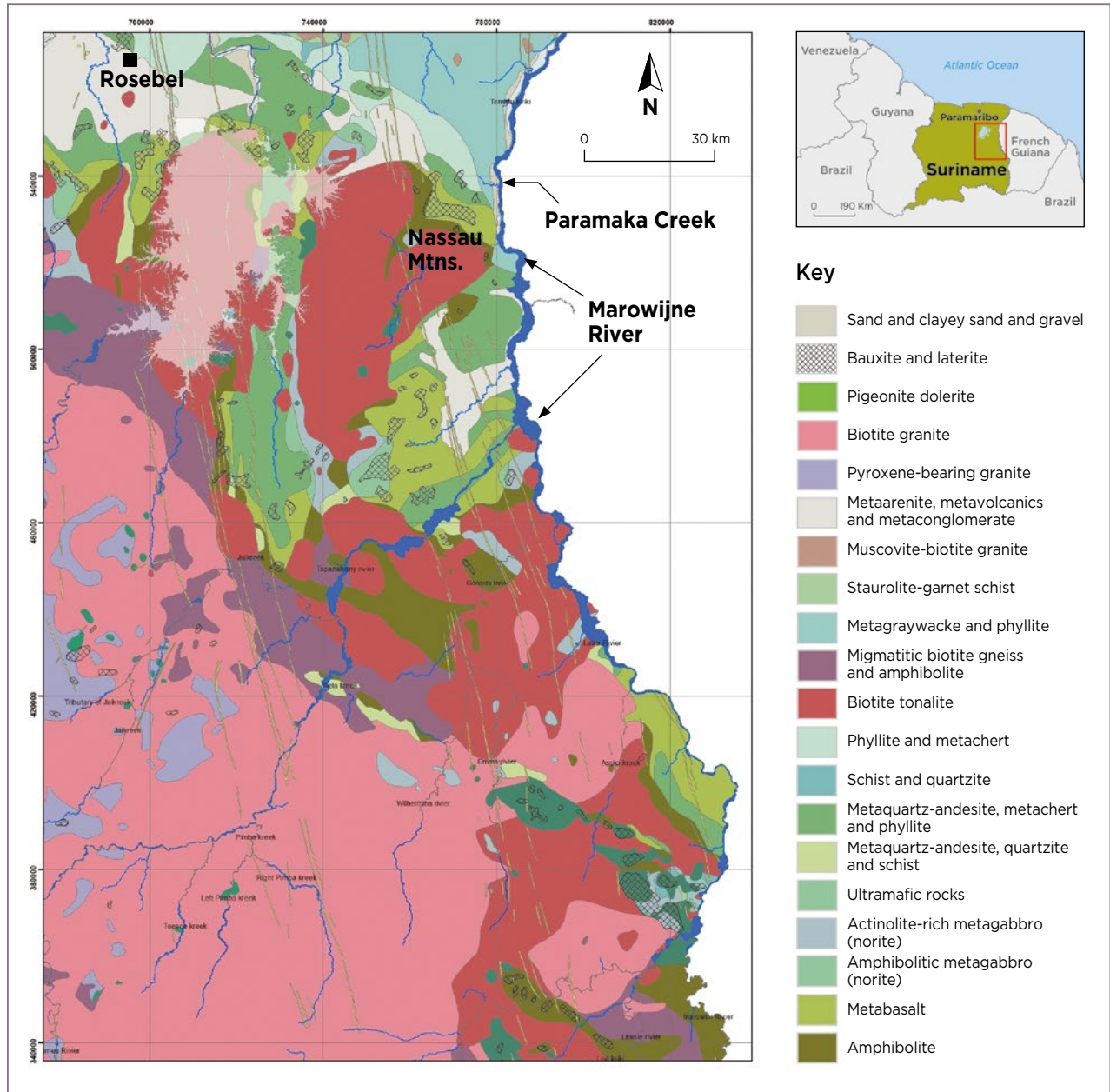


Figure 3: The geology of the Marowijne greenstone belt in north-eastern Suriname is shown on this map, together with known diamond locations in the Rosebel area and in Paramaka Creek (Nassau Mountains). Modified after Geological and Mining Service of Suriname (2018).

We observed luminescence using long-wave (365 nm) and short-wave (254 nm) UV radiation in a darkened room. Growth patterns and luminescence were further observed with a DiamondView instrument using high-intensity ultra-short-wave UV radiation (<230 nm).

Mineral inclusions were analysed using a Thermo Scientific DXR Raman microscope with 532 nm laser excitation. Raman spectra were collected in confocal mode in order to analyse individual inclusions on a micron scale (1–2 μm). Spectra were collected in the 1300–200 cm⁻¹ range to avoid the strong Raman signal at 1332 cm⁻¹ caused by the host diamond.

RESULTS

The characteristics of the diamonds are summarised in Table I and described below.

Weight, Size and Colour

The diamonds ranged from 0.10 to 0.36 ct, with the exception of one 2.12 ct crystal (Figure 1). The majority (seven) of the stones were colourless, one stone was colourless with a green ‘skin’, and two were colourless to slightly greenish. Three stones showed very pale to moderate brown colouration.

Table I: Characteristics of the studied diamonds from Paramaka Creek, Suriname.*

| Sample number | Dimensions (mm) | Weight (ct) | Crystal morphology | Colour | Surface features/radiation spots | Type | N content (ppma) | IaB (%) | UV fluorescence | | DiamondView luminescence and growth patterns | Inclusions |
|---------------|-----------------|-------------|--|---------------------------------|--|------|------------------|---------|-----------------------|------------|---|------------|
| | | | | | | | | | Long-wave | Short-wave | | |
| 19NM01 | 8.0 × 6.5 × 4.3 | 2.12 | Triangular; rounded crystal with a prominent octahedral face | Colourless | Rounded/none | IaA | 250 | 8 | Inert | Inert | Core: concentric growth zoning (alternating green and blue); rim: different domains of green angular growth zoning | None |
| 19NM02 | 3.1 × 2.3 × 2.1 | 0.14 | Octahedron | Colourless | Stepped growth/brown and green | IaA | 100 | 0 | Inert | Inert | Green octahedral graining | None |
| 19NM03 | 3.4 × 2.5 × 2.4 | 0.10 | Flattened crystal with octahedral and dodecahedral faces; trigons present | Very pale brown | Stepped growth, negative trigons/brown | IaAB | 60 | 68 | Inert | Inert | Concentric, irregular growth zoning (alternating blue and green layers) | None |
| 19NM04 | 2.9 × 2.2 × 2.1 | 0.10 | Distorted octahedron with residual dodecahedral faces | Moderate brown | Stepped growth/none | IaAB | 40 | 42 | Inert | Inert | Alternating blue and green octahedral growth layers | None |
| 19NM05 | 4.0 × 2.6 × 2.4 | 0.23 | Distorted octahedral and dodecahedral faces | Colourless, green skin | Stepped growth/green and brown | IaAB | 140 | 80 | Weak (blue) | Inert | Concentric growth zoning with a green core, a blue intermediate zone, and narrow alternating green and blue zones towards the rim | En, Fo |
| 19NM06 | 4.7 × 3.2 × 2.9 | 0.36 | Distorted octahedral and dodecahedral faces | Colourless | Stepped growth/brown | IaAB | 340 | 60 | Inert | Inert | Blue concentric growth zoning with some narrow green zones | Fo |
| 19NM07 | 3.5 × 2.8 × 2.1 | 0.10 | Distorted crystal, mainly dodecahedral faces | Colourless | Dull lustre/none | IaAB | 100 | 77 | Moderate (light blue) | Weak | Blue, with one narrow green concentric growth zone | En |
| 19NM08 | 4.4 × 3.2 × 2.4 | 0.36 | Crystal with smooth octahedral faces (including trigons) and etched dodecahedral faces | Colourless | Negative trigons/none | IaA | 310 | 13 | Inert | Inert | Blue, with one narrow green concentric growth zone near the rim and complex green zoning in one corner | None |
| 19NM09 | 4.2 × 2.2 × 1.6 | 0.12 | Elongated crystal with dodecahedral faces | Colourless to slightly greenish | None/green | IaAB | 310 | 77 | Moderate (light blue) | Weak | Blue concentric growth zoning | None |
| 19NM10 | 3.4 × 3.1 × 2.1 | 0.19 | Distorted crystal; octahedral faces dominant | Colourless to slightly greenish | None/green | IaAB | 250 | 54 | Moderate (light blue) | Weak | Blue concentric growth zoning | None |
| 19NM11 | 3.2 × 2.2 × 2.0 | 0.18 | Distorted dodecahedron with residual octahedral faces | Colourless | Stepped growth/green | IaAB | 220 | 69 | Moderate (light blue) | Weak | Octahedral zoning, showing green core, blue intermediate zone and narrow green zoning at the rim | None |
| 19NM12 | 3.3 × 2.0 × 1.8 | 0.14 | Flattened and elongated dodecahedron | Colourless | None/none | IaAB | 120 | 59 | Weak (blue) | Inert | Blue concentric zoning, with a few green layers in between | None |
| 19NM13 | 2.9 × 2.4 × 1.9 | 0.10 | Slightly distorted (flattened) octahedron | Pale brown | Irregular/green | Ila | nd | 0 | Inert | Inert | Orange-brown octahedral zoning, alternating with narrow inert layers; part of the crystal remained inert | None |

*Abbreviations: En = Enstatite, Fo = Forsterite, nd = not detected.

Morphology and Surface Features

All the studied diamonds consisted of monocrystalline octahedra and dodecahedra (some with transitional forms between these two morphological types). Two octahedra showed typical stepped growth (Figure 4a). The largest crystal was triangular shaped and rounded, and had a prominent octahedral face. It resembled a macle but did not clearly show re-entrant angles. Other crystals were distorted, flattened or elongated.

Surface features consisted of triangular etch pits with negative trigons (Figure 4b), as well as a type of etching known as ‘fine frosting’ (Tappert & Tappert 2011) with numerous micro pits (Figure 4c), giving those diamonds a dull lustre. The crystal faces were almost free of abrasions, with edges that were mostly undamaged. Only a few small surface pits of unknown origin were observed on some of the crystals. The surfaces of two diamonds (samples 19NM04 and 19NM07) showed sets of straight lines parallel to octahedral planes that are indicative of plastic deformation (Tappert & Tappert

2011). Another important surface feature was the presence of green spots (isolated or clusters), and less commonly brown ones (Figure 4d), which indicate the diamonds were exposed to alpha radiation (Tappert & Tappert 2011).

Diamond Type and Nitrogen Content

The FTIR data showed that nine of the studied diamonds were type IaAB (e.g. Figure 5a), which have both A aggregates (nitrogen pairs; band at 1282 cm^{-1}) and B aggregates (four nitrogen atoms surrounding a vacancy; band at 1175 cm^{-1}). Three of the remainder were type IaA (Figure 5b), in which nitrogen as A centres dominates. One diamond had no detectable nitrogen impurities and is thus classified as type IIa (Figure 5c; cf. Breeding & Shigley 2009). The spectra of the IaAB diamonds also showed an absorption at 3107 cm^{-1} (Figure 5a), which in natural diamonds corresponds to an atomic configuration consisting of three nitrogen atoms, a vacancy and hydrogen (VN_3H ; Goss *et al.* 2014).

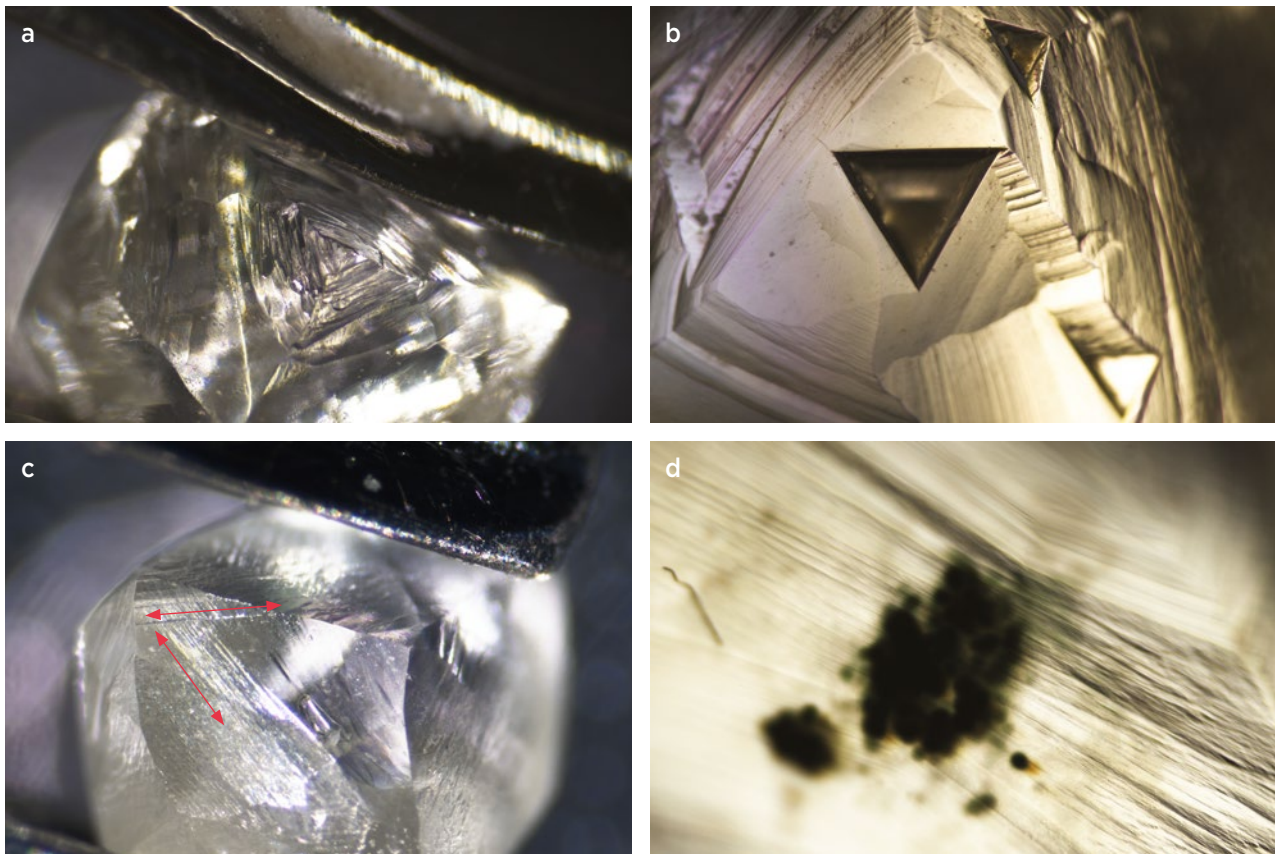


Figure 4: Various surface features are present on the investigated diamonds. (a) One octahedral face of sample 19NM11 shows partially resorbed stepped growth (image width 3.1 mm). (b) A large negative trigon occurs on a stepped octahedral face of sample 19NM03 (image width 1.4 mm). (c) Frosted dodecahedral crystal faces of sample 19NM07 show two faint sets of plastic deformation lines (see arrows; image width 3.7 mm). (d) A cluster of dark green radiation spots (including some brown areas, e.g. on the lower right) and a linear feature associated with radiation damage (left) occur on the surface of sample 19NM05 (image width 1.4 mm). Photomicrographs by R. Naipal.

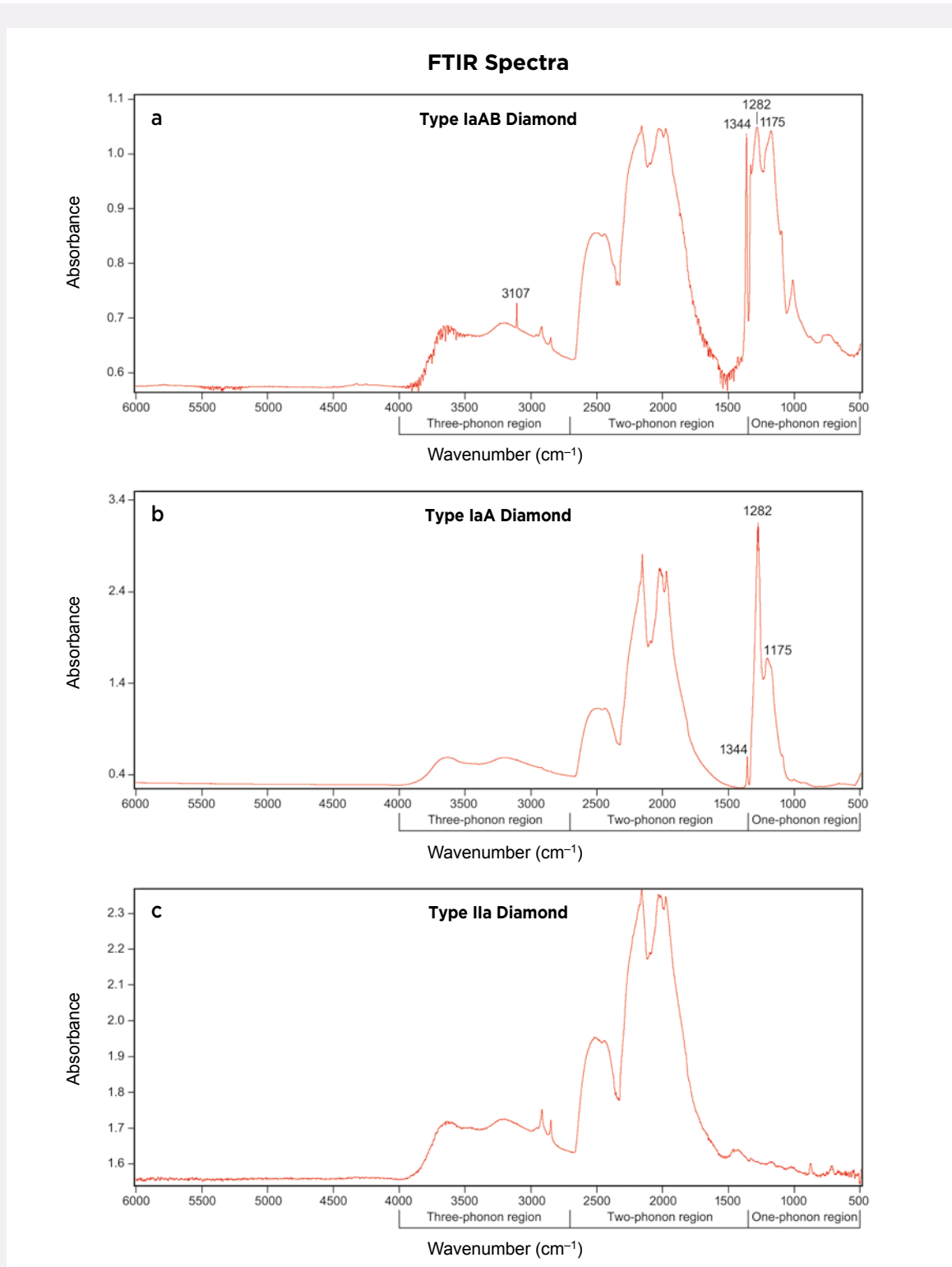


Figure 5: FTIR spectra are shown for the three different diamond types that were documented in this study. The one-phonon region (1332–400 cm⁻¹) is related to nitrogen defects, the two-phonon region (2665–1332 cm⁻¹) characterises carbon (diamond area) and the three-phonon region (4000–2665 cm⁻¹) is also intrinsic to diamond but in addition may show features of hydrogen impurities. **(a)** The spectrum of a type IaAB diamond (19NM05) displays the 1175 cm⁻¹ band of B centres, 1282 cm⁻¹ band of A centres, 1344 cm⁻¹ band of single nitrogen and 3107 cm⁻¹ band of hydrogen-related defects (VN₃H). **(b)** A type IaA diamond (19NM01) yields a spectrum in which A centres are dominant. **(c)** The type IIa diamond (19NM13) displays no detectable spectral features of nitrogen impurities. The features in the 3000–2800 cm⁻¹ region are due to traces of oil left behind on the surfaces of the crystals after cleaning.

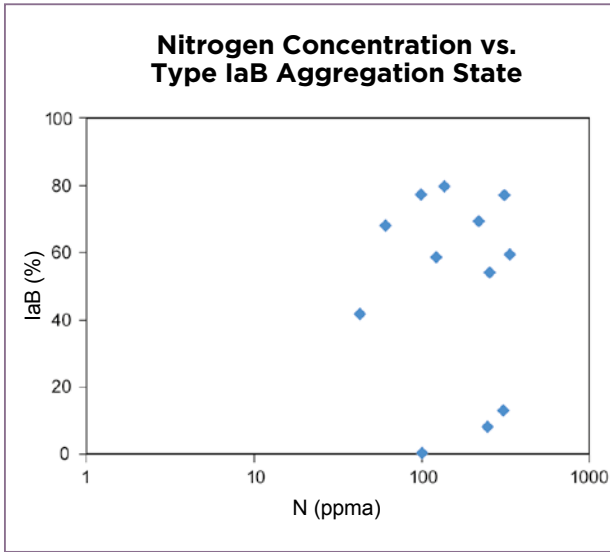


Figure 6: A plot of nitrogen concentration vs. IaB aggregation state shows that three diamonds predominantly contain A aggregates and nine diamonds contain B aggregates up to 80%.

For the single type IIa diamond (19NM13), the absence of detectable IR features in the one-phonon region indicates a nitrogen content of <5 ppm (Breeding & Shigley 2009). The spectra of most of the other diamonds had flat baselines, allowing robust fits during deconvolution, but samples 19NM03 and 19NM06, with variable baselines, gave slightly less reliable results. Overall, the nitrogen content of the 12 N-bearing diamonds ranged from 40 to 340 ppma and the nitrogen aggregation for the IaAB diamonds (expressed as the percentage of IaB content) was 42–80% (Table I; Figure 6).

Luminescence

Diamond can produce variable luminescence due to the interaction of UV radiation with impurities and imperfections in the crystal structure (e.g. Figure 7; Eaton-Magaña *et al.* 2007). Four of the diamonds showed moderate fluorescence to long-wave UV radiation (365 nm) and weak luminescence to short-wave UV (254 nm), and two diamonds showed weak fluorescence to long-wave UV and none to short-wave UV. The other seven crystals were inert (Table I).

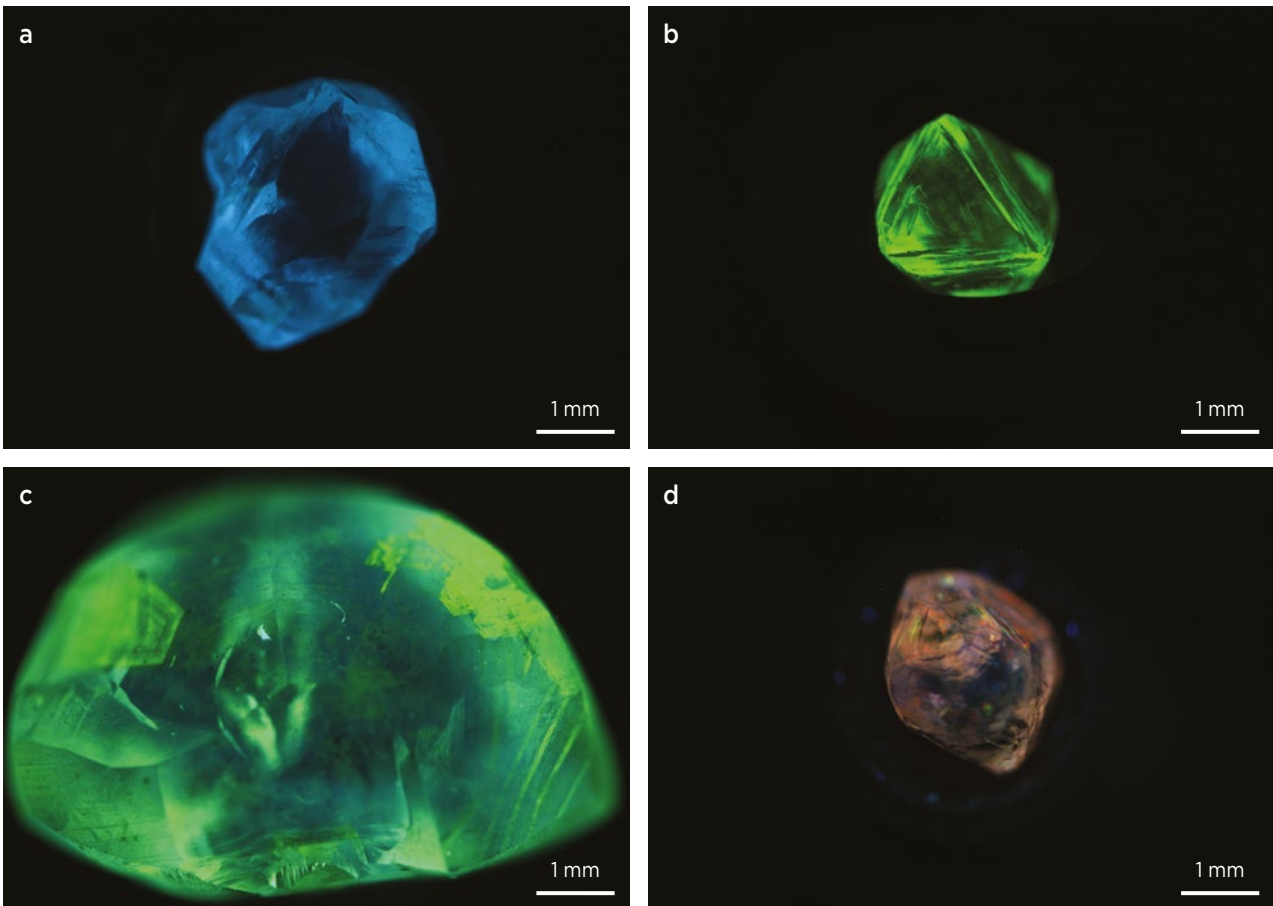


Figure 7: DiamondView images illustrate the range of reactions observed in the Suriname diamonds: (a) common blue fluorescence (19NM10); (b) green fluorescence (19NM02); (c) complex growth zoning (19NM01); and (d) orange-brown fluorescence in a type IIa diamond (19NM13). Photos by R. Naipal.

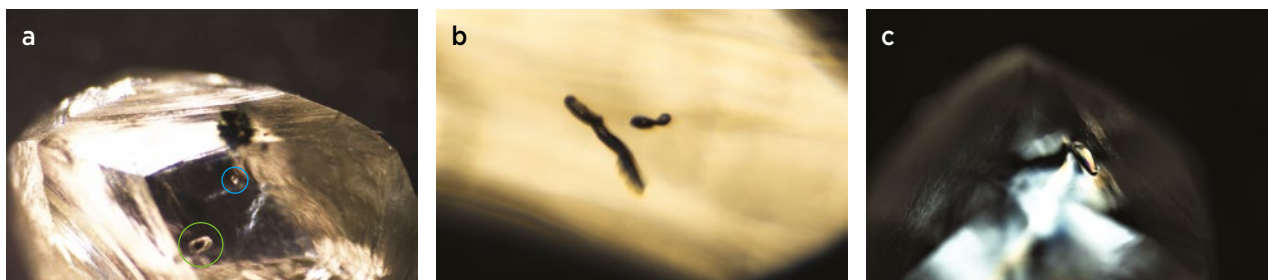


Figure 8: Mineral inclusions in the Suriname diamonds consist of enstatite and/or forsterite. (a) An elongated enstatite inclusion (green circle) coexists with a slightly rounded forsterite (blue circle) in sample 19NM05 (plane-polarised light, image width 3.7 mm). (b) Elongated forsterite inclusions are present in sample 19NM06 (plane-polarised light, image width 1.4 mm). (c) This euhedral, elongated, colourless enstatite occurs in sample 19NM07 (crossed polarisers, image width 2.8 mm). Photomicrographs by J. C. Zwaan.

Using the high-intensity short-wave UV radiation of the DiamondView, all samples fluoresced and revealed growth patterns (e.g. Figure 7). Most of the 12 type Ia diamonds showed blue fluorescence with growth patterns that commonly consisted of narrow green concentric bands. Blue luminescence (Figure 7a) in diamond is caused by nitrogen impurities in the form of N3 centres (three nitrogen atoms surrounding a vacancy). In addition, green fluorescence banding in the diamonds can be related to the H3 defect, which is caused by two nitrogen atoms separated by a vacancy (Breeding & Shigley 2009). One crystal showed overall green luminescence (Figure 7b), which could be due to dominating H3 defects or the presence of Ni-related defects (Wang *et al.* 2007). The patterns seen in the relatively large triangular rounded crystal (19NM01) indicate a complex growth history. Towards the centre, a simple concentric zonation was observed (blue-green), whereas the edges showed different domains of angular patterns (green; see Figure 7c). These structures might be related to different stages of growth.

The one type IIa diamond (19NM13; Figure 7d) fluoresced orange-brown in the DiamondView, although a part of the crystal remained inert. The orange-brown luminescence might be related to the presence of NV centres (cf. Soonthorntantikul & Wang 2016).

Mineral Inclusions

Only four of the 13 studied diamonds were found to contain inclusions, but not all of them could be identified with confidence based on Raman peak positions. Some other inclusions were positioned too deep in the crystals to obtain good Raman spectra.

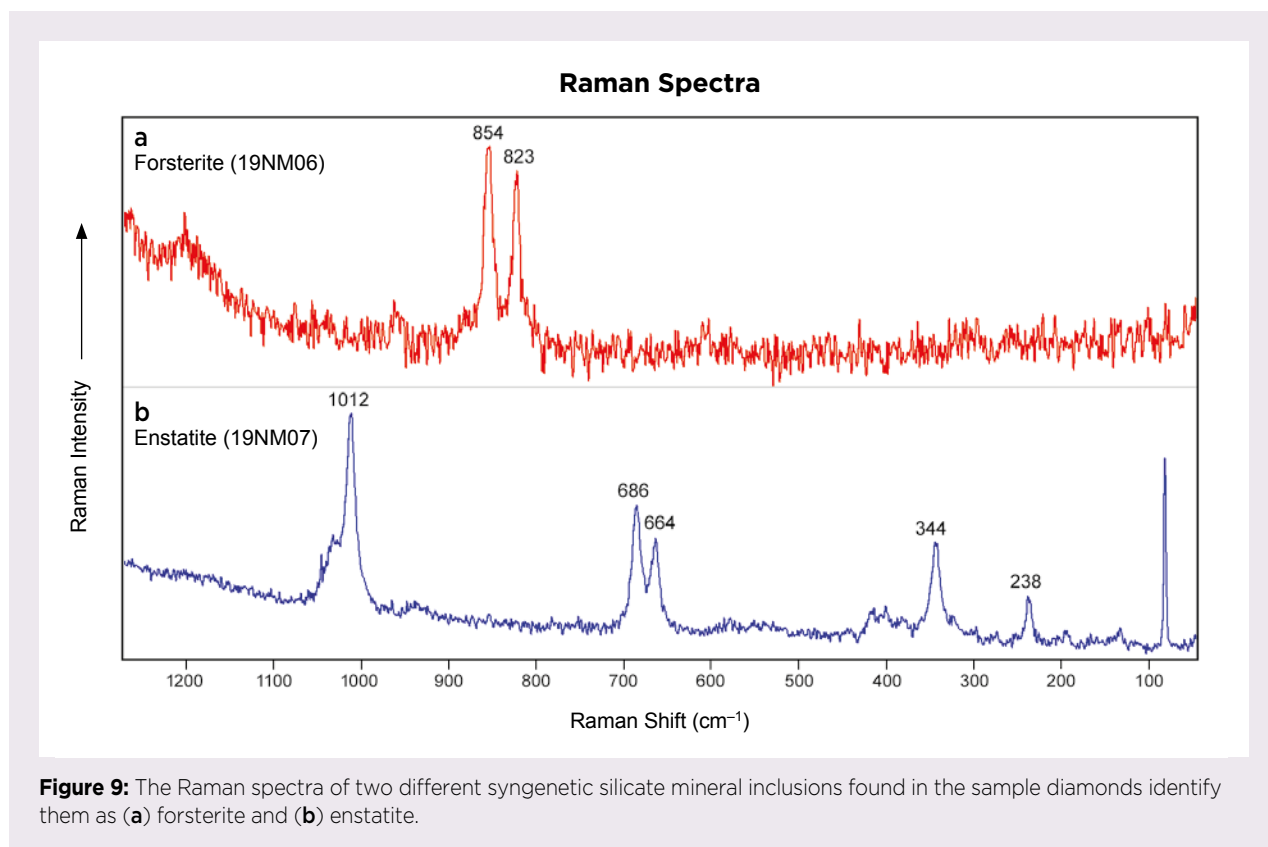
Two different silicates were found in one diamond (19NM05; Table I): a colourless, elongated enstatite and a colourless, rounded forsterite (Figure 8a). Forsterite and enstatite inclusions were also identified in diamonds 19NM06 and 19NM07, respectively (Figures 8b and 8c).

Raman analyses of the forsterite inclusions showed two prominent features at 854 and 823 cm^{-1} (Figure 9a), which are due to $\nu_1 + \nu_3$ frequencies caused by SiO_4 internal symmetric and asymmetric stretching, respectively. With the high spectral resolution of about 2 cm^{-1} , the positions of these analysed features closely corresponded to end-member forsterite (856 and 824 cm^{-1}), indicating olivine with very high forsterite composition (around Fo_{88} ; cf. Chopelas 1991). Raman analyses of the enstatite inclusions (Figure 9b) showed prominent features at 1012 (Si-O stretching), 686, 664 (Si-O bending), 344 and 238 cm^{-1} (metal-oxygen bending and stretching), which is consistent with the spectrum of orthoenstatite (currently simply called enstatite; Chopelas 1999). Since most Raman frequencies in the enstatite-ferrosilite series decrease with increasing Fe content, the measured features are consistent with an almost pure enstatite composition. By comparison, a composition of $\text{En}_{0.975}\text{Fs}_{0.025}$ reported by Huang *et al.* (2000) gave very similar Raman frequencies at 1013, 686, 663, 343 and 239 cm^{-1} .

DISCUSSION

The stepped growth seen on the crystal faces of some of the Suriname diamonds indicates that they grew layer by layer in a relatively stable environment (Robinson 1979; Tappert & Tappert 2011). The trigons or etch pits on their surfaces mainly result from resorption processes that took place during their transport to the earth's surface (e.g. in a kimberlitic melt; Tappert & Tappert 2011). The absence of abrasion and percussion marks on the diamonds does not directly relate to the distance of transport from the diamond host rock; instead, it is likely to reflect the stream-bed gradient and the stream-bed lithology (Robinson 1979).

The observed radiation spots on the diamond surfaces might have been caused by the presence of radioactive



elements, such as U and Th, in minerals adjacent to the diamonds in the alluvial environment (Tappert & Tappert 2011). Irradiation by radioactive decay causes carbon atoms to be expelled from the diamond crystal lattice within 20 μm of the surface, and the resulting vacancies form green colour centres that are present as localised spots or clusters of spots on a diamond's surface (Tappert *et al.* 2006). The green 'skin' present on three of the diamonds resulted from the same process but is probably the product of radioactive groundwater (Tappert & Tappert 2011).

The few brown spots noted on the study diamonds could have been derived from a kinetic reaction (one involving time and temperature) that affected the original green spots (Vance *et al.* 1973). Experiments have shown that green radiation spots turn brown in response to annealing at temperatures between 550 and 600°C (Vance *et al.* 1973; Eaton-Magaña & Moe 2016). As the reaction is time-related, much lower temperatures can produce the same effect over a longer period. Similar cases of green- and brown-spotted diamonds are mostly associated with long-term residence in meta-conglomerates, such as the diamonds in the U-bearing sediments of Witwatersrand, South Africa (Raal 1969); Guaniamo, Venezuela (Channer *et al.* 1998; Kaminsky *et al.* 2000); and Chapada Diamantina, Brazil (Vance *et al.* 1973; Vilela

de Carvalho *et al.* 2018). The Paramaka Creek diamonds might have undergone a similar history of reworking and deposition in the Marowijne greenstone belt sediments. The presence of brown spots suggests that the diamondiferous rocks from the Marowijne greenstone belt must have reached temperatures higher than the greenschist facies or, possibly, were subjected to long periods under greenschist facies conditions.

Source of the Diamonds

Various theories have been proposed for the source of Suriname's diamonds. Van Kooten (1954) proposed that the diamonds from Rosebel were derived from the Rosebel Formation conglomerates in the area, but he did not find any diamonds in unweathered conglomerate outcrops. In addition, Schönberger (1975) washed many samples of weathered Rosebel Formation conglomerates without finding diamonds. Schönberger and de Roever (1974) and Schönberger (1975) suggested that the Rosebel diamonds were derived from an as-yet-undiscovered primary ultramafic source in the area. This conclusion was based on the distribution of the diamonds and the presence of accompanying minerals, such as chromian spinel and fuchsite (chromian muscovite) in the alluvial sediments containing the diamonds.

Recent exploration drilling by Iamgold Corporation

at the Rosebel gold mines showed that there are several conglomerate horizons in the Rosebel Formation, so it is feasible that a conglomerate other than the outcropping one washed by Schönberger (1975) is diamondiferous. Alternatively, it is possible that Schönberger did not wash enough material to find diamonds, as conglomerates and gravels may be very low grade (e.g. only 5 ct/100 t: Jacob *et al.* 2006), requiring the processing of very large samples to assess diamond potential.

Regarding the diamonds from Paramaka Creek (Figure 10), until now there have been no published investigations of their provenance.

Therefore the original primary source of the Suriname diamonds remains unknown, and further fieldwork is needed to look for possible indicator minerals that could lead to the original host rock. However, these minerals might be challenging to find due to the extensive tropical weathering and the possibility of extended fluvial transport during sediment reworking.

The randomly oriented and (partly) euhedral mineral inclusions in the diamonds are considered to be syngenetic. The assemblage of enstatite and forsterite indicates a peridotitic source, possibly harzburgitic (Stachel & Harris 2008). Similar diamond sources have been reported from reworked sedimentary environments (e.g. Chapada Diamantina, Brazil: Tappert *et al.* 2006; Vilela de Carvalho *et al.* 2018) and from alluvial deposits derived

from weathered metakimberlites (e.g. Akwatia, Ghana: Stachel & Harris 1997; Melton *et al.* 2012). Our results for the Suriname diamonds contrast with those from Dachine in neighbouring French Guiana, which are genetically unrelated, of eclogitic origin and occur in volcanoclastic komatiite (Capdevila *et al.* 1999).

CONCLUSIONS

The majority of the diamonds analysed to date from the Marowijne greenstone belt in Suriname are colourless or light brown, sometimes with a green 'skin' or green (and less commonly brown) radiation spots on their surfaces. Few show evidence of damage due to alluvial transport. The coexistence of enstatite with forsterite as mineral inclusions indicates a peridotitic mantle origin. The aggregation state of nitrogen in most of the diamonds (type IaAB) implies that they experienced a higher temperature and/or longer residence time in the mantle than the less-common type IaA specimens. The high clarity of the diamonds and the absence of diamond indicator minerals suggest that they might have experienced extended sedimentary transport from a distal primary source. The Suriname diamonds have a different origin than those from French Guiana (i.e. eclogitic and hosted by volcanoclastic komatiite), but the primary source rock has not yet been found.



Figure 10: Paramaka Creek is an enigmatic source of diamonds, which have been recovered as a by-product of small-scale gold mining. Some of the tailings piles resulting from the gold mining are visible here in the middle and right centre. Photo by N. Sardjoe.

REFERENCES

- Boyd, S.R., Kiflawi, I. & Woods, G.S. 1994. The relationship between infrared absorption and the A defect concentration in diamond. *Philosophical Magazine B*, **69**(6), 1149–1153, <https://doi.org/10.1080/01418639408240185>.
- Boyd, S.R., Kiflawi, I. & Woods, G.S. 1995. Infrared absorption by the B nitrogen aggregate in diamond. *Philosophical Magazine B*, **72**(3), 351–361, <https://doi.org/10.1080/13642819508239089>.
- Breeding, C.M. & Shigley, J.E. 2009. The “type” classification system of diamonds and its importance in gemology. *Gems & Gemology*, **45**(2), 96–111, <https://doi.org/10.5741/gems.45.2.96>.
- Capdevila, R., Arndt, N., Letendre, J. & Sauvage, J.-F. 1999. Diamonds in volcanoclastic komatiite from French Guiana. *Nature*, **399**(6735), 456–458, <https://doi.org/10.1038/20911>.
- Channer, D.M., Cooper, R.E.C. & Kaminsky, F. 1998. The Guaniamo diamond region, Bolivar State, Venezuela: A new kimberlite province. *International Kimberlite Conference: Extended Abstracts*, Cape Town, South Africa, 144–146, <https://doi.org/10.29173/ikc2661>.
- Chopelas, A. 1991. Single crystal Raman spectra of forsterite, fayalite, and monticellite. *American Mineralogist*, **76**(7–8), 1101–1109.
- Chopelas, A. 1999. Estimates of mantle relevant Clapeyron slopes in the MgSiO₃ system from high-pressure spectroscopic data. *American Mineralogist*, **84**(3), 233–244, <https://doi.org/10.2138/am-1999-0304>.
- de Vletter, D.R. 1998. The quest for diamonds in Suriname. In: Wong, T.E., de Vletter, D.R., Krook, L., Zonneveld, J.I.S. & van Loon, A.J. (eds) *The History of Earth Sciences in Suriname*. Royal Netherlands Academy of Arts and Sciences, Netherlands Institute of Applied Geoscience TNO, Amsterdam, the Netherlands, 351–365.
- Eaton-Magaña, S.C. & Moe, K.S. 2016. Temperature effects on radiation stains in natural diamonds. *Diamond and Related Materials*, **64**, 130–142, <https://doi.org/10.1016/j.diamond.2016.02.009>.
- Eaton-Magaña, S., Post, J.E., Heaney, P.J., Walters, R.A., Breeding, C.M. & Butler, J.E. 2007. Fluorescence spectra of colored diamonds using a rapid, mobile spectrometer. *Gems & Gemology*, **43**(4), 332–351, <https://doi.org/10.5741/gems.43.4.332>.
- Geological and Mining Service of Suriname, 2018. *Geological Map of Suriname, 1:500,000*. Geologisch Mijnbouwkundige Dienst van Suriname, Paramaribo, Suriname.
- Goss, J.P., Briddon, P.R., Hill, V., Jones, R. & Rayson, M.J. 2014. Identification of the structure of the 3107 cm⁻¹ H-related defect in diamond. *Journal of Physics: Condensed Matter*, **26**(14), article 145801 (6 pp.), <https://doi.org/10.1088/0953-8984/26/14/145801>.
- Headley, D.E. 1913. Diamonds in Dutch Guiana. *Engineering and Mining Journal*, **94**(18), 888.
- Huang, E., Chen, C.H., Huang, T., Lin, E.H. & Xu, J. 2000. Raman spectroscopic characteristics of Mg-Fe-Ca pyroxenes. *American Mineralogist*, **85**(3–4), 473–479, <https://doi.org/10.2138/am-2000-0408>.
- Jacob, J., Ward, J.D., Bluck, B.J., Scholz, R.A. & Frimmel, H.E. 2006. Some observations on diamondiferous bedrock gully trapsites on Late Cainozoic, marine-cut platforms of the Sperrgebiet, Namibia. *Ore Geology Reviews*, **28**(4), 493–506, <https://doi.org/10.1016/j.oregeorev.2005.03.010>.
- Kaminsky, F.V., Zakharchenko, O.D., Griffin, W.L., Channer, D.M.D. & Khachatryan-Blinova, G.K. 2000. Diamond from the Guaniamo area, Venezuela. *Canadian Mineralogist*, **38**(6), 1347–1370, <https://doi.org/10.2113/gscanmin.38.6.1347>.
- Kroonenberg, S.B., de Roeve, E.W.F., Fraga, L.M., Reis, N.J., Faraco, T., Lafon, J.M., Cordani, U. & Wong, T.E. 2016. Paleoproterozoic evolution of the Guiana Shield in Suriname: A revised model. *Netherlands Journal of Geosciences – Geologie en Mijnbouw*, **95**(4), 491–522, <https://doi.org/10.1017/njg.2016.10>.
- Melton, G.L., McNeill, J., Stachel, T., Pearson, D.G. & Harris, J.W. 2012. Trace elements in gem diamond from Akwatia, Ghana and DeBeers Pool, South Africa. *Chemical Geology*, **314–317**, 1–8, <https://doi.org/10.1016/j.chemgeo.2012.04.025>.
- Naipal R., Kroonenberg, S.B. & Mason, P.R.D. 2019. Ultramafic rocks of the Paleoproterozoic greenstone belt in the Guiana Shield of Suriname, and their mineral potential. Proceedings of the 11th Inter Guiana Geological Conference, Paramaribo, Suriname, *Mededeling Geologisch Mijnbouwkundige Dienst van Suriname*, **29**, 143–146.
- Raal, F.A. 1969. A study of some gold mine diamonds. *American Mineralogist*, **54**(1–2), 292–296.
- Robinson, D.N. 1979. *Surface textures and other features of diamonds*. PhD thesis, University of Cape Town, South Africa, 221 pp., <http://hdl.handle.net/11427/23490>.
- Santos, J.O.S., Potter, P.E., Reis, N.J., Hartmann, L.A., Fletcher, I.R. & McNaughton, N.J. 2003. Age, source, and regional stratigraphy of the Roraima Supergroup and Roraima-like outliers in northern South America based on U-Pb geochronology. *Geological Society of America Bulletin*, **115**, 331–348, [https://doi.org/10.1130/0016-7606\(2003\)115<0331:asarso>2.0.co;2](https://doi.org/10.1130/0016-7606(2003)115<0331:asarso>2.0.co;2).

- Schönberger, H. & de Roever, E.W.F. 1974. Possible origin of diamonds in the Guiana Shield: Comment. *Geology*, **2**(10), 474–475, [https://doi.org/10.1130/0091-7613\(1974\)2%3C474:poodit%3E2.0.co;2](https://doi.org/10.1130/0091-7613(1974)2%3C474:poodit%3E2.0.co;2).
- Schönberger, J.M.H. 1975. Diamond exploration between the Suriname and Saramacca rivers (NE Suriname). *Geologisch Mijnbouwkundige Dienst van Suriname, Mededelingen*, **23**, 228–238.
- Soonthorntantikul, W. & Wang, W. 2016. Lab Notes: Natural colorless type IIa diamond with bright red fluorescence. *Gems & Gemology*, **52**(2), 189–190.
- Stachel, T. & Harris, J.W. 1997. Syngenetic inclusions in diamond from the Birim field (Ghana) – A deep peridotitic profile with a history of depletion and re-enrichment. *Contributions to Mineralogy and Petrology*, **127**(4), 336–352, <https://doi.org/10.1007/s004100050284>.
- Stachel, T. & Harris, J.W. 2008. The origin of cratonic diamonds – Constraints from mineral inclusions. *Ore Geology Reviews*, **34**(1–2), 5–32, <https://doi.org/10.1016/j.oregeorev.2007.05.002>.
- Tan, J.S., Stachel, T. & Morton, R. 2016. Diamonds from the Konawaruk River (Guyana). *GAC-MAC 2016*, Whitehorse, Yukon, Canada, 1–3 June, 95, https://gac.ca/wp-content/uploads/2018/11/2016_GAC2016_AbstractVol.pdf.
- Tappert, R. & Tappert, M.C. 2011. *Diamonds in Nature: A Guide to Rough Diamonds*. Springer-Verlag, Heidelberg, Germany, 142 pp.
- Tappert, R., Stachel, T., Harris, J., Muehlenbachs, K. & Brey, G.F. 2006. Placer diamonds from Brazil: Indicators of the composition of the earth's mantle and the distance to their kimberlitic sources. *Economic Geology*, **101**(2), 453–470, <https://doi.org/10.2113/gsecongeo.101.2.453>.
- van Kooten, C. 1954. *Eerste onderzoek op Diamant: Rosebel Sabanpassie*. Mededelingen van de Geologisch Mijnbouwkundige Dienst van Suriname, No. 11, Paramaribo, Suriname, 64 pp.
- Vance, E.R., Harris, J.W. & Milledge, H.J. 1973. Possible origins of α -damage in diamonds from kimberlite and alluvial sources. *Mineralogical Magazine*, **39**(303), 349–360, <https://doi.org/10.1180/minmag.1973.039.303.12>.
- Veenstra, E. 1983. Petrology and geochemistry of sheet Stonbroekoe, sheet 30, Suriname. *Geologisch Mijnbouwkundige Dienst van Suriname, Mededelingen*, **26**, 1–138 pp.
- Vilela de Carvalho, L.D., Schnellrath, J. & Regina de Medeiros, S. 2018. Mineral inclusions in diamonds from Chapada Diamantina, Bahia, Brazil: A Raman spectroscopic characterization. *REM: International Engineering Journal*, **71**(1), 27–35, <https://doi.org/10.1590/0370-44672016710160>.
- Wang, W., Hall, M. & Breeding, C.M. 2007. Natural type Ia diamond with green-yellow color due to Ni-related defects. *Gems & Gemology*, **43**(3), 240–243, <https://doi.org/10.5741/gems.43.3.240>.

The Authors

Renoesha Naipal

Department of Geosciences, Anton de Kom University of Suriname Leysweg 86, Paramaribo, Suriname, and Department of Earth Sciences, Utrecht University, Princetonlaan 8a, 3584 CB Utrecht, The Netherlands
Email: renoesha.naipal@uvs.edu

Dr J. C. (Hanco) Zwaan FGA

Netherlands Gemmological Laboratory and Naturalis Biodiversity Center, Darwinweg 2, 2333 CR Leiden, The Netherlands
Email: hanco.zwaan@naturalis.nl

Prof. Dr Salomon B. Kroonenberg

Department of Geosciences, Anton de Kom University of Suriname Leysweg 86, Paramaribo, Suriname, and Delft University of Technology, Stevinweg 1, 2628CN Delft, The Netherlands

Dr Leo M. Kriegsman

Department of Research & Education, Naturalis Biodiversity Center, Darwinweg 2, 2333 CR Leiden, The Netherlands, and Department of Earth Sciences, Utrecht University, Princetonlaan 8a, 3584 CB Utrecht, The Netherlands

Prof. Dr Paul R. D. Mason

Department of Earth Sciences, Utrecht University, Princetonlaan 8a, 3584 CB Utrecht, The Netherlands

Acknowledgements

The authors thank the Suriname Environmental and Mining Foundation (SEMIF), Paramaribo, Suriname, for the PhD sponsorship of author RN. We are also grateful to the owners of the diamonds for the loan of samples. We thank David Fisher of De Beers Group (De Beers UK Ltd, Maidenhead, Berkshire) for providing the decomposition spreadsheet for estimating nitrogen concentrations from FTIR spectra. We also thank Bernard Paansa and Benjamin Libby for their continued support during this research. Finally, we extend our gratitude to the Geological and Mining Department of Suriname for access to previous research.

Pink Axinite from Merelani, Tanzania: Origin of Colour and Luminescence

Maxence Vigier and Emmanuel Fritsch

ABSTRACT: Two pink axinites from Merelani, Tanzania, were characterised with standard gemmological techniques, energy-dispersive spectroscopy, and UV-Vis-NIR, Raman and luminescence spectroscopy. We compared them to three other samples from Merelani (pinkish orange, blue and near-colourless) and one brown axinite from Oisans, France. Chemical analysis revealed that the two pink axinites correspond to axinite-(Mg). UV-Vis-NIR spectroscopy revealed that the origin of the pink colouration is a large, asymmetric broad band centred at about 560 nm. Its position and shape are typical for Mn³⁺. Manganese is also present in both samples as Mn²⁺, and we surmise that natural radiation from nearby minerals converted some Mn²⁺ into Mn³⁺. The orange luminescence of the axinites (weaker under short-wave UV radiation) is related to a broad emission band at 631 nm caused by Mn²⁺, and a more unusual red luminescence is associated with features at 688 and 694 nm attributed to Cr³⁺. Raman spectroscopy showed slight variations between the different axinite species, but further research is needed to associate each axinite end member with its characteristic Raman spectrum.

The Journal of Gemmology, 37(2), 2020, pp. 192–205, <https://doi.org/10.15506/JoG.2020.37.2.192>
© 2020 Gem-A (The Gemmological Association of Great Britain)

Axinites are rarely encountered collector's stones that are most commonly brown, but may display attractive blue, yellow to orange, and (rarely) pink to purple colouration. Despite having sufficient hardness (Mohs 6–7), axinite is seldom found mounted in jewellery.

Axinite is the name of a borosilicate mineral group containing four different species (Burke 2008), and three of them have been found in gem quality:

- Axinite-(Fe): Ca₄Fe₂⁺Al₄[B₂Si₈O₃₀](OH)₂, formerly called ferro-axinite (the most common axinite species)
- Axinite-(Mg): Ca₄Mg₂⁺Al₄[B₂Si₈O₃₀](OH)₂, formerly called magnesio-axinite (e.g. Figure 1)
- Axinite-(Mn): Ca₄Mn₂⁺Al₄[B₂Si₈O₃₀](OH)₂, formerly called manganaxinite

A distinctive component of the axinite structure, which has triclinic symmetry, is the B₂Si₈O₃₀ group, in the centre of which two isolated BO₄ tetrahedra and two

Si₂O₇ groups constitute a six-membered ring, while the other cations occupy sites in octahedral coordination with oxygen.

Axinite Colours

Both Fe²⁺ and Mn²⁺ are potentially colour-inducing ions. Nevertheless, axinite-(Mn) can be nearly colourless (Laufer 2007; see also www.mindat.org/min-1459.html) because Mn²⁺ is a poor absorber of visible light. However, when Mn²⁺ is present in a larger atomic proportion than in the axinite structure (e.g. in rhodochrosite, MnCO₃), then this ion can induce colour. All iron-containing axinites (whatever the species) are brown (Faye 1972; Pohl *et al.* 1982; Wilson *et al.* 2009; see also www.mindat.org/min-1459.html). Axinite-(Mg) does not contain any colour-causing cation in its nominal chemical composition, and is thus intrinsically colourless. However, it commonly shows various colours including yellowish orange, brown to pink and purple to blue (Quinn & Breeding 2005; Wilson *et al.* 2009; Pay 2017; see also Figure 1), which are probably due to different minor- and



Figure 1: Axinite from Merelani, Tanzania, can show various colours (top), and some of the samples depicted here exhibit strong reddish orange fluorescence to long-wave UV radiation (bottom). Based on their colouration and origin, all of these stones are most likely axinite-(Mg). The largest faceted gem weighs 4.22 ct. Courtesy of Bill and Elke Vance, Vance Gems; photos by Jeff Scovil.

trace-element impurities. The fourth member of the axinite group, tinzenite—ideally $\text{Ca}_2\text{Mn}_4^2+\text{Al}_4[\text{B}_2\text{Si}_8\text{O}_{30}](\text{OH})_2$ —contains less than 3 Ca per formula unit due to substitution of Ca^{2+} by Mn^{2+} . It appears to be intrinsically yellow to orange (depending on sample thickness), and this colour is presumably induced by Mn^{2+} , which in some cases may colour minerals orange (as in serandite or spessartine).

'Blue' axinite is known to contain vanadium (Jobbins *et al.* 1975), which Schmetzer (1982) related to the blue colouration for the first time, with an absorption band near 575 nm. More recent work clearly demonstrates that blue axinite is coloured by V^{3+} (Arlabosse *et al.* 2008), which induces a broad band at about 592 or 597 nm (Williams *et al.* 2014). This feature causes transmission in the blue region when viewed perpendicular to the flat Tanzanian crystals. A similar absorption feature has been documented in axinite-(Mg) from Merelani, Tanzania (<http://minerals.gps.caltech.edu/FILES/Visible/Axinite/Index.html>). The exact position of the absorption maximum depends on crystal orientation (axinite is biaxial), but overall the colour appears blue to blue-violet. Fritz *et al.* (2007) noted that blue zones in axinite-(Fe) from Pakistan showed an absorption maximum in the 580 nm range, but they did not analyse for vanadium.

A noticeable colour change is sometimes encountered in axinite (e.g. Lauf 2007; Williams *et al.* 2014), appearing blue-grey in fluorescent light or daylight, and purple in incandescent light. To date, this effect has been noticed only in some axinite-(Mg) and axinite-(Mn) specimens from Tanzania.

Axinite Pleochroism and Optic Character

Axinite is commonly described as being pleochroic (Gribble & Hall 1992; Association Française de Gemmologie 2013; see also [http://webmineral.com/data/Axinite-\(Mg\).shtml](http://webmineral.com/data/Axinite-(Mg).shtml)). Pleochroism in Tanzanian axinite was mentioned for the first time by Jobbins *et al.* (1975). The pleochroism ranged from pale blue to violet to grey, and similar colouration was also noted decades later in various Tanzanian axinites (Jang-Green *et al.* 2007; Arlabosse *et al.* 2008; Williams *et al.* 2014), as well as pale yellow to green pleochroism (Milton *et al.* 1953).

Mineralogy textbooks mention axinite as being biaxial positive or negative. However, the optic character is rarely mentioned in gemmological journals. Jobbins *et al.* (1975) observed that Tanzanian axinite is biaxial positive in contrast to most axinites, which are biaxial negative. The book *Gemmes* (Association Française de Gemmologie 2013) indicates that axinite is biaxial negative, except for axinite-(Mg).

Axinite Luminescence

The fluorescence of axinite-(Mg) from Tanzania has been described as a distinct orange-red to long-wave UV radiation (365 nm) and a duller red under short-wave UV (254 nm; Jobbins *et al.* 1975). Similar descriptions of the luminescence for axinite-(Mg) or axinite-(Mn) are noted in the literature (Jang-Green *et al.* 2007; Lauf 2007; Arlabosse *et al.* 2008; Jaszczak & Trinchillo 2013; Pay 2017). By contrast, axinite-(Fe) is inert, which is not surprising since Fe often quenches luminescence (Fritsch & Waychunas 1994).

This Study

The present study investigates the origin of colour and luminescence in two dominantly pale pink axinites from Merelani, Tanzania, and compares their properties to those of axinite showing other colours. In addition to the two gems of interest, three of the other samples also came from Merelani, which has produced both axinite-(Mg) and axinite-(Mn) in gem quality.

Merelani is a famous mineral deposit located in north-east Tanzania, and is best known for its tanzanite and tsavorite (e.g. Wilson *et al.* 2009). The deposit occurs in the Neoproterozoic Mozambique Belt, an area with an extensive geologic history and hosting a variety of gem and mineral deposits (Malisa & Muhongo 1990; Malisa 2003, 2005; Olivier 2006; Feneyrol 2012; Harris *et al.* 2014). The Merelani area is underlain by metacarbonate and metasilicate rocks such as marble and graphite-bearing gneiss, which were affected by greenschist-facies retrograde metamorphism. The axinite there is commonly associated with an assemblage consisting of zoisite (tanzanite), grossular (tsavorite), tremolite, diopside, K-feldspar, muscovite, chlorite, prehnite and zircon.

MATERIALS AND METHODS

The six axinites studied for this report are listed in Table I. The two rare pink axinite cabochons (samples 2999 and 3000) were obtained through Dudley Blauwet. For comparison, two axinite crystals from Merelani (3356 and 3357) were acquired from Joyce van Dronkelaar-Kessy, and a faceted axinite (3355) from this locality was provided by Denis Gravier. In addition, we included a brown axinite (2290a) from Oisans, France, from the personal collection of author EF. All samples were studied in the form that they were originally received except for sample 2290a, which was polished to obtain two parallel windows.

Standard gemmological measurements were recorded for all six samples. RI and optic sign were obtained using an A. Krüss Optronic ER604 refractometer (resolution of 0.01).

Table I: Characteristics of the six axinite samples.

| Sample no. | Locality | Dimensions (mm) | Weight (g) | Sample type | Colour | Photo* |
|------------|--------------------|-------------------|----------------|-------------------------|---|---|
| 2290a | Oisans, France | 10.4 × 8.3 × 2.5 | 0.48 | Parallel-polished rough | Brown |  |
| 2999 | Merelani, Tanzania | 19.8 × 6.0 × 4.8 | 1.11 (5.55 ct) | Cabochon | Bicoloured purplish pink and orangey pink; weak cat's eye |  |
| 3000 | Merelani, Tanzania | 19.2 × 10.6 × 3.4 | 1.18 (5.90 ct) | Cabochon | Pink |  |
| 3355 | Merelani, Tanzania | 4.5 × 3.7 × 2.5 | 0.06 (0.30 ct) | Rectangular cushion | Pinkish orange |  |
| 3356 | Merelani, Tanzania | 26.5 × 22.3 × 2.7 | 4.09 | Flat crystal | Blue |  |
| 3357 | Merelani, Tanzania | 26.0 × 14.7 × 4.9 | 3.29 | Flat crystal | Near-colourless |  |

* Photos by M. Vigier (2290a, 3000, 3356 and 3357) and Orasa Weldon (2999 and 3355).

Hydrostatic SG was measured with a Mettler-Toledo XS104 balance, using a semi-automated system. Reaction to UV radiation was observed with a Vilber-Lourmat VL-215.LC UV lamp, which includes two 15 W UV tubes (long- and short-wave) that are approximately 30 cm long. Observations were done at a fixed distance of 7 cm from the lamp, in a darkened room, against an inert black background. Internal features and pleochroism were observed with a Leica MZ6 binocular microscope with Nossigem gemmological observation attachments, including polarising filters.

Quantitative chemical analyses were obtained for all samples with a JEOL 5800 LV scanning electron microscope (SEM) equipped with a Princeton Gamma Tech

(PGT) energy-dispersive spectrometer (EDS). The instrument featured an IMIX-PTS detector, which includes a 'high-resolution' (115 eV) Ge crystal and an ultra-thin polymer window that, under ideal conditions, can be used to detect elements as light as boron (if present as a major component of the material). The SEM was operated using a beam accelerating potential of 15 kV and a 0.5 nA current, with a 37° take-off angle to the detector. The working distance between the bottom of the column and the sample surface was 15 mm. Standards used were either pure elements or simple compounds. The data were processed using PGT software incorporating a Phi-Rho-Z correction. Oxygen was calculated from the EDS spectrum instead of from stoichiometry. Analytical

precision is estimated at 1–2% for samples that have a perfectly polished, flat surface perpendicular to the beam, which was not the case for most of the stones in this study.

Raman spectroscopy was performed on all samples with a Bruker MultiRAM Fourier-transform Raman spectrometer, equipped with an Nd:YAG laser at 1064 nm. The laser power was nominally 300 mW and the resolution was 4 cm⁻¹. Fifty spectra were accumulated per measurement. To obtain a better-quality Raman spectrum of sample 2290a, we used a Horiba Jobin Yvon T64000 dispersive Raman spectrometer equipped with a 514 nm Ar⁺ laser (resolution of 4 cm⁻¹).

Ultraviolet-visible-near infrared (UV-Vis-NIR) absorption spectra were collected from all samples with a Magilabs GemmoSphere spectrometer, in the spectral range of 365–1000 nm with a sampling interval of 1.3 nm;

only results for the approximately visible range are given in this article. The sample was placed at the bottom centre of an integrating sphere. This setup does not impose the rectilinear pathway of light from lamp to detector (as in standard spectrometers), and thus it analyses all light going through the sample. In addition, any potential luminescence that was excited by visible light in the gem was collected by the instrumentation.

Photoluminescence emission and excitation spectra were obtained for all samples using a Fluorolog-3 instrument from Horiba Jobin Yvon in conjunction with FluorEssence software. A Synapse CCD detector was coupled with an iHR320 spectrometer. Both excitation and emission measurements had a resolution down to 1 nm; enhanced resolution below 1 nm was obtained by juxtaposing several scans to cover a given spectral domain in several sections.

RESULTS

Standard Gemmological Data

The results of RI, optic character and SG measurements are presented in Table II. Because of the difficulties imposed by the shape or surface conditions of the samples, only average RI values (i.e. of the lowest and highest measurements) are reported. However, RI data are not reported for sample 2999 because it was not possible to obtain consistent measurements due to its shape and polish. The optic character of most of our samples was biaxial negative, except for two biaxial positive samples (both of which were axinite-(Mg), as specified below).

All of the axinites displayed pleochroism when observed with polarisers. For thin or pale samples, colour perception

was enhanced by looking down the long direction of the crystals (i.e. longer optical path length). The pleochroic colours are shown in Figure 2 and summarised as follows:

- 2290a and 3356: blue, purple and brown (e.g. Figure 2a)
- 2999 and 3000: pale blue, pink and nearly colourless (e.g. Figure 2b)
- 3355 and 3357: pale blue, purple and yellow (e.g. Figure 2c)

In summary, the pleochroic colours are rather similar from one sample to another, varying mostly in intensity.

UV fluorescence reactions of our samples are described in Table II and illustrated in Figure 3. With the exception

Table II: Standard gemmological properties of the six axinites.

| Sample no. | Average RI | Optic character* | SG | UV luminescence | |
|------------|------------|------------------|------|------------------|----------------------------|
| | | | | Short-wave | Long-wave |
| 2290a | 1.68 | B- | 3.24 | Inert | Inert |
| 2999 | — | — | 3.19 | Weak orange-red | Intense orange |
| 3000 | 1.66 | B+ | 3.15 | Weak orange-red | Intense orange |
| 3355 | 1.68 | B+ | 3.10 | Weak orange-red | Intense orange |
| 3356 | 1.67 | B- | 3.20 | Weak orange-red | Intense orange |
| 3357 | 1.67 | B- | 3.21 | Very weak purple | Moderate orange and purple |

*Abbreviations: B- = biaxial negative, B+ = biaxial positive.

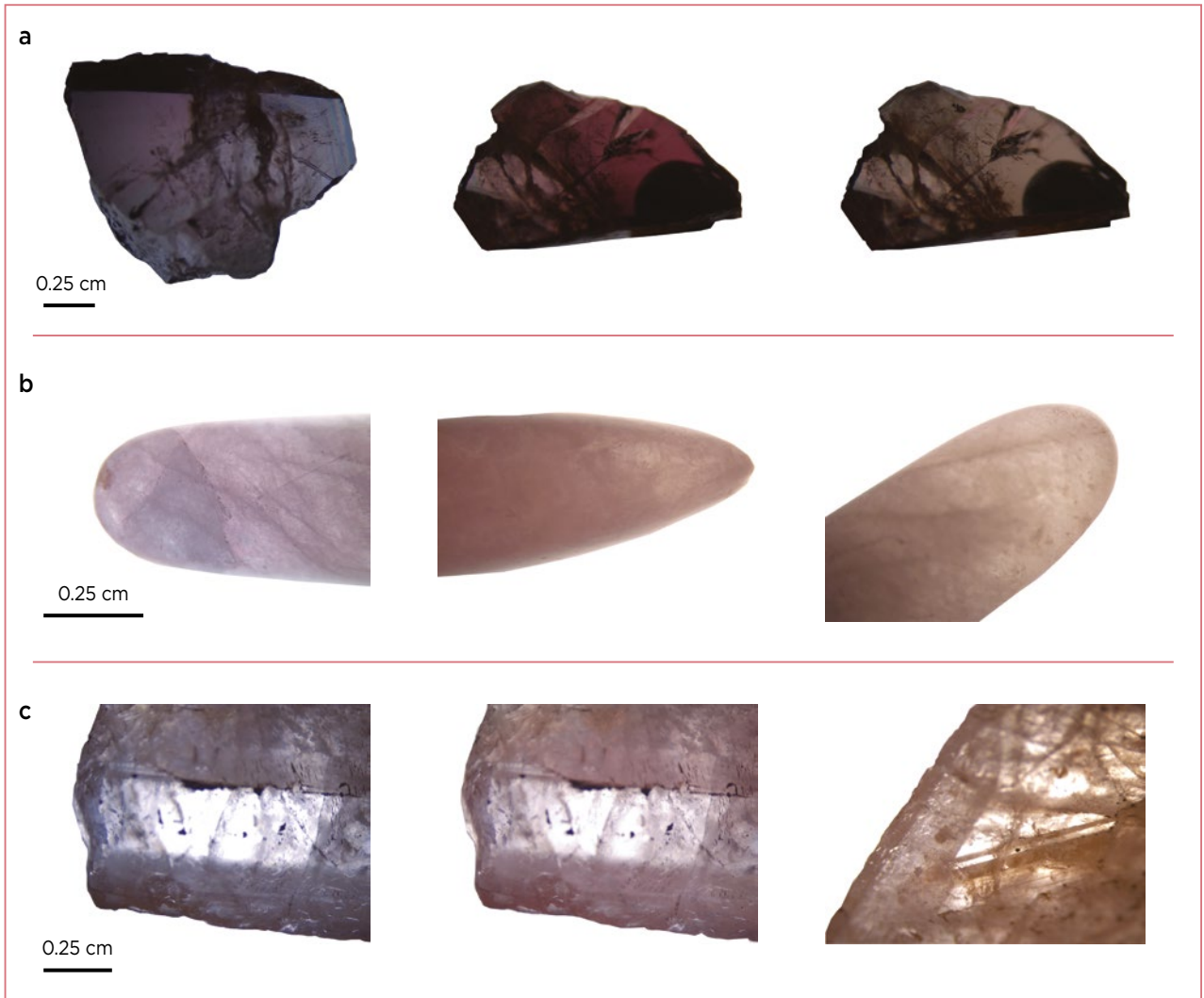


Figure 2: Pleochroism (here described in each photo from left to right) is shown for three representative samples from this study: **(a)** axinite-(Fe) sample 2290a, in blue, purple and brown; **(b)** axinite-(Mg) sample 2999, in pale blue, pink and nearly colourless; and **(c)** axinite-(Mn) sample 3357, in pale blue, purple and yellow. Photomicrographs by M. Vigier.

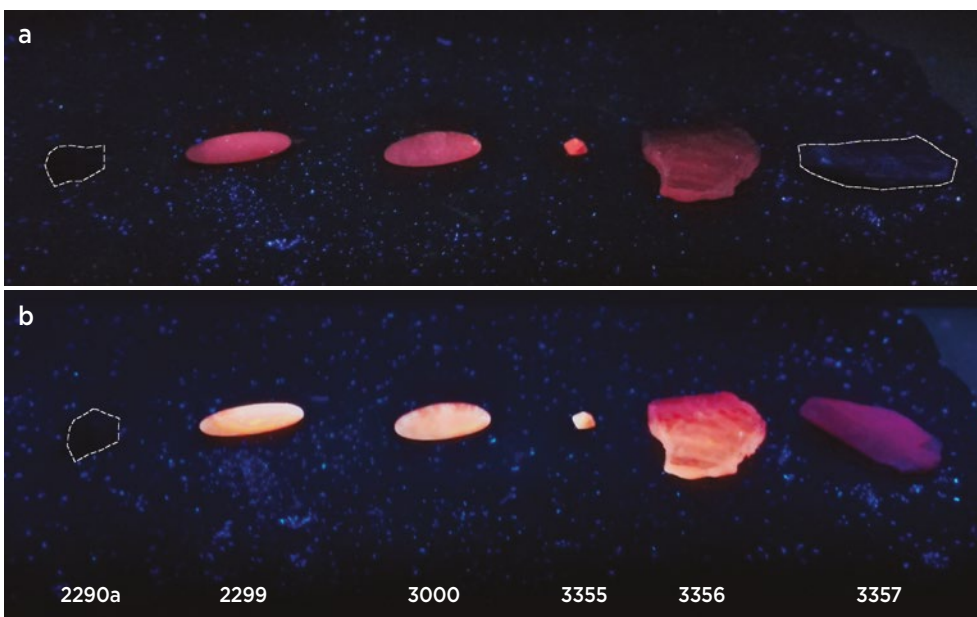


Figure 3: The six axinite samples are shown here in **(a)** short-wave and **(b)** long-wave UV radiation. Those showing very weak or no fluorescence are outlined. See Table I for sample weights. Photos by M. Vigier.



Figure 4: Axinite-(Mg) sample 2999 displays a weak cat's-eye effect, as well as colouration that ranges from orangey pink to purplish pink. The stone weighs 5.55 ct and is cut as a double cabochon. Photo by Orasa Weldon.

of the brown sample (which was inert), the gems emitted mostly orange fluorescence, sometimes with a touch of red. The emission was weaker to short-wave UV, as is the case for the luminescence of many gems. For sample 3356, the crystal termination showed distinctly redder fluorescence than the rest of the stone. Sample 3357 displayed a weak purple luminescence.

Sample 2999 was bicoloured (purplish pink and orangey pink) and also showed weak chatoyancy, as illustrated in Figure 4. Magnification revealed that the cat's-eye effect was caused by reflections (sometimes iridescent) from many small, parallel fractures (possibly cleavages; Figure 5). The somewhat indistinct cat's-eye was directionally aligned along the length of the stone, indicating that the cabochon's elongate high-domed shape mainly controlled the distribution of the chatoyancy. The gem also contained a number of partially healed fissures consisting of fluid inclusions.

Chemical Composition

As axinite is a mineral group, it was desirable to determine which species of axinite our samples represented. For that purpose, SEM-EDS chemical analyses were compared to our Raman spectroscopy data (see below). Chemical analyses of the six samples are presented in Table III, and comparisons with chemical data taken from the literature for each of the three axinite species are available in the online data depository on *The Journal's* website.

We looked for V and Cr with our instrumentation but did not detect either element (detection limits were high, at around 0.1% wt. %). Analysis of sample 3000 gave a total of only about 85%, and a carefully executed second round of analyses gave a similar low total, for which we have no explanation.

Two of the specimens approached end-member compositions—axinite-(Mg) sample 3000 and axinite-(Mn) sample 3356—whereas the other four were of intermediate composition (Figure 6). The bicoloured cabochon (2999) and the faceted stone (3355) were found to be



Figure 5: The cabochon in Figure 4 contains numerous tiny reflective fractures in a fairly consistent orientation that are responsible for its weak chatoyancy. Photomicrograph by Brendan M. Laurs; image width 1.0 mm.

axinite-(Mg) with significant Mn contents, whereas sample 3357 was axinite-(Mn). The brown sample 2290a was axinite-(Fe).

Raman Scattering

The Raman spectra of the six axinites were similar in general shape, as expected because of their common structure. Nevertheless, details of the band positions varied slightly according to the specific species (e.g. Figure 7). For example, the peak at 302 cm^{-1} in axinite-(Mg) was found at 308 cm^{-1} in axinite-(Fe), and the feature at 493 cm^{-1} in axinite-(Mg) moved to 486 cm^{-1} in axinite-(Fe). These were reproducible, measurable differences (which could therefore help with species identification). Although crystallographic orientation was not taken into account for these spectra, it would only affect the peak intensities and not peak positions, as is the case for vibrational spectroscopy.

Visible-range Absorption Spectroscopy

The main goal of this investigation was to determine the origin of the pink to purple colour in axinite. Figure 8 compares the absorption spectra obtained from the two pink axinites. The spectra were obtained perpendicular to the base of each cabochon, and not in a specific crystallographic orientation. However, both the peak positions and intensities may change with orientation, as is the case for electronic transitions. Nevertheless, based on the polarised spectra given for axinite-(Mg) from Merelani at <http://minerals.caltech.edu/FILES/Visible/Axinite/Index.html>, it appears that such changes are rather small.

The pink colouration is related to a broad, asymmetric band with an apparent maximum at about 560 nm

Table III: Chemical composition by SEM-EDS of the six axinite samples.*

| Sample | Axinite-(Fe) | Axinite-(Mg) | Axinite-(Mg) | Axinite-(Mg) | Axinite-(Mn) | Axinite-(Mn) |
|------------------------------------|--------------|--------------------------------|--------------|----------------|--------------|-----------------|
| Number | 2290a | 2999 | 3000 | 3355 | 3356 | 3357 |
| Colour | Brown | Purplish pink and orangey pink | Pink | Pinkish orange | Blue | Near-colourless |
| Locality | France | Tanzania | Tanzania | Tanzania | Tanzania | Tanzania |
| Oxides (wt.%) | | | | | | |
| SiO ₂ | 42.34 | 43.13 | 39.60 | 45.47 | 42.66 | 41.82 |
| Al ₂ O ₃ | 17.01 | 18.01 | 16.19 | 18.37 | 17.33 | 16.76 |
| FeO | 6.94 | 0.10 | 0.11 | nd | 0.08 | 1.84 |
| MgO | 1.56 | 4.62 | 6.82 | 4.36 | 0.55 | 2.27 |
| MnO | 2.16 | 4.14 | 0.19 | 4.86 | 10.28 | 6.00 |
| CaO | 19.37 | 19.97 | 14.99 | 21.22 | 19.32 | 20.17 |
| B ₂ O ₃ calc | 6.02 | 6.21 | 5.56 | 6.49 | 6.05 | 6.00 |
| H ₂ O calc | 1.56 | 1.61 | 1.44 | 1.68 | 1.57 | 1.55 |
| Total | 96.96 | 97.78 | 84.90 | 102.45 | 97.84 | 96.41 |
| Cations per 32 (O, OH) | | | | | | |
| Si | 8.150 | 8.052 | 8.256 | 8.122 | 8.168 | 8.082 |
| B | 2.000 | 2.000 | 2.000 | 2.000 | 2.000 | 2.000 |
| Al | 3.858 | 3.962 | 3.978 | 3.866 | 3.910 | 3.818 |
| Fe tot | 1.118 | 0.016 | 0.020 | nd | 0.012 | 0.298 |
| Mg | 0.448 | 1.286 | 2.120 | 1.160 | 0.156 | 0.654 |
| Mn | 0.352 | 0.654 | 0.034 | 0.736 | 1.668 | 0.982 |
| Ca | 3.994 | 3.994 | 3.348 | 4.060 | 3.964 | 4.176 |
| OH | 2.000 | 2.000 | 2.000 | 2.000 | 2.000 | 2.000 |
| Total cations (excluding OH) | 19.920 | 19.966 | 19.754 | 19.946 | 19.878 | 20.010 |

*Abbreviation: nd = not detected.

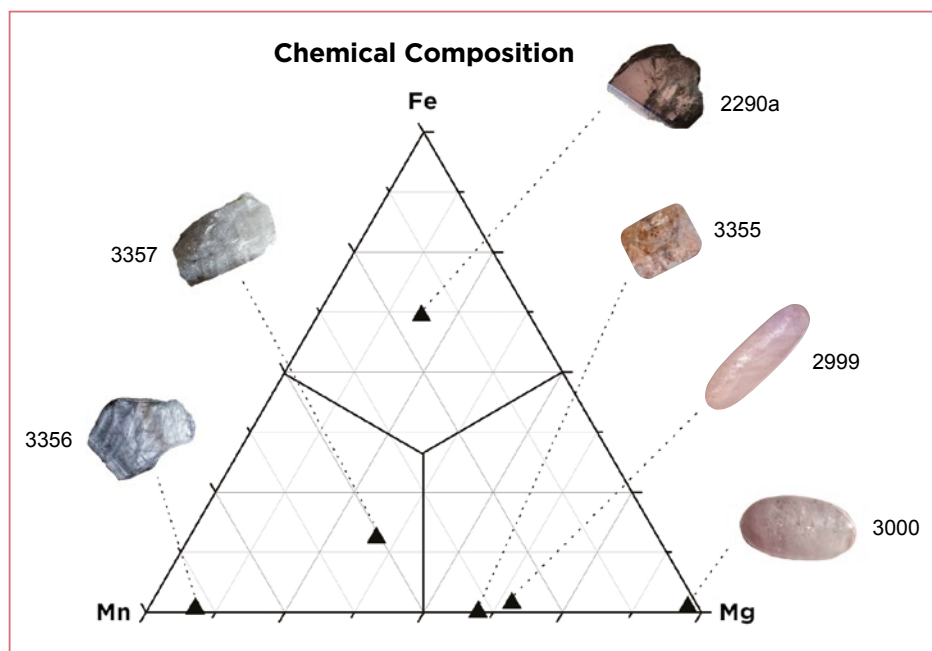


Figure 6: Chemical compositions (molecular proportions) of the six axinite samples are plotted in terms of the three end members axinite-(Fe), axinite-(Mn) and axinite-(Mg).

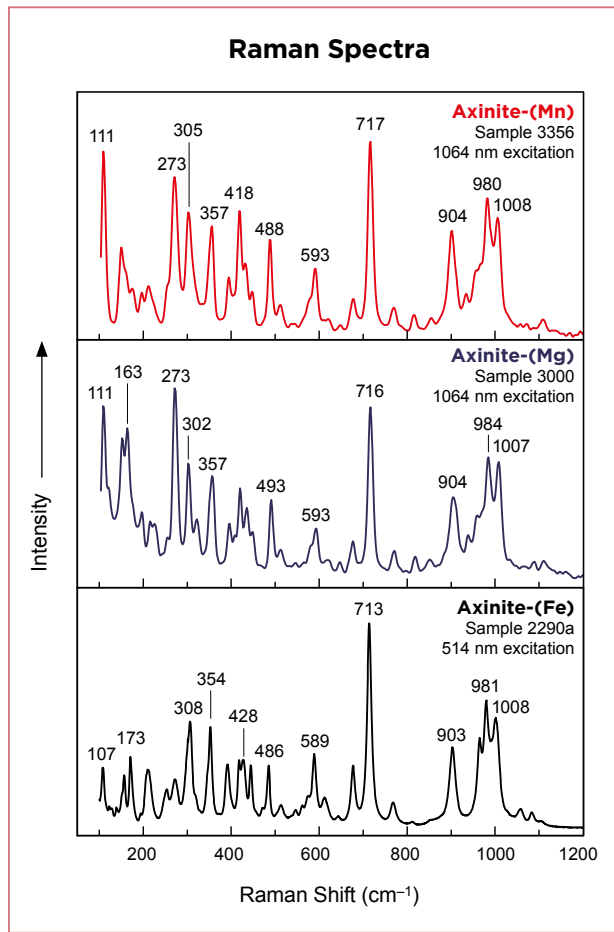


Figure 7: Raman spectra are shown for three samples that are most representative of axinite-(Mn), axinite-(Mg) and axinite-(Fe).

(again, see Figure 8). According to this band position, the ‘pink’ colour is actually a light purple. The band maximum being positioned higher than 550 nm favours a transmission window in the blue, thus inducing purple rather than pink. In sample 2999, a band at about 508 nm is present as well, absorbing green and blue, thus leading to a yellower hue that shifts the pink colour towards orangey pink. When the 508 nm peak is smaller than the one at 560 nm, purplish pink is seen.

Other features include a sharp peak at 412 nm with a shoulder at about 420 nm. These, and the broad band at 508 nm mentioned above, are well-known Mn^{2+} features, which should be accompanied by two weak, broad bands at higher wavelength, not clearly seen here (Burns 1993). Similar features would be expected to colour yellow to orange tinzenite, which is richer in Mn^{2+} . A small sharp feature recorded at 694 nm—appearing as a negative peak with the type of spectrometer used—is also encountered most notably in ruby. It is likely the result of Cr^{3+} emission (see below).

Figure 9 compares the absorption spectra of the pink axinites to those of the non-pink samples. The well-documented band at about 583 nm (depending on orientation) that is due to V^{3+} induced a pale blue-violet colour component, even though vanadium was below the detection limit of our SEM-EDS instrumentation (consistent with Arlabosse *et al.* 2008, although they detected approximately 0.1 wt. % V_2O_3 using long count times). According

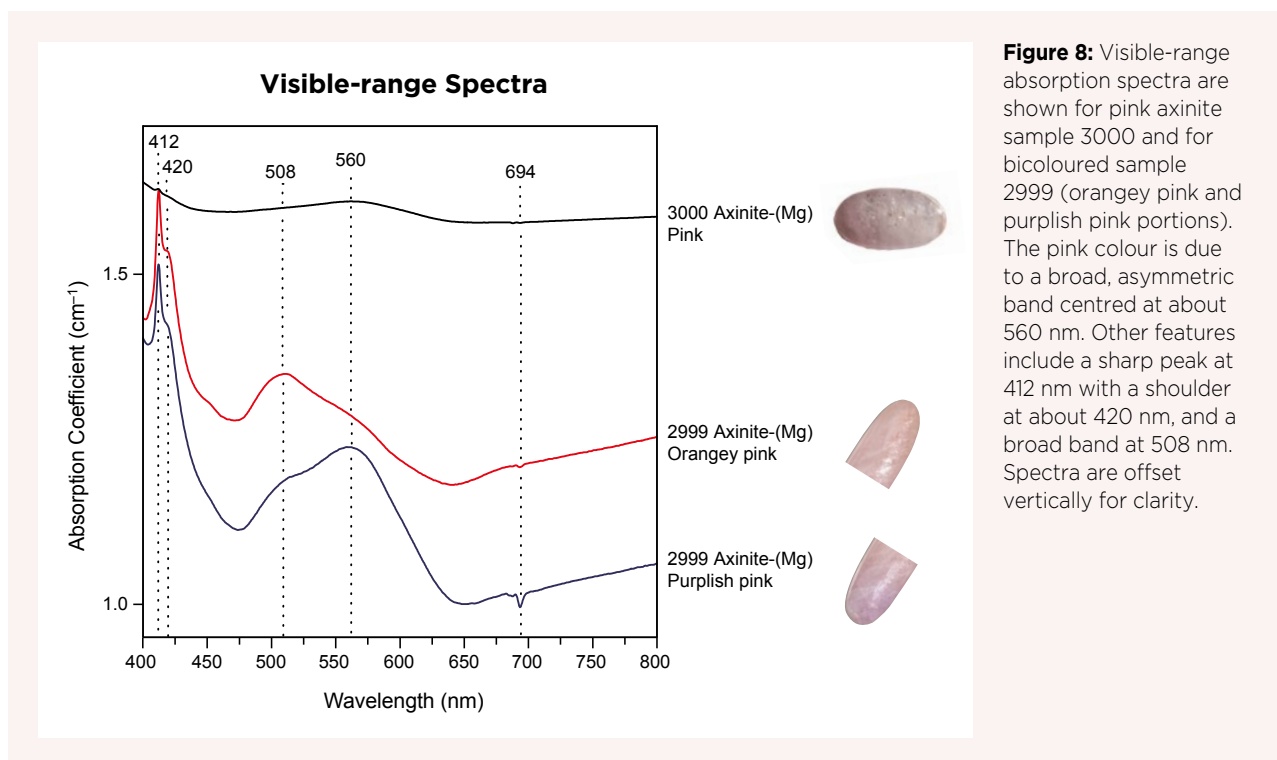


Figure 8: Visible-range absorption spectra are shown for pink axinite sample 3000 and for bicoloured sample 2999 (orangey pink and purplish pink portions). The pink colour is due to a broad, asymmetric band centred at about 560 nm. Other features include a sharp peak at 412 nm with a shoulder at about 420 nm, and a broad band at 508 nm. Spectra are offset vertically for clarity.

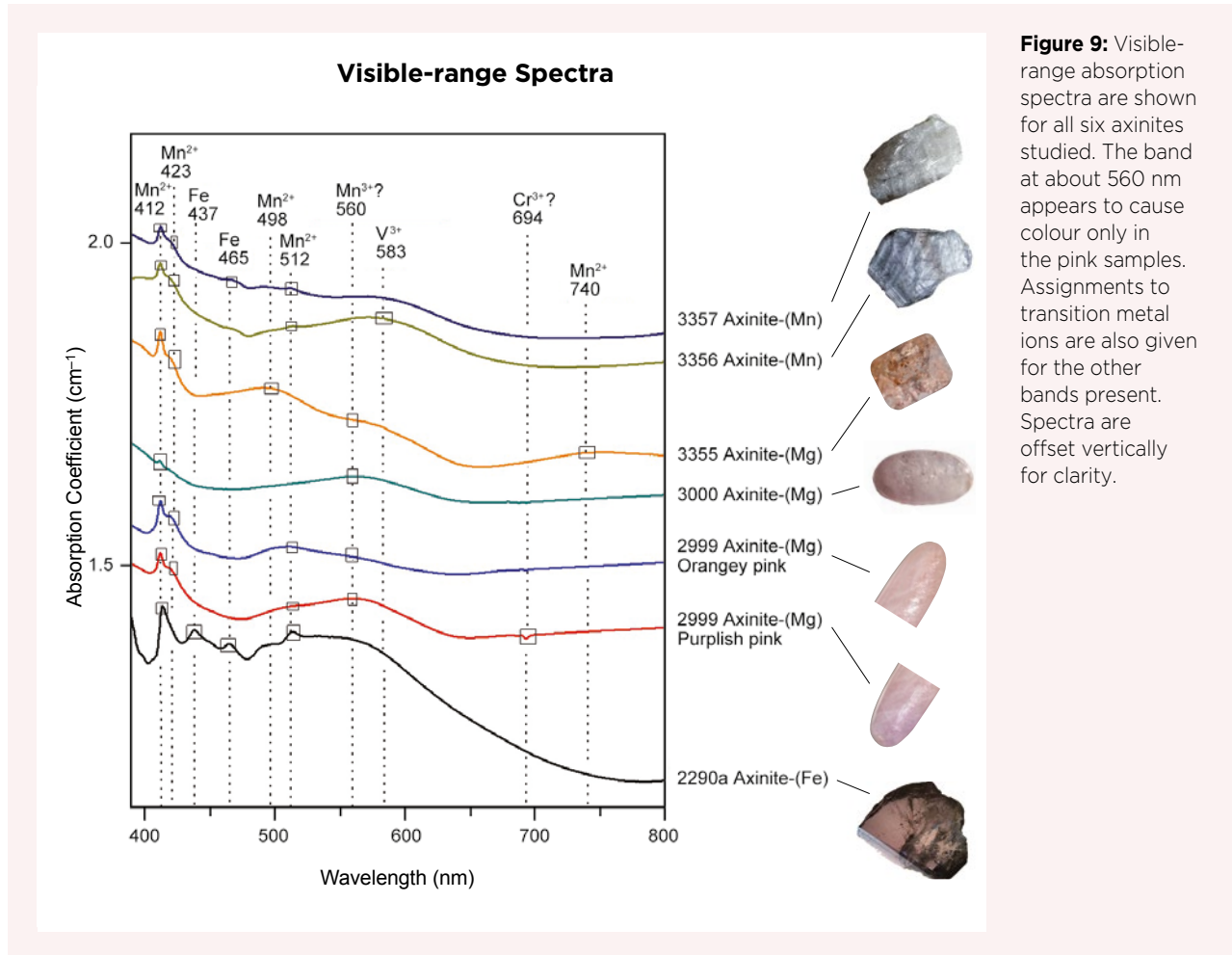


Figure 9: Visible-range absorption spectra are shown for all six axinites studied. The band at about 560 nm appears to cause colour only in the pink samples. Assignments to transition metal ions are also given for the other bands present. Spectra are offset vertically for clarity.

to previous studies, vanadium is not related to pink-to-purple colour in axinite, but rather to blue (Jobbins *et al.* 1975; Schmetzer 1982), as the absorption maximum is located further towards the red region.

Thus, the pink colouration of these axinites is associated with the asymmetric 560 nm band. Such an asymmetric band centred at about 550 nm is a classic feature of Mn^{3+} in many minerals and materials. For example, Mn^{3+} colours pink 'morganite' beryl, purple 'lepidolite' mica and pink-to-red 'rubellite' tourmaline (Reinitz & Rossman 1988; Platonov *et al.* 1989; <http://minerals.caltech.edu/FILES/Visible/mica/index.html>). In addition, we know there is at least 0.19 wt.% MnO in the two pink axinite gems. Therefore, there is enough manganese to have the small amount of Mn^{3+} necessary to cause the colour, as this ion is a strong light absorber. There are no other transition-element ions present that could cause this kind of absorption feature. As a consequence, the only interpretation consistent with all the data is that Mn^{3+} is responsible for the 560 nm feature, and therefore we propose that this ion is responsible for the pink colour in axinite. The pink to purplish pink is a mixture of red (transmission window

above 640 nm) and some blue (transmission window between 450 and 500 nm), whereas in blue axinite the red is nearly fully absorbed.

Photoluminescence Emission and Excitation Spectroscopy

Figure 10 compares emission spectra obtained from two different-luminescing areas (showing typical orange and more reddish fluorescence) of sample 3000 under 365 nm (long-wave UV) excitation. A broad band (slightly less than 100 nm wide) with an apparent maximum at 631 nm is common to both spectra. This band is more intense for the orange-luminescing area. Although 631 nm is at the border between orange and red, the human eye is much more sensitive in the orange region (approximately 590–630 nm) so the perceived colour is a relatively pure orange. Two sharp peaks at 688 and 694 nm in the red region are also present, as expected, in the area of the sample showing more reddish luminescence.

Excitation spectra were then collected from sample 3000 to reveal which wavelengths excite the specific

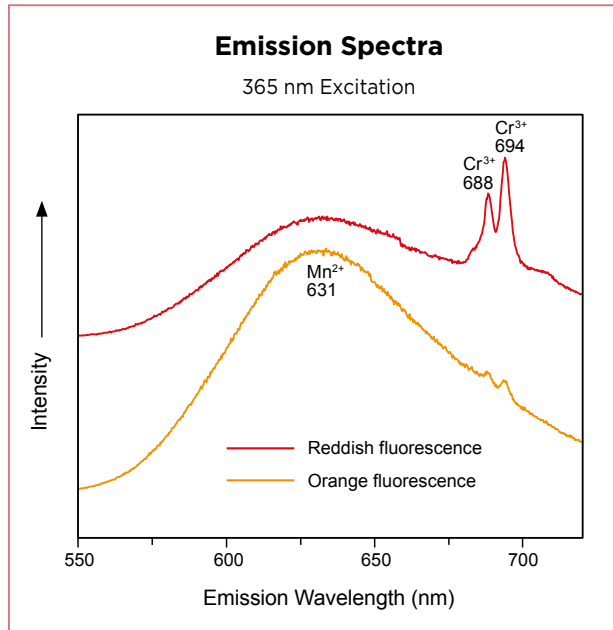


Figure 10: Emission spectra obtained using 365 nm (long-wave UV) excitation from two different areas of sample 3000 demonstrate that the orange luminescence of pink axinite is due to a large band centred at about 631 nm (related to Mn^{2+}) and the reddish fluorescence is caused by the addition of Cr^{3+} features at 688 and 694 nm (top spectrum).

emissions at 631 nm (orange) and 694 nm (red). An excitation spectrum reveals which wavelengths excite a specific emission. These wavelengths thus represent the absorption(s) responsible for the emission, and comparing the excitation spectrum with the absorption spectrum in the visible range helps establish the origin of the luminescence. The excitation of the orange emission at 631 nm (Figure 11) is nearly identical in shape to the absorption of Mn^{2+} in the orangey pink portion of sample 2999 (Figure 8). As a consequence, the orange fluorescence of the axinite can be attributed to Mn^{2+} . This ion is well known to be responsible for this luminescence colour in a number of minerals (e.g. apatite, calcite and other carbonates, spodumene and many other silicates; El Ali *et al.* 1993; Robbins 1994). For the excitation of the red emission at 694 nm (Figure 12a), the features include absorption bands of Mn^{2+} as well as a sharp band about 648 nm, along with underlying, broad absorption in the 550–650 nm region. These last two features might be related to Cr^{3+} absorption, and they are indeed present at about the same positions in the excitation spectrum of ruby (Figure 12b), in which they are known to be due to emission from pairs of chromium ions, that is Cr^{3+} – Cr^{3+} (Robbins 1994; Gaft *et al.* 2005). In addition, the emission doublet (i.e. at 658 and 668 nm in the ruby spectrum) is quite characteristic of Cr^{3+} and

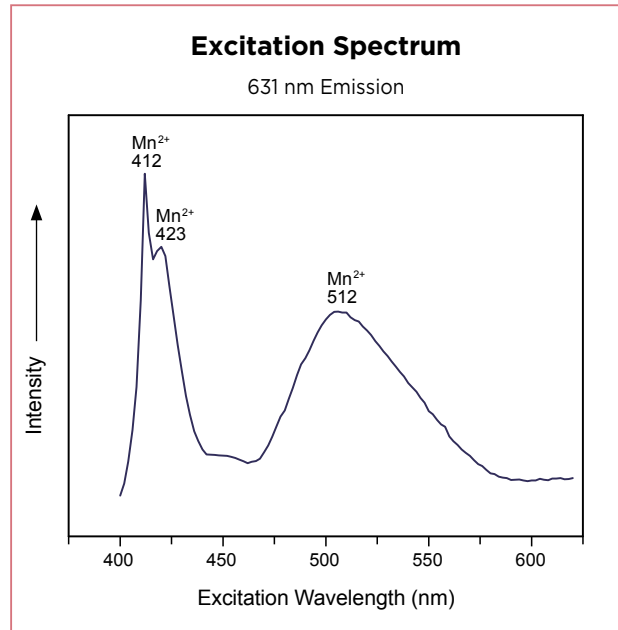


Figure 11: The excitation spectrum of axinite sample 3000 for 631 nm emission shows a close resemblance to the visible-range absorption spectrum of Mn^{2+} (i.e. the orangey pink portion of sample 2999 in Figure 8), which demonstrates that the orange luminescence is due to Mn^{2+} .

has been documented in a number of minerals (Gaft *et al.* 2005). Thus, we surmise that the reddish component of axinite luminescence is due to Cr^{3+} , as also evidenced by the 694 nm feature in the visible absorption spectrum of the pink axinite. This result is not surprising, even though no Cr was detected in our chemical analysis: only trace amounts of chromium are needed to yield a distinct red luminescence. In fact, luminescence is one of the most sensitive techniques available to detect this element, even at very low concentrations (e.g. <1 ppm in solids; Gaft *et al.* 2005).

According to Jobbins *et al.* (1975), the presence of vanadium could reduce luminescence intensity in axinite, and this was verified in a blue colour-zoned crystal (Arlabosse *et al.* 2008). It is possible that V^{3+} could absorb some of the Mn^{2+} emission. However, our blue sample 3356 did not show less fluorescence than the axinites of other colours (i.e. without V).

DISCUSSION

The results obtained for the average RI measurements, optic character and SG values of our samples are consistent with data listed in the gemmological literature for axinite (Liddicoat 1987; O'Donoghue 2006; Association Française de Gemmologie 2013).

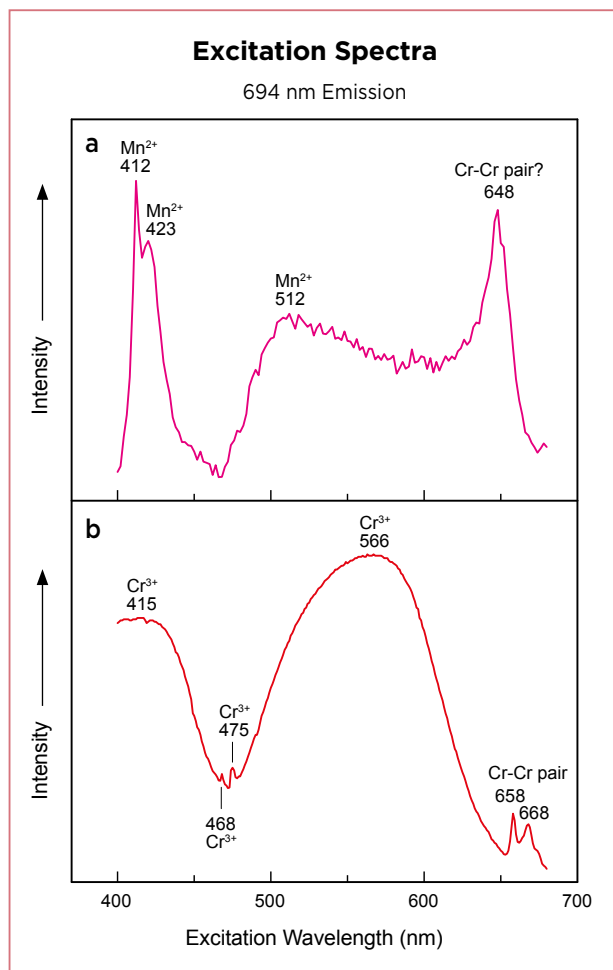


Figure 12: (a) The excitation spectrum of axinite sample 3000 for 694 nm emission is also related to Mn²⁺ absorption (cf. Figure 11), but shows an additional band at about 648 nm along with underlying, broad absorption in the 550–650 nm region. (b) Evidence of these features—asccribed to Cr-Cr ion pairs—is seen in the excitation spectrum of ruby for 694 nm emission.

Our Raman spectroscopy results for axinite-(Fe) were consistent with the detailed work of Frost *et al.* (2007). Although Raman spectroscopy cannot help assess origin of colour or luminescence, the spectra did reveal correlations with the three different axinite species represented by our specimens, providing support and confirmation of their identification based on chemical composition alone. A comparison of the reference spectra for the three axinite species in the RRUFF database also shows some consistent small differences in band positions, possibly due to variations in their chemical composition. Further work is needed to assess the exact Raman spectral band positions for the three axinite species in order for this technique to be helpful for gem identification. Relatively pure representatives of the different axinite end members, especially axinite-(Mn) and axinite-(Mg), should be carefully documented, in

particular to establish the characteristic peak positions as they relate to composition. In addition, obtaining spectra from oriented samples would be helpful for evaluating the influence of crystal orientation on the relative intensity of the various bands.

We propose that Mn³⁺ is responsible for the pink colour of axinite. Ideally, it would have been preferable to obtain crystallographically oriented, polarised absorption spectra to further support our proposition. However, pink axinites are extremely rare and our samples were not transparent, so such spectra could not be obtained at this point. Another possible avenue of research would be to synthesise colourless Mn²⁺-bearing axinite and then try irradiating it to obtain pink colouration due to Mn³⁺.

At the Merelani deposit, the presence of some manganese as Mn³⁺ could be explained by prolonged exposure to nearby naturally occurring radioactive elements. One such source could be U impurities in zircon (Malisa 2005; Feneyrol 2012). In addition, Malisa (2003) detected higher-than-normal levels of U in igneous and sedimentary rocks in this area (although metamorphic units such as the graphite gneiss host rock were not mentioned). A third source of natural radioactivity could be K-bearing minerals present at Merelani, such as the fuchsite variety of muscovite and K-feldspar in the surrounding gneisses. Reinitz and Rossman (1988) showed that pink-to-red tourmaline from granitic pegmatites could be naturally irradiated by gamma rays from ⁴⁰K in the surrounding K-feldspar. At Merelani, the appearance of the pink colour would be expected to occur during retrograde metamorphism since the higher temperatures attained during peak prograde metamorphism (up to 691 °C; Feneyrol 2012) would destroy the pink colour.

CONCLUSION

We conclude that the colouration of the two pink Tanzanian axinites studied for this report results from Mn³⁺ absorption. This colouring agent is likely due to natural irradiation of a small portion of Mn²⁺ that is abundant in this deposit. The UV luminescence of axinite is due to two cations: Mn²⁺ and Cr³⁺. The first induces the dominant orange colour and the second contributes red. The weak cat's-eye effect in one cabochon examined in this study is mostly due to a combination of parallel, reflective fractures (cleavages?) and the elongated high-domed cabochon cut. While characterising our samples with Raman spectroscopy, it became apparent that more work is needed to firmly establish the Raman spectral characteristics of axinite-(Mn), axinite-(Mg) and axinite-(Fe).

REFERENCES

- Arlabosse, J.-M., Rondeau, B. & Fritsch, E. 2008. Gem News International: A blue manganaxinite. *Gems & Gemology*, **44**(1), 81.
- Association Française de Gemmologie 2013. *Gemmes*. Association Française de Gemmologie, Paris, France, 268 pp.
- Burke, E.A.J. 2008. Tidying up mineral names: An IMA-CNMNC scheme for suffixes, hyphens and diacritical marks. *Mineralogical Record*, **39**(2), 131–135.
- Burns, R.G. 1993. *Mineralogical Applications of Crystal Field Theory*, 2nd edn. Cambridge University Press, Cambridge, 551 pp., <https://doi.org/10.1017/CBO9780511524899>.
- El Ali, A., Barbin, V., Calas, G., Cervelle, B., Ramseyer, K. & Bouroulec, J. 1993. Mn²⁺-activated luminescence in dolomite, calcite and magnesite: Quantitative determination of manganese and site distribution by EPR and CL spectroscopy. *Chemical Geology*, **104**(1–4), 189–202, [https://doi.org/10.1016/0009-2541\(93\)90150-h](https://doi.org/10.1016/0009-2541(93)90150-h).
- Faye, G.H. 1972. Relationship between crystal-field splitting parameter, “ Δ_{VI} ”, and $M_{\text{host}}\text{-O}$ bond distance as an aid in the interpretation of absorption spectra of Fe²⁺-bearing materials. *Canadian Mineralogist*, **11**(2), 473–487.
- Feneyrol, J. 2012. *Pétrologie, géochimie et genèse des gisements de tsavorite associées aux gneiss et roches calco-silicatées graphitiques de Lemshuku et Namalulu, Tanzanie*. Doctorat de l’Institut National Polytechnique de Lorraine spécialité Géosciences Thesis, University of Lorraine, France, 885 pp., <https://hal.univ-lorraine.fr/tel-01750042/document>.
- Fritsch, E. & Waychunas, G. 1994. Gemstones. In: Robbins, M. (ed) *Fluorescence: Gems and Minerals Under Ultraviolet Light*. Geoscience Press, Phoenix, Arizona, USA, 149–174.
- Fritz, E.A., McClure, S.F., Shen, A.H., Laurs, B.M., Simmons, W.B. & Falster, A.U. 2007. Gem News International: Color-zoned axinite from Pakistan. *Gems & Gemology*, **43**(3), 254–255.
- Frost, R.L., Bouzaid, J.M., Martens, W.N. & Reddy, B.J. 2007. Raman spectroscopy of the borosilicate mineral ferroaxinite. *Journal of Raman Spectroscopy*, **38**(2), 135–141, <https://doi.org/10.1002/jrs.1574>.
- Gaft, M., Reisfeld, R. & Panczer, G. 2005. *Modern Luminescence Spectroscopy of Minerals and Materials*. Springer-Verlag, Berlin, Germany, 356 pp., <https://doi.org/10.1007/978-3-319-24765-6>.
- Gribble, C.D. & Hall, A.J. 1992. *Optical Mineralogy: Principles and Practice*. Chapman & Hall, New York, New York, USA, 303 pp., <https://doi.org/10.1007/978-1-4615-9692-9>.
- Harris, C., Hlongwane, W., Gule, N. & Scheepers, R. 2014. Origin of tanzanite and associated gemstone mineralization at Merelani, Tanzania. *South African Journal of Geology*, **117**(1), 15–30, <https://doi.org/10.2113/gssaj.117.1.15>.
- Jang-Green, H., Beaton, D., Laurs, B.M., Simmons, W.B. & Falster, A.U. 2007. Gem News International: Two axinite species from Tanzania. *Gems & Gemology*, **43**(4), 373–375.
- Jaszczak, J.A. & Trinchillo, D. 2013. Miracle at Merelani – A remarkable occurrence of graphite, diopside, and associated minerals from the Karo mine, Block D, Merelani Hills, Arusha region, Tanzania. *Rocks & Minerals*, **88**(2), 154–165, <https://doi.org/10.1080/00357529.2013.763671>.
- Jobbins, E.A., Tresham, A.E. & Young, B.R. 1975. Magnesioaxinite, a new mineral found as a blue gemstone from Tanzania. *Journal of Gemmology*, **14**(8), 368–375, <https://doi.org/10.15506/JoG.1975.14.8.368>.
- Lauf, R.J. 2007. Collector’s guide to the axinite group. *Rocks & Minerals*, **82**(3), 216–220, <https://doi.org/10.3200/rmin.82.3.216-221>.
- Liddicoat, R.T. 1987. *Handbook of Gem Identification*, 12th edn. Gemological Institute of America, Santa Monica, California, USA, 362 pp.
- Malisa, E.P.J. 2003. Trace elements characterization of the hydrothermally deposited tanzanite and green grossular in the Merelani–Lelatema shear zone, northeastern Tanzania. *Tanzania Journal of Science*, **29**(1), 45–60, <https://doi.org/10.4314/tjs.v29i1.18366>.
- Malisa, E.P. 2005. Petrography and mineral chemistry of the pelitic and semi-pelitic gneisses of the Merelani tanzanite mining area, northeastern Tanzania. *Tanzania Journal of Science*, **31**(2), 81–92, <https://doi.org/10.4314/tjs.v31i2.18423>.
- Malisa, E. & Muhongo, S. 1990. Tectonic setting of gemstone mineralization in the Proterozoic metamorphic terrane of the Mozambique Belt in Tanzania. *Precambrian Research*, **46**(1–2), 167–176, [https://doi.org/10.1016/0301-9268\(90\)90071-w](https://doi.org/10.1016/0301-9268(90)90071-w).
- Milton, C., Hildebrand, F.A. & Sherwood A.M. 1953. The identity of tinzenite with manganoox axinite. *American Mineralogist*, **38**(11–12), 1148–1158.
- O’Donoghue, M. (ed) 2006. *Gems*, 6th edn. Butterworth-Heinemann, Oxford, 873 pp.
- Olivier, B. 2006. *The geology and petrology of the Merelani tanzanite deposit, NE Tanzania*. PhD thesis, University of Stellenbosch, South Africa, 434 pp., <https://pdfs.semanticscholar.org/94ba/83d0808bc85df942494d1052a5729c903611.pdf>.
- Pay, D. 2017. Gem News International: Magnesio-axinite from Merelani, Tanzania. *Gems & Gemology*, **53**(1), 128–129.
- Platonov, A.N., Taran, M.N. & Klyakhin, V.A. 1989. On two colour types of Mn³⁺-bearing beryls. *Zeitschrift*

der Deutschen Gemmologischen Gesellschaft, **38**(4), 147–154.

- Pohl, D., Guillemette, R., Shigley, J. & Dunning, G.E. 1982. Ferroaxinite from New Melones Lake, Calaveras County, California, a remarkable new locality. *Mineralogical Record*, **13**(5), 293–302.
- Quinn, E.P. & Breeding, C.M. 2005. Lab Notes: Yellowish orange magnesioaxinite. *Gems & Gemology*, **41**(2), 170–171.
- Reinitz, I.M. & Rossman, G.R. 1988. Role of natural radiation in tourmaline coloration. *American Mineralogist*, **73**(7–8), 822–825.
- Robbins, M. 1994. *Fluorescence: Gems and Minerals Under Ultraviolet Light*. Geoscience Press, Phoenix, Arizona, USA, 384 pp.
- Schmetzer, K. 1982. Absorptionsspektroskopie und Farbe von V^{3+} -haltigen natürlichen Oxiden und Silikaten – ein Beitrag zur Kristallchemie des Vanadiums. *Neues Jahrbuch für Mineralogie, Abhandlungen*, **144**(1), 73–106, <https://doi.org/10.1127/njma/144/1982/73>.
- Williams, C., Williams, B. & Laurs, B.M. 2014. Gem Notes: Colour-change axinite-(Mn) from Tanzania. *Journal of Gemmology*, **34**(3), 191–192.
- Wilson, W.E., Saul, J.M., Pardieu, V. & Hughes, R.W. 2009. Famous mineral localities: The Merelani tanzanite mines, Lelatema Mountains, Arusha region, Tanzania. *Mineralogical Record*, **40**(5), 346–408.

The Authors

Maxence Vigier* and **Dr Emmanuel Fritsch** FGA Institut des Matériaux Jean Rouxel, CNRS and University of Nantes, UMR6502, BP32229, F-44322 Nantes Cedex 3, France

Email: Emmanuel.Fritsch@cnrs-imn.fr

* Mr Vigier was a BS student at the time of this research.

Acknowledgements

Dudley Blauwet (Dudley Blauwet Gems, Louisville, Colorado, USA) loaned sample 2999 for an extended period for research. We also thank Joyce van Dronkelaar-Kessy (Kilimanjaro Gemstones, Oostburg, the Netherlands) and Denis Gravier (Gravier & Gemmes, L'Abergement-de-Varey, Jura, France) for providing samples for this study. Prof. Edward Grew (University of Maine, Orono, Maine, USA) considerably improved the original text through a very constructive review. Laurent Lenta (Laboratoire de Planétologie et Géodynamique de Nantes, University of Nantes and CNRS) helped with sample preparation. Féodor Blumentritt (IMN-CNRS, Nantes) provided a helpful review of the manuscript. For Figure 1, we thank Vance Gems for loaning the samples and Dr Jaroslav Hyršl for providing the UV lamp used to take the luminescence image. Melli Rose (University of Arizona, Tucson, Arizona, USA) confirmed the identification of some of the samples in Figure 1 as axinite by Raman analysis.

Gem-A
THE GEMMOLOGICAL ASSOCIATION
OF GREAT BRITAIN

Gem-A's Gemstone Photographer of the Year 2020

Are you a budding gemstone photographer?

Do you love taking photomicrographs of gemstones or capturing the human side of our industry?

Would you like to be featured on the front cover of *Gems & Jewellery*?

Details of our photography competition will be announced in the August issue of *Gems & Jewellery* magazine.

f t in i B



Figure 1: A panoramic view of the town of Yen The in Vietnam's Luc Yen District reveals karst landscapes that host agricultural land and gem mining areas. Photo by T. Sripoonjan.

A Journey to Luc Yen, Vietnam (February 2019)

Tasnara Sripoonjan, Waratchanok Suwanmanee,
Doan Thi Anh Vu and Bhuwadol Wanthanachaisaeng

Vietnam is a long, mostly narrow country with an extensive coastline, measuring about 1,650 km from north to south but only 50 km wide at the narrowest point. The country is endowed with a wide range of mineral resources resulting from its diverse geological history. Since the 1980s, various gem materials including ruby, sapphire and spinel have been obtained from both primary and secondary deposits. Although mining activities decreased in recent years due to government regulations and dwindling reserves, some gems continue to emerge onto the global marketplace.

In January 2019, a research project was initiated by author BW titled 'Potential and Access Opportunity of Blue Sapphire Resources in Vietnam'. The goal was to

investigate actively operating mines and potential gem deposits through two excursions. The first one took place in February 2019 to the Luc Yen District in the mountainous area of northern Vietnam (Figure 1), and the second trip was in June 2019 to Vietnam's southern provinces. Our team consisted of the authors, as well as Thai university professors in geology and earth sciences Drs Krit Won-in, Somruedee Sakkaravej, Natthapong Monarumit, Sarinya Paisarnsombat and Alongkot Fanka, and graduate student Teerarat Pluthametwisute (Figure 2). This report covers the trip to Luc Yen.

The group flew from Bangkok to Vietnam's capital city Hanoi, and then travelled north-west about 250 km by van to Luc Yen in Yen Bai Province. It took about 4½ hours, mostly on asphalt road, to reach the town of Yen The,



which is the capital of Luc Yen District (and therefore this town is commonly known as ‘Luc Yen’). Once in the Luc Yen area, we travelled on more winding, unpaved, secondary roads.

Geology of Luc Yen: The Luc Yen area has distinctive topography—commonly featuring karst landforms caused by the tropical weathering of marble bedrock—including steep hillslopes, sinkholes, caves and dramatic valleys. The geological setting of the gem deposits in

Luc Yen can be divided into two north-west-trending domains separated by the Chay River Fault: Tan Huong-Truc Lau and Khoan Thong-An Phu (Figure 3). Tan Huong-Truc Lau pertains to metamorphic belts associated with a large-scale structure known as the Ailao Shan-Red River shear zone, which is located on the south-west side of the Chay River. This area is mainly composed of sillimanite-biotite-garnet gneiss and mica schist that are locally intercalated with marble and amphibolite. On the Chay River’s north-eastern side,



Figure 2: The research team—shown here at Minh Tien near An Phu village—consists of (from left to right): Teerarat Pluthametwisute, Tasnara Sripoonjan, Alongkot Fanka, Sarinya Paisarnsombat, Waratchanok Suwanmanee, Somruedee Sakkaravej, Krit Won-in, Doan Thi Anh Vu, Bhuwadol Wanthanachaisaeng and Natthapong Monarumit. Photo courtesy of T. Sripoonjan.

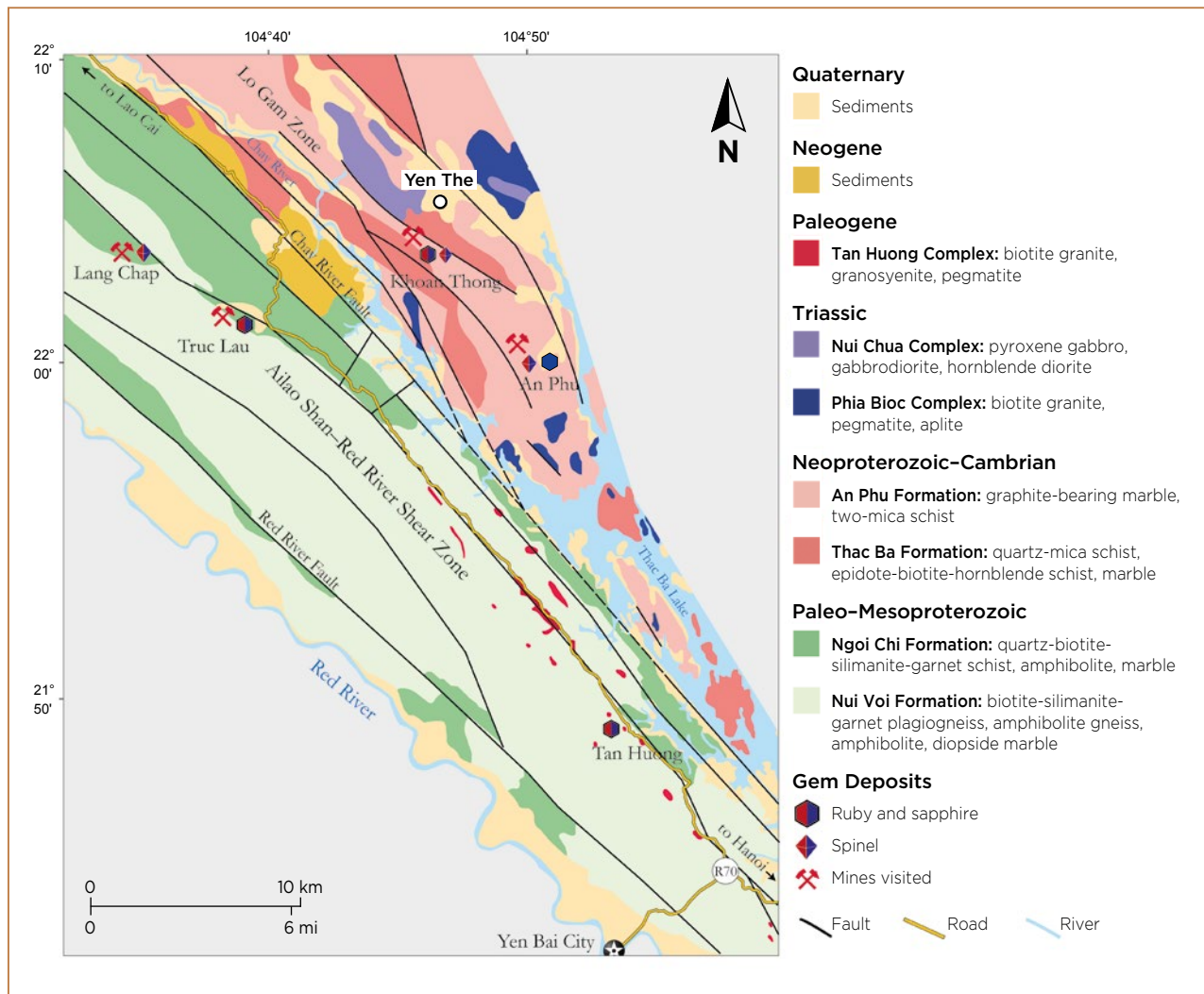


Figure 3: Gem deposits in the Luc Yen District include gneiss-hosted occurrences south-west of the Chay River Fault (e.g. Truc Lau and Lang Chap) and marble-hosted occurrences along the Lo Gam structural zone (e.g. Khoan Thong and An Phu). Adapted from Khoi *et al.* (2016).

the Khoan Thong-An Phu domain is mostly underlain by metasedimentary gneisses and mica schists together with marble. These rocks are locally intruded by granitic and pegmatitic dykes.

Truc Lau Deposit: The most recently discovered gem mining area in Yen Bai (opened in the 2000s) exploits eluvial and alluvial sediments. Rubies and sapphires are hosted by a gravel paleoplacer that underlies swamps and rice fields situated in a relatively large valley about 5 km long (Figure 4). High-quality star rubies have been found in this area. We visited one of the mining areas, but no work was being done on the weekend. Several small pits, approximately 2 m across and 2 m deep, were dug with hand tools by artisanal miners. The authors were told that a considerable quantity of corundum (usually very low or non-gem quality) was being found at that time.

Lang Chap Deposit: Located in remote jungle terrain near Khanh Hoa village, to the west-south-west of Yen The, Lang Chap (Figure 5) requires a four-wheel-drive vehicle to negotiate the muddy road, and is about a 1½-hour drive from the Truc Lau deposit. The area is underlain by weathered metamorphic rocks, including garnet schist. The miners excavate secondary deposits using primitive equipment. According to local gem traders, although recent production has been very limited, some high-quality spinel (including pinkish orange padparadscha-like material) is occasionally recovered.

Khoan Thong Deposit: Also called Tan Linh by locals, Khoan Thong (Figure 6) was formerly a flourishing gem mining area that was exploited by some Vietnamese-Thai joint ventures as well as independent miners. An abundance of gem-quality rubies and sapphires were

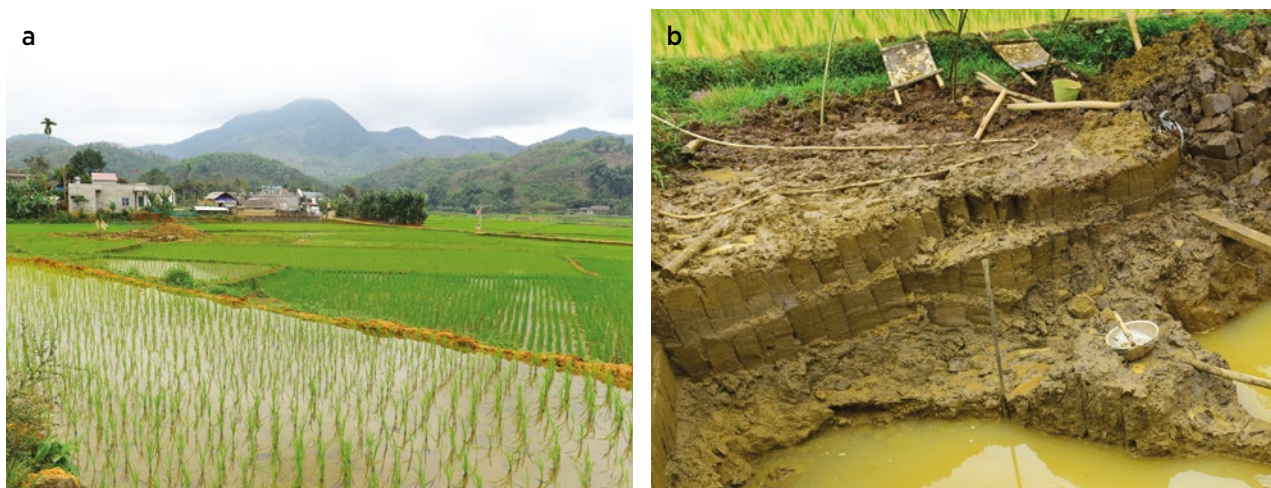


Figure 4: (a) Some gem mining in the Truc Lau area takes place within rice fields. (b) Small pits dug with hand tools explore secondary gem deposits at Truc Lau. Photos by T. Sripoonjan.



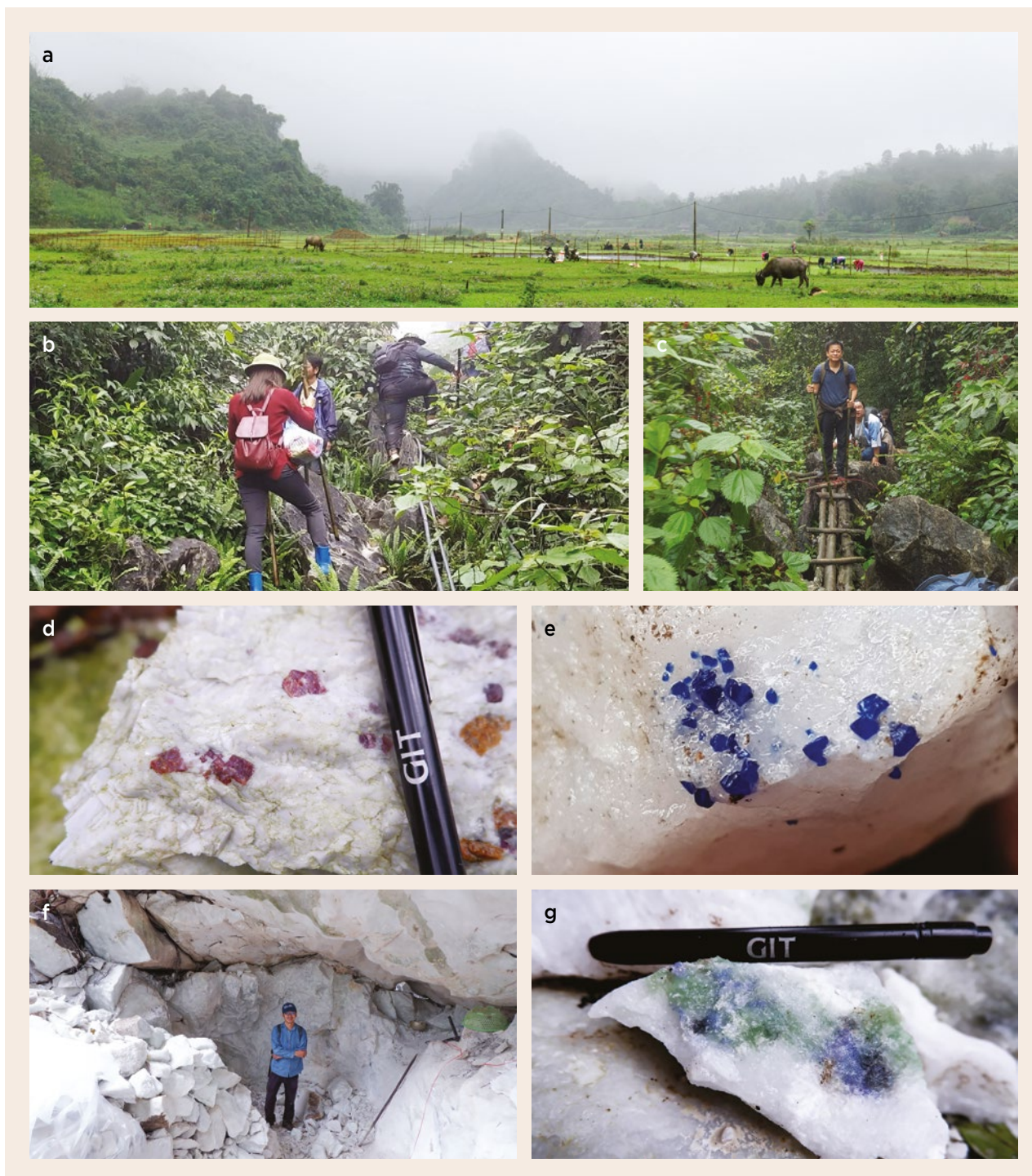
Figure 5: (a) The deposit at Lang Chap is being mined for spinel. (b) Spinel crystals are found embedded in pieces of white marble matrix. (c) Loose pieces of gem-quality spinel are also screened from the gravels. (d) These fine-quality spinels (up to about 1+ ct) reportedly came from the Lang Chap area (see tweezers for scale). Photos by T. Sripoonjan (a and c), T. Pluthametwisute (b) and B. Wanthanachaisaeng (d).

recovered there. An engraved stone sign at the entrance of the valley is inscribed with a message of thanks from Vietnam's prime minister to the group of geologists who discovered the gem deposit. Very little mining was underway during our visit. At one active operation near the foothills, we recovered some very small fine-quality rubies. We were told that other gems—such as sapphire, spinel and tourmaline—are also found there. Some of the gem-bearing soil was stockpiled near a small reservoir for

washing in the future. We also saw mined-out primary deposits such as (1) a rock face consisting of marble and calc-silicate rocks, partly intruded by granitic and pegmatitic veins; and (2) a tunnel driven into one of the hillsides. The primary deposits were mined for ruby, sapphire and spinel (all typically cabochon quality), as well as tourmaline, pargasite and humite. At the home of a local miner we saw some rough and cut stones that were reportedly from this deposit.



Figure 6: (a) The Khoan Thong deposit is situated in a magnificent valley. (b) An inscription in stone is dedicated to the geologists who discovered the gem treasures there. (c) Small fine-quality rubies were found by the authors in secondary deposits. (d) Gems were also produced from primary deposits. (e) Black tourmaline is present in pegmatitic rocks. (f) Cabochon-quality rubies and sapphires (averaging about 2 ct) from Khoan Thong are offered for sale. All photos by T. Sripoonjan.



An Phu Deposits: Minh Tien, one of the most famous gem-mining areas in Vietnam, is located near An Phu village to the south-east of Yen The. We visited some mines that could only be reached by trekking for about 5 km (at least 3 hours) up a marble mountain that was about 750 m high (Figure 7). Along the way, we passed rice fields that were mined in places by the locals. As we ascended, the trail became flanked by dense vegetation and in places was shrouded by bamboo. It was wet and slippery, and our trek gradually became steeper among

Figure 7: (a) Near An Phu village, agricultural land used for rice cultivation also hosts secondary gem deposits. (b) The trail to the An Phu spinel deposits is steep and slippery, and surrounded by dense jungle. (c) Wooden footbridges are used to cross grikes and sinkholes in the karst terrain. (d) Crystals of red-purple spinel and orange clinohumite are embedded in white marble host rock. (e) A cluster of 'cobalt'-blue spinels (up to about 3 mm each) shows attractive colouration. (f) At about 600 m elevation, miners have used a pneumatic jackhammer to extract spinel from the marble. (g) Blue spinel is associated with green pargasite in this sample from An Phu. Photos by T. Sripoonjan, except image e by B. Wanthanachaisaeng.

sharp karst outcrops. Small wooden footbridges crossed solution fissures (grikes) and sinkholes. Eventually, we reached a marble cliff that had been mined for red, pink and purple spinel. Another nearby area was mined for 'cobalt'-blue spinel, which was most probably hosted by a forsterite-rich lens in the marble. These spinels were extracted using hand tools and a jackhammer. We obtained a number of attractively coloured spinel samples, some of which were associated with orange clinohumite or green pargasite. We also visited a mine near An Phu village where fine blue sapphire was found.

Luc Yen Gem Market: A local gem market was established in 1987 in Yen The (Figure 8), and continues to serve as the centre for trading in gemstones, rough material and crystal specimens from northern Vietnam. There were more than 50 vendors who opened daily at 6:30 am and closed before noon. Buyers were comprised of Vietnamese tradespeople from Hanoi and Ho Chi Minh City, as well as foreigners from various countries. The gems on display included spinel (most abundant), ruby, sapphire, aquamarine, fluorite, quartz, tourmaline, opal and jade, among others. Of particular interest to





Figure 8: (a) The sellers at the Yen The gem market are mostly women. (b) Spinel is the most popular gem material offered there. (c) A wide variety of faceted gemstones, reportedly from local mines, are offered for sale. (d) Nearby shops display carved stones and sculptures. (e) Blue sapphires from Luc Yen show light to dark blue colouration. (f and g) Gem 'paintings' are created using various crushed materials. Photos by T. Sripoonjan (a-e) and B. Wanthanachaisaeng (f and g).

the authors were high-quality blue sapphires that were reportedly from the An Phu area. Initial asking prices for gemstones were usually relatively high but prices were negotiable. Cabochon-quality material and some ornamental stones were typically offered at reasonable prices. The street near the gem market hosted more than 30 gem and jewellery shops, mostly displaying carved stones, sculptures and mineral specimens. Also offered were gem 'paintings' created using a variety of crushed gem materials (some of which were dyed) that were affixed with spray adhesive.

Reference

- Khoi, N.N., Hauzenberger, C.A., Tuan, D.A., Häger, T., Nam, N.V. & Duong, N.T. 2016. Mineralogy and petrology of gneiss hosted corundum deposits from the Day Nui Con Voi metamorphic range, Ailao Shan–Red River shear zone (North Vietnam). *Neues Jahrbuch für Mineralogie, Abhandlungen*, **193**(2), 161–181, <https://doi.org/10.1127/njma/2016/0300>.

Acknowledgements

This project was supported by Thailand Science Research and Innovation TSRI/RDG62T0037. We are also grateful to Nguyen Van Tich and Nguyen Thi Huong Quynh for information and assistance in the field.

Tasnara Sripoonjan (tasnara@hotmail.com) is an independent researcher and former research scientist with The Gem and Jewelry Institute of Thailand in Bangkok. Waratchanok Suwanmanee and Doan Thi An Vu are graduate students at Chulalongkorn University in Bangkok. Dr Bhuwadol Wanthanachaisaeng is a lecturer at the College of Creative Industry, Srinakarinwirot University, Bangkok.

Gem-A Notices

Gifts to the Association

Gem-A is most grateful to the following for their generous donations that will support continued research and teaching:

Barbara Kolator, United Kingdom, for a black coral branch from Hawaii, USA, collected in the 1940s–50s; rough blue opal from Durango, Mexico; and petrified wood from Holbrook, Arizona, USA.

Helen Serras-Herman, USA, for alabaster onyx (banded gypsum) and drusy quartz specimens from Arizona, along with a pamphlet on lapidary materials.

Webinars with Gem-A Live

At the end of March 2020, the UK began a period of national lockdown as a measure to combat the COVID-19 pandemic. Unfortunately, this meant that Gem-A had to cancel and postpone some in-house gemmology workshops and classes. This was a great disappointment for all the Gem-A team, but we didn't let it stop us from sharing our passion for gemstone education! On 1 April we launched a series of 'Gem-A Live' webinars, which

have enabled hundreds of gemmology enthusiasts from around the world to get a free, weekly dose of fresh gem knowledge and ask our webinar hosts questions on the subjects presented.

The webinars, which cover topics such as titanium diffusion in sapphire, flux-healed ruby and composite gemstones, have been uploaded to Gem-A's new YouTube channel, **Gem-A Official Channel**, and are available to watch online now: www.youtube.com/c/GemAOfficialChannel.



One of our Gem-A Live hosts, Julia Griffith FGA DGA EG, sharing live gemmology with the global Gem-A community.

Upcoming Events: Watch this Space...



September 2020: Jewellery & Gem World Hong Kong

From 15 to 19 September 2020, Gem-A will return to Hong Kong to exhibit at Jewellery & Gem World 2020. Gem-A will exhibit at booth 3M204; if you're planning to attend, please come along to say hello to our team, find out about our courses and ask us any questions you like. We look forward to seeing you there.

A celebration of entrants to Gem-A's Gem Empathy Award at the 2019 Hong Kong Jewellery & Gem Fair.

Update: Gem-A Graduation and Presentation of Awards, London

Gem-A have made the very difficult decision to cancel the Gem-A Graduation and Presentation of Awards evening that was scheduled to take place in November 2020. We have held this prestigious event for as long as anyone at Gem-A HQ can remember, and we are deeply saddened we will not get to celebrate our Graduates' achievements in the traditional sense. We are looking at alternatives to ensure that we can still honour the accomplishments of our Graduates and will release details as soon as they are ready. This year's ceremony was due to take place at an exciting new venue, London's historic Church House, a Grade II listed building which neighbours London's iconic Westminster Abbey and Houses of Parliament. We look forward to holding a combined 2020/2021 Gem-A Graduation and Presentation of Awards in this great building next year.

London's Church House, situated in the heart of Westminster.



All events are subject to change due to the ongoing COVID-19 pandemic. Please check your Gem-A Membership emails and the Gem-A website for updates.



Refresh your knowledge



ACCESS ANY TIME



LEARN SOMETHING NEW!



Refresh your knowledge



Have you watched the Gem-A webinar series on the Gem-A YouTube Channel?

www.youtube.com/c/GemAOfficialChannel



Learning Opportunities

Note: Event dates and formats are subject to change depending on the COVID-19 situation.

CONFERENCES AND SEMINARS

Goldschmidt Virtual 2020

21–26 June 2020

Online

<https://goldschmidt.info/2020/index>

Session of interest: Geochemistry of Gem Minerals – Indicators of Earth’s History from Mantle Evolution to Crustal Provenance

Hong Kong International Jewellery Show

3–6 August 2020

Hong Kong

https://event.hktdc.com/fair/hkjewellery-en/s/291-General_Information/HKTDC-Hong-Kong-International-Jewellery-Show/Event-Schedule.html

Note: Includes a seminar programme

NAJA 54th Ace® It Mid-Year Conference

8–11 August 2020

Location to be determined

www.najaappraisers.com/html/conferences.html

Dallas Mineral Collecting Symposium

20–23 August 2020

Dallas, Texas, USA

www.dallassymposium.org

Amberif 2020: 27th International Fair of Amber & Jewellery

26–29 August 2020

Gdańsk, Poland

<http://amberif.amberexpo.pl/title,Jezyk,lang,2.html>

Note: Includes a seminar programme

19th Rendez-Vous Gemmologiques de Paris

7 September 2020

Paris, France

www.afgems-paris.com/rdv-gemmologique

Association for the Study of Jewelry and Related Arts (ASJRA) Annual Conference

12 September 2020

New York, New York, USA

www.jewelryconference.com

International Jewellery London (IJL)

13–15 September 2020

London

www.jewellerylondon.com

Note: Includes a seminar programme

Jewellery & Gem World Hong Kong

13–19 September 2020

Hong Kong

<https://exhibitions.jewellerynet.com/9jg/>

Note: Includes a seminar programme

Denver Gem & Mineral Show

18–20 September 2020

Denver, Colorado, USA

www.denvermineralshow.com

Note: Includes a seminar programme

inArt 2020: 4th International Conference on Innovation in Art Research and Technology

30 September–3 October 2020

Paris, France

<https://inart2020.sciencesconf.org>

CIBJO Congress

5–7 October 2020

Dubai, United Arab Emirates

www.cibjo.org/2020-cibjo-congress-to-take-place-in-dubai-october-5-7-hosted-by-dmcc

2020 American Society of Appraisers (ASA) International Conference

11–13 October 2020

Chicago, Illinois, USA
www.appraisers.org/Education/conferences/asa-international-conference

Japan Jewellery Fair 2020

14–16 October 2020
 Tokyo, Japan
www.japanjewelleryfair.com/en
Note: Includes a seminar programme

Munich Show: Mineralientage München

30 October–1 November 2020
 Munich, Germany
<https://munichshow.de/?lang=en>
Note: Includes a seminar programme

Chicago Responsible Jewelry Conference

5–7 November 2020
 Chicago, Illinois, USA
<https://responsiblejewelryconference.com>

14th International Conference on New Diamond and Nano Carbons (NDNC)

10–14 January 2021
 Kanazawa, Japan
www.ndnc2020.org

23rd FEEG Symposium—25th Anniversary

23–24 January 2021
 Paris, France
www.feeg-education.com/symposium

NAJA 55th Ace® It Winter Conference

31 January–1 February 2021
 Tucson, Arizona, USA
www.najaappraisers.com/html/conferences.html

AGTA Gemfair Tucson

2–7 February 2021
 Tucson, Arizona, USA
<https://agta.org/agta-gem-fair-tucson>
Note: Includes a seminar programme

Tucson Gem and Mineral Show

11–14 February 2021
 Tucson, Arizona, USA
www.tgms.org/show
Note: Includes a seminar programme

Inhorgenta Munich

19–22 February 2021

Munich, Germany
www.inhorgenta.com/index.html
Note: Includes a seminar programme

10th National Opal Symposium

31 March–1 April 2021
 Coober Pedy, Australia
www.opalsymposium.org

American Gem Society Conclave

26–28 April 2021
 Louisville, Kentucky, USA
www.conclave2021.americangemsociety.org

37th International Gemmological Conference (IGC 2021)

17–21 May 2021
 Tokyo, Japan
www.igc-gemmology.org
Note: Includes field trips to jadeite deposits and a pearl farm

Swiss Gemmological Society Conference

30 May–1 June 2021
 St Gallen, Switzerland
<http://gemmologie.ch/en/current>

Diamonds – Source to Use 2020

9–10 June 2021
 Johannesburg, South Africa
www.saimm.co.za/saimm-events/upcoming-events/diamonds-source-to-use-2020

Jewellery in Texts: Texts in Jewellery

19 June 2021
 London
www.societyofjewelleryhistorians.ac.uk/news

NAJ Summit

19–21 June 2021
 Northamptonshire, East Midlands
www.naj.co.uk/summit
Note: Includes the IRV Valuers' Conference (19–21 June), NAJ's Better Business Seminar (20–21 June), the Retail Jewellers' Congress (21 June) and more

The Goldsmiths' Company Jewellery Materials Congress

18–20 July 2021
 London
www.assayofficelondon.co.uk/events/event-programme-202021

Sainte-Marie-aux-Mines Mineral & Gem Show

24–27 June 2021

Sainte-Marie-aux-Mines, France

www.sainte-marie-mineral.com*Note:* Includes a seminar programme**9th International Conference Mineralogy and Museums**

24–26 August 2021

Sofia, Bulgaria

www.bgminsoc.bg*Note:* Gem minerals and archaeogemmology are among the topics that will be covered.**3rd European Mineralogical Conference (emc2020)**

29 August–2 September 2021

Krakow, Poland

<https://emc2020.ptmin.eu>*Sessions of interest:* The Geology of Gem Deposits:

A Session in Honour of Gaston Giuliani; Materials Sciences and Archaeometry for Cultural Heritage

NAJA 56th Ace® It Mid-Year Conference

30–31 August 2021

Chicago, Illinois, USA

www.najaappraisers.com/html/conferences.html**31st International Conference on Diamond and Carbon Materials**

5–9 September 2021

Palma, Mallorca, Spain

www.elsevier.com/events/conferences/international-conference-on-diamond-and-carbon-materials**3rd International Conference on Tourmaline (TUR2021)**

9–11 September 2021

Elba Island, Italy

www.tur2021.com**OTHER EDUCATIONAL OPPORTUNITIES****Gem-A Workshops and Courses**

Gem-A, London

<https://gem-a.com/education>**Lectures with The Society of Jewellery Historians**

Society of Antiquaries of London,

Burlington House, London

www.societyofjewelleryhistorians.ac.uk/current_lectures

- Gordon M. Walkden—The Rocks of Britain: Our Victorian Jewellery
22 September 2020
- Kirstin Kennedy—TBA
27 October 2020
- Charlotte Gere—Colour in Victorian Jewellery
24 November 2020
- Jonathan Boyd—TBA, on his work as a jeweller
26 January 2021
- Jack Ogden—Presidential Address (following AGM)
23 February 2021
- Carol Michaelson—Chinese Jade Jewellery and Ornaments from the Neolithic to the Present
27 April 2021
- Gonçalo de Vasconclo e Sousa—TBA, on Portuguese jewellery
25 May 2021
- Karl Schmetzer—The late 14th-Century Royal Crown of Blanche of Lancaster
22 June 2021
- TBA
28 September 2021
- Three speakers TBA—New Research on Jewellery
26 October 2021
- Ute Decker—Sculptural Minimalism & Fairtrade Gold: Philosophy, Provenance and Process
23 November 2021

New Media



The Collection of EF Watermelon: Masterworks of the American Gem Art Movement

Ed. by Günther Neumeier, 2018 (printed 2019).

EF Watermelon, Old Lyme, Connecticut, USA, 104 pages, illus., ISBN 978-0692058442. USD52.00 hardcover.

This book documents the lifelong collecting passion of two gentlemen: Richard Freeman and James Elliot. This passion extended to three talented American gemstone artists: Susan Allen, Michael Christie and Turkmenistan-born Nicolai Medvedev. A statement by one of the artists (Susan Allen) on the book's title page sums up the pursuit of this gem art collection: 'A lifelong commitment to preserve the unique work of Susan Allen, Michael Christie and Nicolai Medvedev created an unexpected gift; a strong thread of purpose to our lives. The thread moved through time and tuned us to a resonance that was precious in its degree of presence.'

While the book contains little text, the writing is interesting and informative. An introduction by James Elliot details the start of the EF Watermelon partnership, which began in 1977 in Tucson (Arizona, USA) with a purchase of some tourmalines. This led to several buying trips to Brazil, and the establishment of Freeman and Elliot as world-class gem collectors. In the early 1980s they met Susan Allen, Michael Christie and Nicolai Medvedev. Thus began the journey that developed into a lifelong friendship and successful business. The introduction is followed by a foreword from C. R. 'Cap' Beesley titled 'The Renaissance of the American Gem Art Movement', in which he states 'This outstanding collection of objects of art celebrates an important phase

in the realm of artistic achievement. It also celebrates and embodies the life's work of both the artists and the individuals that recognised the value and collectability of their creative endeavors'.

Next, renowned gem artist Lawrence Stoller provides a tribute to Susan Allen, noting that her technique of carving a transparent gemstone from the back requires her to think and carve in reverse. Then, world-famous gem photographer Robert Weldon describes photographing Allen's carvings. This brings us to page 10 and an introduction by Patrick Gaffey of Allen's carvings in the EF Watermelon collection, which are featured on the next 49 pages in full-page images. While it's impossible for me to select a favourite, the lion's head on page 13 is exceptional.

Page 60 brings us to Gaffey's introduction to Michael Christie. His elegant essence bottles are unique and exquisite, and are often enhanced by internal carvings by Susan Allen. I particularly liked Christie's quote, 'It's about loveliness', which describes the objects he creates from a wide variety of gem materials. The next 11 pages are filled with this loveliness, again documented perfectly by Weldon's photographs.

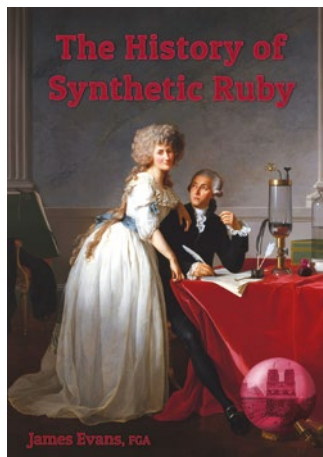
The final portion of the collection is again introduced by Gaffey, who gives a brief history of master artist Nicolai Medvedev. He is known for his complex boxes of gem intarsia, the most intricate form of stone inlay art. The following 27 pages show Medvedev's magnificent creations. The book concludes with an index of the works pictured, along with their dates of creation.

How fortunate we are that Jim Elliot and Richard Freeman were able to create the fabulous EF Watermelon art collection to showcase the magnificent creations of these three artists, which they share with us through this fine book. The works in this collection were also documented in a 76-page publication by EF Watermelon titled *The American Gem Art Collection of EF Watermelon Catalog* (2018, ISBN 978-0692058459), which provides information on each piece, including a brief description, dimensions and when it was created (and, for pieces by Michael Christie, the artist's original renderings). Both books can be ordered by emailing efwatermeloncoll@yahoo.com.

Bill Larson FGA

Pala International

Fallbrook, California, USA



The History of Synthetic Ruby

By James Evans, 2020.
Lustre Gemmology Ltd,
Sheffield, South Yorkshire,
<https://lustregemmology.com/shop>, 60 pages, illus.,
ISBN 978-1916165205.
GBP18.00 softcover.

This pocket-sized book relates the historical background of synthetic ruby from 1782, when small rubies were first fused together, to the beginning of industrial production in 1902.

In Part I, 'The First Synthetic Ruby', the author traces the early developments, including the contributions of Antoine-Laurent Lavoisier, Robert Hare, Edward Daniel Clarke and Marc Antoine Augustin Gaudin. After Lavoisier invented the oxygen blowpipe in 1782, he was the first to fuse rubies together and the first to synthesise corundum from alumina. Thus, ruby fusion and synthesis first occurred 37 years earlier than previously thought. The next advances in blow-type technology were made by Hare. Clarke was the first to document corundum globules produced from the fusion of alumina in 1820, and Gaudin was pivotal as the first to produce synthetic ruby in 1834 by adding potassium chromate. The resulting material, unfortunately, was opaque.

The second part, 'The Gemmological Revolution', examines further developments which led to the production of large, transparent synthetic rubies on an industrial scale. Jacques-Joseph Ébelmen synthesised microscopic transparent rubies from a solution in 1847. Thirty years later Edmund Frémy and Charles Feil succeeded in synthesising transparent rubies of an appreciable size. Geneva flame-fusion synthetic rubies, from an unknown inventor, appeared in 1886. They were large and transparent, and were the first synthetic gemstones to trouble the jewellery industry. Auguste Verneuil developed a more efficient flame-fusion technique in 1892 and published the details of his method in 1902. The industrial production of synthetic ruby then began, which placed these vibrant red gems within reach of the general public.

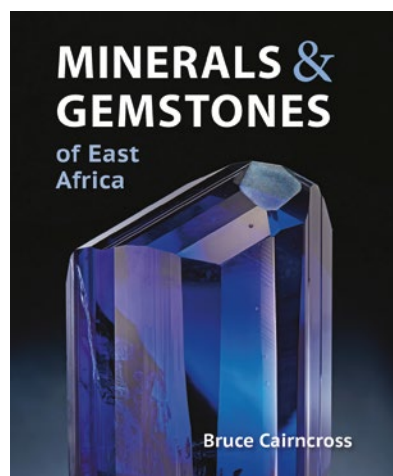
This book grew out of the author's Gemmology Diploma project and is successful in presenting the most accurate, up-to-date information available on the subject.

The work is well-researched and not overly technical, with easy-to-read text, and it is nicely illustrated with 40 images. It also includes an extensive bibliography. The author is passionate and knowledgeable about the subject, and the work is well-suited for enthusiasts of early gem history, gemmology students and gemmology tutors. *The History of Synthetic Ruby* is an enjoyable read and I highly recommend it.

Guy Lalous

FEEG

Brussels, Belgium



Minerals and Gemstones of East Africa

By Bruce Cairncross, 2019. Struik Nature/Penguin Random House South Africa, Cape Town, www.penguinrandomhouse.co.za/book/minerals-gemstones-east-africa/9781775845560, 160 pages, illus., ISBN 978-1775845560 or e-ISBN 978-1775846987. ZAR250.00 softcover or GBP6.99 Kindle edn.

This attractive book on both mineral specimens and cut gemstones of East Africa contains extensive information and features numerous fine, full-colour photographs of excellent specimens from talented mineral and gem photographers, including Jeff Scovil, Mark Mauthner, Malte Sickinger, the author himself and many others.

Gemstone expert Bruce Bridges sets the theme in the foreword on page 6 by noting the worldwide importance of the gem and mineral bounty of East Africa. A preface and introduction follow. The latter includes a brief review of the geology of East Africa, mentioning

Peter Keller's 1992 book titled *Gemstones of East Africa*, which covered Kenya, Tanzania and Uganda. This new book expands to showcase all five countries that make up East Africa: Burundi, Kenya, Rwanda, Tanzania and Uganda. Each country is discussed briefly in the introduction, noting the mineral resources found there, along with geographic maps.

The heart of the book (pages 22–132) consists of a thorough documentation in alphabetical order—from actinolite to zoisite—of each important mineral found in the region. This is an invaluable resource, easy to use and quite complete, and includes nomenclature, properties, illustrations and information on each species' occurrence in East Africa. For the majority of minerals the illustrations feature both a crystal and cut gemstone; the most important species have much more. For example, grossular has seven pages with more than 20 photographs. Zoisite has 11 pages filled with information and great photos of many world-class specimens, both crystals and cut gems.

The author has done an excellent job of documenting rare stones that only collectors are likely to know, such

as wurtzite from Merelani and taaffeite from Tunduru in southern Tanzania. He mentions Ethiopian emeralds and opals as being outside the scope of this book but important enough to include; each is covered with photos and descriptive information.

Following the excellent 110-page alphabetical section, the author includes a page listing type-mineral species from East Africa, and an additional page of acknowledgements. These are followed by a valuable 'References and Further Reading' section (seven pages). The book concludes with an index that uses bold italic font to indicate pages containing illustrations.

Dr Bruce Cairncross is an accomplished author—and an excellent photographer—who has written many excellent books, mostly on minerals of southern Africa. This new volume on East Africa is of interest to mineral and gem collectors and gemmologists everywhere. I can highly recommend it as having real value for any library.

Bill Larson FGA

Pala International

Fallbrook, California, USA

Other Book Titles

COLOURED STONES

Mineralogy and Geochemistry of Gems

Ed. by Panagiotis Voudouris, Stefanos Karampelas, Vasilius Melfos and Ian Graham, 2020. MDPI, Basel, Switzerland, 528 pages, ISBN 978-3039280766 or e-ISBN 978-3039280773, <https://doi.org/10.3390/books978-3-03928-077-3>. CHF115.50 softcover or free PDF. *Note:* This book is a printed edition of a special issue of the journal *Minerals*.

Moldavite: The Gemstone that Fell to the Earth

By Ladislav David Rejl, 2019. Self-published, 300 pages, ISBN 978-1792326516. USD75.00 hardcover.

CULTURAL HERITAGE

Along the Amber Route: St Petersburg to Venice

By C. J. Schüler, 2020. Sandstone Press, Inverness, Scotland, 320 pages, ISBN 978-1912240913 or e-ISBN 978-1912240920. GBP16.99 hardcover or eBook.

Byzantium and the West: Jewelry in the First Millennium

By Jeffrey Spier, 2020. Paul Holberton Publishing, London, 200 pages, ISBN 978-0983854647. GBP35.00 softcover.

Magical Gems in Their Contexts

Ed. by Kata Endreffy, Árpád M. Nagy and Jeffrey Spier, 2019. Proceedings of the International Workshop Held at the Museum of Fine Arts, Budapest, Hungary, 16–18 February 2012, *Studia Archaeologica* No. 229, L'Erma di Bretschneider, Rome, Italy, 382 pages, ISBN 978-8891312976 or e-ISBN 978-8891313003. EUR230.00 hardcover or EUR184.00 eBook.

A Taste for Green: A Global Perspective on Ancient Jade, Turquoise and Variscite Exchange

Ed. by Carlos Rodríguez-Rellán, Ben A. Nelson and Ramón Fábregas Valcarce, 2020. Oxbow Books, Barnsley, South Yorkshire, 192 pages, ISBN 978-1789252743 or ASIN B082KB4F33. GBP45.00 hardcover or GBP27.00 Kindle edn.

GEM LOCALITIES

Minerals of the Grenville Province: New York, Ontario, and Québec

By George W. Robinson, Jeffrey Chiarenzelli and Michael Bainbridge, 2019. Schiffer Publishing, Atglen, Pennsylvania, USA, 208 pages, ISBN 978-0764357657. USD34.99 softcover.

Minerals from Marbles of Carrara and the Apuan Alps [Italy]

By Cristian Biagioni, Paolo Orlandi, Stefano Camarda, Matteo Chinellato, Roberto Appiani, Lorenzo del Chiaro and Giovanni Sanguineti, 2019. LoGisma, Florence, Italy, 144 pages, ISBN 978-8894926156. EUR35.00 hardcover.

GENERAL REFERENCE

Gemmological Tables for the Identification of Gemstones, Synthetic Stones, Artificial Products and Imitations/Gemmologische Tabellen zur Bestimmung von Edelsteinen, Synthesen, künstlichen Produkten und Imitationen, 4th edn.

By Ulrich Henn, Tom Stephan and Claudio C. Milisenda, 2020. Deutsche Gemmologische Gesellschaft e.V. and German Gemmological Association, Idar-Oberstein, Germany, 42 pages, ISBN 978-3000648564 (English) or ISBN 978-3000648557 (German). EUR25.00 softcover.

Gems and Gemmology: An Introduction for Archaeologists, Art-Historians and Conservators

By Stefanos Karampelas, Lore Kiefert, Danilo Bersani and Peter Vandenabeele, 2020. Short Introductions to Cultural Heritage Science, Springer, Cham, Switzerland, 112 pages, ISBN 978-3030354480 or e-ISBN 978-3030354497, <https://doi.org/10.1007/978-3-030-35449-7>. EUR62.39 hardcover or EUR50.28 eBook.

Mineral Collections in Arizona [USA]

Ed. by Wendell E. Wilson, 2020. Mineralogical Record, Tucson, Arizona, USA, 200 pages. USD25.00 softcover.

Mineral Collections in the Pacific Northwest [USA]

Ed. by Wendell E. Wilson, 2019. Mineralogical Record, Tucson, Arizona, USA, 192 pages. USD25.00 softcover.

The Munich Show/Mineralientage München: Wer sammelt...

Ed. by The Munich Show, 2019. Christian Weise

Verlag GmbH, Munich, Germany, 208 pages, ISBN 978-3921656907 (in German). EUR28.00 hardcover.

Physical Properties of Diamond and Sapphire

By Roshan L. Aggarwal and Anant K. Ramdas, 2019. CRC Press and Taylor & Francis Group, Boca Raton, Florida, USA, 76 pages, ISBN 978-0367235086 or e-ISBN 978-0429283260. USD65.00 hardcover or USD19.80 eBook.

INSTRUMENTATION

Chemical Analysis in Cultural Heritage

Ed. by Luigia Sabbatini and Inez Dorothé van der Werf, 2020. Walter de Gruyter GmbH, Berlin, Germany, 473 pages, ISBN 978-3110456417, e-ISBN 978-3110456486 (ePub) or e-ISBN 978-3110457537 (PDF), <https://doi.org/10.1515/9783110457537>. EUR139.95 hardcover, ePub or PDF.

Handbook of Mineral Spectroscopy, Vol. 1: X-ray Photoelectron Spectra

By J. Theo Kloprogge and Barry Wood, 2020. Elsevier, Amsterdam, The Netherlands, 532 pages, ISBN 978-0128045220 or e-ISBN 978-0128045237, <https://doi.org/10.1016/c2015-0-01704-x>. EUR285.00 hardcover or eBook.

Modern Raman Spectroscopy – A Practical Approach, 2nd edn.

By Ewen Smith and Geoffrey Dent, 2019. John Wiley & Sons Ltd, Hoboken, New Jersey, USA, 256 pages, ISBN 978-1119440550 or e-ISBN 978-1119440598, <https://doi.org/10.1002/9781119440598>. USD75.00 hardcover or eBook.

Vibrational (Infrared and Raman) Spectra of Minerals and Related Compounds

By Nikita V. Chukanov and Marina F. Viggasina, 2020. Springer, Cham, Switzerland, 1,376 pages, ISBN 978-3030268022 or e-ISBN 978-3030268039, <https://doi.org/10.1007/978-3-030-26803-9>. CHF271.50 hardcover or CHF217.00 eBook.

JEWELLERY HISTORY

Adorning Fashion: The History of Costume Jewellery to Modern Times

By Deanna Farneti Cera, 2019. ACC Art Books, Woodbridge, Suffolk, 400 pages, ISBN 978-1788840477. GBP60.00 hardcover.

“Living Nobly”: Jewelry of the Renaissance Courts
By Beatriz Chadour-Sampson and Sandra Hindman,
2020. Les Enluminures, Paris, France, 115 pages, ISBN
978-2956702429. USD18.00 softcover.

JEWELLERY AND OBJETS D'ART

The Cartiers: The Untold Story of a Jewelry Dynasty
By Francesca Cartier Brickell, 2019. Ballantine
Books, New York, New York, USA, 656 pages,
ISBN 978-0525621614 or e-ISBN 978-0525621621.
USD35.00 hardcover or USD13.99 ePub.

Chaumet Tiaras

By Natasha Fraser-Cavassoni and Clare Phillips, 2020.
Thames & Hudson, New York, New York, USA, 256
pages, ISBN 978-0500210284. USD125.00 hardcover.

Gemstones: A Jewelry Maker's Guide to Identifying and Using Beautiful Rocks

By Judith Crowe, 2019. F + W Media, Blue Ash,
Ohio, USA, 192 pages, ISBN 978-1632506825.
USD29.99 hardcover.

Hunt: Kadri Mälk's Jewellery Collection

By Kadri Mälk, Viivi Luik, Liesbeth den Besten,
Una Meistere and Tanel Veenr, 2020. Arnoldsche
Art Publishers, Stuttgart, Germany, 400 pages,
ISBN 978-3897905924 (in English and Estonian).
EUR44.00 hardcover.

Jewellery in Context: A Multidisciplinary Framework for the Study of Jewellery

By Marjan Unger, 2020. Arnoldsche Art Publishers,
Stuttgart, Germany, 232 pages, ISBN 978-3897905771.
EUR15.00 softcover.

Jewelry

By Petra Hölscher, 2020. Arnoldsche Art Publishers,
Stuttgart, Germany, 520 pages, ISBN 978-3897905856
(in English and German). EUR58.00 hardcover.

Jiro Kamata: Voices

By Makiko Akiyama, Levi Higgs, Otto Künzli,
Kellie Riggs, Sool Park and Yaman Shao, 2019.
Arnoldsche Art Publishers, Stuttgart, Germany,
272 pages, ISBN 978-3897905795 (in English,
Chinese and Japanese). EUR44.00 hardcover.

Lacloche Joailliers

By Laurence Mouillefarine and Veronique
Ristelhueber, 2020. Les Éditions Norma, Paris, France,

320 pages, ISBN 978-2376660248 (in French and
English). EUR60.00 hardcover.

Magnitude: Cartier High Jewelry

By François Chaille and Capucine Juncker, 2020.
Flammarion, Paris, France, 256 pages, ISBN
978-2080204332. USD125.00 hardcover (English edn).

Margit Hart Mindscapes

By Carl Aigner, Mirella Cisotto Nalon, Nina
Schedlmayer and Jonathan Wahl, 2019. Arnoldsche
Art Publishers, Stuttgart, Germany, 128 pages,
ISBN 978-3897905764 (in English and German).
EUR28.00 softcover.

Sam Kramer: Jeweler on the Edge

By Toni Greenbaum, 2020. Arnoldsche Art
Publishers, Stuttgart, Germany, 160 pages, ISBN
978-3897905641. EUR28.00 hardcover.

Van Cleef & Arpels – Time, Nature, Love

By Nicolas Bos, Franco Cologni, Vivienne Becker and
Stefano Papi, 2019. Skira, Milan, Italy, 272 pages,
ISBN 978-8857241777. EUR50.00 hardcover.

ORGANIC/BIOGENIC MATERIALS

Mediterranean Cold-Water Corals:

Past, Present and Future

Ed. by Covadonga Orejas and Carlos Jiménez, 2019.
Springer, Cham, Switzerland, ISBN 978-3319916071
or e-ISBN 978-9811314599, <https://doi.org/10.1007/978-3-319-91608-8>. EUR207.99 hardcover or
EUR160.49 eBook.

SOCIAL STUDIES

The Anthropology of Precious Minerals

Ed. by Elizabeth Ferry, Annabel Vallard and Andrew
Walsh, 2019. University of Toronto Press, Toronto,
Ontario, Canada, 216 pages, ISBN 978-1487503178,
e-ISBN 978-1487517342 (ePub) or e-ISBN
978-1487517335 (PDF). CAN55.00 hardcover,
ePub or PDF.

Thread and Fire: Textiles and Jewellery from the Isles of Indonesia and Timor

By Linda S. McIntosh, 2020. River Books Co. Ltd,
Bangkok, Thailand, 344 pages, ISBN 978-6164510357.
THB2,800.00 hardcover.

Literature of Interest

COLOURED STONES

Characteristic features of lapis lazuli from different provenances, revised by μ XRF, ESEM, PGAA and PIXE. N. Renate, F. Ines, K. Zsolt, S.-N. Zoltán and K. Imre, *Journal of Geological Resource and Engineering*, **7**(2), 2019, 57–69, <https://doi.org/10.17265/2328-2193/2019.02.003>.*

Chemical composition and spectrum characteristic of nephrite from Luodian, Guizhou Province and Dahua, Guangxi Province. L. Li, Z. Liao, Q. Zhong, Z. Zhou, M. Lai and D. Cui, *Journal of Gems & Gemmology*, **21**(5), 2019, 18–24 (in Chinese with English abstract).

Crystal gazing – Magnesiotaafeite. J.-M. Arlabosse, *Gemmology Today*, March 2020, 28–29, www.worldgemfoundation.com/GTMARCH2020DV.*

Emeralds from the most important occurrences: Chemical and spectroscopic data. S. Karampelas, B. Al-Shaybani, F. Mohamed, S. Sangsawong and A. Al-Alawi, *Minerals*, **9**(9), 2019, article 561 (29 pp.), <https://doi.org/10.3390/min9090561>.*

Exploration of inclusion characteristic and formation environment of a kind of petroleum-bearing quartz. X. Ye, Z. Qiu, Y. Zhang and L. He, *Journal of Gems & Gemmology*, **21**(6), 2019, 31–39 (in Chinese with English abstract).

Gem-quality green Cr-bearing andradite (var. demantoid) from Dobšiná, Slovakia. J. Štubňa, P. Bačík, J. Fridrichová, R. Hanus, Ľ. Illášová, S. Milovská, R. Škoda, T. Vaculovič *et al.*, *Minerals*, **9**(3), 2019, article 164 (12 pp.), <https://doi.org/10.3390/min9030164>.*

Gemmological characteristic of a kind of purple jade: Phosphosiderite. L. Yu, L. Li, S. Cao, F. Wang and L. Guo, *Journal of Gems & Gemmology*, **21**(6), 2019, 40–49 (in Chinese with English abstract).

Gemmological and mineralogical characteristics of turquoise from Tongling, Anhui Province. J. Liu, Y. Wang, F. Liu, C. He and F. Liu, *Journal of Gems & Gemmology*, **21**(6), 2019, 58–65 (in Chinese with English abstract).

Gemmological characteristics and color origin of blue-violet iolite. S. Cheng, Y. Yang and R. Mou, *Superhard Material Engineering*, **31**(4), 2019, 60–63 (in Chinese with English abstract).

Gemmological characteristics and colouring mechanism of a light blue opal. Z. Mo and M. Deng, *Superhard Material Engineering*, **31**(4), 2019, 64–68 (in Chinese with English abstract).

Gemmological and spectral characterization of brownish yellow tourmaline from Mozambique. Q. Liao, W. Huang, Q. Zhang and J. Pei, *Spectroscopy and Spectral Analysis*, **39**(12), 2019, 3844–3848 (in Chinese with English abstract).

The impact of cut on colored gemstones. L. Elser, *GemGuide*, **39**(2), 2020, 8–11.

Impact of different standard lighting sources on red jadeite and color quality grading. X. Pan, Y. Guo, Z. Liu, Z. Zhang and Y. Shi, *Earth Sciences Research Journal*, **23**(4), 2019, 371–378, <https://doi.org/10.15446/esrj.v23n4.84113>.*

Infrared spectra and inclusions of emeralds from Pakistan. H. Guo and X. Yu, *Acta Petrologica et Mineralogica*, **38**(5), 2019, 724–732 (in Chinese with English abstract).

Inhabituelle anorthite colorée par des inclusions chromifères [Unusual anorthite colored by chromiferous inclusions]. J.-M. Arlabosse and J. Boemo, *Revue de Gemmologie A.F.G.*, No. 206, 2018, 9–11 (in French).

L'état de l'art sur les saphirs australiens [State of the art on Australian sapphires]. I. Graham, N. Raffan, R. Bottrill, D.M. Duncan, W.D. Birch, P.J. Downes and S.M. Stocklmayer, *Revue de Gemmologie A.F.G.*, No. 207, 2019, 8–11, 13–21 (in French).

Mondstein aus den Alpen [Moonstone from the Alps]. U. Henn, B. Huaysan and T. Stephan, *Gemmologie: Zeitschrift der Deutschen Gemmologischen Gesellschaft*, **68**(3/4), 2019, 37–48 (in German with English abstract).

Our friends the inclusions. The detective at the party of inclusions. Seventh episode. L. Costantini and C. Russo, *Rivista Italiana di Gemmologia/Italian Gemmological Review*, No. 8, 2020, 7–14.

A resounding mantra of the gemstone geographical origin. A. Scarani and P. Minieri, *Rivista Italiana di Gemmologia/Italian Gemological Review*, No. 8, 2020, 68–74.

9

A review of the classification of opal with reference to recent new localities. N.J. Curtis, J.R. Gascooke, M.R. Johnson and A. Pring, *Minerals*, 9(5), 2019, article 299 (20 pp.), <https://doi.org/10.3390/min9050299>.*

Statistical luminescence method for determining the region of origin of emeralds. V.I. Solomonov, A.V. Spirina, M.P. Popov, M.A. Ivanov and A.I. Lipchak, *Journal of Optical Technology*, 86(7), 2019, 446–451, <https://doi.org/10.1364/jot.86.000446>.

Study on inclusions in almandine garnet from Vemireddipalle area, Krishna District, Andhra Pradesh, India. N. Sultana, *International Journal of Scientific Research in Science and Technology*, 6(4), 2019, 82–85, <https://doi.org/10.32628/ijsrst196418>.*

Turmalin mit Coltan Einschlüssen – ein Beispiel von natürlicher Selbstbestrahlung [Tourmaline with coltan inclusions – An example of auto-irradiation]. H. A. Hänni, C.C. Milisenda and H.A.O. Wang, *Gemmologie: Zeitschrift der Deutschen Gemmologischen Gesellschaft*, 68(3/4), 2019, 55–60 (in German with English abstract).

What is jade? Musings of a jade enthusiast. I. Mercer, *Australian Gemmologist*, 27(2), 2019, 56–64.

World sapphire market update 2020. R. Hughes and E.B. Hughes, *GemGuide*, 39(1), 2020, 4–10.

CULTURAL HERITAGE

Analyse Gemmologique de la bague de George Sand [Gemological analysis of George Sand's ring]. D. Chabert, G. Panczer and G. Riondet, *Revue de Gemmologie A.F.G.*, No. 207, 2019, 27–31 (in French).

The Beverley gems: Algernon Percy's notebook. C. Wagner, *Gemmae: An International Journal on Glyptic Studies*, 1, 2019, 137–154, <https://doi.org/10.19272/201914201010>.

Étude gemmologique d'objets de joaillerie du X^{ème} siècle, trésor de Preslav, Bulgarie [Gemological study of 10th century jewellery objects, Preslav treasure, Bulgaria]. E. Strack and R.I. Kostov, *Revue de Gemmologie A.F.G.*, No. 206, 2018, 23–28 (in French with English abstract).

Metamorphoses of Tithonus in Roman glyptic. V. Dasen, *Gemmae: An International Journal on Glyptic Studies*, 1, 2019, 63–80, <https://doi.org/10.19272/201914201005>.

Multum in Parvo [exhibition of ancient cameos]. T. Holman, *Gems&Jewellery*, 29(2), 2020, 22–23.

A second seal of Alaric, Rex Gothorum. G. Kornbluth, *Gemmae: An International Journal on Glyptic Studies*, 1, 2019, 105–126, <https://doi.org/10.19272/201914201008>.

Trésor de la tombe kv 62, Toutânkhamon [Treasure of the tomb KV 62, Tutankhamun]. E. Gonthier, *Revue de Gemmologie A.F.G.*, No. 207, 2019, 22–26 (in French).

DIAMONDS

Blood, sweat & fears [diamonds from West Africa]. J. Asplund, *Gemmology Today*, March 2020, 60–65, www.worldgemfoundation.com/GTMARCH2020DV.*

Considerations to valuing colored diamonds. S.M. Robertson, *GemGuide*, 39(3), 2020, 4–7.

Diamond-forming media through time – Trace element and noble gas systematics of diamonds formed over 3 billion years of Earth's history. S. Timmerman, M.Y. Krebs, D.G. Pearson and M. Honda, *Geochimica et Cosmochimica Acta*, 257, 2019, 266–283, <https://doi.org/10.1016/j.gca.2019.05.014>.

Multi-analytical characterization of Fe-rich magnetic inclusions in diamonds. M. Piazzzi, M. Morana, M. Coisson, F. Marone, M. Campione, L. Bindi, A.P. Jones *et al.*, *Diamond and Related Materials*, 98, 2019, article 107489 (9 pp.), <https://doi.org/10.1016/j.diamond.2019.107489>.

A new approach to understanding diamond surface features based on a review of experimental and natural diamond studies. Y. Fedortchouk, *Earth-Science Reviews*, 193, 2019, 45–65, <https://doi.org/10.1016/j.earscirev.2019.02.013>.

Origin of milky optical features in type IaB diamonds: Dislocations, nano-inclusions, and polycrystalline diamond. T. Gu, H. Ohfujii and W. Wang, *American Mineralogist*, 104(5), 2019, 652–658, <https://doi.org/10.2138/am-2019-6699>.

Provenance of pink diamonds: Argyle type and non-Argyle from four continents. B. Deljanin, *GemGuide*, 39(3), 2020, 8–11.

FAIR TRADE

Blood diamonds: An analysis of the state of affairs and the effectiveness of the Kimberley Process.

M. Schulte and C.M. Paris, *International Journal of Sustainable Society*, **12**(1), 2020, 51–75, <https://doi.org/10.1504/ijssoc.2020.105017>.

The slow agony of the Kimberley process. Ethics in the COVID-19 times. P. Minieri, *Rivista Italiana di Gemmologia/Italian Gemological Review*, No. 8, 2020, 31–43.

9

GEM LOCALITIES

The best of British [Whitby jet and Blue John].

L. Bailey, *Gems&Jewellery*, **29**(2), 2020, 32–35.

A future in amethyst [Rwanda]. D. Craig, *Gems&Jewellery*, **29**(2), 2020, 10–12.

Gem-quality zircon megacrysts from placer deposits in the Central Highlands, Vietnam—Potential source and links to Cenozoic alkali basalts.

V.B.T. Sinh, Y. Osanai, C. Lenz, N. Nakano, T. Adachi, E. Belousova and I. Kitano, *Minerals*, **9**(2), 2019, article 89 (18 pp.), <https://doi.org/10.3390/min9020089>.*

Gemstone buying in Brazil - 20 years on. G. Walsh, *Australian Gemmologist*, **27**(2), 2019, 65–70.

Interesting occurrence of rubies in Macedonia.

L. Illášová and I. Turnovec, *Gemologický spravodajca*, **9**(1), 2019, 14–19, www.gu.fpv.ukf.sk/images/GS/2019_1_illasoiva.pdf (in Slovak with English abstract).*

L'Oregon sunstone ou la renaissance d'un phénix [Oregon sunstone or the rebirth of a phoenix].

E. Thoreux, *Revue de Gemmologie A.F.G.*, No. 207, 2019, 4–7 (in French).

L'Oural, un trésor minier au coeur de la Russie [The Urals, a mining treasure in the heart of Russia].

N. Belenkov, *Revue de Gemmologie A.F.G.*, No. 206, 2018, 19–22 (in French).

Pink amethyst from El Choique mine, Patagonia, Argentina. A.L. Rainoldi, G.R. Rossman, L. Di Martino and A. Oteiza, *Mineralogical Record*, **51**(2), 2020, 293–303.

Tourmaline aus Namibia [Tourmaline from Namibia].

U. Henn, T. Stephan and B. Huaysan, *Gemmologie: Zeitschrift der Deutschen Gemmologischen Gesellschaft*, **68**(3/4), 2019, 15–36 (in German with English abstract).

Visite des mines d'émeraude de Las Cunas

(Esmeraldas Santa Rosa) et Las Pavas (Vetas Sierra Alta) [Visit to the emerald mines of Las Cunas (Esmeraldas Santa Rosa) and Las Pavas (Vetas Sierra Alta)]. D. Giard, *Revue de Gemmologie A.F.G.*, No. 206, 2018, 16–18 (in French).

INSTRUMENTATION

Gemology toys for girls and boys [handheld gem testers].

N. Zolotukhina, *Gemmology Today*, March 2020, 66–69, www.worldgemfoundation.com/GTMARCH2020DV.*

Quantitative assessment of the precious stones color by machine vision.

A.S. Kushkoeva, A.N. Chertov, E.V. Gorbunova, A.A. Alekhin, V.S. Peretyagin, D.E. Troshkin, J. Beyerer and F. Puente León, *SPIE Optical Metrology, Automated Visual Inspection and Machine Vision III*, **11061**, 2019, article 110610L (7 pp.), <https://doi.org/10.1117/12.2526026>.

Sensitive and rapid oxygen isotopic analysis of nephrite jade using large-geometry SIMS.

A.K. Schmitt, M.-C. Liu and I.E. Kohl, *Journal of Analytical Atomic Spectrometry*, **34**(3), 2019, 561–569, <https://doi.org/10.1039/c8ja00424b>.

Slick magnet [magnetism for gem identification].

K. Feral, *Gemmology Today*, March 2020, 36–41, www.worldgemfoundation.com/GTMARCH2020DV.*

MISCELLANEOUS

The changing role of international trade shows in today's internationalisation process of SMEs: An application to SMEs in the diamond sector.

D. Nassar and Y. Nauwelaerts, *Journal of Creativity and Business Innovation*, **5**, 2019, 5–42, www.journalcbi.com/international-trade-shows-in-diamond-sector.html.*

A comparative mathematical analysis of the internal reflections in a spherical concave faceted vs. a plane faceted gem.

R. Zancanella, *Rivista Italiana di Gemmologia/Italian Gemological Review*, No. 8, 2020, 44–51.

9

Rabbit's eye red and golden red. GIT'S new ruby color standards.

T. Leelawatanasuk, W. Atichat, V. Pisutha-Arnond, C. Sutthirat and J. Jakkawanvibul, *Rivista Italiana di Gemmologia/Italian Gemological Review*, No. 8, 2020, 53–55.

9

NEWS PRESS

Are laboratory-grown diamonds the more ethical choice to say ‘I do’? O. Milman, *The Guardian*,

10 March 2020, www.theguardian.com/lifeandstyle/2020/mar/10/diamonds-lab-grown-climate-change.*

The guilt-free engagement ring is here. C. Ballentine, Bloomberg, 20 February 2020, www.bloomberg.com/news/articles/2020-02-20/ethical-engagement-rings-that-are-truly-eco-friendly-guilt-free.*

London’s jewelry ‘garden’ [Hatton Garden].

R. Garrahan, *New York Times*, 10 February 2020, www.nytimes.com/2020/02/10/fashion/jewelry-hatton-garden-london.html.*

Pearls are forever. V. Gomelsky, *New York Times*, 10 February 2020, www.nytimes.com/2020/02/10/fashion/jewelry-pearls-engagement-rings.html.*

Spinel: ‘The great impostor’ no more. K. Beckett, *New York Times*, 10 February 2020, www.nytimes.com/2020/02/10/fashion/jewelry-spinel-christies-sothebys-cartier.html.*

The woman shaking up the diamond industry [Eira Thomas of Lucara]. E.

Caesar, *New Yorker*, 27 January 2020, www.newyorker.com/magazine/2020/02/03/the-woman-shaking-up-the-diamond-industry.*

ORGANIC/BIOGENIC GEMS

DNA fingerprinting: An effective tool for taxonomic identification of precious corals in jewelry. B.

Lendvay, L.E. Cartier, M. Gysi, J.B. Meyer, M.S. Krzemnicki, A. Kratzer and N.V. Morf, *Scientific Reports*, **10**(1), 2020, article 8287 (12 pp.), <https://doi.org/10.1038/s41598-020-64582-4>.*

Étude spectrale de deux ambres des Alpes françaises et suisses : l’allingite et la planfayonite [Spectral study of two ambers from the French and Swiss Alps: Allingite and planfayonite].

Y. Maquignon and D. Decrouez, *Revue de Gemmologie A.F.G.*, No. 206, 2018, 4–8 (in French).

Global ivory market prices since the 1989

CITES ban. M.C. Sosnowski, T.G. Knowles, T. Takahashi and N.J. Rooney, *Biological Conservation*, **237**, 2019, 392–399, <https://doi.org/10.1016/j.biocon.2019.07.020>.*

Ivory and rhino horn – Australia’s plan to close the ‘back door’ on illegal trade. K. Morrissey, *Australian Gemmologist*, **27**(2), 2019, 71–73.

A journey into the Mediterranean coral (*Corallium rubrum*) manufacturing process. F. Sequino and S. Coppola, *Rivista Italiana di Gemmologia/Italian Gemmological Review*, No. 8, 2020, 57–67. 9

The visual identification of beeswax [amber].

H. Zhu, S. Chen and T. Li, *Superhard Material Engineering*, **31**(5), 2019, 59–62 (in Chinese with English abstract).

PEARLS

Impact of selected the [sic] household chemicals on pearls. A. Čičková and J. Štubňa, *Gemologický spravodajca*, **9**(2), 2019, 5–17, www.gu.fpv.ukf.sk/images/GS/2019_2_cickova.pdf (in Slovak with English abstract).*

*(in Slovak with English abstract).**

Pearl formation in the Japanese pearl oyster (*Pinctada fucata*) by CaCO₃ polymorphs: Pearl quality—specific biomineralization processes and their similarity to shell regeneration. Y. Sato and A. Komaru, *Aquaculture Research*, **50**(6), 2019, 1710–1717, <https://doi.org/10.1111/are.14057>.

A preliminary study of quantification method of Chinese freshwater pearl. N. Geng, L. Li, C. Xu, Y. Huang and Z. Shen, *Journal of Gems & Gemmology*, **21**(5), 2019, 68–74 (in Chinese with English abstract).

SIMULANTS

Environmental non-colored round brilliant synthetic moissanite’s changes evaluation of fire and brightness. F. Liu, Y. Guo, J. Tang and Z. Ma, *Ekoloji*, **28**(107), 2019, 4783–4792, <http://ekolojidergisi.com/download/environmental-non-colored-round-brilliant-synthetic-moissanites-changes-evaluation-of-fire-and-6086.pdf>.*

Fake and synthetic minerals; A way to sustain the gem supply. A. Calik, O. Karaca, C. Yasar and E.U. Ulugergerli, in A.K. Agnihotri, K.R. Reddy and A. Bansal, Eds., *Environmental Geotechnology. Lecture Notes in Civil Engineering*. Springer,

Singapore, 2019, 319–328, https://doi.org/10.1007/978-981-13-7010-6_30.

Identification of an emerald imitation. H. Zhu, C. Fan, T. Li, G. Shan, B. Sun and X. Ma, *Superhard Material Engineering*, **31**(6), 2019, 47–50 (in Chinese with English abstract).

Moonstone imitation: Alkyd resin. A. Hu, Y. Chen, X. Gu and H. Wang, *Journal of Gems & Gemmology*, **21**(5), 2019, 65–67 (in Chinese with English abstract).

SYNTHETICS

Gemmological characteristic of synthetic diamond “Lightbox jewelry”. H. Dai, S. Tang, T. Lu, J. Cheng, Z. Song, D. Jiang, X. Wu, X. Zhang *et al.*, *Journal of Gems & Gemmology*, **21**(5), 2019, 38–47 (in Chinese with English abstract).

Research on laboratory testing features of chemical vapor deposition in overgrowth diamonds. S. Tang, J. Su, T. Lu, Y. Ma, J. Ke, Z. Song, J. Zhang, X. Zhang *et al.*, *Rock and Mineral Analysis*, **38**(1), 2019, 62–70 (in Chinese with English abstract).

Synthesis and characteristics of type Ib diamond doped with NiS as an additive. J.K. Wang, S.S. Li, N. Wang, H.J. Liu, T.C. Su, M.H. Hu, F. Han *et al.*, *Chinese Physics Letters*, **36**(4), 2019, article 046101 (6 pp.), <https://doi.org/10.1088/0256-307x/36/4/046101>.

TREATMENTS

Epoxy resin filled aquamarine. J. Štubňa, *Gemologický spravodajca*, **9**(1), 2019, 5–13, www.gu.fpv.ukf.sk/images/GS/2019_1_stubna.pdf (in Slovak with English abstract).*

Hydrogen-rich green diamond color-treated by multi-step processing. W. Huang, P. Ni, T. Shui and G. Shi, *Gems & Gemology*, **55**(3), 2019, 398–405, <https://doi.org/10.5741/GEMS.55.3.398>.*

Spectroscopic characteristic of orange red to purple colour-treated diamond from Lotus Colors, Inc. U.S.A. M. Qu and A.H. Shen, *Journal of Gems & Gemmology*, **21**(2), 2019, 17–23 (in Chinese with English abstract).

Ungewöhnliche Behandlungen – Stabilisierte Aquamarine und gefarbte Feldspäte [Uncommon treatments – Stabilised aquamarines and dyed feldspars]. T. Stephan, C.C. Milisenda, S. Müller and B. Huaysan, *Gemmologie: Zeitschrift der Deutschen Gemmologischen Gesellschaft*, **68**(3/4), 2019, 61–64 (in German with English abstract).

COMPILATIONS

Gemmologie Aktuell [Gemmology News]. Blödite • Sapphire with unusual inclusion scenery • Aventurescent beryl. *Gemmologie: Zeitschrift der Deutschen Gemmologischen Gesellschaft*, **68**(3/4), 2019, 9–14 (in German and English).

CONFERENCE PROCEEDINGS

1st Pearl Symposium. Manama, Bahrain, 14–15 November 2019, 36 pp., www.danat.bh/wp-content/uploads/2019/11/PEARL-SYMPOSIUM-V12.pdf.*

46th Rochester Mineralogical Symposium. Rochester, New York, USA, 11–14 April 2019, 42 pp., www.rasny.org/minsymp/Program%20Notes%20RMS%2046%20web.pdf.*

Amberif 2019: Baltic Amber (Succinite): An Intriguing Resin. Gdańsk, Poland, 22 March, 26 pp., http://amberif.amberexpo.pl/mtgsa2010/library/File/AMBERIF/2019/Amberif_2019_pl_eng_18_03_2019_rgb.pdf.*

MAESA 2019: Earth Sciences and Sustainable Development. Yangon, Myanmar, 29 November–1 December 2019, 133 pp., www.maesa.org/download/MAESA2019-Proceedings%20&%20Abstracts.pdf (see pp. 74–82 for abstracts of session titled ‘Mineralogy, Gemology and Genesis of Gem Deposits’).*

*Article freely available for download, as of press time

ERRATUM

In the Gem-A Notices section of *The Journal* Vol 36, No. 8 (pp. 776–785), Yi Shen (and not Li Shen, as mentioned in the errata included in Vol. 37 No. 1) should have been listed under ‘Gemmology Diploma Passes with Distinction’ rather than ‘Gemmology Diploma Passes’. *The Journal* apologises for the error.



Gem-A

THE GEMMOLOGICAL ASSOCIATION
OF GREAT BRITAIN



Study gemmology online!

- Online class groups
- Virtual learning
- Interactive quizzes
- Start your journey to FGA Membership with online learning by leading provider, Gem-A



COURSES BEGIN IN SEPTEMBER 2020

Contact education@gem-a.com for an application form

Creating gemmologists since 1908





PAUL WILD

EXCELLENCE IN
GEMSTONE INNOVATION



PARAIBA

*Extravagant and equally elegant: the Paraiba tourmaline is a star –
rarer than diamonds and highly valuable.*

MINING • CUTTING • CREATION

PAUL WILD OHG • AUF DER LAY 2 • 55743 KIRSCHWEILER • GERMANY
T: +49.(0)67 81.93 43-0 • F: +49.(0)67 81.93 43-43 • E-MAIL: INFO@PAUL-WILD.DE • WWW.PAUL-WILD.DE